Modeling and numerical simulation applied to the prediction of the effect of drugs in the cardiovascular system

Sara Costa Faya

Modeling and numerical simulation applied to the prediction of the effect of drugs in the cardiovascular system

THÈSE DE DOCTORAT

présentée par

Sara Costa Faya

pour obtenir le grade de

DOCTEUR DE SORBONNE UNIVERSITÉ

Spécialité : Mathématiques Appliquées

Soutenue publiquement le 16 décembre 2024 devant le jury composé de :

Simone Deparis	Rapporteur
Miguel A. Fernández	Directeur de thèse
Pieter-Jan Guns	Invité
Damiano Lombardi	Co-directeur de thèse
Marie Postel	Examinatrice
Yves Renard	Rapporteur
Anne-Virginie Salsac	Présidente
Marina Vidrascu	Invitée

Après avis favorables des rapporteurs: Simone Deparis et Yves Renard

Thèse préparée au sein de l'équipe-projet COMMEDIA
Centre de Recherche Inria de Paris
et Laboratoire Jacques-Louis Lions (Sorbonne Université et CNRS)

A mis padres.

Acknowledgements

First of all, I want to thank my supervisors, *Miguel A. Fernández*, *Damiano Lombardi*, and *Marina Vidrascu*. This thesis wouldn't exist without your guidance, support, and contributions. *Miguel*, thank you for your advice and feedback throughout my PhD. You pushed me out of my comfort zone, helping me grow into a more independent researcher. Your insistence on precision and structure taught me how to think and work in a mathematically rigorous way, and this is something that doesn't always come naturally to a physicist! Your deep knowledge and expertise were fundamental to the development of this thesis, and I'm truly grateful for everything you've shared with me. *Damiano*, thank you for your patience and for always being available to help, no matter how many questions I had. Your ability to simplify even the most complex ideas with clear, physical examples opened my mind to new ways of thinking. You encouraged me to approach problems independently and gave me the confidence to keep going when things got challenging. Our discussions were always inspiring and prepared me to face the next steps. *Marina*, thank you for bringing your deep knowledge of solid mechanics and finite elements to this work. Your experience was really important to so much of what I've learned during these years. Our debugging sessions, where we solved problems like detectives, were not just productive but also fun. I especially appreciated your advice and support when revising my work. You always knew how to bring clarity and keep things moving forward. I've learned so much from each of you, not just about research, but about how to approach problems and develop as a professional!

A big thank you to *Simone Deparis* and *Yves Renard* for taking the time to review this thesis. I truly appreciate your detailed feedback and your thoughtful, kind, and constructive remarks. I also extend my gratitude to *Anne-Virginie Salsac* and *Marie Postel* for agreeing to be part of my jury.

I couldn't have completed this project without the financial support provided by INSPIRE, part of the EU Horizon 2020 Research and Innovation Programme under the Marie Skłodowska-Curie GA 858070. It has been a pleasure to have the opportunity to be one of the early-stage researchers of the INSPIRE team. *Pieter-Jan*, I want to especially thank you for everything you've done to make this PhD network a reality. I find your dedication and hard work truly inspirational. You didn't just coordinate the project and bring together researchers from different backgrounds: you created a real sense of community and promoted interdisciplinary collaborations. On a personal level, you introduced me to safety pharmacology and gave me the chance to do a secondment in Antwerp. That experience allowed me to discover the experiment that became the core of the mathematical models in my PhD. I also deeply appreciate you taking the time to be part of my jury and attending my defense. *Paz*, muchísimas gracias por el increíble trabajo que hiciste como project manager de INSPIRE. Tu dedicación para coordinarlo todo, organizar experiencias como las summer schools y mantenernos al día con tus correos claros y precisos, hizo que este camino fuese más sencillo y enriquecedor. Gracias por tu

cercanía y por estar siempre dispuesta a ayudarme cuando lo he necesitado. ¡Hemos tenido la suerte de contar con la mejor project manager posible!

I want to take a moment to thank everyone in the INSPIRE network: *Benji, Bohdan, Brigitta, Callan, Charles, Chris, Dustin, Elham, Haibo, Marieke, Martina, Patrizia, and Tommaso*. Each one of you has contributed in a unique way to making this journey special. Our shared moments during the summer schools and annual meetings were filled with fun, learning, and unforgettable experiences. I am truly grateful for the connections we've built. A special thanks to *Callan* for working with me throughout my PhD on the experimental part of my models, for all the support during my time in Antwerp, and for always being kind to me. To *Elham* and *Haibo*, thank you for working with me on the CEMRACS project under *Damiano's* supervision and for being such great friends throughout. *Elham*, I'll always remember the fun we had, our German discussions, and your spontaneity and honesty, which I really appreciate. *Haibo*, you were an awesome office mate, and I always enjoyed our talks and meals outside together.

Also, thanks to all the present and former members of COMMEDIA. Many thanks to *Marloes* for helping me implement the fibers of the model, for everything we learned together, and for the pleasure of working with her. A special mention to my friends *Fabien, Margherita, María, Marguerite, Mirco, Oscar, Sebastien, and Vicente*. *Fabien*, merci pour être toujours la bonne humeur incarnée et notre roi des jeux de société. *Margherita*, grazie per essere stata sempre qui per me in questi anni. *María*, gracias por ser siempre casa y el alma de todas las fiestas. *Marguerite*, merci de m'inspirer avec ta passion pour l'écologie et ta façon calme et réfléchie d'aborder la vie. *Mirco*, nonostante tu sia stato un flash in COMMEDIA, grazie per tutto il divertimento. *Sebastien*, merci d'avoir été notre prof de français et de toujours être partant pour tous les plans, petits ou grands. *Vicente*, gracias por ser un torbellino de energía y nuestro programador de confianza. Y por último, *Oscar*, por ser como un hermano para mí, mi apoyo en todo, mi gemelo ideológico y mi *animal defender*. Le doy gracias a la vida por habernos cruzado en el camino. Y recuerda siempre: L'honnêteté avant tout.

A big thanks to my friends from back home: *Amparo, Carmen, Javi, Laura, Noelia, Nerea, and Rebeca*. *Amparo*, por todos los momentos que hemos compartido y nuestras noches que nunca olvidaré. *Carmen*, no tengo palabras para agradecerte todo lo que has hecho por mí, siempre ayudándome en todo y siendo una inspiración para llegar a donde estoy hoy. *Javi*, gracias por aguantar mis agobios y siempre reírnos de ellos después. *Laura*, siempre estás ahí para mí, no importa qué, y eso vale oro. *Nerea*, mi amiga *de y para* toda la vida, gracias por seguir conmigo desde que éramos pequeñas. *Noelia*, gracias por todos los buenos momentos y por tu honestidad, que siempre aprecio un montón. *Rebeca*, mi confesora oficial, gracias por escucharme siempre, pase lo que pase y saber que siempre nos tenemos. Gracias también a mi otra *Nerea*, aunque su casa ahora sea Barcelona. Amiga, atleta desde la infancia y ahora una doctora y entrenadora maravillosa. ¡Sois lo mejor!

Gracias al Arca de Noe y a mi grupo de entrenos por la motivación y todos los buenos ratos. Y un gracias enorme a *Noe*, por estar siempre ahí y por hacer que dé lo mejor de mí.

To all my Paris friends, especially *Carla, Inês, Nouhaila, Rita, and Yucânia*, thank you for making me feel at home from the moment I arrived in France. You've been my support all these years. Uma menção especial para *Inês* por ser sempre uma amiga incrível e tornar

tudo isso possível. To *Agustín*, *Santi*, and *Yonah*, I'm so happy we met at CEMRACS and that our friendship has only gotten stronger with time.

To my Erasmus team, you made that time unforgettable. *Ceci* and *Leti*, vuestra energía, determinación y amistad permanecerá siempre. *Amparo*, mi mitad, gracias por estar siempre ahí y por la conexión especial que compartimos.

There are probably many people I didn't mention, but I want to sincerely thank everyone who has been part of this process and contributed in any way to helping me get here.

Gracias a toda mi familia, que ha sido un pilar fundamental en este camino. Gracias a mis padres, por ser mi mayor apoyo en todo momento. Siempre habéis estado ahí, con vuestro amor incondicional, confiando en mí, apoyándome y ayudándome en todo lo que he necesitado. Me habéis dado todo: oportunidades, cariño, y la libertad para volar y perseguir mis sueños, incluso cuando eso significaba estar lejos de casa. A pesar de la distancia, habéis encontrado la manera de estar conmigo en cada paso, con videollamadas, viajes, mensajes y esos pequeños gestos que han hecho que nunca me sintiera sola. Aunque no os lo diga lo suficiente, sois lo más importante para mí y los mejores padres que podría haber tenido. Esta tesis también es vuestra. A mi abuela *Amalia*, gracias por haber crecido siempre conmigo, por cuidarme desde pequeña, por toda tu paciencia y nuestras travesuras. Tu presencia a lo largo de los años ha sido muy importante en mi vida. A *María*, por todos los momentos compartidos y por ser siempre un baúl lleno de sorpresas. A mi *Paino* y a *Bea*, gracias por toda la diversión, las risas, la picardía y las cosas que me habéis enseñado, junto con mis primos *Olivia* y *Nicolás*. A mis abuelos *Lolita* y *Óscar*, que aunque ya no estén, siempre han sido y seguirán siendo una gran inspiración para mí. Sé que estarían muy orgullosos de donde he llegado. Gracias por todo lo que me dejaron, por las lecciones y las vivencias que me ayudaron a ser la persona que soy hoy. A mi abuelo *Óscar*, por su paciencia, por enseñarme tanto, las *falcatruadas*, y por creer siempre en mí. Y a mi abuela *Lolita*, aunque la sacara de quicio, por todas las risas, las canciones, los bailes y los momentos inolvidables que vivimos juntas. Siempre os llevaré en mi corazón.

To *Dani*, for always being my unconditional support. Thank you for always being by my side, especially during the toughest moments at the end of the thesis. Thank you for being the rationality and serenity that balances my chaos, for the trust we have in each other, for being my home, and for making my life better. You are my safe space, the one who brings out the best in me, and with whom I can be fully myself and experience my *tontería*. I couldn't have made it this far without you. To all the amazing things we will build together in the future.

Paris, France *Sara*
December 2024

Modélisation et simulation numérique appliquées à la prédiction de l'effet des médicaments sur le système cardiovasculaire

Résumé: Cette thèse est consacrée à la modélisation mathématique et à la simulation numérique de l'impact des médicaments sur les tissus cardiovasculaires dans un contexte de pharmacologie de sécurité. Les composés chimiques peuvent influencer la rigidité artérielle en affectant à la fois les composantes actives et passives de la paroi des vaisseaux.

Dans la première partie, nous développons et validons un modèle mathématique à partir des résultats expérimentaux obtenus dans l'installation expérimentale ROTSAC (Leloup et al., 2019), qui permet d'étudier l'influence de vasoconstricteurs et vasodilatateurs sur la rigidité artérielle dans des études pharmacologiques. Dans cette expérience, des segments aortiques sont montés sur deux crochets métalliques parallèles et soumis à une charge dynamique imposée. Nous développons un modèle de coque 3D avec des fibres actives décrivant le comportement du tissu. Les paramètres intervenant dans les lois constitutives du modèle sont identifiés par une méthode d'optimisation à partir de données réelles. Le modèle obtenu est capable de reproduire les données expérimentales et de prédire le comportement du système dans des scénarios autres que ceux utilisés pour l'estimation des paramètres. Cela permet d'évaluer différents scénarios représentant l'impact des molécules sur les contributions actives ou passives de la paroi artérielle.

Dans la deuxième partie, nous présentons un modèle mathématique plus complet pour simuler l'installation *ex vivo* mentionnée précédemment. Ce modèle inclut la mécanique du contact pour prendre en compte les interactions entre le tissu et les composants rigides. Les principales contributions de cette partie concernent l'utilisation d'un modèle de coque 3D et la comparaison de trois méthodes numériques différentes (lagrangien augmenté, Nitsche et pénalisation) appliquées à la mécanique du contact. À notre connaissance, c'est la première fois que la méthode de Nitsche est utilisée dans le cadre des coques 3D.

Enfin, nous présentons une analyse comparative entre différentes approches (réseaux neuronaux artificiels, méthodes statistiques et modélisation mathématique) qui ont été employées dans des études *in vivo* afin d'examiner les effets du vieillissement sur le système cardiovasculaire des chiens. En particulier, la rigidité artérielle est l'un des principaux facteurs liés à l'état de santé cardiovasculaire. Dans cette partie, un modèle 0D en boucle fermée pour la circulation globale est développé. Les paramètres relatifs à la rigidité artérielle et à la résistance de la circulation périphérique sont identifiés à partir de données réelles de télémétrie. Le modèle calibré est capable de prédire le comportement du système vasculaire du chien en fournissant des résultats comparables à ceux obtenus avec des méthodes d'apprentissage automatique ou statistiques.

Mots-clés: Modélisation mathématique du tissu artériel, Modèles de coque 3D, Mécanique du contact, Validation par rapport aux données expérimentales, Pharmacologie de sécurité

Modeling and numerical simulation applied to the prediction of the effect of drugs in the cardiovascular system

Abstract: The present thesis is devoted to the mathematical modeling and the numerical simulation of the impact of drugs on cardiovascular tissue in the context of safety pharmacology. Chemical compounds can influence arterial stiffness by affecting both the active and passive components of the vessels' wall.

In the first part, we develop and validate a mathematical model against experimental results obtained in the ROTSAC experimental setup (Leloup et al., 2019), which investigates how arterial stiffness is influenced by vasoconstrictors and vasodilators in pharmacological studies. In this experiment, aortic segments are mounted on two parallel metal hooks and stretched with an imposed dynamic load. We develop a 3D-shell model with active fibers describing the behavior of the tissue. The model parameters involved in the constitutive laws are identified using real data by means of an optimization method. The resulting model is able to reproduce the experimental data and predict the system's behavior in different settings beyond those used for parameter estimation. This enables the assessment of different scenarios concerning the impact of the molecules on the active or passive contributions of the arterial wall.

In the second part, we present a more complete mathematical model for simulating the aforementioned *ex vivo* setup. It includes a contact mechanics model to account for the interactions between the tissue and rigid components. The main contribution of this part is the use of a 3D-shell model and a comparison of three different numerical methods (augmented Lagrangian, Nitsche and penalty) applied to contact mechanics. To the best of our knowledge, this is the first time that Nitsche's method has been used in the context of 3D-shells.

Lastly, we present a comparative analysis of artificial neural networks, statistical, and mathematical modeling methods employed in *in vivo* studies to examine the aging effects on dogs' cardiovascular system. In particular, arterial stiffness is one of the main factors related to the cardiovascular health status. In this part, a closed-loop 0D model for the global circulation is developed. The parameters related to the arterial stiffness and the peripheral circulation resistance are identified using real telemetry data. The calibrated model is able to assess changes in the vascular system of dogs and deliver results comparable to those obtained with machine learning or statistical methods.

Keywords: Mathematical modeling of arterial tissue, 3D-shell models, Contact mechanics, Validation against experimental data, Safety pharmacology

Contents

Nomenclature

Notation	Meaning
ACh	Acetylcholine
AFM	Atomic Force Microscopy
AP	Arterial Pressure
BDF	Backward Differentiation Formula
CGS	Centimeter-Gram-Second
CRS	Control Random Search
CMA-ES	Covariance Matrix Adaptation Evolution Strategy
CNN	Convolutional Neural Network
DEANO	2-(N,N-diethylamino)-diazenolate-2-oxide sodium salt hydrate
ECG	Electrocardiogram
EC	Endothelial Cell
ECM	Extracellular Matrix
FEM	Finite Element Method
IACUCs	Institutional Animal Care and Use Committees
ICH	International Conference on Harmonization
KKT	Karush-Kuhn-Tucker
KR	Krebs-Ringer
L-NAME	L-Nitro arginine methyl ester
LVP	Left Ventricular Pressure
MITC	Mixed Interpolated Tensorial Components
MLP	Multilayer Perceptron
MR	Magnetic Resonance
MRI	Magnetic Resonance Imaging
NO	Nitric Oxide
ODE	Ordinary Differential Equation
PE	Phenylephrine
PET	Positron Emission Tomography
PM	Pressure Myography
PWV	Pulse Wave Velocity
RMSE	Relative Mean Squared Error

Continued from previous page

Notation	Meaning
RNN	Replicator Neural Networks
ROTSAC	Rodent Oscillatory Tension Set-up to study Arterial Compliance
SAM	Scanning Acoustic Microscopy
SMC	Smooth Muscle Cell
WM	Wire Myography
3Rs	Refinement, Reduction and Replacement
5HT	Serotonin
50K	Potassium

Thesis general context

Professor Gerhard Zbinden noted in the 1970s that traditional preclinical toxicity studies were inadequate for identifying adverse pharmacodynamic effects on vital physiological functions (Williams, 1990; Bass et al., 2004, 2015). These limitations highlighted a significant gap in predicting human health effects or consequences experienced by individuals as a result of a treatment, particularly regarding the impact of drugs on organ systems such as the cardiovascular, respiratory, and central nervous systems. This realization led to the development of safety pharmacology, a specialized field aimed at evaluating functional adverse effects of therapeutics before human exposure. The field was officially recognized with guidelines such as the International Conference on Harmonization (ICH) S7A (Anon, 2001), which underscored its importance in the comprehensive safety assessment of new drugs.

Safety pharmacology complements preclinical toxicology studies by focusing on the potential toxic effects that drugs might have on both their intended targets and other unintended physiological systems (Anon, 2001; Bass et al., 2015). This approach is now an important component of non-clinical safety profiling, essential for ensuring that new therapeutics are both safe and effective (Morimoto et al., 2015). It also plays a vital role in reducing the attrition rates[1] of drugs during preclinical, clinical, and post-marketing phases (Bowes et al., 2012; Trame et al., 2016).

One of the most significant challenges in drug development is cardiovascular safety, which has emerged as a leading cause of drug attrition from preclinical stages to post-approval (Laverty et al., 2011; Ferri et al., 2013). Cardiovascular-related issues can account for up to 45% of all drug failures (Redfern et al., 2010; Valentin et al., 2010). These complications often involve subtle yet high-risk cardiovascular effects that may not be detected during early testing phases but become apparent when drugs are used on a larger scale or over longer periods (Redfern et al., 2010). Such issues can lead to temporary or permanent discontinuation of treatment to manage the associated cardiovascular risks. These complications, linked to both cardiovascular and non-cardiovascular drugs, can manifest as changes in blood pressure, cardiac function, and vascular health (Laverty et al., 2011; Versmissen et al., 2019; Belcik et al., 2012).

In recent years, mathematical modeling has emerged as a valuable tool in safety pharmacology, offering the ability to simulate and predict the cardiovascular impact of drugs before they reach clinical trials (Musuamba et al., 2021; Passini et al., 2017; Gintant et al., 2016). These computational approaches can replicate complex physiological processes, allowing researchers to explore various scenarios and identify potential risks helping to reduce the need for extensive animal testing. In addition to their applications in safety

[1]Drug attrition refers to the high rate of failure that drug candidates experience during clinical development, often due to safety concerns, lack of efficacy, or unacceptable toxicity.

pharmacology, mathematical models have broader implications in medical research and device development. These models enable detailed studies of the cardiovascular system's dynamics, offering insights that are often difficult to obtain through traditional experimental methods. Mathematical modeling and numerical simulations enhance our understanding of biomechanics by facilitating early detection of abnormalities and personalized treatments, while also being significant for the design, testing, and evaluation of medical devices for performance and safety prior to clinical use (Cain, 2011; LaDisa et al., 2003; Kabil et al., 2016).

Position of the thesis

The primary objective of this work is to explore mathematical modeling and numerical simulations in combination with experimental data with the purpose of describing the impact of drugs in the cardiovascular tissue.

Among all the topics of interest in safety pharmacology, we focus on arterial stiffness, that is the predominant cause of increased pulse pressure, a recognized marker of vascular health in the general population cardiovascular events. Arterial stiffness is a cardiovascular parameter that cannot be measured directly and is typically quantified through indirect measurements. This makes mathematical modeling essential, as it can help to estimate quantities that can not be experimentally measured and to give us information of parameters that have a link with the stiffness.

Thesis outline and main contributions

This section offers a detailed review of the contributions across each chapter. A summary and description are also provided at the start of every chapter for clarity and completeness.

- **Chapter 1.** This is an introductory chapter. We begin by presenting the general background in safety pharmacology, discussing the interest in arterial stiffness, and reviewing different methods for experimentally assessing it, including an *ex vivo* setup called ROTSAC (Leloup et al., 2016), which will serve as the motivation for Chapters 2 and 3; then we discuss the problem which consists of assessing if an animal is aging given telemetric experimental data.

- In **Chapter 2** we consider a simplified mathematical model of the ROTSAC experiment described in the previous chapter. We model the arterial wall as a passive hyperelastic material using a 3D-shell model with a layer of active fibers. Model parameters are identified by means of an optimization procedure. Different scenarios to evaluate the impact of the active contribution of smooth muscle cells (SMCs) on arterial stiffness are explored. The model has been validated against *ex vivo* measurements and the numerical results are presented.

- **Chapter 3** provides a more comprehensive mathematical model for the simulation of the ROTSAC setup. No geometrical simplications are made and a model for

contact mechanics is considered to incorporate contact between the elastic and rigid elements. The main contribution of this chapter is a comparison of different numerical approaches (augmented Lagrangian, Nitsche and penalty methods) when a 3D-shell model is used.

- **Chapter 4** provides a preliminary study with the purpose of comparing different methodologies used for assessing the effects of aging, motivated by applications in safety pharmacology and, in particular, the stiffening of the arteries with age. Specifically, the chapter evaluates and contrasts statistical, machine learning, and mathematical modeling approaches.

Author's bibliography

- Papers in peer reviewed journals (based on Chapter 4):

  1. Elham Ataei Alizadeh, Sara Costa Faya, Haibo Liu, Damiano Lombardi, Sylvain Bernasconi, Pieter-Jan Guns and Michael Markert. **Comparison of statistical, machine learning, and mathematical modelling methods to investigate the effect of ageing on dog's cardiovascular system.** ESAIM Proc., 73:2–27, 2023, hal-03933957.

- Submitted papers (based on Chapter 2):

  2. Sara Costa Faya, Callan Wesley, Marina Vidrascu, Miguel A. Fernández, Pieter-Jan Guns, Damiano Lombardi. **Validation of a mathematical model of arterial wall mechanics with drug induced vasoconstriction against *ex vivo* measurements**, hal-04597238, 2024.

Chapter 1

Introduction

This chapter provides the underlying context for the work presented in the subsequent chapters. An overview of safety pharmacology is given, emphasizing the importance of understanding drug-induced effects on arterial stiffness. We provide a comprehensive review of the current methods for assessing arterial stiffness and discuss how age-related changes in the cardiovascular system can influence drug effects, underscoring the importance of considering the age of laboratory animals in safety pharmacology studies. The chapter concludes by presenting the objectives of the thesis.

Contents

1.1 Safety Pharmacology

Ensuring the safety of medicines is of critical importance. The drug development process consists of several stages (Deore et al., 2019), each fundamental for guaranteeing the safety and efficacy of new therapeutic agents. The process begins with the discovery and preclinical phases, where potential drug candidates are identified and initially tested *in vitro*[1] and *in vivo*[2] in animal models to assess their safety and biological activity. This is followed by the clinical development phase, which includes Phase I (safety and dosage), Phase II (efficacy and side effects), Phase III (confirmation and comparison with standard treatments), and finally, Phase IV (post-marketing surveillance) to monitor long-term effects.

Safety concerns identified during drug development can often lead to substantial project delays and late-stage drug attrition, as evidenced in the literature Cook et al. (2014); Harrison (2016); Laverty et al. (2011); Morgan et al. (2018); Valentin and Redfern (2017). The current preclinical testing paradigm, established more than 30 years ago by the Organisation for Economic Co-operation and Development (2020) and the International Council for Harmonisation of Technical Requirements for Pharmaceuticals for Human

[1] *In vitro* studies are those performed outside a living organism in a controlled environment.
[2] *In vivo* experiments are conducted within a living organism.

Use (2015), provides guidelines for toxicity testing of pharmaceutical substances using toxicology species. These guidelines have significantly contributed to ensuring human drug safety by standardizing the evaluation processes and ensuring that all potential adverse effects are systematically investigated before clinical trials.

However, despite these established protocols, the elimination of risk is not entirely possible. The predictive value and detection of organ-specific toxicities are highly dependent on the target organ and the drug entity under investigation (Atienzar et al., 2016; Hornberg et al., 2014). Each drug candidate can interact with biological systems in unique ways, making it difficult to generalize findings from one drug to another. Additionally, species-specific differences in drug metabolism and target organ sensitivities can lead to discrepancies between preclinical and clinical outcomes. Over the past few decades, the pharmaceutical industry has made considerable efforts towards the development, evaluation, and implementation of bioanalytical, mathematical modeling, and *in vitro* models. These advancements enabled improvements in the hazard identification and risk assessment of preclinical drug candidates (Goh et al., 2015; van de Waterbeemd, 2009). The integration of *omics* technologies (Chen and Snyder, 2013), such as genomics, proteomics, and metabolomics, holds promise for identifying biomarkers that can more accurately predict adverse reactions and individual susceptibilities. Innovations such as machine learning and artificial intelligence are also being integrated into drug safety assessments to analyze complex data sets and identify patterns that may predict adverse outcomes, thus improving the predictive accuracy of preclinical models (Bass et al., 2015). Other examples of possible breakthrough technologies include hiPSC-based humanized *in vitro* assays, organ-on-chip (Ingber, 2022) platforms or molecular and functional imaging capabilities (i.e. Positron Emission Tomography (PET), Magnetic Resonance Imaging (MRI) and ultrasound imaging).

The need to reduce drug attrition places greater emphasis on identifying compound-related safety liabilities early in drug development, ideally prior to candidate selection. Early identification of potential toxicities can prevent costly late-stage failures and improve the overall efficiency of the drug development process (Greene and Naven, 2009). These factors, coupled with increased diversification of biological and non-biological modalities, necessitate the adoption of approaches that address existing gaps in safety assessment with fully integrated, fit-for-purpose test systems and safety biomarkers.

In the 1970s, Professor Gerhard Zbinden identified that the existing standards for preclinical toxicity testing were inadequate for detecting acute pharmacodynamic side effects that could pose risks to participants in clinical trials (Bass et al., 2015). This insight led to the development of the field of *safety pharmacology*, which was officially defined by the ICH S7A guidelines (Anon, 2001) as "those studies that investigate the potential undesirable pharmacodynamic effects of a substance on physiological functions in relation to exposure in the therapeutic range and above". ICH S7A emphasizes the importance of *in vivo* telemetry studies in non-rodent species to assess drug-induced hemodynamic effects, while ICH S7B focuses on detecting risks of Torsades de Pointes arrhythmias through a combination of *in vitro* and *in vivo* assays. While hemodynamic effects observed in *in vivo* telemetry studies show acceptable translation to humans (Bhatt et al., 2019) they provide limited mechanistic insight, making it sometimes difficult to develop an integrated clinical

risk assessment and associated mitigation and management plan. Additionally, innovative mathematical approaches may help to extract hidden information from hemodynamic data sets. For instance, the attractor analysis enables quantification of temporal changes in pressure waveform morphology (Aston, 2018). Further, integrating experimentally obtained parameters in a mathematical model of vascular biomechanics and hemodynamic regulation may help to understand hemodynamic changes during drug toxicity studies.

Safety pharmacology is currently undergoing a transformative phase, characterized by the integration of cutting-edge technologies and methodologies aimed at enhancing drug safety evaluations while reducing reliance on traditional animal testing. This shift reflects an evolving landscape where new approaches continuously address the limitations of conventional safety testing methods. Central to this evolution is the application of the principles of the 3Rs (i.e.refinement, reduction, and replacement of *in vivo* animal studies) (Russell and Burch, 1959). These principles guide the development of new methods and technologies that aim to minimize animal use and enhance animal welfare in research. For instance, innovations such as organ-on-a-chip platforms and sophisticated mathematical models allow for more accurate prediction of human drug responses without the need for extensive animal testing. Refinement is achieved through the use of non-invasive techniques like telemetry and advanced imaging (e.g., ultrasound and MRI), which reduce animal suffering by minimizing discomfort and stress. Reduction is further supported by high-throughput screening methods that lower the number of animals needed by providing extensive data from fewer experiments. Additionally, adopting social group housing for laboratory animals helps improve their welfare by reducing stress and promoting natural behaviors. Collectively, these advancements embody the ethical commitment to the 3Rs, fostering more humane and scientifically robust approaches to drug safety evaluation.

The application of mathematical models plays thus a key role in safety pharmacology. These models, enable the computer simulation of various aspects of cardiac function from genes to whole organ systems, provide insights into potential cardiac risks before any physical testing. In parallel, *in vitro* methodologies have advanced significantly. Human induced pluripotent stem cell hiPSC-derived cardiomyocytes, which mimic the properties of mature ventricular cells, are increasingly used to evaluate drug effects on cardiac function and structure. These cells offer a valuable tool for assessing potential cardiotoxicity in a controlled environment, bridging computational predictions and practical laboratory tests. The Comprehensive *in vitro* Proarrhythmia Assay initiative exemplifies the integration of hiPSC-derived cardiomyocytes with mathematical modeling, offering more accurate predictions of proarrhythmic risks. For instance, advanced *in vitro* models using human cells and tissues, as well as sophisticated mathematical modeling techniques, have been developed to better predict human responses (Chang et al., 2022; Owens, 2023).

The cardiovascular system is especially susceptible to adverse drug effects, making its assessment a cornerstone of safety pharmacology (Guns et al., 2020; Bass et al., 2015). Standard methods for evaluating cardiovascular safety include electrocardiogram (ECG) assessments in conscious animals and *in vitro* assays, such as the human Ether-à-go-go-Related Gene (hERG) channel assay (Weaver and Valentin, 2019). Additionally, the assessment of arterial wall integrity and *arterial stiffness* is critical, as these are significant predictors of cardiovascular morbidity and mortality (Shirwany and Zou, 2010; Vlachopoulos,

2010). Novel techniques such as cardiac imaging and biomarkers, along with advanced computational models of cardiac electrophysiology, are being used to enhance the predictive value of preclinical cardiovascular safety assessments (for review see Easter et al. (2009); Hasselgren et al. (2013); Myatt et al. (2018)). Furthermore, integrating patient-specific data through personalized medicine approaches can help predict individual cardiovascular risks more accurately, thereby improving the safety profiles of new drugs.

However, introducing novel methodologies in safety pharmacology is a major challenge, since through validation of the technology, robust confidence in the biology of the test system and its predictive value for human biology is required. As such, the threshold for introducing new technologies and associated read-out in safety pharmacology is high. Consequently, many promising technologies may never translate into useful applications, unless a coordinated and collaborative approach is adopted. Moreover, exploring, validating and eventually implementing novel technologies comes at a significant economic cost, requires time and represents an uncertain return on investment. Collaborative efforts among academia, industry, and regulatory bodies are crucial to developing standardized protocols and best practices for these advanced safety assessments.

In this thesis, we explore the integration of mathematical modeling and numerical simulation with experimental data to address some questions in drug safety assessment and disease research. Using both *ex vivo*[3] and *in vivo* experimental data, we apply a mathematical modeling approach to investigate some biological questions related to arterial stiffness. Our main focus is to develop a mathematical model adapted to drug toxicity studies, providing insights into specific safety pharmacology concerns. Additionally, we perform a comparative analysis of artificial neural networks, statistical methods, and mathematical modeling techniques to examine the impact of aging on cardiovascular systems in dogs.

1.2 Evaluation of arterial stiffness

Arterial stiffness is a complex, dynamic parameter influenced by the arterial wall's composition and the actions of SMCs. Due to the limitations of noninvasive and invasive methods in humans, animal studies are essential for understanding the changes in arterial stiffness due to disease or lifestyle modifications.

The remainder of this chapter is structured as follows. In Section 1.2, we discuss the arterial stiffness, a predictor of cardiovascular disease risk, and an overview of techniques for its evaluation. We also address the motivation behind Chapters 2 and 3, which involves simulating an *ex vivo* setup (ROTSAC) designed to study arterial stiffness. Lastly, in Section 1.3 we present the main objectives of the thesis: firstly, the exploration of a mathematical model of arterial wall mechanics capable of simulating the active contribution of SMCs to arterial stiffness and its validation against experimental data of the ROTSAC setup with a simplified geometry; secondly, a mathematical model for contact mechanics that enables the simulation of the ROTSAC setup with its real geometry; finally, the

[3] *Ex vivo* refers to experiments conducted on tissues, organs, or cells outside a living organism, typically in a controlled laboratory environment.

comparison of different techniques on *in vivo* data to deepen our understanding of age-related physiological changes, giving some light on the strengths and limitations of each method.

1.2.1 Arterial stiffness and its cellular contributions

Arterial stiffness is a significant indicator of cardiovascular health and a predictor of various cardiovascular diseases, with its value more than doubling with age (McEniery et al., 2005). This increase in stiffness is associated with changes such as elastin degradation, collagen cross-linking, and dysfunction in endothelial cells (ECs) and SMCs (O'Rourke and Hashimoto, 2007). Although the underlying mechanisms are not yet fully understood, they are linked to adverse cardiovascular outcomes like myocardial infarction, stroke, cognitive decline, and dementia (Li et al., 2017).

To understand arterial stiffness, it's important to first examine the structure of the arterial wall (see Figure 1.1) and its components. The arterial wall consists of three layers (Gonzalez-Clemente et al., 2021): the intima, media, and adventitia. The intima, the innermost layer, is made up of a single layer of ECs. These cells are essential in regulating vascular tone, permeability, and responses to mechanical forces such as shear stress (Gimbrone and García-Cardeña, 2016).

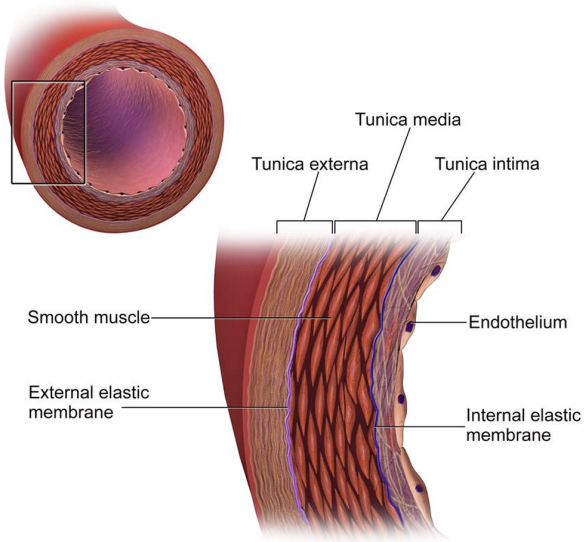

Figure 1.1: Representation of the structure of the arterial wall. Image from Bardin (2022).

The media, the middle and most substantial layer, is composed of SMCs embedded in an extracellular matrix (ECM) containing collagen, elastin, and proteoglycans. This layer is vital for the artery's contractile function, allowing it to adapt to variations in blood pressure and flow. The interplay between collagen, which imparts tensile strength, and elastin, which provides elastic recoil, is fundamental for maintaining arterial elasticity

and compliance[4] (Lacolley et al., 2017). The adventitia, the outermost layer, includes connective tissue, fibroblasts, and small blood vessels that support the artery structurally and anchor it to surrounding tissues.

SMCs in the media contribute to arterial stiffness through both their contractile activity and their role in ECM remodeling. When stimulated by factors such as mechanical stretch, vasoactive substances (e.g., angiotensin II, endothelin-1), or changes in blood pressure, SMCs contract, reducing arterial diameter and increasing wall tension. This process directly increases arterial stiffness (Lacolley et al., 2017). On the other hand, relaxation of SMCs, triggered by vasodilators like nitric oxide (NO) and prostacyclin, allows the artery to expand and accommodate blood flow, thus reducing stiffness.

Moreover, SMCs influence arterial stiffness by modifying the ECM. In conditions such as aging and hypertension, there is increased collagen production and cross-linking coupled with decreased elastin synthesis, leading to a stiffer arterial wall (Sehgel et al., 2013). SMCs can also switch from a contractile to a synthetic phenotype in response to pathological stimuli, a change that involves increased proliferation, migration, and ECM production, which further stiffens the arteries (Lacolley et al., 2017).

ECs play a significant role in regulating arterial stiffness through their release of vasoactive substances. NO, produced by endothelial nitric oxide synthase in response to shear stress, is one of the key substances. NO diffuses to SMCs, stimulating guanylate cyclase and increasing cyclic guanosine monophosphate levels, which leads to SMC relaxation. This mechanism helps to decrease arterial stiffness by increasing arterial diameter and reducing wall tension (Bellien et al., 2010). Additionally, ECs produce other vasoactive agents like endothelin-1, prostacyclin, and angiotensin II, which affect SMC contractility and ECM composition. The balance of these factors is crucial for normal arterial stiffness, and imbalances can contribute to conditions like hypertension and atherosclerosis (Leloup et al., 2019).

Understanding both the roles of SMCs and ECs in arterial stiffness is crucial for developing methods to measure it. Clinically, the detailed study of arterial stiffness and its underlying mechanisms remains challenging. While invasive measurements can be conducted in people undergoing catheterization as part of routine clinical treatment, these studies are limited to individuals with cardiovascular diseases, making comparisons to a healthy cohort difficult (Butlin et al., 2020). Moreover, the long timescale over which arterial stiffening occurs in humans complicates longitudinal studies, making animal models essential for understanding the fundamental mechanisms of arterial stiffness.

In what follows, we provide an overview of the *in vivo* and *ex vivo* techniques available to quantify and investigate arterial stiffness in animals. These techniques allow quantification of the pressure dependency of arterial stiffness and assessment of active (smooth muscle and vascular endothelium) and passive (elastin and collagen) contributions to arterial stiffness.

[4] Arterial compliance is the ability of an artery to expand and contract in response to pressure changes.

1.2.2 Assessment of arterial stiffness based on *in vivo* and *ex vivo* methods

The evaluation of arterial stiffness has traditionally relied on *in vivo* techniques, with Pulse Wave Velocity (PWV) being the most commonly used parameter. PWV is calculated as the speed at which the pressure wave generated by cardiac contraction travels through the arterial tree (Ghosh et al., 2019; Wang et al., 2016). Faster PWV values indicate stiffer arteries and are associated with an increased risk of cardiovascular events (Vlachopoulos, 2010; Laurent et al., 2001). The measurement of PWV can be performed globally, assessing the stiffness of the entire arterial system, or locally, focusing on specific arterial segments such as the carotid or femoral arteries. There are several possibilities to measure the PWV.

- *Applanation tonometry*. It is a widely used technique for measuring PWV globally. This method (Doupis et al., 2016) involves the placement of pressure sensors at two arterial sites (e.g., carotid and femoral arteries) to record the pressure waveforms and calculate the time delay between them. The distance between the two sites is then used to calculate PWV. While this method is non-invasive and relatively easy to perform, it has several limitations, including the potential for errors in distance measurement and the influence of factors such as blood pressure and heart rate.

- *Ultrasound imaging*. Ultrasound imaging (Sahani et al., 2016) uses high-frequency sound waves to create images of the body's internal structures and provides a non-invasive method for assessing PWV locally by measuring the velocity of the pressure wave within a specific arterial segment, such as the carotid artery. Traditional ultrasound was too slow to capture the propagation of arterial pulses, but newer techniques using unfocused plane waves allow for measurements with high temporal resolution (several thousand frames per second) (Luo et al., 2012). This fast imaging can track the pulse wave as it moves through an artery, visualizing the displacement or velocity of the arterial wall. PWV is then calculated from the slope of this wavefront. However, since these methods capture PWV at specific time points, they may not fully account for changes in stiffness that occur as the artery stretches under pressure, which can lead to discrepancies with other stiffness measures. This technique offers greater spatial resolution compared to applanation tonometry, allowing for the assessment of stiffness in specific regions of interest. However, it requires more expensive ultrasound equipment and ultrafast imaging. On top, it is not yet on (all) commercial systems and still in research phase, the validation is pending and is applicable to superficial arteries only (Segers et al., 2020a).

- *Magnetic resonance imaging* (MRI) is another advanced technique (Grotenhuis et al., 2009) used for measuring PWV, particularly in large arteries like the aorta. The computation of PWV with MRI was first discussed in 1989 (Mohiaddin and Longmore, 1989). Growing interest in faster and more reliable MR imaging techniques has led to a noticeable rise in studies using MRI to measure PWV (Wentland et al., 2014). The simplest way to calculate PWV from MR data is by determining the time delay between two flow waveforms (Boese et al., 2000; Mohiaddin, 1992; van der Meer et al.,

2007). This can be done by taking two 2D phase contrast slices and getting the flow waveforms from each (Laffon et al., 2005; Leeson et al., 2006; van der Meer et al., 2007), or more easily by capturing one 2D slice in the thoracic aorta that covers both the ascending and descending parts, giving you two waveforms (Shan et al., 2012). 4D Flow MRI is an advanced imaging technique that captures the movement of blood in three dimensions over time, making it a four-dimensional (4D) representation of blood flow, and it has also been used to compute PWV (Gu et al., 2005; Markl et al., 2003). Information on the flow field can be extracted for every location within the image volume. A 4D flow MRI approach provides the opportunity to derive other hemodynamic parameters of interest from the same scan, including wall shear stress, pressure gradients across stenoses, and other parameters which can be valuable in understanding the mechanisms underlying arterial stiffness (Hope et al., 2013). A major limitation to the widespread use of MR-based PWV measurements is the lack of availability of commercial software (Wentland et al., 2014).

However, the *in vivo* techniques come with some limitations to evaluate arterial stiffness. While PWV is a valuable predictor of cardiovascular health, *in vivo* methods do not effectively separate the contribution of the cellular (endothelial function, smooth muscle function) and noncellular (elastin fragmentation, collagen cross-linking, vascular wall remodeling) components to arterial stiffness (Butlin et al., 2020). Traditionally, arterial stiffness was attributed solely to the passive biomechanical properties of the aorta (Leloup et al., 2016, 2019), but recent research (Kerage et al., 2014; Sehgel et al., 2013) has highlighted the active roles of SMCs and ECs in modulating stiffness through the regulation of vascular tone. To overcome these limitations, *ex vivo* setups have been developed to isolate and analyze both passive and active aspects of arterial stiffness independently of *in vivo* factors such as heart rate or blood pressure (De Moudt et al., 2022a; Leloup et al., 2016, 2019).

Ex vivo characterization of arterial stiffness is a valuable approach for understanding the mechanical properties of blood vessels outside the physiological environment and generally provides more information on the mechanisms behind stiffness changes (Butlin et al., 2020). Various techniques, including tensile testing, myography, scanning acoustic microscopy, nanoindentation, and atomic force microscopy, have been employed to assess both the active (vascular tone, regulated by vascular SMCs and ECs) and passive (that encompasses ECM structural proteins) contributions to vessel stiffness (Butlin et al., 2020). These methods allow for a detailed examination of the mechanical properties of the arterial wall and its individual components at different scales, providing insights that are often not achievable through *in vivo* measurements. We discuss below the main *ex vivo* techniques used to measure different aspects of arterial stiffness in animal studies.

Pressure myography (PM) is a widely used technique to assess the mechanical properties of vessels under physiological conditions (Butlin et al., 2020). Unlike PWV, PM is performed *ex vivo*, requiring small blood vessel samples obtained through biopsy (Akhtar et al., 2011). This method involves mounting an isolated vessel segment on cannulas and perfusing it with controlled pressure, enabling measurement of changes in vessel diameter in response to varying pressures. The sample is placed inside a calcium-free medium to maintain

a naturally relaxed state for measuring its biomechanical responses of contraction and dilation (Akhtar et al., 2011). This technique is particularly useful for studying the active contribution of SMCs to arterial stiffness by observing the vessel's response to vasoactive stimuli such as angiotensin II or norepinephrine (Mulvany and Halpern, 1977).

One of the key advantages of PM is its ability to preserve the natural passive behaviors of arteries by maintaining the integrity of their circumferential layers of elastin, collagen, and SMCs (Navindaran et al., 2023). This method reduces external factors during the experiment and also enables the analysis of arteries outside the physiological pressure range, a challenge for *in vivo* approaches (van der Bruggen et al., 2021). However, a significant drawback is the high expenses associated with commercial PM systems, due to the limited number of suppliers (Lawton et al., 2019). Additionally, the technique assumes that the vessel has uniform mechanical properties along its length and cannot detect any heterogeneity (Navindaran et al., 2023). Furthermore, it is limited to very small blood vessel samples, which complicates the study of larger arteries (Akhtar et al., 2011).

Wire myography (WM) is another technique used to assess arterial stiffness (Mulvany and Halpern, 1977). Contrary to PM, in WM it is needed to mount a vessel segment on two thin wires and stretching it under isometric conditions to measure the force generated by the vessel in response to various stimuli. This technique allows for precise measurement of vascular tone and the effects of pharmacological agents on vascular smooth muscle contractility (Angus et al., 2000). However, WM primarily captures isometric tension, which may not fully represent the *in vivo* mechanics of the vessel (Butlin et al., 2020).

More advanced techniques such as scanning acoustic microscopy, nanoindentation, and atomic force microscopy offer the ability to assess the mechanical properties of individual layers and components within the vessel wall.

Scanning Acoustic Microscopy (SAM) uses high-frequency sound waves to generate detailed images of the vessel structure and to measure the stiffness of different layers within the arterial wall (Akhtar et al., 2016). The image contrast in a SAM derives from differences in the propagation speed of acoustic waves through a material; the wave speed is related to the elastic properties of the material, in particular Young's modulus (Liang and Blomley, 2003). This method allows resolving distinct features such as collagen fibers (Akhtar et al., 2016). Gathering both histological and mechanical data could be valuable for arterial stiffening studies (Akhtar et al., 2011), considering the structural changes in collagen and elastin, which are the primary load-bearing elements in large arteries (Graham et al., 2011). One of the key advantages of SAM is its ability to produce images of the mechanical properties of the vessel wall without physically altering the sample (Yu, 2020). This non-destructive testing is ideal for assessing the heterogeneity of mechanical properties across different layers of the artery, which is not possible with traditional methods such as pressure or wire myography (Lopez-Andres et al., 2012). While SAM provides valuable insights into the mechanical properties of blood vessels, its high cost and complexity (Yazdan Mehr et al., 2015) may limit its widespread use in routine assessments of arterial stiffness.

Nanoindentation technology with high spatial resolution and force sensitivity is widely used to measure the mechanical properties of hard biomaterials and tissues (Wu et al., 2020). Nanoindentation involves pressing an indenter into the tissue to measure its resistance to

deformation (Qian and Zhao, 2018). This technique can precisely measure the stiffness of specific regions of the arterial wall, enabling the study of spatial variations within the vessel wall. Because of its small probe size, nanoindentation can be used to measure local material properties in small, thin, and heterogeneous samples. Nanoindentation is also useful for measuring mechanical properties of microstructural features within bulk samples, characterizing the properties of individual constituents within composite or heterogeneous samples, or mapping mechanical properties across a sample surface (Ebenstein and Pruitt, 2006). However, nanoindentation requires careful sample preparation and calibration (Barone et al., 2010) to ensure accurate and reproducible results.

Atomic Force Microscopy (AFM) provides high resolution measurements, often at the cellular or subcellular level (Radmacher, 1997). AFM involves scanning a sharp tip across the surface of the tissue to generate a detailed topographical map and to measure the mechanical properties of individual components (Navindaran et al., 2023). AFM's main advantage is its ability to detect very small changes in mechanical properties at the nanoscale, even in physiologically relevant environments like hydrated conditions or dynamic settings (Navindaran et al., 2023; Bae et al., 2016). Despite these benefits, AFM has limitations. It generally assesses samples in an unloaded state, which can result in stiffness measurements that are lower than those observed under physiological loading conditions (Bae et al., 2016). Additionally, interpreting AFM data requires complex mathematical models to understand mechanical properties from force-displacement curves, which rely on various assumptions and can be prone to errors (Stylianou et al., 2019). Tip blunting, where the geometry of the AFM tip changes due to the sample's stiffness, can also impact the accuracy of measurements (Navindaran et al., 2023).

An *ex vivo* setup to study arterial stiffness: ROTSAC

More recently, alternative methods have been proposed to assess the vascular stiffness response in a more physiologically relevant manner. Customized organ bath setups have been developed to apply strain or force oscillations at magnitudes and frequencies that mirror those experienced by blood vessels in the body (Butlin et al., 2020; Langewouters et al., 1985b,a). These setups are designed to generate pressure-diameter loops, which are graphical representations of how the diameter of a blood vessel changes in response to varying pressures. By analyzing these loops, researchers can quantify both the stiffness and the viscoelasticity of the vessels (Leloup et al., 2019). The viscoelastic properties, which describe how the vessel's material properties change with time and deformation, are relevant for understanding the blood vessel's ability to accommodate pulsatile blood flow. These methods provide a view of the mechanical behavior of blood vessels under conditions that closely replicate the actual physiological environment.

The Rodent Oscillatory Tension Set-up to study Arterial Compliance (ROTSAC) setup was developed to address the limitations of traditional *in vivo* and *in vitro* methods by providing an *ex vivo* environment in which arterial segments can be studied in isolation under controlled conditions (De Moudt et al., 2022b). The ROTSAC was mainly developed to study elastic behavior of aortic segments while stretched at physiological frequencies and amplitudes. This setup allows for an assessment of the system's consistency, verification of

the *ex vivo* impact of heightened distension pressure and SMC tone on stiffness metrics, evaluation of aortic stiffness in isolated segments from two genetic mouse models with known aortic stiffness issues, and testing of the morphological and mechanical preservation of aortic segments when subjected to high-frequency oscillation (Leloup et al., 2016).

The experiments performed with the ROTSAC setup (see Figure 1.2), begin with the dissection of aortic segments from euthanized mice, typically focusing on the thoracic aorta. These segments are then mounted on a system of two parallel metal hooks in an 8 ml organ bath, which is filled with a physiological saline solution (Krebs-Ringer) to maintain the tissue in a controlled environment. The organ bath is equipped with a heating system that ensures the temperature is kept at 37°C, simulating the thermal conditions found within the living organism. The two hooks secure the segment within the setup and allow it to be subjected to controlled mechanical forces. The aortic segment is connected to a force-length transducer, that measures both the force and displacement of the upper hook. The upper hook was connected to the aluminum lever of the force-length transducer and this lever was connected to a coil suspended in a strong field of a permanent magnet. The system was controlled by a current source. When current was passed through this coil, a force was developed. The displacement of the lever was measured by means of a photo-electric system. The transducer is connected to a data acquisition system (Powerlab 8/30 and LabChart 7, ADInstruments, Oxford, UK) that records the force and displacement data at a high sampling rate of 1 kHz. From these measurements, various biomechanical parameters such as arterial compliance and the Peterson modulus, a measure of arterial stiffness, can be derived. These parameters provide valuable insights into how the mechanical properties of arteries change under different physiological and pathological conditions.

To simulate the physiological conditions, the setup is designed to subject the aortic segments to cyclic stretching, typically at a frequency of 10 Hz, corresponding to the heart rate of a mouse (approximately 600 beats per minute). This cyclic stretching is implemented through the force-length transducer, which dynamically adjusts the length of the aortic segment in a controlled manner, thereby simulating the pulsatile nature of blood flow. The relationship between the force exerted by the vessel and its diameter is used to calculate the internal pressure within the segment, P, employing the Laplace equation:

$$P = \frac{F}{l\,D},$$

with F the force, l the length and D the diameter of the vessel segment. Force was measured directly by the transducer. The diameter of the vessel segment at a given preload was derived from the displacement of the upper hook, being directly proportional to the inner circumference:

$$D = \frac{2\,w}{\pi},$$

with w the outer distance between the hooks (to approximate the inner circumference of the vessel segment). This allows for the generation of pressure-diameter loops for analyzing the mechanical properties of the arterial wall. The pressure-stiffness relationship was evaluated under physiological conditions (using Krebs-Ringer solution), in a maximally-contracted state (induced by 2 μM phenylephrine (PE), serotonin (5HT) or potassium (50K) reflecting

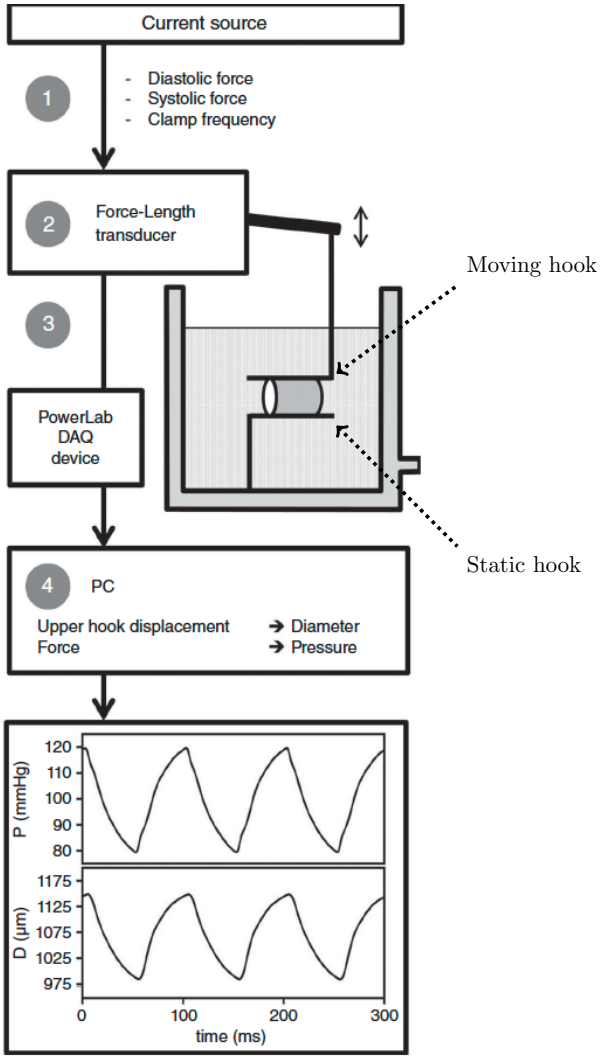

Figure 1.2: Schematic diagram of the ROTSAC. Image from Leloup et al. (2016).

active components), and in the absence of active stiffness (utilizing 2 μM of DEANO, a NO donor to negate any contribution of SMC contraction).

As previously mentioned, recent insights emphasize the significant role of active factors, particularly vascular SMC tone, in modulating arterial stiffness. The ROTSAC setup demonstrated that inducing SMC contraction using PE resulted in a significant increase in isobaric stiffness. Further, when NO production was inhibited in PE-stimulated aortic segments, isobaric stiffness increased by 80% compared to baseline measurements. This substantial increase underscores the importance of NO in regulating arterial stiffness, particularly in elastic arteries like the aorta, which produce high levels of basal NO. This finding aligns with previous *in vivo* studies in rodents and humans that have highlighted the direct relationship between basal NO production and arterial stiffness.

To validate the sensitivity of the ROTSAC setup, the study utilized two genetic mouse

models. The ROTSAC setup proved effective for investigating the biomechanical properties of isolated aortic segments. It allows for the independent manipulation of pulse pressure, stretch frequency, and the composition of the extracellular fluid, facilitating a detailed examination of SMC tone and mechanical stimuli on arterial compliance. This *ex vivo* approach is advantageous for studying these factors separately, which is not always possible *in vivo* due to the complexity of physiological conditions.

However, the ROTSAC setup has some limitations. Unlike perfusion-based setups, it does not measure luminal pressure directly and instead relies on indirect calculations using the Laplace relationship. This method assumes a thin, isotropic, and homogeneous vessel wall, which may not fully apply to the mouse aorta, potentially affecting the interpretation of absolute pressure values. Additionally, the lack of perfusion means that endothelial cells are not exposed to shear stress, which can stimulate NO production. Finally, isolation of the aorta removes neurogenic and hormonal stimuli that also influence arterial mechanics, which can lead to discrepancies between *ex vivo* and *in vivo* measurements.

Despite these drawbacks, the ROTSAC setup is valuable for providing rapid and detailed assessments of aortic biomechanics with minimal tissue requirements. It complements other methodologies by offering insights into the effects of SMC tone, mechanical stimuli, and NO production on arterial stiffness. This approach is relevant for understanding arterial aging, hypertension, and developing targeted therapies for cardiovascular health.

1.3 Objectives of the thesis

In drug discovery and development, while significant advancements have been made in *in vitro* and *in silico*[5] methodologies, these approaches have not yet fully replaced the need for live animal testing in assessing the comprehensive effects of test compounds within a living system (Committee, 1985; Service, 1993). Despite their growing sophistication and potential, *in vitro* and *in silico* models still face limitations in replicating the complex interactions and systemic responses observed in whole organisms. Consequently, researchers and Institutional Animal Care and Use Committees (IACUCs) continue to navigate the challenges of implementing the 3Rs in animal research.

In this thesis, we explore the capabilities of various mathematical models in combination with *ex vivo* and *in vivo* experimental data to answer questions of safety pharmacology. There are mainly three parts: in the first one, we investigate a mathematical model to reproduce *ex vivo* experimental data of arterial compliance under the action of vasoconstrictors and vasodilators related to pharmacological studies. Model parameters are identified by means of an optimization procedure. The objective is to provide insights on the mechanical behavior of arterial segments and the role of SMCs in arterial stiffness, which cannot be measured directly through experimentation. For symmetry reasons, a simplified geometry of the ROTSAC setup has been considered in this first part; in the second part, we provide a more complete model of the ROTSAC setup using the real geometry. In order to do so, contact between the elastic and the tissue needs to be considered since the simulations could not have been performed otherwise. The main contribution of this part is a comparison

[5]Using computer simulations to predict biological behavior.

between three different numerical approaches for contact mechanics; finally, in the last part of the thesis we aim at comparing different classes of methods for assessing the impact of aging in the context of safety pharmacology by analyzing *in vivo* cardiovascular data collected from laboratory dogs.

As previously stated, the goal of the first part of this thesis is to provide a mathematical model of vasoconstriction/vasodilation that can reproduce the ROTSAC experiment and conditions without recalibrating the parameters. This research is relevant for gaining a deeper understanding of the mechanical behavior of the aorta under different pressure conditions. The structure and function of the arterial wall are complex and many multi-component models of the arterial wall have been developed in recent years (Valentin et al., 2009; Weisbecker et al., 2015; Bellini et al., 2014; Stålhand et al., 2016) to understand the dynamic nature of the biological system and to answer questions that experiments alone have not yet addressed. These models, which focus on the elastic behavior of the vascular wall, are based on experiments studying the mechanical properties of vascular tissue under different stress-strain conditions (Stergiopulos et al., 1998; Holzapfel et al., 2000; Zulliger et al., 2004; Holzapfel et al., 2005; Sommer and Holzapfel, 2012). Many structure-based passive mechanical models of blood vessels have been extensively studied (Lanir, 1983; Wuyts et al., 1995; Dahl et al., 2008; Lokshin and Lanir, 2009; Hollander et al., 2011; Rachev and Shazly, 2019), but there remains still a notable gap in the development of the models addressing active properties. Over the past decade, various methods have been proposed to simulate smooth muscle contractility (Rachev and Hayashi, 1999; Stålhand et al., 2008; Murtada et al., 2010; Schmitz and Böl, 2011; Murtada et al., 2012). However, despite significant progress, the active component of vascular contractility has not been systematically included in these models (Coccarelli et al., 2018).

The majority of models concerning SMCs rely on either 0D ordinary differential equations or 1D formulations (Rachev and Shazly, 2019; Fay and Delise, 1973; Lee and Schmid-Schönbein, 1996; Yang et al., 2003a,b; Bursztyn et al., 2007; Murtada et al., 2010; Jin et al., 2020). Based on their 1D model (see Stålhand et al. (2008)), Stålhand et al. (2011) developed a mechanochemical 3D continuum model for SMC contraction. For instance, in Coccarelli et al. (2018), a 3D hyperelastic structural model coupled with blood flow is presented. The proposed computational framework, that takes into account the passive and the active behavior of SMCs, accounts for vascular responses to mechanical and pharmacological stimuli.

By evaluating and integrating different methods, this research aims to enhance our understanding of cardiovascular dynamics and contribute to safer, more effective pharmacological assessment. In Chapter 2 of this thesis, we propose a mathematical framework that combines passive hyperelasticity (Holzapfel et al., 2000; Gasser et al., 2006) with active fibers to simulate the active behavior of SMCs. Using 3D-shell elements (Chapelle et al., 2004a; Chapelle and Bathe, 2010) and incorporating the Ogden hyperelastic law (Geymonat and Ciarlet, 1982) for the passive component, the model captures nonlinear strain-stress relationships, enabling realistic simulations of arterial behavior under varying dynamical conditions. The model integrates an affine stress-strain constitutive law for SMC fibers (Aletti et al., 2015), enabling the simulation of vasoconstriction and vasodilation. Due to the symmetry of the ROTSAC setup, a simplified geometrical configuration has been

considered in the mathematical model as we will see in Chapter 2. The objective of Chapter 2 is twofold: firstly, to show the predictive capabilities of the model. Secondly, we aim to explore whether vasoconstriction or vasodilation driven by vasoactive substances impact solely the SMCs (*scenario I*) or if the compounds introduce additional intrinsic stiffness (reflected by the Young modulus E) (*scenario II*). The model has a set of parameters that are unknown and are identified through an optimization process. The results of the parameter estimation procedure enable to understand which is the most plausible scenario between the two previously stated. Through validation against experimental data, the model provides valuable insights into the mechanical dynamics of SMC contraction, offering a promising approach for understanding vascular function and exploring the simulation of *in vivo* data.

In Chapter 3, we aim at providing a more comprehensive mathematical model of the ROTSAC setup presented in Chapter 2 with the purpose of assessing the limitation of the model of Chapter 2. Specifically, Chapter 3 does not use any geometrical assumption, and it became clear that it was necessary to incorporate the interaction between the tissue and the hooks in order to simulate the experiment with its real geometry. The main contribution of this part of the thesis is the investigation of various numerical methods for handling contact, including augmented Lagrangian, Nitsche and penalty. In particular, to the best of our knowledge, this is the first time that Nitsche's method is used with 3D-shell models (Fabre et al., 2021).

In Section 1.2, we highlighted arterial stiffness as a key indicator of cardiovascular health, discussing its relevance in both clinical assessments and drug development with special focus on *ex vivo* studies. To study arterial stiffness, is also important to consider the influence of age, especially in preclinical *in vivo* studies, that are performed to evaluate how drugs affect living organisms. Age-related changes in the cardiovascular system can alter the effects of drugs, making it essential to consider the age of laboratory animals when interpreting results in safety pharmacology studies. Aging significantly affects arterial stiffness, as the arterial walls undergo structural changes that reduce their elasticity. Over time, the degradation of elastin and the accumulation of collagen and calcium deposits make the arteries more rigid. In this section, we introduce the impact of age on the cardiovascular function of laboratory animals and its implications for drug safety assessments.

Age-related changes in the cardiovascular system can substantially alter how drugs are processed and responded to in *in vivo* studies. These physiological changes, such as increased arterial stiffness, reduced arterial compliance, and altered blood flow dynamics (Meurs et al., 1996; Paul-Emile Roy and George Rona, 1976; Templeton et al., 1979), affect the pharmacokinetics and pharmacodynamics of drugs (Polaka et al., 2022). This means that as animals age, the way a drug is absorbed, distributed, metabolized, and excreted can differ significantly from that in younger animals. Consequently, understanding and accounting for the age of laboratory animals is essential to ensure that preclinical studies accurately reflect a drug's safety and efficacy (Strasser et al., 1993; Jackson et al., 2017).

For example, older animals might present cardiovascular conditions inherent to aging, which could confound the assessment of a drug's effects. This underscores the need to distinguish between age-related changes and drug-induced effects. Failing to account for these variables could lead to misleading conclusions about a drug's safety profile,

particularly if the drug behaves differently in older versus younger animals.

Additionally, in safety pharmacology studies, it is vital to determine an appropriate wash-out period between treatments, especially in cross-over designs where animals are exposed to multiple drugs (Chris Delaney and Suissa, 2009). This ensures that residual effects from a prior treatment do not skew the results of subsequent experiments. Before an animal is re-enrolled in a study, it must undergo thorough clinical and physiological evaluations to confirm that it is healthy and that its cardiovascular system is functioning normally (Kovalcsik et al., 2006). These steps are crucial to maintaining the reliability of study results and the well-being of the animals involved.

The last part of this thesis focuses on exploring and evaluating different approaches to analyze *in vivo* hemodynamic data obtained from animal studies. These data, which capture cardiovascular activity over several weeks, are collected from animals that undergo multiple cycles of testing and recovery. A key question emerges: at any point in time, is an animal sufficiently recovered to participate in a new experiment? This can be rephrased as: given its baseline data and assuming its initial condition met the experimental criteria, how much has the animal's state changed over time? (Q_1) Additionally, can we identify the individual animal based on its data from a previous time point? (Q_2)

This issue can be approached as a semi-supervised learning problem. Initially, we know that the animal is in a suitable state for experimentation, so we can label its data as *suitable*. As the animal's condition changes, we can then determine the point at which it may no longer be fit for further testing. A related challenge involves monitoring the animal during an experiment that significantly alters its cardiovascular function, labeling this state as *altered*. In this scenario, we have examples of both altered and unaltered states, allowing for a more conventional supervised learning approach.

Various methods can be applied to address questions Q_1 and Q_2. In Chapter 4 we aim to determine which methods are most effective. The methods under consideration come from fields such as statistics, machine learning, and mathematical modeling. Among these methods, there are statistical approaches, that consist on techniques (see Hodge and Austin (2004) for a survey) for detecting outliers and performing statistical tests like Rousseeuw and Hubert (2018) are adapted to our specific needs, helping to identify deviations from the expected state. Given the semi-supervised nature of the problem, deep learning methods (Chalapathy and Chawla, 2019) such as an architecture called replicator (see Dau et al. (2014); Hawkins et al. (2002)) can be explored and adapted to suit this context. Finally, simple parametric models, such as 0D models of hemodynamics (Segers et al., 1997; Mirramezani and Shadden, 2020; Liang and Liu, 2005) and electrophysiology, can be developed to simulate the data. These models are then calibrated to match individual animal data, using Bayesian filtering to define and detect altered states. Our goal is to describe the main observable hemodynamics quantities and their evolution in time. In the present case, since we have the ECG data, we have considered a 0D lumped parameter model of the left ventricle (see Moulton et al. (2017)), coupled with a model of the global circulation. The model includes parameters such as compliance and resistance, which are influenced by aging. As arteries stiffen with age, compliance typically decreases, while resistance, reflecting opposition to blood flow, tends to increase due to factors like arteriosclerosis and heightened systemic vascular resistance. Estimating these

parameters, which cannot be directly measured experimentally, at various stages of the dogs' life will help determine whether they change with age. A comparison between the three fore-mentioned approaches is explored in Chapter 4 of the thesis in order to answer the questions previously stated.

Chapter 2

Validation of a mathematical model of arterial wall mechanics with drug induced vasoconstriction against *ex vivo* measurements

In this chapter we investigate a mathematical model in order to reproduce experimental data of arterial compliance under the action of vasoconstrictors and vasodilators related to pharmacological studies. The considered model is a 3D-shell with active fibers. Model parameters are identified by means of an optimization procedure. The resulting model was able to reproduce the experimental data and predict the system behavior in scenarios other than those used for the parameter estimation. The results suggest that smooth muscle cells contraction modulates stiffness through direct fiber-induced regulation of vascular tone, while parameters related to the passive arterial wall component remain relatively stable across different vasoactive scenarios.

The results of this chapter have been reported in:

- S. Costa Faya, C. Wesley, M. Vidrascu, M.A. Fernández, P.-J. Guns, D. Lombardi. Validation of a mathematical model of arterial wall mechanics with drug induced vasoconstriction against *ex vivo* measurements, hal-04597238, 2024.

Contents

2.1 Introduction

Arterial compliance, the capacity of the aorta to extend and recoil, is crucial for regulating cardiac output and maintaining blood flow in the systemic circulation (Thomas and Sumam, 2016). Conversely, arterial stiffness, the inverse of compliance, is a predictor of cardiovascular health (Shirwany and Zou, 2010; Vlachopoulos, 2010). Pulse wave velocity (PWV) serves as a non-invasive method to evaluate arterial stiffness in both human and animal subjects, indicating the speed of propagation of blood pressure waves (Ghosh et al., 2019; Wang et al., 2016). PWV measurement can provide a comprehensive assessment of arterial stiffness either globally, using applanation tonometry (Sahani et al., 2016; Zhang et al., 2014), or locally, via ultrasound imaging (Vlachopoulos, 2010; Sharif et al., 2019). For additional techniques beyond applanation tonometry and ultrasound imaging, readers are encouraged to consult Segers et al. (2020b). During aging, PWV increases due to arterial remodeling in response to prolonged hemodynamic stress, reflecting changes in the extracellular matrix such as the elastin: collagen ratio, which affects structural wall stiffness (Shirwany and Zou, 2010; De Moudt et al., 2022b).

Traditionally, arterial stiffness was attributed solely to the passive biomechanical properties of the aorta (Leloup et al., 2016). However, recent investigations have underscored the dynamic involvement of vascular smooth muscle cells (SMCs) and endothelial cells (ECs) in regulating arterial stiffness through modulation of vascular tone (Zulliger et al., 2004; Kerage et al., 2014; Sehgel et al., 2013). This active stiffness modulation, facilitated by adjustments in vascular tone, enables adaptation to acute hemodynamic stress through vasoconstriction by SMCs and release of vasoactive molecules by ECs (Lacolley et al., 2017). While PWV is an independent predictor of cardiovascular health, it lacks the ability to provide detailed insights into passive or active modifications of arterial stiffness (Leloup et al., 2016, 2019). To address this, arterial stiffness can be studied in dedicated *ex vivo* setups, offering the advantage of isolating passive stiffness and evaluating active modulation independent of *in vivo* factors, such as heart rate or blood pressure (De Moudt et al., 2022b; Leloup et al., 2016, 2019). Previously, our Rodent Oscillatory Tension Setup for measuring Arterial Compliance (ROTSAC) effectively distinguished between active and passive contributions to arterial stiffness (Leloup et al., 2016, 2019). Interestingly, we previously demonstrated that vasoconstrictors increased active stiffness at lower pressures while simultaneously reducing overall stiffness at higher pressures (Leloup et al., 2019; De Moudt et al., 2022a).

The present work is aimed to develop a mathematical model that most accurately recapitulates the pressure-diameter relationship of the elastic modulus[1] E_p, which is adjusted for diameter dependency. This investigation is essential for understanding mechanical behavior of the aorta under varying pressure conditions. We aimed to establish a model capable of simulating the active contribution of SMCs to arterial stiffness. The objective of this work is twofold: firstly, our model has been designed with the purpose of reproducing the available experimental data of the setup proposed in Leloup et al. (2016). Secondly, we aim to get insight whether SMCs contraction modulates stiffness through a direct fiber-induced

[1] E_p is the Peterson modulus of elasticity and is defined in the next section.

regulation of vascular tone (*scenario I*) and, additionally, also through indirect adjustment of intrinsic stiffness (reflected by the Young modulus E) (*scenario II*), and to what extent changes in geometry (i.e., diameter) are modulating biomechanical assessment. A specific question was whether the *in silico* model could reflect the collagen unloading phenomena at elevated pressures that we previously reported (Leloup et al., 2019; De Moudt et al., 2022a).

The chapter is organized as follows: Section 2.2 provides details on the experimental setup and discusses the available data for the simulations. It also presents the mathematical model used to simulate the arterial wall with active behavior. Section 2.3 showcases some numerical results. Section 2.4 presents the conclusions and future work of this study.

2.2 Methods

In this section, the experimental methods and the collected data that have been employed for the numerical simulations are presented. It also provides an overview of the structural model that has been used to reproduce the experimental data and to give some insight of the fore-mentioned scenarios. Finally, this section introduces the methodology employed for parameter estimation and model validation.

2.2.1 Experimental data

Evaluation of vascular reactivity

For the evaluation of vascular reactivity, aortic segments were set at a preload of 20 mN to achieve a loading equivalent to blood pressure of 100 mmHg. SMC contraction was assessed by incremental concentrations of phenylephrine (PE; ranging from 3 nM to 3 μM), an α1-adrenergic receptor agonist. Subsequently, endothelium-dependent relaxations were evaluated by cumulative concentrations of acetylcholine (ACh; ranging from 3 nM to 10 μM), a muscarinic receptor agonist. To mitigate the influence of nitric oxide (NO), L-Nitro arginine methyl ester (L-NAME; 300 μM), a non-selective NO synthase inhibitor, was administered. Furthermore, exogenous nitric oxide donor, 2-(N,N-diethylamino)-diazenolate-2-oxide sodium salt hydrate (DEANO; ranging from 0.03 nM to 10 μM) was administered to investigate endothelium-independent SMC relaxation.

For the evaluation of vascular reactivity, we have used isometric data from 9 aortic segments.

Ex vivo stiffness

The *ex vivo* stiffness of aortic segments was assessed using the ROTSAC, as detailed by Leloup et al. (2016) (see Figure 2.1). Briefly, 2 mm aortic segments were placed between two parallel hooks within 10 mL organ baths. These segments were submerged in Krebs-Ringer (KR) solution maintained at 37 °C, with a gas mixture of 95% O2 and 5% CO2, and pH adjusted to 7.4. The composition of the Krebs-Ringer solution comprised NaCl 118 mM, KCl 4.7 mM, CaCl2 2.5 mM, KH2PO4 1.2 mM, MgSO4 1.2 mM, NaHCO3 25 mM, CaEDTA 0.025 mM, and glucose 11.1 mM. Force and displacement of the upper hook were

controlled and recorded using a force length transducer. Aortic segments underwent cyclic stretching between alternating preloads, mimicking "diastolic" and "systolic" transmural pressures at a frequency of 10 Hz, corresponding to the physiological heart rate in mice (600 beats per minute). Transmural pressure was determined using the Laplace relationship. Aortic extension was calibrated through optical camera imaging, capturing pictures at different stretches to calibrate the upper hook and allowing calculation of vessel diameters during systole and diastole. Subsequently, the Peterson modulus of elasticity, E_p, was computed at various pressure levels. E_p was calculated using the formula:

$$E_p = D_0 \frac{\Delta P}{\Delta D},$$

where ΔP represents the difference in pressure (maintained constant at 40 mmHg), D_0 denotes the "diastolic" diameter, and ΔD indicates the change in diameter between "diastolic" and "systolic" pressure. The protocol encompassed the assessment of arterial stiffness (E_p) at different pressures, ranging from 60 – 100 mmHg up to 120 - 160 mmHg, with incremental intervals of 20 mmHg. The pressure-stiffness relationship was evaluated under physiological conditions (using Krebs-Ringer solution), in a maximally-contracted state (induced by 2 μM PE, serotonin (5HT) or potassium (50K) reflecting active components), and in the absence of active stiffness (utilizing 2 μM of DEANO, a nitric oxide donor to negate any contribution of SMC contraction).

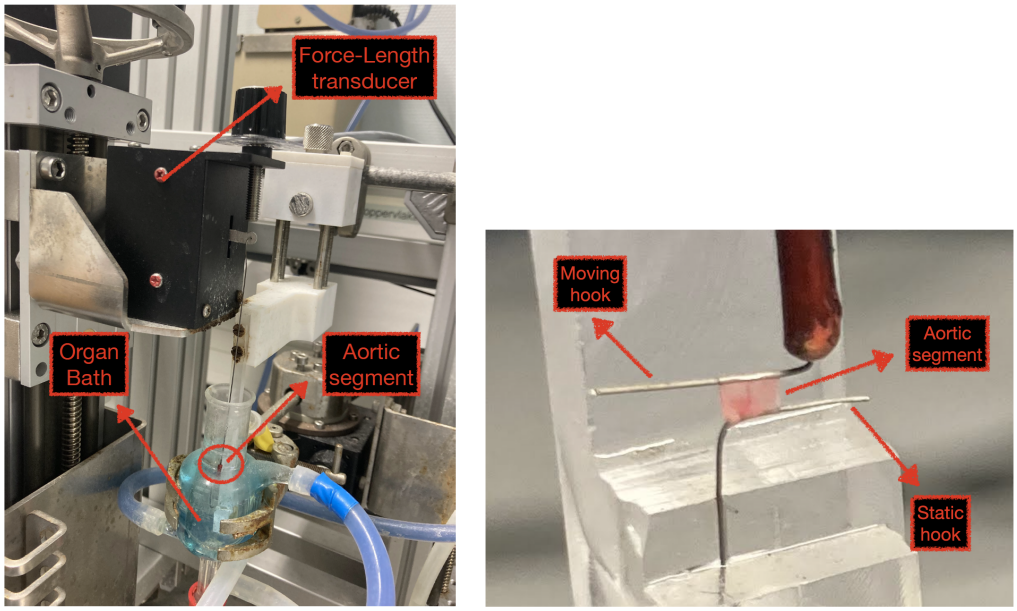

Figure 2.1: ROTSAC experimental setup (left) and augmented view of the aortic segment mounted on the hooks (right).

Regarding the ROTSAC experiments, we have used data from other 15 segments divided in four sets of five, two, two and six segments, respectively. The ROTSAC data are presented in Table 2.1.

Pressures (mmHg)	**Sets**	**KR**	**PE**	**5HT**	**50K**	**DEANO**
60 - 100	Set 4: 6 segments	✓	✓			✓
80 - 120	Set 1: 5 segments	✓	✓			
	Set 2: 2 segments	✓		✓		
	Set 3: 2 segments	✓			✓	
	Set 4: 6 segments	✓	✓			✓
100 - 140	Set 4: 6 segments	✓	✓			✓
120 - 160	Set 4: 6 segments	✓	✓			✓

Table 2.1: ROTSAC data of 15 aortic segments where KR stands for Krebs-Ringer; PE, 5HT, and 50K are the vasoconstrictors; DEANO is the vasodilator.

2.2.2 Mathematical modeling

Arteries form an anisotropic structure composed of three primary layers (for more details, please refer to Bit et al. (2020)): the adventitia, situated on the outermost part, contains collagen fibers and acts as a protective covering for the artery; below the adventitia lies the media layer, housing SMCs that are responsible for vascular tone regulation; and the innermost intima, lined with ECs, serves as a protective barrier between the bloodstream and arterial wall.

In the present work, the arterial wall is modeled as a passive hyperelastic material using a 3D-shell model. Shell models are particularly useful in cardiovascular simulations when the thickness-to-size ratio of the solid structure is small, as is the case for the arterial wall. Specifically, 3D-shell models employ a quadratic kinematic assumption on displacements, making them well-suited for capturing the large deformations of the arterial wall during experiments. These models provide notable advantages, such as enabling the application of general 3D constitutive relations within the shell context and accurately capturing through-thickness stress variations. For a comprehensive overview of shell models, please refer to Chapelle and Bathe (2010); Bischoff and Ramm (1997).

Additionally, a layer of fibers is included to describe the SMCs induced vasoconstriction and vasodilation phenomena. Since the focus is primarily on the media layer, the fibers are aligned with the circumferential direction (Coccarelli et al., 2018; Liu, 1998; O'Connell et al., 2008; Murtada and Holzapfel, 2014). The anisotropic behavior of the passive matrix due to collagen fibers is neglected.

Owing to the symmetry of the ROTSAC setup (Figure 2.2(left)), a simplified geometrical configuration has been considered in the mathematical model. It consists of one of the lateral sides of the tissue mounted on the hooks, as presented in Figure 2.2(right), which is here assumed to be flat in the stress-free configuration.

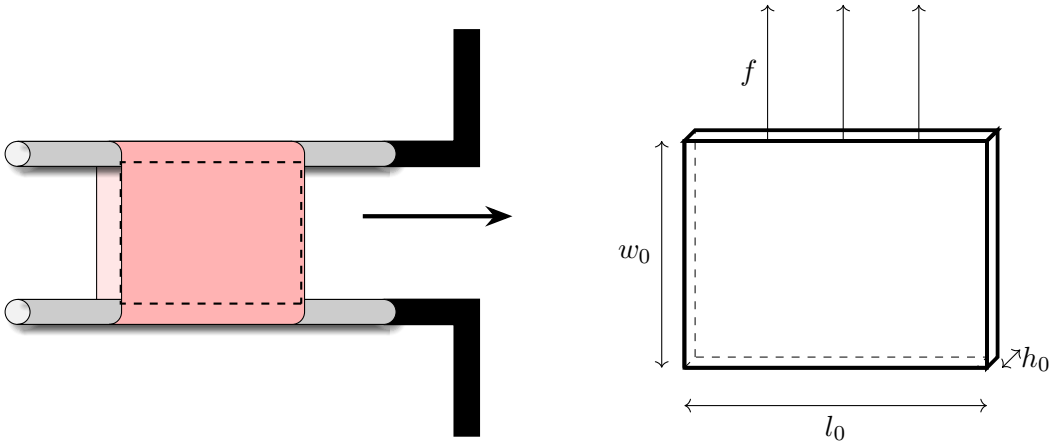

Figure 2.2: Schematics of the ROTSAC setup (left) and simplified geometry considered in the mathematical model (right).

2.2.2.1 Geometric definition of a shell

The objective of this section is to provide the necessary concepts of differential geometry needed to present the 3D-shell model. For a more detailed overview, please refer to Chapelle and Bathe (2010).

Along this work, we consider that the solid reference configuration Ω is defined by its mid-surface $\mathcal{S}$ (see Figure 2.3). We consider a smooth enough mapping

$$\boldsymbol{\phi} : \omega \subset \mathbb{R}^2 \longrightarrow \mathbb{R}^3,$$

parametrizing the solid mid-surface, i.e., $\mathcal{S} = \boldsymbol{\phi}(\omega)$, where ω denotes a reference domain in $\mathbb{R}^2$. Let (ξ^1, ξ^2) denote the coordinates used in $\mathbb{R}^2$ (hence in ω), and assume that $\boldsymbol{\phi}$ is such that, at each point of the mid-surface, the vectors

$$\boldsymbol{a}_m(\xi^1, \xi^2) := \frac{\partial \boldsymbol{\phi}}{\partial \xi^m}(\xi^1, \xi^2), \quad m = 1, 2, \quad \forall (\xi^1, \xi^2) \in \omega,$$

are linearly independent. These vectors form a basis for the tangential plane to the mid-surface, which is referred to as the covariant basis. The unit vector normal to the tangential plane is defined as

$$\boldsymbol{a}_3 := \frac{\boldsymbol{a}_1 \times \boldsymbol{a}_2}{||\boldsymbol{a}_1 \times \boldsymbol{a}_2||}.$$

We also introduce the contravariant basis of the tangential plane $(\boldsymbol{a}^1, \boldsymbol{a}^2)$, such that

$$\boldsymbol{a}_m \cdot \boldsymbol{a}^n = \delta_m^n, \quad m, n = 1, 2,$$

where δ represents the Kronecker symbol.

The metric tensor is given by

$$a_{mn} := \boldsymbol{a}_m \cdot \boldsymbol{a}_n,$$

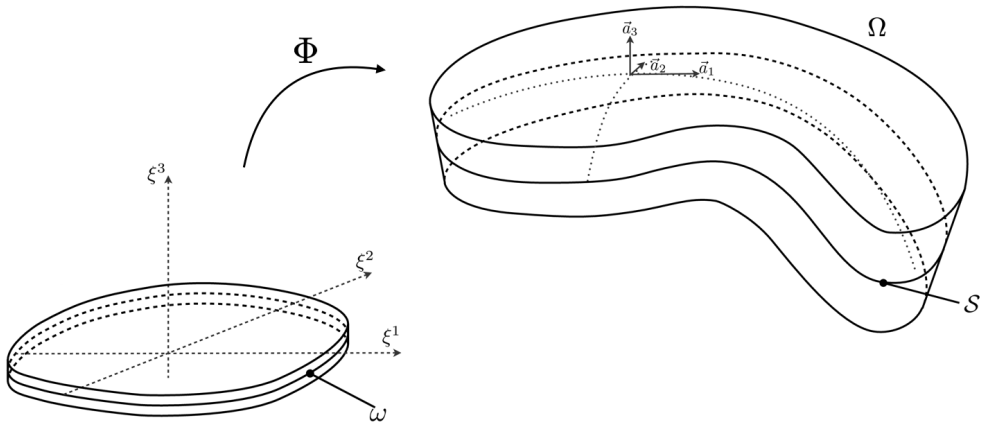

Figure 2.3: Geometric description of a shell.

or in contravariant components

$$a^{mn} := \boldsymbol{a}^m \cdot \boldsymbol{a}^n.$$

Finally, we consider the mapping

$$\boldsymbol{\Phi} : \omega \times (-1,1) \longrightarrow \mathbb{R}^3, \quad \boldsymbol{\Phi}(\xi^1,\xi^2,\xi^3) := \boldsymbol{\phi}(\xi^1,\xi^2) + \xi^3 \frac{t(\xi^1,\xi^2)}{2} \boldsymbol{a}_3(\xi^1,\xi^2), \tag{2.1}$$

where ξ^3 is the curvilinear coordinate perpendicular to the mid-surface and $t(\xi^1,\xi^2)$ represents the local thickness of the arterial wall. Therefore, the reference configuration Ω is assumed to be parametrized by $\boldsymbol{\Phi}$, i.e., $\Omega = \boldsymbol{\Phi}(\omega \times (-1,1))$. The mapping $\boldsymbol{\Phi}$ is

We now introduce the 3D covariant base vectors

$$\boldsymbol{g}_i(\xi^1,\xi^2,\xi^3) := \frac{\partial \boldsymbol{\Phi}}{\partial \xi^i}(\xi^1,\xi^2,\xi^3), \quad i = 1,2,3, \quad \forall (\xi^1,\xi^2,\xi^3) \in \omega(-1,1),$$

and the contravariant base vectors, such that

$$\boldsymbol{g}_i \cdot \boldsymbol{g}^j = \delta_i^j, \quad i,j = 1,2,3.$$

The 3D metric tensor of the entire body, is expressed in its covariant-covariant components as

$$g_{ij} := \boldsymbol{g}_i \cdot \boldsymbol{g}_j, \quad i,j = 1,2,3,$$

and the components of the twice-contravariant metric tensor are

$$g^{ij} := \boldsymbol{g}^i \cdot \boldsymbol{g}^j, \quad i,j = 1,2,3.$$

2.2.2.2 3D-shell model

Let $\Omega \subset \mathbb{R}^3$ denote the reference (stress-free) configuration of the tissue segment. The boundary of $\partial\Omega$ is partitioned into three subsets: Γ_N, which corresponds to the upper boundary of the domain where the force is applied to stretch the tissue; Γ_D, representing

the part of the aortic segment attached to the lower hook, which is clamped during the whole experiment; and Γ_L, that are the lateral boundaries of the aortic segment. We denote by $\mathbf{n}$ the outward unit normal on the boundary Γ_N. The reference configuration Ω is characterized by l_0, w_0 and h_0, that are the stress-free length, width and thickness, respectively, as shown in Figures 2.2(right) and 2.4.

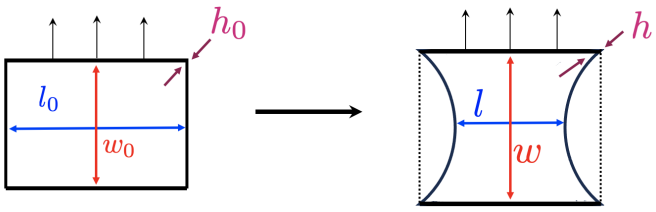

Figure 2.4: Geometric configuration of the solid. On the left the reference configuration and on the right the deformed one.

The deformation of the continuum medium is given as the map $\boldsymbol{\varphi} : \Omega \times [0, T] \longmapsto \mathbb{R}^3$. The deformation gradient $\mathbf{F}$, is expressed as $\mathbf{F}(\boldsymbol{x}, t) = \boldsymbol{\nabla}_{\boldsymbol{x}} \boldsymbol{\varphi}(\boldsymbol{x}, t)$, and its determinant J, as $J(\boldsymbol{x}, t) = \det(\mathbf{F}(\boldsymbol{x}, t))$. The displacement field $\mathbf{d}$ is defined as $\mathbf{d}(\boldsymbol{x}, t) = \boldsymbol{\varphi}(\boldsymbol{x}, t) - \boldsymbol{x}$.

The equilibrium of the system is given by the following nonlinear elastodynamics boundary value problem:

$$\begin{cases} \rho \partial_{tt} \mathbf{d} - \operatorname{div}(\mathbf{F}(\mathbf{d})\boldsymbol{\Sigma}(\mathbf{d})) = \mathbf{0}, & \text{in } \Omega, \\ \mathbf{F}(\mathbf{d})\boldsymbol{\Sigma}(\mathbf{d})\mathbf{n} = \mathbf{f}_s, & \text{on } \Gamma_N, \\ \mathbf{d} = \mathbf{0}, & \text{on } \Gamma_D, \end{cases} \tag{2.2}$$

where ρ stands for the density of the tissue, $\mathbf{f}_s$ represents the time-dependent pulling force and

$$\boldsymbol{\Sigma}(\boldsymbol{d}) = J\boldsymbol{F}^{-1}(\boldsymbol{d})\boldsymbol{\sigma}(\boldsymbol{d})\boldsymbol{F}^{-T}(\boldsymbol{d}), \tag{2.3}$$

is the second Piola-Kirchhoff stress tensor of the tissue, being $\boldsymbol{\sigma}(\boldsymbol{d})$ the Cauchy stress tensor.

The active SMC fibers are assumed to be perfectly attached to the solid so that to model the active behavior of the artery wall, an active-stress formalism (Ambrosi and Pezzuto, 2012) is chosen, which consists in adding an active component to the passive stress tensor (Decoene et al., 2023), viz.,

$$\boldsymbol{\Sigma}(\mathbf{d}) = \boldsymbol{\Sigma}_p(\mathbf{d}) + \boldsymbol{\Sigma}_a(\mathbf{d}),$$

with $\boldsymbol{\Sigma}_a(\mathbf{d})$ and $\boldsymbol{\Sigma}_p(\mathbf{d})$ respectively denoting the active and passive components of the stress.

The simplest hyperelastic material model is the Saint-Venant Kirchhoff model, which is just an extension of the geometrically linear elastic material model to the geometrically nonlinear regime.

The strain energy density function for the Saint-Venant Kirchhoff model is

$$W(\mathbf{E}) = \frac{\lambda}{2}(tr(\mathbf{E}))^2 + \mu\, tr(\mathbf{E}^2), \tag{2.4}$$

where

$$\mathbf{E}(\mathbf{d}) := \frac{1}{2}(\mathbf{C} - \mathbf{I}), \tag{2.5}$$

is the Green-Lagrange strain tensor and $\mathbf{C} := \mathbf{F}^T \cdot \mathbf{F}$ stands for the right Cauchy-Green deformation tensor. Equation (2.4) can be written in terms of the invariants of $\mathbf{C}$ as

$$W = \left(\frac{\lambda}{8} + \frac{\mu}{4}\right) I_1^2 - \frac{\mu}{2} I_2 - \left(\frac{3\lambda}{4} + \frac{\mu}{2}\right) I_1 + \frac{9\lambda}{8} + \frac{3\mu}{4},$$

where λ is the first Lamé parameter and μ is the shear modulus or the second Lamé parameter, given by

$$\lambda = \frac{\nu E}{(1+\nu)(1-2\nu)}, \quad \mu = \frac{E}{2(1+\nu)},$$

being E the Young modulus and ν the Poisson's ratio.

The Saint-Venant Kirchhoff constitutive law is well-suited for materials with small deformations and linear stress-strain behavior. However, in scenarios involving large deformations and nonlinear stress-strain responses, such as those often encountered in biological tissues, this model may not offer accurate representations.

An Ogden hyperelastic constitutive law is chosen to describe the homogeneous and isotropic passive component, since it accommodates large deformations and nonlinear material responses, providing a more accurate representation for the behavior of complex materials like biological tissue (Lohr et al., 2022; Nedrelow et al., 2023). We hence have

$$\mathbf{\Sigma}_p = 2\frac{\partial W}{\partial \mathbf{C}},$$

where the strain energy density function W is given by the relation (Geymonat and Ciarlet, 1982):

$$W = c_1(I_1 - 3) + c_2(I_2 - 3) + a(I_3 - 1) - (c_1 + 2c_2 + a)ln(I_3), \tag{2.6}$$

in terms of the invariants of $\mathbf{C}$, namely, $I_1 = \mathrm{tr}(\mathbf{C})$, $I_2 = \frac{1}{2}(I_1^2 - \mathbf{C} : \mathbf{C})$, and $I_3 = \det(\mathbf{C}) = J^2$.

In (2.6), the constants c_1, c_2 and a stand for the material parameters. Interest lies in establishing a relation between the Ogden parameters and the Lamé parameters so that c_1, c_2 and a can be expressed as a function of the Young modulus, E, and the Poisson ratio, ν. The asymptotic behavior of the Ogden law is examined as $|\mathbf{E}| \longrightarrow 0$, aiming to identify it with the Saint-Venant Kirchhoff law (2.4). Upon conducting a limit development up to second order in $\mathbf{E}$, it can be demonstrated (refer to the detailed computation in Trabelsi (2004); Ciarlet (1988)) that

$$\begin{cases} 2c_1 + 2c_2 = \mu, \\ c_2 + a = \dfrac{\lambda}{4}, \\ \lambda + 2\mu = 2b, \\ b = 2c_1 + 4c_2 + 2a. \end{cases}$$

Usually c_2 can be chosen such that $c_2 = c_1/\kappa$, with $\kappa \in [2, 100]$. After doing some algebra, it is possible to write

$$\begin{cases} c_1 = \dfrac{E}{4(1+\nu)(1+\frac{1}{\kappa})}, \\ c_2 = \dfrac{c_1}{\kappa}, \\ a = \dfrac{\nu E}{4(1+\nu)(1-2\nu)} - \dfrac{c_1}{\kappa}. \end{cases}$$

The elastodynamics equations (2.2) can be reformulated in weak variational form as follows

$$\begin{cases} \text{Find } \mathbf{d} \in \mathbf{V} \text{ such that} \\ \displaystyle\int_\Omega \rho \partial_{tt}\mathbf{d} \cdot \mathbf{v} + \int_\Omega \boldsymbol{\Sigma}(\mathbf{d}) : \delta_{\mathbf{d}}\mathbf{E}(\mathbf{d})\mathbf{v} = \int_{\Gamma_N} \mathbf{f_s} \cdot \mathbf{v}, \quad \forall \mathbf{v} \in \mathbf{V}, \end{cases} \tag{2.7}$$

where $\mathbf{V}$ is the space of admissible displacements, $\mathbf{E}$ is the Green-Lagrange strain tensor, given by equation (2.5), and $\delta_{\mathbf{d}}\mathbf{E}(\mathbf{d})\mathbf{v}$ stands for the differential of $\mathbf{E}$ in the direction $\mathbf{v}$. In curvilinear coordinates, the Green-Lagrange strain tensor writes

$$E_{ij}(\boldsymbol{d}) := \frac{1}{2}(\boldsymbol{g}_i \cdot \boldsymbol{d}_{,j} + \boldsymbol{g}_j \cdot \boldsymbol{d}_{,i} + \boldsymbol{d}_{,i} \cdot \boldsymbol{d}_{,j}), \tag{2.8}$$

and the first order infinitesimal variation is given by

$$\delta_{\mathbf{d}} E_{ij} := \frac{1}{2}(\boldsymbol{g}_i \cdot \delta_{\mathbf{d}}\boldsymbol{d}_{,j} + \boldsymbol{g}_j \cdot \delta_{\mathbf{d}}\boldsymbol{d}_{,i} + \boldsymbol{d}_{,i} \cdot \delta_{\mathbf{d}}\boldsymbol{d}_{,j} + \boldsymbol{d}_{,j} \cdot \delta_{\mathbf{d}}\boldsymbol{d}_{,i}).$$

A fundamental drawback of the full 3D model (2.7) is that, due to the thin-walled nature of Ω, 3D finite element approximations of (2.7) suffer from artificial stiffening phenomena, known as numerical locking (see, e.g., Chapelle and Bathe (2010)), which often requires highly refined meshes across the thickness and can hence become computationally expensive in practice. These issues are traditionally avoided by considering reduced models based on shell theory in combination with an appropriate treatment of numerical locking at the discrete level (see, e.g., Chapelle and Bathe (2010); Bischoff and Ramm (1997)). In this work, we consider a 3D-shell modeling approach based on a quadratic kinematic behavior along the transverse coordinate (see Chapelle et al. (2004b)), without any plane stress assumption. This enables the use of general constitutive laws. The basic idea consists in replacing, in (2.7), the original full 3D space $\mathbf{V}$ by the following reduced space:

$$\mathbf{V}^{\text{sh}} := \left\{ \mathbf{v} \in \mathbf{V} \,:\, \mathbf{v} = \mathbf{v}_0 + \mathbf{v}_1\xi^3 + \mathbf{v}_2(\xi^3)^2, \quad \mathbf{v}_i \in \left[H^1(\mathcal{S})\right]^3, \quad i = 0, 1, 2 \right\}, \tag{2.9}$$

where ξ^3 corresponds to the local transverse coordinate of Ω and $\mathcal{S}$ to the mid-surface of Ω (see Figure 2.3). The resulting 3D-shell model hence reads as follows:

$$\begin{cases} \text{Find } \mathbf{d} \in \mathbf{V}^{\text{sh}} \text{ such that} \\ \displaystyle\int_\Omega \rho \partial_{tt}\mathbf{d} \cdot \mathbf{v} + \int_\Omega \boldsymbol{\Sigma}(\mathbf{d}) : \delta_{\mathbf{d}}\mathbf{E}(\mathbf{d})\mathbf{v} = \int_{\Gamma_N} \mathbf{f}_{\text{s}} \cdot \mathbf{v}, \quad \forall \mathbf{v} \in \mathbf{V}^{\text{sh}}. \end{cases} \tag{2.10}$$

The numerical approximation of (2.10) is performed via the finite element method, in which the space $\mathbf{V}^{\text{sh}}$ is replaced by the discrete space $\mathbf{V}_h^{\text{sh}}$ spaned by quadratic displacements across the thickness and affine on each section (Chapelle et al., 2004b; Libai and Simmonds, 2005; Chapelle and Bathe, 2010). This yields a $\mathbb{P}_1 \otimes \mathbb{P}_2$ prismatic element with 9 nodes (see Figure 2.5). Numerical locking is avoided using a MITC (Mixed Interpolated Tensorial Components) approach which guarantees robustness with respect to the thickness parameter.

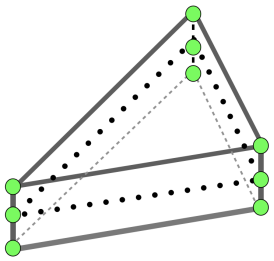

Figure 2.5: $\mathbb{P}_1 \otimes \mathbb{P}_2$ 3D-shell element.

In order to be able to apply MITC techniques, it is necessary to compute the first and second derivatives of the stored energy with respect to the Green-Lagrange tensor. The second order infinitesimal variation is given by

$$d\delta_{\mathbf{d}} E_{ij} := \frac{1}{2}(d\boldsymbol{d}_{,i} \cdot \delta_{\mathbf{d}} \boldsymbol{d}_{,j} + d\boldsymbol{d}_{,j} \cdot \delta_{\mathbf{d}} \boldsymbol{d}_{,i}),$$

The Green-Lagrange tensor is a nonlinear function of the displacement $\boldsymbol{d}$ and Newton's algorithm is selected for this purpose. At each time of the backward Euler time discretization, a nonlinear problem has to be solved. The bilinear form appearing in this algorithm is the following:

$$A = A^L + A^{NL},$$

with

$$A^L := \int_\Omega \frac{\partial^2 W}{\partial E_{ij} \partial E_{kl}} dE_{kl} \delta_{\mathbf{d}} E_{ij} d\Omega,$$

$$A^{NL} := \int_\Omega \frac{\partial W}{\partial E_{ij}} d\delta_{\mathbf{d}} E_{ij} d\Omega,$$

and the corresponding nonlinear right-hand side

$$F^{NL} := \int_\Omega \frac{\partial W}{\partial E_{ij}} \delta_{\mathbf{d}} E_{ij} d\Omega.$$

All the simulations presented in this work have been performed using FELiScE[2].

[2] https://gitlab.inria.fr/felisce

2.2.2.3 Active fiber model

The main hypotheses regarding the fibers are the following:

- The fibers are part of the shell and are distributed through the thickness in the circumferential direction;
- There is no sliding between the fibers and the shell;
- The fibers are characterized by an affine stress-strain constitutive law.

Here, we consider the active fibers model proposed in Aletti et al. (2015), so that

$$\boldsymbol{\Sigma}_a := (k_0 + k_1 e_{\mathbf{ff}})\mathbf{f} \otimes \mathbf{f}, \tag{2.11}$$

where k_0 denotes the pre-stress of the fiber, k_1 is the elastic modulus, $e_{\mathbf{ff}}$ is the fiber deformation and $\mathbf{f}$ is the unitary tangent vector to the fiber direction. The deformation along the fiber directions is given by the relation $e_{\mathbf{ff}} = \mathbf{f}^T\mathbf{E}\mathbf{f}$, where $\mathbf{E}$ is the Green-Lagrange strain tensor.

2.2.3 Parameter estimation and model validation

The mathematical model (2.7), together with the hyperelastic law (2.6) and the fibers constitutive law (2.11), contains a set of parameters (Young modulus, E; active pre-stress, k_0, and elastic modulus, k_1, of the fibers; κ, that stems from the Ogden's law; initial length, l_0, width, w_0, and thickness, h_0, of the aortic segment[3]) that are unknown and are determined through a parameter estimation procedure. After spatial and temporal discretization, the model (2.7), with (2.6) and (2.11), yield the nonlinear system

$$F\big(\boldsymbol{f}_s, \boldsymbol{\theta}; \boldsymbol{Y}\big) = 0, \tag{2.12}$$

where $\boldsymbol{f}_s$ is the given force, that can be measured, $\boldsymbol{\theta} = (E, k_0, k_1, \kappa; l_0, w_0, h_0)$ are the model parameters and $\boldsymbol{Y}$ is the model output, that corresponds to the displacement degrees of freedom. The inputs of the model are $\boldsymbol{\theta}$ and $\boldsymbol{f}_s$.

The purpose of the parameter estimation is evaluating some unknown inputs of the model such that the outputs match the experimental measurements. The parameter estimation problem can be formulated as follows: given the force $\boldsymbol{f}_s$, the discrete model (2.12) and the experimental data, find the parameters $\boldsymbol{\theta}$ that minimize the discrepancy between the simulated model predictions and measurements. Mathematically, this problem can be formulated as the optimization problem

$$\min_{\substack{\boldsymbol{\theta}\in\boldsymbol{W} \\ F\left(\boldsymbol{f}_s,\boldsymbol{\theta},\boldsymbol{Y}\right)=0}} J\big(\boldsymbol{Y}\big), \tag{2.13}$$

where $J : \mathbb{R}^n \to \mathbb{R}$ is given cost function (viz., discrepancy between simulation and measurements) and $\boldsymbol{W} \subset \mathbb{R}^n$ stands for the set of admissible parameters. In this chapter, problem (2.13) is solved via a Control Random Search (CRS) optimization algorithm.

[3] All the segments have an approximated length of 2 mm and width of 1 mm. However, there might be slight differences between them and the initial configuration needs thus to be estimated.

Initially, the estimation is done for each aortic segment under Krebs-Ringer solution. Subsequently, estimations are conducted following the administration of a vasoactive drug, either a vasoconstrictor or vasodilator. The results of the parameter estimation provides hence insight on whether the compound solely impacts SMCs (scenario I) or additionally introduces additional intrinsic stiffness (scenario II). Specifically, if only the fiber parameters from the active contribution, such as k_0 and k_1, are affected, it suggests that the first scenario is the most plausible one. However, if the Young's modulus also needs modification, then the compound is likely to introduce stiffness (scenario II). To establish a range for the active pre-stress parameter, data from isometric experiments have been used.

To solve the optimization problem (2.13), a CRS2 with local mutation optimization algorithm (Kaelo and Ali, 2006) that is implemented in the NLopt (nonlinear optimization) package by Johnson (2014) has been employed.

2.2.3.1 Optimization algorithm

To obtain the parameters for each aortic segment, a CRS algorithm is used for optimization (Price, 1978). The optimization problem is formulated it (2.13). A point $\boldsymbol{\theta}_{opt}$ is considered a global minimizer of J if $J_{opt} = J(\boldsymbol{\theta}_{opt}) \leq J(\boldsymbol{\theta})$ for all $\boldsymbol{\theta} \in \boldsymbol{W}$.

CRS algorithms are better in high-dimensional problems compared to DIRECT algorithms. Unlike gradient-based methods, CRS algorithms do not use properties of the function being optimized. The only requirements are that $J(\boldsymbol{\theta})$ can be computed for any $\boldsymbol{\theta} \in \boldsymbol{W}$, and the explicit expression of the function being optimized must be known.

In each step of the algorithm, $n+1$ points are randomly chosen to create a simplex in n-dimensional space. One of these points becomes the pole, and the next trial point is determined by reflecting this pole relative to the centroid of the remaining points. This process generates primary trial points for exploration and secondary trial points for convergence, with the choice between them depending on the algorithm's success rate. If the success rate is below 50%, and a primary trial fails, a secondary point is selected for the next trial, maintaining a balanced approach between exploration and convergence during optimization.

In summary, the CRS algorithm is a heuristic, direct search method that begins by populating a set S with a large sample ($N >> n$) distributed uniformly over the search space $\boldsymbol{W}$. This sample is gradually contracted by replacing the worst point in S with a better trial point, forming a simplex with $n+1$ randomly chosen points from S. This process continues until a specified stopping condition is met.

The main issues with CRS are its lack of robustness in locating the global minimum and its decreased efficiency in convergence, particularly after reaching the region of the global minimum. To enhance the robustness and efficiency of CRS, Kaelo and Ali proposed variants such as CRS2, suggesting modifications to the trial point generation schemes (Price, 1983). Specifically, a CRS algorithm with local mutation for optimization is chosen (Kaelo and Ali, 2006).

In the original algorithm, if a trial point fails to improve upon the current worst point in the sample S, it is discarded, and a new simplex is formed using a new set of $n+1$ points from S.

In CRS with local mutation, the unsuccessful trial point is not discarded but used to obtain a second trial point. The point generation scheme is modified by introducing a local mutation technique. Whenever a trial point generated in CRS fails to replace the current worst point in S, local mutation generates a second trial point exploring the region around the current best point in S by reflecting the trial point through the current best point. This modification is utilized whenever a trial point fails to yield a function value that can replace the current worst point in S.

The introduction of local mutation has enhanced these algorithms' robustness in finding the global minimum and efficiency in reducing the number of function evaluations and CPU time. Additionally, the local mutation technique expedites convergence as soon as the region of the global minimizer is reached.

2.2.3.2 Parameter estimation in baseline conditions

During the ROTSAC static calibration, the experimental measurements are the length (l_m) and the width (w_m) of the aortic segments for some given forces $\boldsymbol{f}_s$ while when the segments are dynamically stretched, the measured data is the width ($\tilde{w}_m$). In this case, the cost function of the parameter estimation problem (2.13) has the following form

$$J_1(\boldsymbol{Y}) = \sqrt{\frac{1}{k}\sum_{i=1}^{k}\left|l^{(i)}(\boldsymbol{Y}) - l_m^{(i)}\right|^2 + \left|w^{(i)}(\boldsymbol{Y}) - w_m^{(i)}\right|^2} + \sqrt{\frac{1}{n}\sum_{i=1}^{n}\left|\tilde{w}^{(i)}(\boldsymbol{Y}) - \tilde{w}_m^{(i)}\right|^2}. \quad (2.14)$$

Here, $l_m^{(i)}$ and $w_m^{(i)}$ represent the measured length and width, respectively, during static experimental calibration, with $i = 1, ..., k$ denoting the number of measurements. $\tilde{w}_m^{(i)}$ denotes the measured width during oscillation, with $i = 1, ..., n$ indicating the number of measurements. $l^{(i)}(\boldsymbol{Y})$ and $w^{(i)}(\boldsymbol{Y})$ represent the predicted values of length and width, respectively, during static experimental calibration, while $\tilde{w}^{(i)}(\boldsymbol{Y})$ denotes the predicted value of width during the oscillation.

2.2.3.3 Parameter estimation in the presence of vasoactive substances

Determination of the range of the pre-stress

The isometric experiments provide data that show the force exerted by the vessel in response to a specific vasoconstrictor (or vasodilator) dosage within a static setup. The relevance of these experiments, is that they can provide an estimation of the range of the value of the active pre-stress at each drug concentration C, with C being either C^{PE}, the PE concentration, or C^{DEANO}, the DEANO concentration. In particular, the ROTSAC measurements were taken at $C = 2\ \mu$M and the isometric data allow the estimation of the range of the value of k_0 at the specified C.

We consider that the total measured force is

$$F_m = \beta + F_1, \quad (2.15)$$

where β is the force at zero concentration and F_1 is the isometric force felt by the upper hook in the presence of a vasoactive substance. Assume that the relation between F_1 and

the active pre-stress, k_0, is linear and can be expressed as $F_1 = \alpha\, k_0$. The mathematical model (2.7)–(2.11), has been used applying homogeneous Dirichlet boundary conditions on the upper and on the lower boundary of the domain Ω to estimate α. Substituting the expression for F_1 in (2.15), $F_m = \beta + \alpha k_0$.

Using the following tension-dose relationship (Yosibash and Priel, 2012), the active pre-stress results

$$k_0(C; m, EC_{50}) = S_{\max}^{\mathrm{PE}} \frac{[C^{\mathrm{PE}}]^m}{[C^{\mathrm{PE}}]^m + EC_{50}^m} - S_{\max}^{\mathrm{DEANO}} \frac{[C^{\mathrm{DEANO}}]^m}{[C^{\mathrm{DEANO}}]^m + EC_{50}^m}, \tag{2.16}$$

where $S_{\max}^{\mathrm{PE}}$ is the maximal tension for PE (saturation level), $S_{\max}^{\mathrm{DEANO}}$ is the maximal tension for DEANO, m is the slope parameter and EC_{50} the concentration at which 50% of maximal force is obtained.

Finally, the expression of the total measured force is

$$F_m = \beta + \alpha \left(S_{\max}^{\mathrm{PE}} \frac{[C^{\mathrm{PE}}]^m}{[C^{\mathrm{PE}}]^m + EC_{50}^m} - S_{\max}^{\mathrm{DEANO}} \frac{[C^{\mathrm{DEANO}}]^m}{[C^{\mathrm{DEANO}}]^m + EC_{50}^m} \right). \tag{2.17}$$

During the isometric experiments, the aortic segments have been preloaded with a force $\beta = 20$ mN in the absence of drugs ($C^{\mathrm{PE}} = C^{\mathrm{DEANO}} = 0$) and also $S_{\max}^{\mathrm{PE}}$ and $S_{\max}^{\mathrm{DEANO}}$ are known. By employing the previous F_m - dose relation, a fitting of the measured forces to equation (2.17) to estimate the values of m and EC_{50} was performed. After fitting the measured force for several concentrations in the set of aortic segments, it is possible to determine the range of k_0 for a vasodilator or for a vasoconstrictor.

From equation (2.16), it can be remarked that when there is only PE in the organ bath, $C^{\mathrm{DEANO}} = 0$ and the second term vanishes. After DEANO has been added on the bath, C^{PE} is equal to the concentration at saturation, so $C^{\mathrm{PE}} = 3\,\mu$M.

Dynamic oscillation

In the context of ROTSAC dynamic oscillation with vasoconstrictors/vasodilators, two scenarios are tested. In the first one, only the active fiber parameters k_0 and k_1 are subject to estimation, while E, l_0, w_0, and h_0 remain fixed based on the corresponding segment in Krebs-Ringer solution. Conversely, in the second scenario, parameters E, k_0, k_1, and h_0 are open to estimation, with l_0 and w_0 held constant. The key distinction lies in allowing E to vary during estimation for the second scenario, whereas only the active fiber parameters are adjusted in the first one. Here the parameter estimation is done when a vasoconstrictor (PE, 5HT, or 50K) or a vasodilator (DEANO) are added to the Krebs-Ringer solution to assess the effects. The available experimental measurements are the values of width ($\tilde{w}_m$) of the aortic segment dynamically stretched at 80-120 mmHg. Under the effect of a drug, the cost function of the minimization problem (2.13) is

$$J_2(\boldsymbol{Y}) = \sqrt{\frac{1}{n} \sum_{i=1}^{n} \left| \tilde{w}^{(i)}(\boldsymbol{Y}) - \tilde{w}_m^{(i)} \right|^2}, \tag{2.18}$$

where $\tilde{w}_m^{(i)}$ is the measured experimental value of the width and $\tilde{w}^{(i)}(\boldsymbol{Y})$ is the predicted value of the width at each point $i = 1, ..., n$ during the oscillation. Since there are no static

experimental calibration data with drugs, there is no information of the length in the case of a vasoactive substance on the organ bath. The changes in the fiber parameters k_0, k_1 and in E, h_0, will help to assess the fore-mentioned scenarios.

2.3 Numerical results

First, the results that arise from the parameter estimation of the model are presented. Next, numerical simulation (in baseline conditions and in the presence of vasoactive compounds) is performed. While various vasoconstrictors have been employed, the outcomes are primarily focused on PE due to its resemblance to the others. Finally, the behavior of the aortic segments under varying pressure conditions is explored.

2.3.1 Static experimental calibration

The static experimental calibration measurements of the length and width at different preloads (10, 20, 30, 40 and 50) were considered for estimating the parameters $\boldsymbol{\theta}$ of each aortic segment in the baseline case (Krebs-Ringer solution), together with the dynamic data at 80 - 120 mmHg (using the cost function (2.14) with $k = 5$ and $n = 80$). The static part of results for the set of fifteen aortic segments considered in this studio are shown in Figure 2.6.

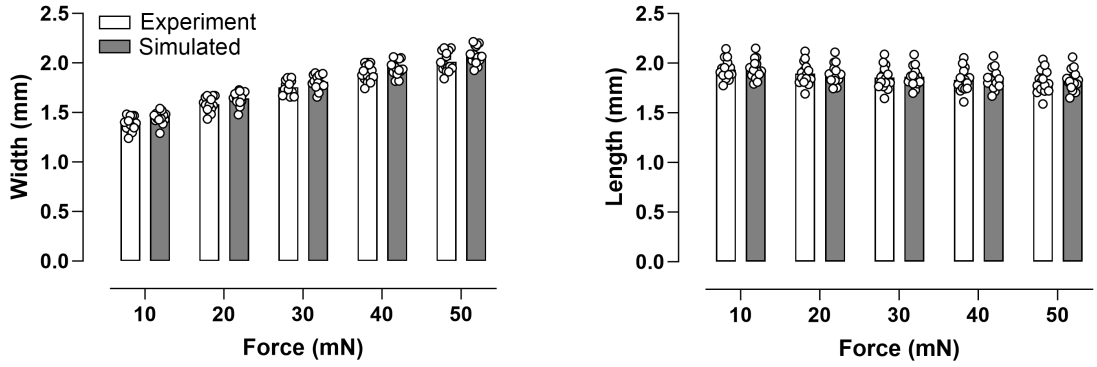

Figure 2.6: Comparison between experimental and simulated static experimental calibrations.

2.3.2 Simulation in the presence of vasoactive substances

Estimation of the range of the pre-stress from the isometric data

First, throughout the isometric tests, where a second set of nine aortic segments was considered, the average Relative Mean Squared Error (RMSE) between the experimental and simulated data across all fittings of the isometric force (2.17) in the presence of PE (2 μM) is 0.56% $\pm$ 0.38%, while 1.86% $\pm$ 0.63% for DEANO, (2 μM) (see the fittings in Figure 2.7).

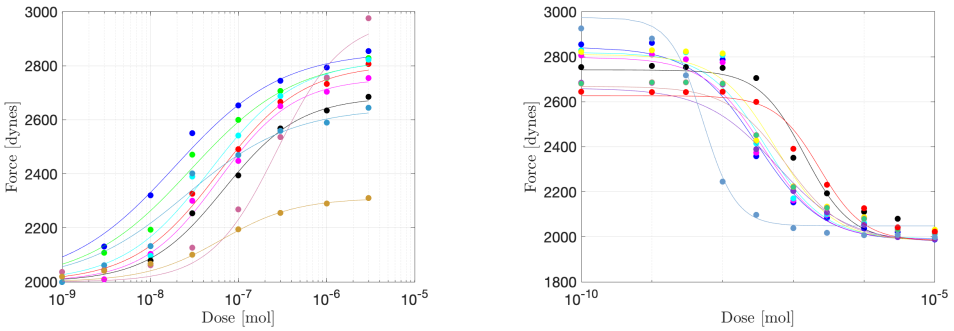

Figure 2.7: Fitting of F_m to equation (2.17) for PE (left) and for DEANO (right) in semilog scale.

The results at $C = 2\,\mu$M for PE or DEANO – the concentration at which dynamic measurements were taken – are shown in Figure 2.8 (left).

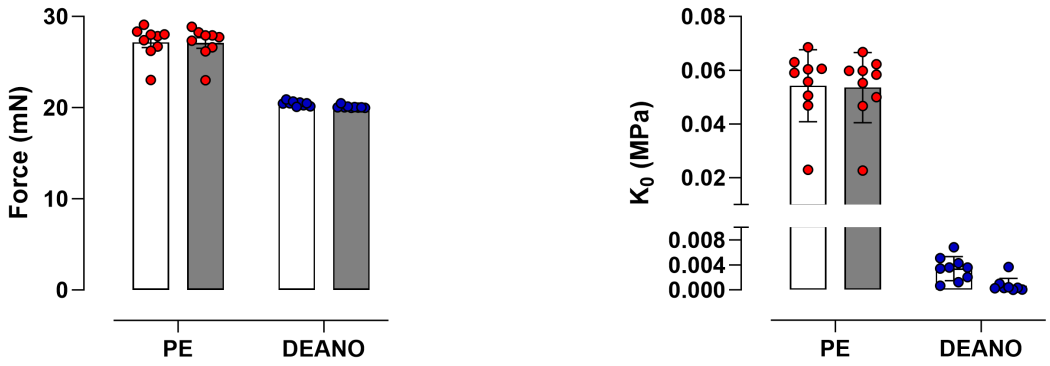

Figure 2.8: Isometric force F_m at $C = 2\,\mu$M (left); pre-stress at $C = 2\,\mu$M (right).

Upon examination of the values of the pre-stress, k_0, for the available set of aortic segments at a concentration of $C = 2\,\mu$M, the range of k_0 for PE and DEANO can be identified (see Figure 2.8 (right)). The observed range of k_0 was [0.023, 0.067] MPa for PE and [-0.00014, 0.0043] MPa for DEANO. The fitting for all the concentrations is presented in Figure 2.9.

Simulation of ROTSAC dynamic oscillation data

Next, parameters were estimated and numerical simulations of experimental data were conducted across 15 segments using a Krebs-Ringer solution (using the cost function (2.14)). From the set of all segments, Table 2.2 details the estimated parameters for one aortic segment (seg #1) under baseline, contracted, and dilated conditions, with corresponding experimental and simulated datasets shown in Figures 2.10A and 2.10B. Figure 2.10 illustrates the impact of vasoconstrictors and vasodilators on arterial behavior (with the parameter estimation performed using the cost function (2.18) with $n = 80$). Particularly, Figure 2.10C displays the Peterson modulus derived from experimental and

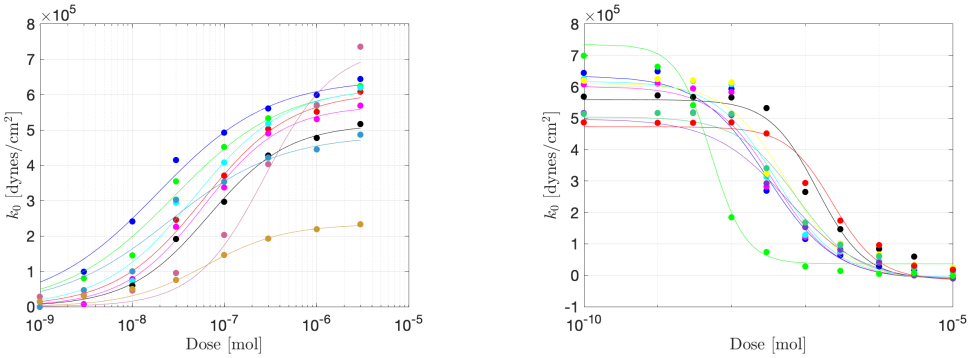

Figure 2.9: k_0 for PE (left) and for DEANO (right) on a semilog scale.

simulated data under KR, PE, and DEANO conditions, while aortic segments underwent oscillations within the pressure range of 80 - 120 mmHg. This graphical representation highlights differences in stiffness across these conditions, with PE exhibiting heightened stiffness relative to baseline, and DEANO resulting in comparable stiffness to baseline. Such observations underscore the model's adeptness in capturing the vascular system's mechanical responses to various vasoactive agents.

Parameter	KR	PE	DEANO
E (MPa)	0.13248	0.13248	0.12717
k_0 (MPa)	$6.4 \cdot 10^{-6}$	0.01	$-1.348 \cdot 10^{-4}$
k_1 (MPa)	0.191	0.457	0.188
	l_0 (mm) $= 1.97$	w_0 (mm) $= 0.13$	h_0 (μm) $= 53$

Table 2.2: Parameters and stress-free configuration for KR, PE, and DEANO for seg #1 in scenario II for PE and DEANO.

Correlation plots (Figures 2.10D, 2.10E, 2.10F) were generated to measure the concordance between simulated and experimental data across different conditions. A statistical covariance matrix $Q \in \mathbb{R}^{2\times N}$ was computed to quantify variability and correlation, with $N \in \mathbb{N}$ representing the number of points. From Q, a matrix $C = \frac{1}{N-1} Q\, Q^T \in \mathbb{R}^{2\times 2}$ was derived to reveal the shape and orientation of ellipses. The eigenvectors of C represent the principal axes of the ellipse and the square root of its eigenvalues will determine the ellipse's width and height, with one of them reflecting the average difference between simulated and experimental data (RMSE) and another one giving an idea of the standard deviation of the fits. Overall, the correlation plots demonstrate a consistent match between the simulated and experimental data, indicating the model's capability in capturing the SMCs behavior under KR, PE, and DEANO.

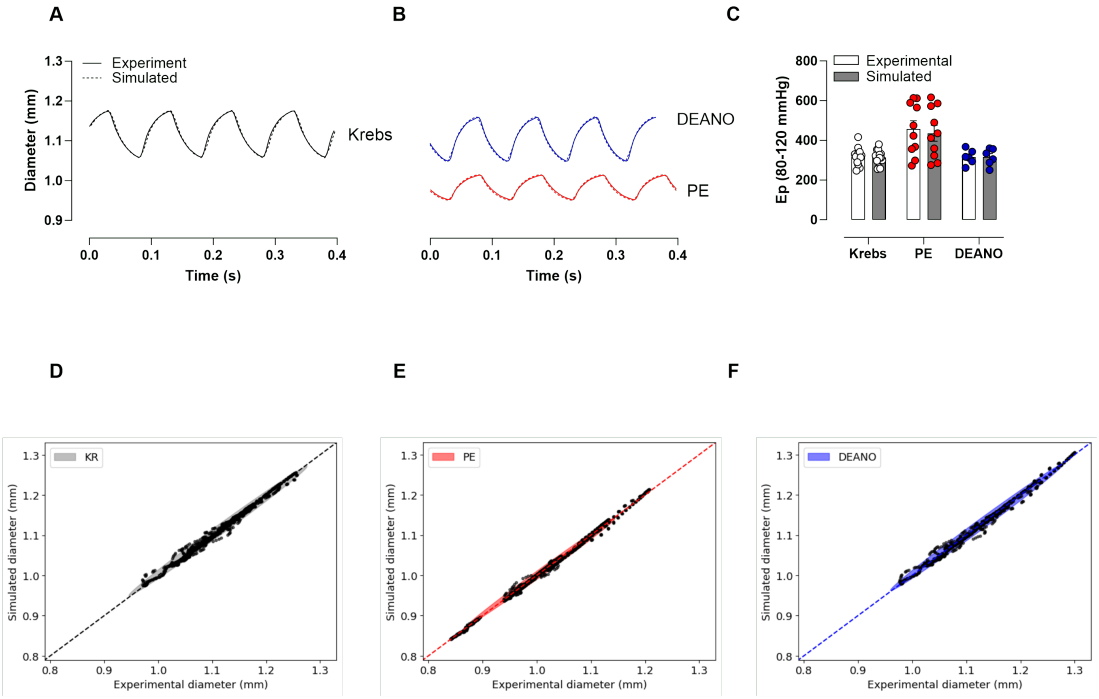

Figure 2.10: Analysis of the impact of PE and DEANO when the segments are dynamically stretched at 80 - 120 mmHg. Time evolution of the experimental and simulated diameters of seg #1 (A, B); Peterson modulus (C); Correlation between experimental and simulated diameters (D, E, F). The ellipse intersects the unity line, which depicts where the simulated and experimental data would coincide perfectly, being the center of the ellipse the average position of the points.

Assessing the role of SMCs

Finally, comparisons between the changes of fiber parameters (k_0 and k_1) in the presence of a vasoconstrictor or vasodilator with E and h_0 constant (scenario I) or with re-estimation of E and h_0 (scenario II) were investigated. The analysis depicted in Table 2.3 illustrates the effectiveness of integrating k_0 and k_1 under constant E and h_0 conditions to fit dynamical experimental data within the pressure range of 80 - 120 mmHg.

KR (%)	Scn1 PE (%)	Scn2 PE (%)	Scn1 DEANO (%)	Scn2 DEANO (%)
0.60	1.60	0.44	0.63	0.58

Table 2.3: Average of the RMSE of the dynamic fittings for Krebs-Ringer and in both scenarios (Scn1 or Scn2) at 80 - 120 mmHg.

The mean RMSE values for the dynamic fittings are all below 2%, indicating that both scenarios provide accurate representations of the compound's effects on SMCs. Although the second scenario may yield a slightly better fit, the error in the first scenario is sufficiently

low with just fiber parameter adjustments, suggesting that modifying the Young's modulus is generally unnecessary. However, in cases where the error is larger, it may indicate that the compound also affects the intrinsic stiffness of the vessel, necessitating adjustments to parameters such as the Young modulus or thickness. Overall, the results suggest that the change of k_0 and k_1 in the presence of a vasoconstrictor or vasodilator with E and h_0 constant, is generally sufficient, but there might be cases where improvements can be made by re-estimating E and h_0.

The active fiber parameters were changed in the presence of a vasoconstrictor with respect to the baseline (Figures 2.11A and 2.11B). The pre-stress is also seen to increase with the introduction of a vasoconstrictor (Figure 2.11A, $p < 0.01$). The active elastic modulus experienced an increase (Figure 2.11B, $p < 0.01$), indicating an augmentation in vessel stiffness. No differences were reported in the change in Young modulus following constriction with PE (Figure 2.11C). Overall, the majority of segments underwent a Young modulus change within the range of [-1, 1] %. While some cases exhibited a slightly larger deviation, on the whole, the scenario in which the change of fiber parameters (k_0 and k_1) in the presence of a vasoconstrictor or vasodilator with E and h_0 constant appears to be a plausible one. No changes in aortic thickness were reported following PE stimulation (Figure 2.11D).

For simplicity, the results for DEANO were excluded from the graphs as they closely resemble those of KR. However, the response to DEANO is more complex to interpret, where the pre-stress may either rise or fall relative to the baseline. It's important to acknowledge that DEANO was administered alongside the vasoconstrictor in the organ bath, making it challenging to isolate its specific effect. Among vasodilators, changes in pre-stress exhibit diverse patterns—sometimes increasing, other times decreasing. Vasodilators typically lower blood pressure and wall tension by dilating vessels and enhancing compliance, resulting in an overall reduction in pre-stress. However, the complex interaction of compensatory mechanisms and individual variations can influence the effect on pre-stress. On the other hand, with the other parameters (k_1, E and h_0) the obtained results are very close to the ones of KR.

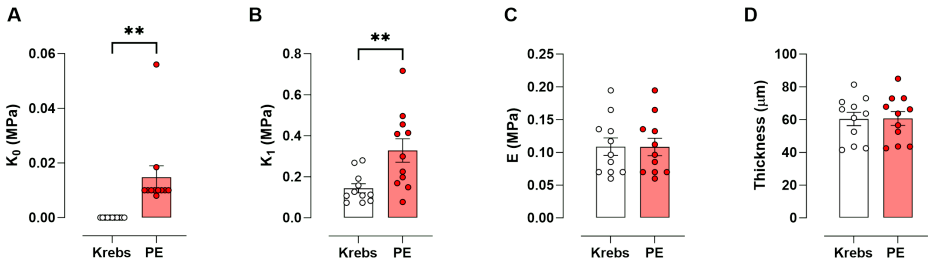

Figure 2.11: Vessel parameters under different conditions. Change of the pre-stress (A), fibers elastic modulus (B), Young modulus (C) and thickness (D) for PE with respect to the baseline. The values for a vasodilator (DEANO) are omitted since they are very similar to the ones of KR.

Evaluating the model in different pressure ranges

After presenting the estimated parameters for each scenario, additional model validation was conducted by examining the predictability across different pressure ranges. The outcomes corresponding to the segment with parameters outlined in Table 2.2 (seg #1) are illustrated in Figure 2.12. The oscillations were represented only for KR and PE since the ones for DEANO are very similar to the ones of KR.

When aortic segments were stretched in Krebs-Ringer solution, the original estimated parameters were able to reproduce the data both in the ranges of 60 - 100 mmHg to 100 - 140 mmHg. However, there was an underestimation at higher pressures (120 - 160 mmHg). One possible explanation could be because the segments exhibited plasticity and did not recover the reference configuration (l_0, w_0 and h_0) instantaneously. Consequently, it was necessary to take into account that the reference configuration had changed after large forces were applied. Then, a re-estimation of l_0, w_0 and h_0 was needed for the pressure range 120 - 160 mmHg, while the rest of the parameters (E, k_0 and k_1) were kept constant. After PE was added to the Krebs-Ringer solution, the change of the reference configuration was observed in all the pressure ranges so, again, the re-estimation of the initial length, width, and thickness was necessary. Finally, once DEANO was added to the organ bath, a similar behavior was observed, so the re-estimation was only needed for the highest pressure range.

From a biological perspective, the underestimation at higher pressures can be attributed to the properties of the arterial wall. When subjected to elevated forces, such as those experienced at higher pressure ranges, arterial segments may encounter layers of collagen within their structure. This discrepancy is particularly pronounced in KR solution, where the arterial segments experience greater pressure-induced deformation. Conversely, when PE is added, the effects are mitigated to some extent. This is because PE-induced constriction leads to smaller diameter arteries, reducing the likelihood of encountering collagen layers and thus minimizing the bouncing effect.

From a mathematical point of view, the underestimation arises from a different perspective. Rather than adjusting the stiffness of the model, which remains constant, the observed phenomenon can be explained by changes in the reference configuration of the arterial segments. When subjected to higher pressures, the segments exhibit plasticity and fail to immediately return to their original reference configuration (l_0, w_0, and h_0). This deviation from the reference configuration needs a (re)estimation of these parameters to capture the behavior of the arterial segments under the new pressure conditions. In summary, while from a biological perspective the focus is on altering stiffness to explain the observed phenomena, from a mathematical one, the adjustment of the configuration parameters to account for the changes in arterial behavior is done.

The active pressure-stiffness curve (Figure 2.13B) demonstrates elevated arterial stiffness levels at lower mean pressures (80, 100 mmHg) in contrast to those observed under KR (Figure 2.13A) and DEANO (Figure 2.13C) conditions. This distinction is further evident in the corresponding diameter measurements, where exposure to PE (Figure 2.13E) yielded smaller diameters relative to those observed under KR (Figure 2.13D) and DEANO (Figure 2.13F) conditions. Consequently, this phenomenon leads to an augmented arterial

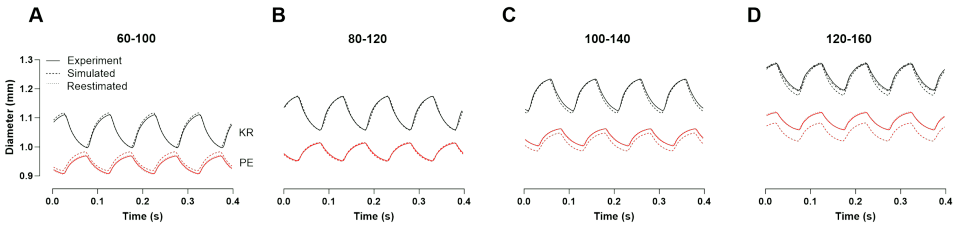

Figure 2.12: Pressure steps under Krebs-Ringer and PE of one aortic segment

stiffness, indicative of an enhanced buffering capacity and concomitant elevation in vascular tone. However, as mean pressures increase, the recruitment of collagen emerges as the predominant load-bearing component within the aortic wall. The absence of stiffer collagen fibers within our current model results in an underestimation of stiffness values at highest pressure (Figure 2.13A, 2.13B, 2.13C).

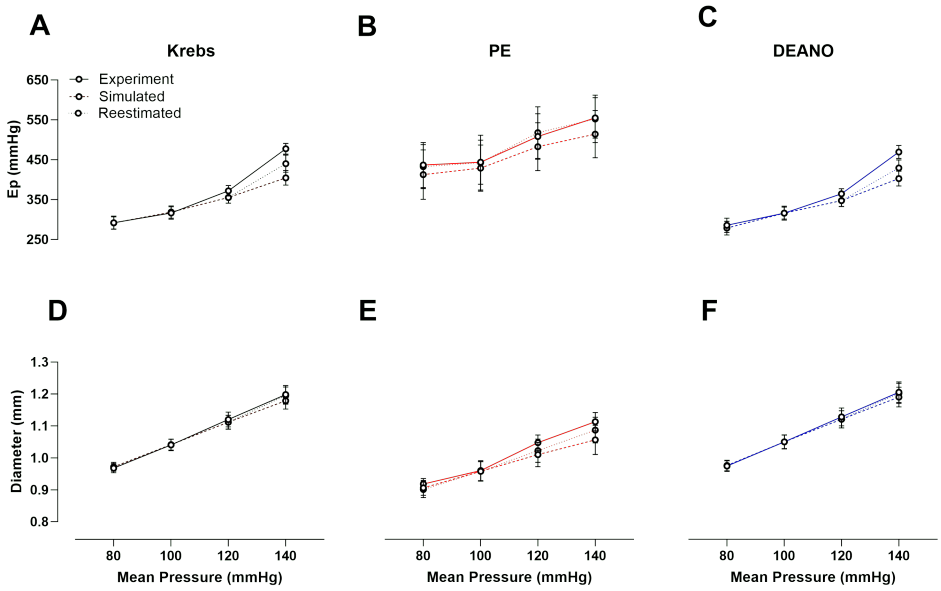

Figure 2.13: Diastolic diameter and Peterson modulus for KR, PE and DEANO under different pressure steps.

2.4 Discussion

In this chapter, we introduced a mathematical framework with a limited and manageable set of parameters, capable of capturing both vasoconstriction and vasodilation. This framework facilitates the understanding of the mechanical behavior of arterial segments and the role of SMCs in arterial stiffness, while also reproducing the experimental data.

The proposed mathematical model combines in parallel an hyperelastic 3D-shell with an active fiber description of the SMCs. An Ogden hyperelastic law is used for the passive component while the active component is based on an affine stress-strain relationship.

This model was calibrated using isometric data to simulate the action of molecules on SMCs. Importantly, we not only established the model but also validated it against experimental data and explored two distinct scenarios to evaluate the impact of the active contribution of SMCs on arterial mechanics. Furthermore, the model was tested with different pressure conditions beyond those used for parameter estimation, demonstrating its capacity of representing the pressure-diameter relationship except some deviations observed at higher pressures.

Although structure-based passive mechanical models of blood vessels have been studied extensively (Lanir, 1983; Wuyts et al., 1995; Dahl et al., 2008; Lokshin and Lanir, 2009; Hollander et al., 2011; Rachev and Shazly, 2019), there remains a notable gap in the development of models addressing active properties. Mechanical studies of active vessels have predominantly relied on phenomenological models, primarily due to the complex micro-environment of SMCs and the coupled mechanical and chemical kinetics (Gestrelius and Borgström, 1986; Yang et al., 2003a; Stålhand et al., 2011). The majority of the active blood vessel constitutive models suggest uniaxial length-tension relationships in the circumferential direction as motivated by the circumferential arrangement of SMCs (Clark and Glagov, 1985; Wolinsky and Glagov, 1967; Hansen et al., 1980; O'Connell et al., 2008).

The choice between 0D, 1D, 2D, or 3D models is influenced by the level of spatial detail required and the complexity of the phenomena under investigation. 1D models are usually validated against *in vitro* data (Westerhof et al., 1971) and present a higher computational efficiency in comparison to 3D models. However, with low-dimensional models it is not possible to account for the detailed structural features of the wall, such as nonlinearity, anisotropy, and residual stresses while 3D structural models become essential when detailed spatial information is necessary to capture complex vessel geometries and interactions. The majority of models concerning SMCs rely on either 0D ordinary differential equations or 1D formulations (Rachev and Hayashi, 1999; Fay and Delise, 1973; Lee and Schmid-Schönbein, 1996; Yang et al., 2003a,b; Bursztyn et al., 2007; Murtada et al., 2010; Jin et al., 2020). For instance, Jin et al. (2020) used a 1D model to simulate arterial blood pressure, blood flow, wall shear stress, and luminal diameter during flow-mediated dilation tests, employing principles of mass and momentum conservation alongside an elastic tube law for pressure changes. Coccarelli et al. (2021) and Liu (2014) focused on characterizing the biomechanical features of SMC contractility, whilst Chen et al. (2013) introduced a structural passive model alongside a 2D active vascular smooth muscle model capable of predicting axial vasoactivity. Furthermore, Murtada et al. (2012) implemented Hill's three-element model coupled with the four-state latch model by Hai and Murphy to capture electromechanical activation in the pig carotid media, successfully predicting isometric contraction, sudden extensions, and length-tension relationships.

In general, there is a lack of studies modeling SMC activation within the continuum mechanics framework. For example, Stålhand and co-authors developed in Stålhand et al. (2011) a mechanochemical 3D continuum model for SMC contraction based on their one-dimensional model (see Stålhand et al. (2008)). However, although the model has

been developed in a 3D continuum framework, uniaxial examples have been shown, only. Coccarelli et al. (2018) introduces a 3D-derived, fiber-reinforced, hyperelastic structural model, coupled with an axisymmetric, reduced-order model for blood flow. This model incorporates the relationship between vessel transmural pressure and lumen area via a Holzapfel–Ogden type law, while also considering residual stresses along the vessel's thickness and length. Despite the increased complexity and parameter count compared to standard pressure-area tube laws, the advantages of employing such a model are numerous. Firstly, it can account for various conditions and pharmacological agent effects, such as axial loading, fiber dispersion, residual stress, and potentially active contractility. Secondly, the structural model developed by Holzapfel and colleagues that is used in Coccarelli et al. (2018) captures the nonlinear behavior of vascular tissue, especially under blood pressure loads significantly above the physiological range.

In our study, the 3D structural model proposed shares some similarities from the other 3D models proposed but also brings new contributions. Our model integrates a 3D hyperelastic law for the passive component, strengthened by active fibers. Unlike the approach in Coccarelli et al. (2018) or Stålhand et al. (2011), we have not included the chemical driving mechanism. However, we have employed 3D-shell finite elements to avoid numerical locking and manage large displacements, as evidenced in dynamic simulations. In contrast to Coccarelli et al. (2018), which performs the model validation through isometric tests, our model is validated as well through uniaxial static tests with biaxial deformation measurements and uniaxial dynamical ones. In general, with this type of models we could incorporate them in *in vivo* more complex geometries and be able to describe a full hemodynamic model.

One of the interests of the present study was to determine whether the contraction of SMCs directly affects vascular tone by regulating stiffness through the fibers or whether this regulation indirectly adjusts intrinsic stiffness, as indicated by changes in the Young modulus. Additionally, the investigation explored the extent of alterations in geometry, such as changes in diameter, influence biomechanical assessments. Taking a look at how the pre-stress and elastic modulus of the fibers change compared to the baseline conditions gives us more understanding about the regulation of vascular tone. For vasoconstrictors, we observed an increase in pre-stress, reflecting increased arterial tension and reduced compliance. Conversely, the response to DEANO exhibited a more subtle variation, with pre-stress showing variable changes, influenced by the complex interplay of vasodilation and previously vasoconstriction compensatory mechanisms. Similarly, the elastic modulus exhibited distinct trends: vasoconstrictors tended to increase vessel stiffness, while vasodilators often leaded to a decrease or maintenance of elasticity, highlighting the dynamic nature of vascular responses to vasoactive compounds. In addition to the observed changes in pre-stress and elastic modulus of the active fibers, it is remarkable that the parameters associated with the passive component of the arterial wall, such as Young's modulus and thickness, exhibited minimal variation across conditions. The fact that there was no notable change, suggests that alterations in arterial mechanics primarily stem from the active component governed by SMC activity rather than intrinsic vessel properties. The Young's modulus staying comparatively stable indicates that the intrinsic stiffness of the vessel, represented by the passive component, remains largely unchanged. Instead, the

variations in the fiber parameters point towards the crucial role of SMCs in mediating vasoconstriction and dilation, with minimal contribution from changes in intrinsic stiffness.

The simulated arterial stiffness values demonstrated a consistent decrement at higher pressures across all examined conditions in comparison to experimental values, necessitating a re-estimation. This observed discrepancy may potentially stem from the inherent limitations of the current model, which does not account for the recruitment of stiffer collagen fibers situated in the adventitial layer. These fibers are known to be recruited in a pressure-dependent manner within the aorta. Consequently, the model's omission of collagen loading contributes to an underestimation of stiffness values at highest pressures.

Overall, our work introduces a mathematical model to explore arterial mechanics, shedding light on the roles of SMCs. Moving forward, future research could focus on refining and validating the model to better capture the complex dynamics of arterial mechanics. A more sophisticated model with a realistic geometry that also accounts for the contact between the aortic segment and the hooks is, in fact, presented in the next chapter. Future work could address limitations such as the lack of consideration for collagen loading, which may influence parameter estimation accuracy, particularly at higher pressures. Moreover, the application of the model to *in vivo* data holds promising prospects for advancing our understanding of vascular physiology and guiding the development of further experiments. By integrating experimental findings and clinical data, the model can contribute to more accurate predictions of vascular behavior under physiological and pathological conditions.

Chapter 3

Full mathematical model with different contact methods

The aim of this chapter is to provide a more comprehensive mathematical model of the ROTSAC setup. In particular, no geometrical assumptions are made and contact between the tissue and the hooks is considered. We present a comparison between different numerical approaches for contact, including augmented Lagrangian, Nitsche and penalty methods with the 3D-shell modeling of the vascular wall of Chapter 2.

Contents

3.1 Motivation

This chapter transitions from the mathematical model presented in Chapter 2 to a more detailed and realistic representation of the ROTSAC setup, previously described in Section 1.2.2 and presented in Figure 2.1 (left). We recall that, 2 mm aortic segments are mounted between two parallel hooks in 10 mL organ baths. Segments are immersed in Krebs-Ringer solution. A close view of an aortic segment mounted in the hooks can be found in Figure 2.1 (right). Force and displacement of the upper hook are controlled and assessed using a force length transducer. The lower hook is static. During the experimental calibration, measurements of the length and the width of the aortic segments at different preloads (10, 20, 30, 40 and 50 mN) are recorded. Moreover, segments were

subjected to cyclic stretching, between alternating preloads, emulating "diastolic" and "systolic" transmural pressures at 10 Hz frequency mimicking the physiological heart rate in mice. The pressure-stiffness relationship was determined under a physiological condition, a maximally-contracted state (with vasoconstrictors), as well as in the absence of active stiffness (with vasodilators). One must notice that the applied tensions are quite high given the size of the aortic segments, that undergo extreme deformations.

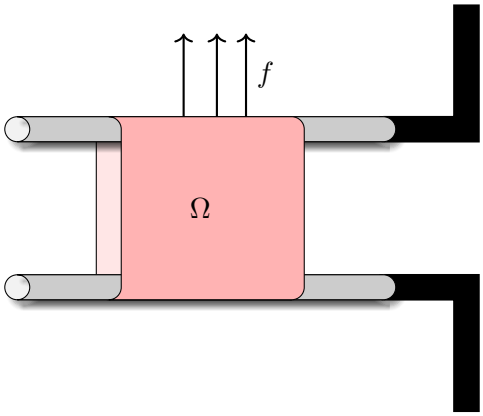

Figure 3.1: Schematic diagram of the ROTSAC.

In Chapter 2, we assumed a simplified geometrical configuration for the simulation of the ROTSAC experimental setup, which consisted on one lateral side of the tissue mounted on the hooks. This was based on the approximation that the aortic segment is flat in its stress-free state (see Figure 2.2). In this chapter, we consider the geometry displayed in Figure 2.1 (right), that can be represented by the schematic diagram of Figure 3.1. For this purpose, we need to incorporate in the mathematical model the contact between the elastic body and the hooks, that are treated as rigid bodies. The lower hook (static hook) is clamped, while a force, f, is applied to the upper moving hook. The moving hook is considered a rigid body with a single degree of freedom, which is vertical translation. The dynamics of the moving hook are given by Newton's second law, balancing the applied force with the contact force experienced by the hook.

Since the late 1970s, with the introduction of the Finite Element Method (FEM), contact mechanics has been a fundamental area of applied mathematics. Notable contributions in the literature include works Timoshenko and Goodier (1970); Francavilla and Zienkiewicz (1975); Hughes et al. (1976); Belytschko et al. (2000); Chouly et al. (2023). Given the extreme tensions experienced by the aortic segments, robust numerical methods are required to simulate the ROTSAC experiment accurately. In the present chapter, we explore and compare different numerical methods (augmented Lagrangian, Nitsche and penalty) for the discrete treatment of contact.

Augmented Lagrangian formulations are a type of mixed methods in which the inequality constraints on the multipliers are removed by introducing non-smooth terms in the variational formulation. A semi-smooth Newton algorithm can be used to deal with the nonlinear terms. The reader is referred to Simo and Laursen (1992); Laborde and Renard

(2008); Poulios and Renard (2015) for contact treated via augmented Lagrangian.

An extension of *Nitsche's method* to contact problems has been reported in (Chouly and Hild, 2013; Chouly et al., 2015; Mlika et al., 2017; Chouly et al., 2017). A salient feature of this approach is that it enforces the contact conditions in a strongly consistent fashion without the need of introducing additional unknowns (Lagrange multipliers). The application of Nitsche's method to contact problems involving thin-walled structures raises a fundamental difficulty. Indeed, for traditional reduced models based on the plane stress assumption, it yields the penalty method. To the best of our knowledge, Nitsche's method has been proposed for 3D plates in Fabre et al. (2021) (see also Gustafsson et al. (2019) for an alternative approach) but its application to 3D-shells has not yet been explored. In this chapter, we extend its use to 3D-shells. A challenge in applying Nitsche's method to 3D-shells arises from the inclusion of stresses in the contact terms. This complexity stems from the need to compute the stresses and its derivatives to construct the Jacobian for the numerical resolution.

The *penalty method* (Kikuchi and Song, 1981; Kikuchi and Oden, 1988; Chouly and Hild, 2012) can be viewed as a simplification of Nitsche's method in which the normal stress is neglected in the contact term, which basically amounts to penalize the contact condition. In contrast to Nitsche's method, the penalty method is not strongly consistent. From the computer implementation point of view, this method is one the simplest. However, the penalty parameter must be carefully chosen to balance numerical stability and convergence. The penalty parameter needs to be as small as possible to mimic the nonpenetration condition, but not too small in order to ensure the convergence of any iterative solver for the nonlinear problem.

This chapter is organized as follows: Section 3.2 provides the governing equations for contact mechanics in large strain scenarios and, in particular, the mathematical model for the ROTSAC setup including contact. Section 3.3 presents the formulations for each contact method. Section 3.4 compares the numerical results of these three methods across different numerical examples. Finally, Section 3.5 presents the conclusions and future perspectives of this chapter.

3.2 Contact in large displacements and deformations

We present in this section some notations for the setting of contact problems. Since the tissue experiences large deformations during the experiment, the contact model is developed within the framework of large deformations. Contact can be classified into two types: bilateral and unilateral. Bilateral contact involves two or more deformable bodies, whereas unilateral contact occurs between a deformable solid and a rigid solid. In this thesis, we focus on unilateral contact.

We begin by establishing notations for large strain tensors and algebraic operators, addressing various scenarios where a deformable body governed by hyperelasticity (Ciarlet (1988); Bonet and Wood (2008)) comes into contact with one or two rigid bodies. The reference domain of the elastic solid is denoted by $\Omega \subset \mathbb{R}^3$, and its boundary is denoted as $\partial\Omega$. The deformation of the continuum medium is given as the bijective map $\boldsymbol{\varphi}$ from the

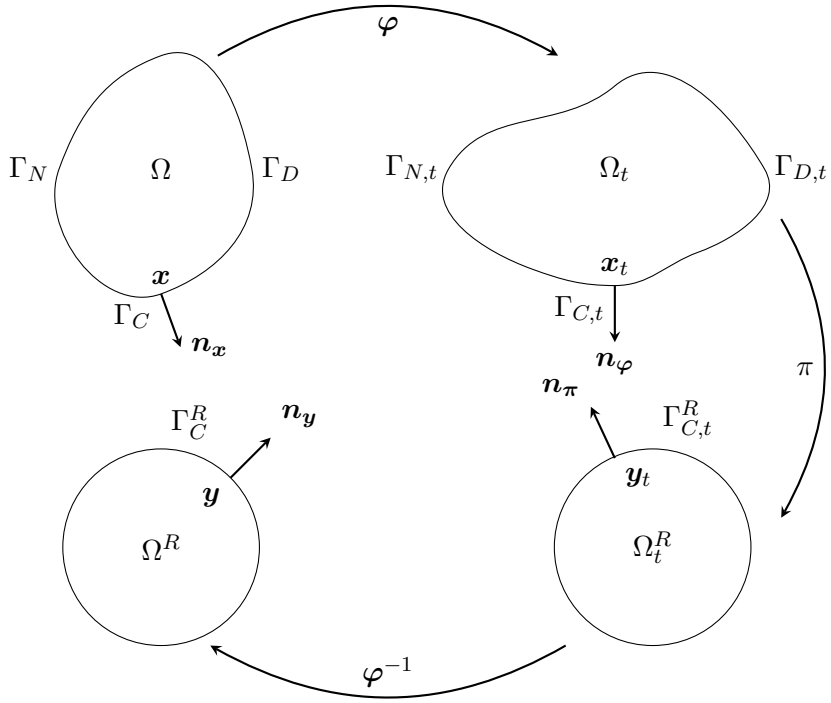

Figure 3.2: Notation for large deformation contact problem in the reference and deformed configurations for unilateral contact.

reference configuration Ω to the current configuration $\Omega_t(t)$:

$$\begin{aligned} \boldsymbol{\varphi} : \Omega \times [0,T] &\longrightarrow \mathbb{R}^3 \\ (\boldsymbol{x}, t) &\longmapsto \boldsymbol{x}_t = \boldsymbol{\varphi}(\boldsymbol{x}, t). \end{aligned}$$

We denote by $\boldsymbol{d}$ the displacement field:

$$\mathbf{d}(\boldsymbol{x}, t) = \boldsymbol{\varphi}(\boldsymbol{x}, t) - \boldsymbol{x}.$$

The boundary of the elastic body is assumed to be partitioned in three non-overlapping parts Γ_D (the Dirichlet boundary), Γ_N (the Neumann boundary) and Γ_C (the potential contact boundary), deformed to $\Gamma_{D,t}$, $\Gamma_{N,t}$ and $\Gamma_{C,t}$, respectively. Each body could be, as well, subjected to volume forces. In the reference configuration, the unit outward normal vector to Γ_C at $\boldsymbol{x}$ is denoted by $\boldsymbol{n}_{\boldsymbol{x}}$, while in the deformed configuration, the unit outward normal vector to $\Gamma_{C,t}$ at $\boldsymbol{x}_t$, is represented by $\boldsymbol{n}_{\boldsymbol{\varphi}}$ (see Figure 3.2).

As it is usual in the contact mechanics literature, we adopt a biased, or master–slave paradigm (see for instance Laursen (2002), Wriggers (2006), Hallquist et al. (1985), or Benson and Hallquist (1990)), which consists in enforcing the unilateral contact conditions solely on one of the two (potential) contact boundaries. Following a master-slave strategy, we consider part of $\partial\Omega$ as a slave surface (or contactor) and some other part as master (or target) surface. In what follows, we consider the elastic body Ω as the slave and the rigid one, denoted by Ω^{R}, as the master. The contact boundary of the master surface will

be denoted as Γ_C^R in the reference configuration, with the unit outward normal vector at any point $\boldsymbol{y}$ on the master surface, given by $\boldsymbol{n}_y$. In the deformed configuration, $\Gamma_C^R \subset \partial\Omega^R$ transforms to $\Gamma_{C,t}$. Remark that slave and master surfaces have to be defined in such a way that the corresponding surfaces $\Gamma_{C,t}$ and $\Gamma_{C,t}^R$ are likely to form a contact pair. For unilateral contact with a rigid *static* body $\Gamma_{C,t}^R = \Gamma_C^R$ and $\Omega^R = \Omega_t^R$.

The map which associates potential contacts from the slave surface on the master surface is:

$$\begin{aligned} \boldsymbol{\pi} : \Gamma_{C,t} &\longrightarrow \Gamma_{C,t}^R \\ \boldsymbol{x}_t &\longmapsto \boldsymbol{y}_t = \boldsymbol{\pi}(\boldsymbol{x}_t). \end{aligned}$$

Unlike in the small deformation framework, this mapping is not a given datum, but depends on the displacement $\boldsymbol{d}$. There are mainly two possibilities to build this mapping: projection and ray-tracing. The most classic strategy is projection (see Laursen (2002)), and it consists on defining a point $\boldsymbol{y}_t$, as the closest point projection of $\boldsymbol{x}_t$ onto the deformed master surface. In ray-tracing, the idea is to define $\boldsymbol{y}_t$ as the closest intersection of the master surface with the line passing through point $\boldsymbol{x}_t$ and having direction vector $\boldsymbol{n}_{\boldsymbol{\varphi}}$ (see Poulios and Renard (2015)).

In the present chapter, ray-tracing is used for defining the mapping between the slave and master surfaces and the corresponding gap function. Since we have a simple parametrization of the master surface, the ray-tracing projections can be evaluated analytically, as explained in Section A.1, Appendix A. The main motivation for using ray-tracing instead of the classical projection is for achieving a simpler expression for the tangent problem, due to the fact that $\boldsymbol{n}_{\boldsymbol{\varphi}}$ has a simpler derivative than the unit normal vector to the deformed master surface, $\boldsymbol{n}_{\boldsymbol{\pi}}$.

The gap function for ray-tracing, is given by

$$g = \boldsymbol{n}_{\boldsymbol{\varphi}} \cdot (\boldsymbol{\pi}(\boldsymbol{\varphi}(\boldsymbol{x}, t)) - \boldsymbol{\varphi}(\boldsymbol{x}, t)) \quad \text{on} \quad \Gamma_C. \tag{3.1}$$

The nonpenetration condition then reads

$$g(\boldsymbol{d}) \geq 0 \quad \text{on} \quad \Gamma_C, \tag{3.2}$$

and there always holds

$$\boldsymbol{\pi}(\boldsymbol{\varphi}(\boldsymbol{x}, t)) = \boldsymbol{\varphi}(\boldsymbol{x}, t) + g(\boldsymbol{d})\mathbf{n}_{\boldsymbol{\varphi}}. \tag{3.3}$$

The contact conditions in large deformations are written in terms of the first Piola-Kirchhoff stress tensor, $\boldsymbol{\Pi}(\boldsymbol{d})$, given by

$$\boldsymbol{\Pi}(\mathbf{d}) = J\boldsymbol{\sigma}(\boldsymbol{d})\boldsymbol{F}^{-T}(\boldsymbol{d}), \tag{3.4}$$

where J is the determinant of the deformation gradient and $\boldsymbol{\sigma}(\boldsymbol{d})$ is the Cauchy stress tensor. When contact occurs ($\boldsymbol{\Pi}(\boldsymbol{d})\boldsymbol{n}_x < 0$), the normals $\mathbf{n}_{\boldsymbol{\varphi}}$ and $\mathbf{n}_{\boldsymbol{\pi}}$ are opposite. The quantity $\boldsymbol{\Pi}(\boldsymbol{d})\boldsymbol{n}_x$ represents the surface force at a point $\boldsymbol{x}$ in the reference configuration, and it should be negative or zero. As a result, contact conditions (see, e.g., (Chouly et al., 2023, Chapter 11)) can be written as:

$$\begin{array}{lcll} g(\boldsymbol{d}) & \geq & 0, \quad \text{on} \quad \Gamma_C, \\ \boldsymbol{\Pi}(\boldsymbol{d})\boldsymbol{n}_x \cdot \boldsymbol{n}_{\boldsymbol{\varphi}} & \leq & 0, \quad \text{on} \quad \Gamma_C, \\ \boldsymbol{\Pi}(\boldsymbol{d})\boldsymbol{n}_x \cdot \boldsymbol{n}_{\varphi}\, g(\boldsymbol{d}) & = & 0, \quad \text{on} \quad \Gamma_C. \end{array} \tag{3.5}$$

These conditions are commonly referred to as Karush-Kuhn-Tucker (KKT) or Hertz-Signorini-Moreau conditions. The condition $g(\boldsymbol{d}) \geq 0$ prevents the elastic body from penetrating the rigid solid. The second condition, $\boldsymbol{\Pi}(\boldsymbol{d})\boldsymbol{n}_x \cdot \boldsymbol{n}_{\boldsymbol{\varphi}} \leq 0$, ensures that contact forces are repulsive. The third one, $\boldsymbol{\Pi}(\boldsymbol{d})\boldsymbol{n}_x \cdot \boldsymbol{n}_{\varphi}\, g(\boldsymbol{d}) = 0$, known as complementarity condition, can be interpreted as follows: when the contact force is non zero (contact), then necessarily the elastic body must stick to the rigid solid and if, at any point, the elastic body is detached from the rigid solid, then the contact force must be zero (no contact).

Full mathematical model of the ROTSAC setup

In what follows, we present the mathematical model for the ROTSAC setup including contact. The geometric configuration is shown in Figure 3.3.

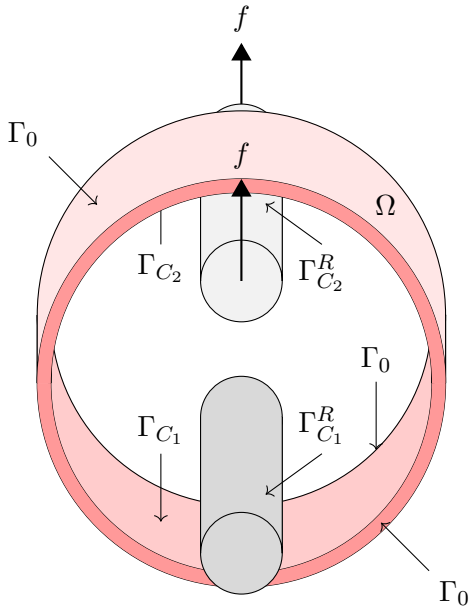

Figure 3.3: Geometric reference configuration of the ROTSAC.

The elastic body can be in contact with the lower hook (static hook) and, with the upper moving hook, both of them treated as rigid bodies. The displacement of the upper hook is given by $\boldsymbol{s} := s(t)\boldsymbol{e}_y$, where $\boldsymbol{e}_y$ is the unit vector on the vertical direction and $s(t) \in \mathbb{R}$. The map which associates each point of the elastic body to a potential contact point on the moving hook is given by

$$\begin{aligned} \boldsymbol{\pi}_2 : \Gamma_{C_2,t} &\longrightarrow \Gamma^R_{C_2,t} \\ \boldsymbol{x}_t &\longmapsto \boldsymbol{y}_t = \boldsymbol{\pi}_2(\boldsymbol{x}_t), \end{aligned}$$

and, similarly, for the static hook

$$\begin{aligned} \boldsymbol{\pi}_1 : \Gamma_{C_1,t} &\longrightarrow \Gamma^R_{C_1,t} \\ \boldsymbol{x}_t &\longmapsto \boldsymbol{y}_t = \boldsymbol{\pi}_1(\boldsymbol{x}_t), \end{aligned}$$

where the subscripts 1 and 2 refer to the static and moving hook, respectively. Then, the gap function introduced in (3.1) for the moving hook reads

$$g_2(\boldsymbol{d}, s) := \boldsymbol{n}_{\boldsymbol{\varphi}} \cdot (\boldsymbol{\pi}_2(\boldsymbol{\varphi}(\boldsymbol{x}, t)) - \boldsymbol{\varphi}(\boldsymbol{x}, t)) \quad \text{on} \quad \Gamma_{C_2},$$

and, the one for the static hook

$$g_1(\boldsymbol{d}) := \boldsymbol{n}_{\boldsymbol{\varphi}} \cdot (\boldsymbol{\pi}_1(\boldsymbol{\varphi}(\boldsymbol{x}, t)) - \boldsymbol{\varphi}(\boldsymbol{x}, t)) \quad \text{on} \quad \Gamma_{C_1}.$$

We can introduce a Lagrange multiplier λ as a new unknown for the contact force:

$$\lambda := \boldsymbol{\Pi}(\boldsymbol{d})\boldsymbol{n}_x \cdot \boldsymbol{n}_{\boldsymbol{\varphi}}, \tag{3.6}$$

which, owing to (3.5), must be nonpositive. Then, the solid equilibrium for frictionless contact for the ROTSAC setup in large deformations with the nonpenetration conditions (3.5) and the equation of the moving hook, reads as follows: find the elastic solid displacement $\boldsymbol{d} : \Omega \times \mathbb{R}^+ \to \mathbb{R}^3$, the vertical displacement of the upper hook $s : \mathbb{R}^+ \to \mathbb{R}$ and the contact Lagrange multipliers $\lambda_i : \Gamma_{C_i} \times \mathbb{R}^+ \to \mathbb{R}$, $i = 1, 2$ such that

$$\begin{cases} \rho \partial_{tt} \boldsymbol{d} - \mathbf{div}(\boldsymbol{\Pi}(\boldsymbol{d})) = \mathbf{0}, & \text{in } \Omega, \\ \boldsymbol{\Pi}(\boldsymbol{d})\boldsymbol{n}_x \cdot \boldsymbol{n}_{\boldsymbol{\varphi}} = \lambda_2, & \text{on } \Gamma_{C_2}, \\ \boldsymbol{\Pi}(\boldsymbol{d})\boldsymbol{n}_x \cdot \boldsymbol{n}_{\boldsymbol{\varphi}} = \lambda_1, & \text{on } \Gamma_{C_1}, \\ \boldsymbol{\Pi}(\boldsymbol{d})\boldsymbol{n}_x \cdot \boldsymbol{\tau} = 0, & \text{on } \Gamma_{C_2}, \\ \boldsymbol{\Pi}(\boldsymbol{d})\boldsymbol{n}_x \cdot \boldsymbol{\tau} = 0, & \text{on } \Gamma_{C_1}, \\ g_2(\boldsymbol{d}, s) \geq 0, \quad \lambda_2 \leq 0, \quad \lambda_2 g_2(\boldsymbol{d}, s) = 0, & \text{on } \Gamma_{C_2}, \\ g_1(\boldsymbol{d}) \geq 0, \quad \lambda_1 \leq 0, \quad \lambda_1 g_1(\boldsymbol{d}) = 0, & \text{on } \Gamma_{C_1}, \\ m\ddot{s} - f + \displaystyle\int_{\Gamma_{C_2}} \lambda_2 \, \boldsymbol{n}_{\boldsymbol{\varphi}} \cdot \boldsymbol{e}_y = 0, \end{cases} \tag{3.7}$$

where ρ stands for the density of the elastic solid, m the mass of the moving hook and f the force applied on it.

3.3 Numerical methods for contact

In this section we discuss three numerical methods for the approximation of the contact problem (3.7): the augmented Lagrangian method, the Nitsche's method, and the penalty method.

The fundamental ingredient in the derivation of these methods (notably augmented Lagrangian and Nitsche's method), is the formulation of the inequality constraints as nonlinear identities. Considering the positive part operator $[\cdot]_+$:

$$[x]_+ := \max\{0, x\},$$

for an arbitrary positive function γ on the slave contact boundary Γ_C, the contact conditions (3.5) can be rewritten alternatively as (see Alart and Curnier (1988) or (Chouly et al., 2023, Proposition 6.1, Chapter 6)):

$$\boldsymbol{\Pi}(\boldsymbol{d})\boldsymbol{n}_x \cdot \boldsymbol{n}_\varphi = -\left[-\boldsymbol{\Pi}(\boldsymbol{d})\boldsymbol{n}_x \cdot \boldsymbol{n}_\varphi - \gamma g(\boldsymbol{d})\right]_+. \tag{3.8}$$

Alternatively, considering the negative part operator $[\cdot]_-$:

$$[x]_- := \max\{-x, 0\},$$

conditions (3.5) can be expressed as

$$\boldsymbol{\Pi}(\boldsymbol{d})\boldsymbol{n}_x \cdot \boldsymbol{n}_{\boldsymbol{\varphi}} = -\left[\boldsymbol{\Pi}(\boldsymbol{d})\boldsymbol{n}_x \cdot \boldsymbol{n}_{\boldsymbol{\varphi}} + \gamma g(\boldsymbol{d})\right]_- . \tag{3.9}$$

A salient feature of the relations (3.8) and (3.9) is that they transform KKT type conditions, involving inequality constraints, into a single nonlinear equality, which can then be used to derive consistent numerical approximations.

3.3.1 Augmented Lagrangian method

Augmented Lagrangian formulations are mixed approaches in which inequality constraints are replaced by the following nonlinear identities from (3.6), (3.8) and (3.9):

$$\lambda = -\left[\lambda + \gamma g(\boldsymbol{d})\right]_- , \quad \text{or} \quad \lambda = -\left[-\lambda - \gamma g(\boldsymbol{d})\right]_+ . \tag{3.10}$$

Let us recall that for hyperelastic bodies, the energy potential W (Ciarlet, 1988) depends on the deformation through the tensor $\boldsymbol{e}$. Also, the expression of the second Piola-Kirchhoff stress tensor, $\boldsymbol{\Sigma} = \boldsymbol{F}^{-1}\boldsymbol{\Pi}$, with $\boldsymbol{F} = \boldsymbol{\nabla}\boldsymbol{\varphi}$ the deformation gradient tensor, is obtained thanks to

$$\boldsymbol{\Sigma} = \frac{\partial W}{\partial \boldsymbol{E}}.$$

We introduce the energy functional of the whole system, $\mathcal{J}(\dot{\boldsymbol{d}}, \boldsymbol{d}, \dot{s}, s)$, defined as

$$\mathcal{J}(\dot{\boldsymbol{d}}, \boldsymbol{d}, \dot{s}, s) := \frac{1}{2}\int_\Omega \rho|\partial_t \boldsymbol{d}|^2 - \int_\Omega W(\boldsymbol{E}) + \frac{1}{2}m|\dot{s}|^2 + f\, s, \tag{3.11}$$

where the first two terms are the kinetic and the potential energy of the elastic body, respectively. The third term is the kinetic energy of the moving hook and, finally, $f\, s$ represents the work done by the external forces acting on the moving hook. Force equilibrium of the considered elastic body and the hooks, can be represented by the saddle point of the following Lagrangian

$$\mathcal{L}(\dot{\boldsymbol{d}}, \boldsymbol{d}, \dot{s}, s, \lambda_2, \lambda_1) := \mathcal{J}(\dot{\boldsymbol{d}}, \boldsymbol{d}, \dot{s}, s) + \int_{\Gamma_{C_2}} \lambda_2 g_2(\boldsymbol{d}, s) + \int_{\Gamma_{C_1}} \lambda_1 g_1(\boldsymbol{d}),$$

under the constraints $\lambda_2 \leq 0$ and $\lambda_1 \leq 0$. Using (3.10), the augmented Lagrangian function, that avoids the need for an additional constraint on λ_2 or λ_1, writes (see (Chouly et al., 2023, Lemma 7.2, Chapter 7)):

$$\mathcal{L}_\gamma(\dot{\boldsymbol{d}}, \boldsymbol{d}, \dot{s}, s, \lambda_2, \lambda_1) := \mathcal{J}(\dot{\boldsymbol{d}}, \boldsymbol{d}, \dot{s}, s) + \frac{1}{2\gamma}\int_{\Gamma_{C_2}} [\lambda_2 + \gamma g_2]_-^2 - \lambda_2^2 + \frac{1}{2\gamma}\int_{\Gamma_{C_1}} [\lambda_1 + \gamma g_1]_-^2 - \lambda_1^2, \tag{3.12}$$

where $\gamma := \gamma_0\, E/h$ is the augmentation parameter, with $\gamma_0 > 0$, E being the Young's modulus and h the mesh size. For augmented Lagrangian formulations, it is generally

preferred to use the negative part operator to write the contact conditions (3.10), notably because of the chosen convention for the gap ($g(\boldsymbol{d}) \geq 0$) (Chouly et al., 2023).

The optimality system of $\mathcal{L}_\gamma$ is the following

$$\begin{cases} \dfrac{\mathrm{d}}{\mathrm{d}t} D_{\dot{\boldsymbol{d}}} \mathcal{J}[\delta \dot{\boldsymbol{d}}] - D_{\boldsymbol{d}} \mathcal{J}[\delta \boldsymbol{d}] - \displaystyle\int_{\Gamma_{C_2}} [\lambda_2 + \gamma g_2]_- D_{\boldsymbol{d}} g_2[\delta \boldsymbol{d}] \\ \qquad\qquad - \displaystyle\int_{\Gamma_{C_1}} [\lambda_1 + \gamma g_1]_- D_{\boldsymbol{d}} g_1[\delta \boldsymbol{d}] = 0 \quad \forall \delta \boldsymbol{d}, \\ -\dfrac{1}{\gamma} \displaystyle\int_{\Gamma_{C_2}} (\lambda_2 + [\lambda_2 + \gamma g_2]_-)\, \delta\lambda_2 = 0 \quad \forall \delta\lambda_2, \\ -\dfrac{1}{\gamma} \displaystyle\int_{\Gamma_{C_1}} (\lambda_1 + [\lambda_1 + \gamma g_1]_-)\, \delta\lambda_1 = 0 \quad \forall \delta\lambda_1, \\ \dfrac{\mathrm{d}}{\mathrm{d}t} D_{\dot{s}} \mathcal{J}[\delta \dot{s}] - D_s \mathcal{J}[\delta s] - \displaystyle\int_{\Gamma_{C_2}} [\lambda_2 + \gamma g_2]_- D_s g_2[\delta s] = 0 \quad , \end{cases} \tag{3.13}$$

where the derivative of the gap g_2 (analogue for g_1) in direction $\delta \boldsymbol{d}$ (obtained in (A.6), Appendix A) writes

$$D_{\boldsymbol{d}} g_2[\delta \boldsymbol{d}] = \frac{-\boldsymbol{n}_{\boldsymbol{\pi}}}{\boldsymbol{n}_{\boldsymbol{\pi}} \cdot \boldsymbol{n}_{\boldsymbol{\varphi}}} \left(\delta \boldsymbol{d}(\boldsymbol{x}) + g_2(\boldsymbol{d}, s) D_{\boldsymbol{d}} \boldsymbol{n}_{\boldsymbol{\varphi}}[\delta \boldsymbol{d}]\right). \tag{3.14}$$

It should be noted that, at any point of the slave surface, either contact occurs, in which case $\boldsymbol{n}_{\boldsymbol{\pi}} = -\boldsymbol{n}_{\boldsymbol{\varphi}}$, or contact does not occur, resulting in $[\lambda_2 + \gamma g_2]_- = 0$. This means that the term $\boldsymbol{n}_{\boldsymbol{\pi}} / (\boldsymbol{n}_{\boldsymbol{\pi}} \cdot \boldsymbol{n}_{\boldsymbol{\varphi}})$ that would appear in the optimality system due to $D_{\boldsymbol{d}} g_2[\delta \boldsymbol{d}]$ can be simply replaced by $-\boldsymbol{n}_{\boldsymbol{\varphi}}$. The derivative of the gap in direction δs, denoted as $D_s g_2[\delta s]$, is given by equation (A.13). We can apply the same logic as we did with $D_{\boldsymbol{d}} g_2[\delta \boldsymbol{d}]$ to conclude that $D_s g_2[\delta s]$ can be replaced by $\boldsymbol{n}_{\boldsymbol{\varphi}}$. Remarking additionally that $\boldsymbol{n}_{\boldsymbol{\varphi}} \cdot D_{\boldsymbol{d}} \boldsymbol{n}_{\boldsymbol{\varphi}}[\delta \boldsymbol{d}] = 0$, the substitution of (3.14) in (3.13) leads to

$$\begin{cases} \dfrac{\mathrm{d}}{\mathrm{d}t} D_{\dot{\boldsymbol{d}}} \mathcal{J}[\delta \dot{\boldsymbol{d}}] - D_{\boldsymbol{d}} \mathcal{J}[\delta \boldsymbol{d}] + \displaystyle\int_{\Gamma_{C_2}} [\lambda_2 + \gamma g_2]_- \boldsymbol{v} \cdot \boldsymbol{n}_{\boldsymbol{\varphi}} \\ \qquad\qquad + \displaystyle\int_{\Gamma_{C_1}} [\lambda_1 + \gamma g_1]_- \boldsymbol{v} \cdot \boldsymbol{n}_{\boldsymbol{\varphi}} = 0 \quad \forall \boldsymbol{v} \in \mathbf{V}^{\mathrm{sh}}, \\ -\dfrac{1}{\gamma} \displaystyle\int_{\Gamma_{C_2}} (\lambda_2 + [\lambda_2 + \gamma g_2]_-)\, \delta\lambda_2 = 0 \quad \forall \mu \in \Lambda_2, \\ -\dfrac{1}{\gamma} \displaystyle\int_{\Gamma_{C_1}} (\lambda_1 + [\lambda_1 + \gamma g_1]_-)\, \delta\lambda_1 = 0 \quad \forall \mu \in \Lambda_1, \\ \dfrac{\mathrm{d}}{\mathrm{d}t} D_{\dot{s}} \mathcal{J}[\delta \dot{s}] - D_s \mathcal{J}[\delta s] - \displaystyle\int_{\Gamma_{C_2}} [\lambda_2 + \gamma g_2(\boldsymbol{d}, s)]_- \boldsymbol{e}_y \cdot \boldsymbol{n}_{\boldsymbol{\varphi}} = 0 \quad . \end{cases} \tag{3.15}$$

where $\mathbf{V}^{\mathrm{sh}}$ is given by (2.9), $\Lambda_2 := L^2(\Gamma_{C_2})$ and $\Lambda_1 := L^2(\Gamma_{C_1})$. Using the expression for the derivatives for the energy terms, we obtain the variational formulation of (3.7) for the

augmented Lagrangian method. It reads

$$\begin{cases} \text{For } t>0 \text{ find } \boldsymbol{d}(t)\in \mathbf{V}^{\mathrm{sh}}, \lambda_1(t)\in\Lambda_1, \lambda_2(t)\in\Lambda_2 \text{ and } s(t)\in\mathbb{R} \text{ such that:} \\ \displaystyle\int_\Omega \rho\partial_{tt}\boldsymbol{d}\cdot\boldsymbol{v} + \int_\Omega \boldsymbol{\Pi}(\boldsymbol{d}):\boldsymbol{\nabla}\boldsymbol{v} + \int_{\Gamma_{C_2}} [\lambda_2+\gamma g_2(\boldsymbol{d},s)]_-\,\boldsymbol{v}\cdot\boldsymbol{n}_{\boldsymbol{\varphi}} \\ \displaystyle + \int_{\Gamma_{C_1}} [\lambda_1+\gamma g_1(\boldsymbol{d})]_-\,\boldsymbol{v}\cdot\boldsymbol{n}_{\boldsymbol{\varphi}} = 0, \quad \forall \boldsymbol{v}\in\mathbf{V}^{\mathrm{sh}}, \\ \displaystyle -\frac{1}{\gamma}\int_{\Gamma_{C_2}} (\lambda_2+[\lambda_2+\gamma g_2(\boldsymbol{d},s)]_-)\,\mu = 0, \quad \forall \mu\in\Lambda_2, \\ \displaystyle -\frac{1}{\gamma}\int_{\Gamma_{C_1}} (\lambda_1+[\lambda_1+\gamma g_1(\boldsymbol{d})]_-)\,\mu = 0, \quad \forall \mu\in\Lambda_1, \\ \displaystyle m\ddot{s} = f + \int_{\Gamma_{C_2}} [\lambda_2+\gamma g_2(\boldsymbol{d},s)]_-\,\boldsymbol{e}_y\cdot\boldsymbol{n}_{\boldsymbol{\varphi}}. \end{cases} \tag{3.16}$$

For the spatial discretization of the system defined by (3.16), we adopt a finite element approximation. Let $\{\mathcal{T}_h\}_{0<h<1}$ be a family of triangulations of Ω, fitted to $\partial\Omega$. Every triangulation $\mathcal{T}_h$ is composed of a single layer of prismatic elements (see Figure 2.5). Every prism $K\in\mathcal{T}_h$ can be decomposed in a tensorial way such that $K = T\otimes S$, where T represents a triangle in $\partial\Omega$ and S represents a segment. Let us define the following finite element spaces:

$$\mathbf{V}_h^{\mathrm{sh}} := \left\{ \boldsymbol{v}\in\mathbf{V}^{\mathrm{sh}} : \boldsymbol{v}|_K \in [\mathbb{P}_1(T)\otimes\mathbb{P}_2(S)]^3, \quad K = T\otimes S, \forall K\in\mathcal{T}_h \right\}, \tag{3.17}$$

$$\Lambda_{i,h} := \{\mu\in\Lambda_i : \mu|_K\in\mathbb{P}_1(K), \quad \forall K\in\Gamma_{C_i}\cap\mathcal{T}_h\} \quad \text{for} \quad i\in\{1,2\}. \tag{3.18}$$

Then the formulation of (3.16) in the discrete setting reads:

$$\begin{cases} \text{For } t>0 \text{ find } \boldsymbol{d}_h(t)\in\mathbf{V}_h^{\mathrm{sh}}, \lambda_{1,h}(t)\in\Lambda_{1,h}, \lambda_{2,h}(t)\in\Lambda_{2,h} \\ \text{and } s(t)\in\mathbb{R} \text{ such that:} \\ \displaystyle\int_\Omega \rho\partial_{tt}\boldsymbol{d}_h\cdot\boldsymbol{v}_h + a_h(\boldsymbol{d}_h;\boldsymbol{v}_h) + \int_{\Gamma_{C_2}} [\lambda_{2,h}+\gamma g_2(\boldsymbol{d}_h,s)]_-\,\boldsymbol{v}_h\cdot\boldsymbol{n}_{\boldsymbol{\varphi}} \\ \displaystyle + \int_{\Gamma_{C_1}} [\lambda_{1,h}+\gamma g_1(\boldsymbol{d}_h)]_-\,\boldsymbol{v}_h\cdot\boldsymbol{n}_{\boldsymbol{\varphi}} = 0, \quad \forall \boldsymbol{v}_h\in\mathbf{V}_h^{\mathrm{sh}}, \\ \displaystyle -\frac{1}{\gamma}\int_{\Gamma_{C_2}} (\lambda_{2,h}+[\lambda_{2,h}+\gamma g_2(\boldsymbol{d}_h,s)]_-)\,\mu_h = 0, \quad \forall \mu_h\in\Lambda_{2,h}, \\ \displaystyle -\frac{1}{\gamma}\int_{\Gamma_{C_1}} (\lambda_{1,h}+[\lambda_{1,h}+\gamma g_1(\boldsymbol{d}_h)]_-)\,\mu_h = 0, \quad \forall \mu_h\in\Lambda_{1,h}, \\ \displaystyle m\ddot{s} = f + \int_{\Gamma_{C_2}} [\lambda_{2,h}+\gamma g_2(\boldsymbol{d}_h,s)]_-\,\boldsymbol{e}_y\cdot\boldsymbol{n}_{\boldsymbol{\varphi}}, \end{cases} \tag{3.19}$$

where $a_h(\boldsymbol{d}_h;\boldsymbol{v}_h)$ denotes the discrete stiffness term in the 3D-shell in which a reinterpolation procedure of the strain components (MITC tying) is used to mitigate numerical locking phenomena, notably for small thickness values (see, e.g., Chapelle and Bathe (2010)).

Considering an implicit Euler scheme, the fully discrete version of (3.16) reads as

$$\begin{cases} \text{For } t>0 \text{ find } \boldsymbol{d}_h^n(t)\in \mathbf{V}_h^{\mathrm{sh}}, \lambda_{1,h}^n(t)\in\Lambda_{1,h}, \lambda_{2,h}^n(t)\in\Lambda_{2,h} \\ \text{and } s^n(t)\in\mathbb{R} \text{ such that:} \\ \displaystyle\int_\Omega \rho \frac{\boldsymbol{d}_h^n-2\boldsymbol{d}_h^{n-1}+\boldsymbol{d}_h^{n-2}}{(\Delta t)^2}\cdot\boldsymbol{v}_h \; + a_h(\boldsymbol{d}_h^n;\boldsymbol{v}_h) \\ \displaystyle+\int_{\Gamma_{C_2}} \left[\lambda_{2,h}^n+\gamma g_2(\boldsymbol{d}_h^n,s^n)\right]_- \boldsymbol{v}_h\cdot\boldsymbol{n}_{\boldsymbol{\varphi}} \\ \displaystyle+\int_{\Gamma_{C_1}} \left[\lambda_{1,h}^n+\gamma g_1(\boldsymbol{d}_h^n)\right]_- \boldsymbol{v}_h\cdot\boldsymbol{n}_{\boldsymbol{\varphi}}=0, \quad \forall \boldsymbol{v}_h\in\mathbf{V}_h^{\mathrm{sh}}, \\ \displaystyle-\frac{1}{\gamma}\int_{\Gamma_{C_2}} \left(\lambda_{2,h}^n+[\lambda_{2,h}^n+\gamma g_2(\boldsymbol{d}_h^n,s^n)]_-\right)\mu_h=0, \quad \forall\mu_h\in\Lambda_{2,h}, \\ \displaystyle-\frac{1}{\gamma}\int_{\Gamma_{C_1}} \left(\lambda_{1,h}^n+[\lambda_{1,h}^n+\gamma g_1(\boldsymbol{d}_h^n)]_-\right)\mu_h=0, \quad \forall\mu_h\in\Lambda_{1,h}, \\ \displaystyle m\frac{s^n-2s^{n-1}+s^{n-2}}{(\Delta t)^2}=f+\int_{\Gamma_{C_2}}[\lambda_{2,h}^n+\gamma g_2(\boldsymbol{d}_h^n,s^n)]_-\,\boldsymbol{e}_y\cdot\boldsymbol{n}_{\boldsymbol{\varphi}}. \end{cases} \tag{3.20}$$

with $\Delta t>0$ the time-discretization parameter and $t^n:=n\Delta t$, where $n\in\mathbb{N}$. At each time step of the backward Euler time-discretization, a nonlinear problem has to be solved and a Newton's algorithm has been selected, whose implementation details are presented in Section A.4.1, Appendix A.

3.3.2 Nitsche's method

Nitsche's method provides a single primal formulation without the need of a Lagrange multiplier. The basic idea consists in using the relation (3.8) on the weak formulation or to eliminate the Lagrange multiplier in the augmented Lagrangian formulation (3.19) via the identity (3.6). By using the Green formula in the solid momentum equation, we get

$$\int_\Omega \rho\partial_{tt}\boldsymbol{d}\cdot\boldsymbol{v}+\int_\Omega \boldsymbol{\Pi}(\boldsymbol{d}):\boldsymbol{\nabla}\boldsymbol{v}-\int_{\Gamma_{C_2}}\boldsymbol{\Pi}(\boldsymbol{d})\boldsymbol{n}_x\cdot\boldsymbol{n}_{\boldsymbol{\varphi}}\boldsymbol{v}\cdot\boldsymbol{n}_{\boldsymbol{\varphi}} - \int_{\Gamma_{C_1}}\boldsymbol{\Pi}(\boldsymbol{d})\boldsymbol{n}_x\cdot\boldsymbol{n}_{\boldsymbol{\varphi}}\boldsymbol{v}\cdot\boldsymbol{n}_{\boldsymbol{\varphi}}=0, \quad \forall\boldsymbol{v}\in\mathbf{V}^{\mathrm{sh}},$$

where $\mathbf{V}^{\mathrm{sh}}$ is given by (2.9) and assuming that the displacement is smooth enough. Using the contact condition (3.8), we get that:

$$\begin{aligned}&\int_\Omega \rho\partial_{tt}\boldsymbol{d}\cdot\boldsymbol{v}+\int_\Omega \boldsymbol{\Pi}(\boldsymbol{d}):\boldsymbol{\nabla}\boldsymbol{v}+\int_{\Gamma_{C_2}}[-\gamma g_2(\boldsymbol{d},s)-\boldsymbol{\Pi}(\boldsymbol{d})\boldsymbol{n}_x\cdot\boldsymbol{n}_{\boldsymbol{\varphi}}]_+\boldsymbol{v}\cdot\boldsymbol{n}_{\boldsymbol{\varphi}} \\ &+\int_{\Gamma_{C_1}}[-\gamma g_1(\boldsymbol{d})-\boldsymbol{\Pi}(\boldsymbol{d})\boldsymbol{n}_x\cdot\boldsymbol{n}_{\boldsymbol{\varphi}}]_+\boldsymbol{v}\cdot\boldsymbol{n}_{\boldsymbol{\varphi}}=\mathbf{0}, \quad \forall\boldsymbol{v}\in\mathbf{V}^{\mathrm{sh}},\end{aligned}$$

which motivates the following spatial semi-discrete approximation of (3.7)

$$\begin{cases} \text{For } t>0, \text{ find } \boldsymbol{d}_h(t)\in \mathbf{V}_h^{\text{sh}} \text{ and } s(t)\in\mathbb{R} \text{ such that:} \\ \displaystyle\int_\Omega \rho\partial_{tt}\boldsymbol{d}_h\cdot\boldsymbol{v}_h + a_h(\boldsymbol{d}_h;\boldsymbol{v}_h) + \int_{\Gamma_{C_2}} [-\gamma g_2(\boldsymbol{d}_h,s) - \boldsymbol{\Pi}(\boldsymbol{d}_h)\boldsymbol{n}_x\cdot\boldsymbol{n}_{\boldsymbol{\varphi}}]_+\boldsymbol{v}_h\cdot\boldsymbol{n}_{\boldsymbol{\varphi}} \\ \displaystyle + \int_{\Gamma_{C_1}} [-\gamma g_1(\boldsymbol{d}_h) - \boldsymbol{\Pi}(\boldsymbol{d}_h)\boldsymbol{n}_x\cdot\boldsymbol{n}_{\boldsymbol{\varphi}}]_+\boldsymbol{v}_h\cdot\boldsymbol{n}_{\boldsymbol{\varphi}} = \mathbf{0}, \quad \forall \boldsymbol{v}_h\in\mathbf{V}_h^{\text{sh}}, \\ \displaystyle m\ddot{s} = f + \int_{\Gamma_{C_2}} [-\gamma g_2(\boldsymbol{d}_h,s) - \boldsymbol{\Pi}(\boldsymbol{d}_h)\boldsymbol{n}_x\cdot\boldsymbol{n}_{\boldsymbol{\varphi}}]_+ \ \boldsymbol{e}_y\cdot\boldsymbol{n}_{\boldsymbol{\varphi}}, \end{cases} \tag{3.21}$$

where $\mathbf{V}_h^{\text{sh}}$ is the 3D-shell finite element space (3.17); the term $a_h(\boldsymbol{d}_h;\boldsymbol{v}_h)$ denotes the discrete stiffness term in the 3D-shell, where a reinterpolation technique for the strain components (MITC tying) is used to reduce numerical locking; and $\gamma := \gamma_0\, E/h$ where $\gamma_0 > 0$ is the Nitsche's parameter, that must be chosen sufficiently large to ensure well-posedness. Formulation (3.21) corresponds to the nonsymmetric variant of the Nitsche's method proposed in (Chouly and Hild, 2013, Chapter 6).

For the ROTSAC setup, the fully-discrete numerical approximation of (3.7) using an implicit Euler scheme reads

$$\begin{cases} \text{For } t>0, \text{ find } \boldsymbol{d}_h^n(t)\in \mathbf{V}_h^{\text{sh}} \text{ and } s^n(t)\in\mathbb{R} \text{ such that:} \\ \displaystyle\int_\Omega \rho\frac{\boldsymbol{d}_h^n - 2\boldsymbol{d}_h^{n-1} + \boldsymbol{d}_h^{n-2}}{(\Delta t)^2}\cdot\boldsymbol{v}_h \ + a_h(\boldsymbol{d}_h;\boldsymbol{v}_h) \\ \displaystyle + \int_{\Gamma_{C_2}} [-\gamma g_2(\boldsymbol{d}_h^n,s^n) - \boldsymbol{\Pi}(\boldsymbol{d}_h^n)\boldsymbol{n}_x\cdot\boldsymbol{n}_{\boldsymbol{\varphi}}]_+\boldsymbol{v}_h\cdot\boldsymbol{n}_{\boldsymbol{\varphi}} \\ \displaystyle + \int_{\Gamma_{C_1}} [-\gamma g_1(\boldsymbol{d}_h^n) - \boldsymbol{\Pi}(\boldsymbol{d}_h^n)\boldsymbol{n}_x\cdot\boldsymbol{n}_{\boldsymbol{\varphi}}]_+\boldsymbol{v}_h\cdot\boldsymbol{n}_{\boldsymbol{\varphi}} = 0, \quad \forall \boldsymbol{v}_h\in\mathbf{V}_h^{\text{sh}}, \\ \displaystyle m\frac{s^n - 2s^{n-1} + s^{n-2}}{(\Delta t)^2} = f + \int_{\Gamma_{C_2}} [-\gamma g_2(\boldsymbol{d}_h^n,s^n) - \boldsymbol{\Pi}(\boldsymbol{d}_h^n)\boldsymbol{n}_x\cdot\boldsymbol{n}_{\boldsymbol{\varphi}}]_+ \ \boldsymbol{e}_y\cdot\boldsymbol{n}_{\boldsymbol{\varphi}}. \end{cases} \tag{3.22}$$

A notable aspect of this method is that it consistently enforces the contact conditions without adding additional unknowns (Lagrange multipliers). The implementation details of the Newton iterations associated to the numerical resolution of (3.22), are provided in Section A.4.2, Appendix A.

3.3.3 Penalty method

One of the most popular numerical approaches for contact is the so-called penalty method. This method can for instance be derived from relation (3.8) by noting that for large values of γ, that expression motivates the approximation

$$\boldsymbol{\Pi}(\boldsymbol{d})\boldsymbol{n}_x\cdot\boldsymbol{n}_{\boldsymbol{\varphi}} \simeq -\left[-\gamma g(\boldsymbol{d})\right]_+ = -\frac{1}{\varepsilon}\left[-g(\boldsymbol{d})\right]_+, \tag{3.23}$$

where $\epsilon > 0$ denotes the corresponding small penalty parameter

$$\frac{1}{\varepsilon} := \gamma = \gamma_0\frac{E}{h}, \tag{3.24}$$

with $\gamma_0 > 0$, E the Young's modulus and h the characteristic element size. Note that the approximation (3.23) is not strongly consistent, so that a certain amount of penetration between the two bodies can be expected at the discrete level, unless ε is sufficiently small.

By combining (3.23) with the argument used in the previous section, the spatial semi-discrete penalty method is given by

$$\begin{cases} \text{For } t > 0, \text{ find } \boldsymbol{d}_h(t) \in \mathbf{V}_h^{\text{sh}} \text{ and } s(t) \in \mathbb{R} \text{ such that:} \\ \displaystyle\int_\Omega \rho \partial_{tt} \boldsymbol{d}_h \cdot \boldsymbol{v}_h + a_h(\boldsymbol{d}_h; \boldsymbol{v}_h) + \frac{1}{\varepsilon} \int_{\Gamma_{C_2}} [-g_2(\boldsymbol{d}_h, s)]_+ \boldsymbol{v}_h \cdot \boldsymbol{n}_{\boldsymbol{\varphi}} \\ \displaystyle + \frac{1}{\varepsilon} \int_{\Gamma_{C_1}} [-g_1(\boldsymbol{d}_h)]_+ \boldsymbol{v}_h \cdot \boldsymbol{n}_{\boldsymbol{\varphi}} = 0, \quad \forall \boldsymbol{v}_h \in \mathbf{V}_h^{\text{sh}}, \\ \displaystyle m\ddot{s} = f + \frac{1}{\varepsilon} \int_{\Gamma_{C_2}} [-g_2(\boldsymbol{d}_h, s)]_+ \ \boldsymbol{e}_y \cdot \boldsymbol{n}_{\boldsymbol{\varphi}}. \end{cases} \tag{3.25}$$

which after time-discretization yields the fully discrete scheme

$$\begin{cases} \text{For } t > 0 \text{ find } \boldsymbol{d}_h^n(t) \in \mathbf{V}_h^{\text{sh}} \text{ and } s^n(t) \in \mathbb{R} \text{ such that:} \\ \displaystyle\int_\Omega \rho \frac{\boldsymbol{d}_h^n - 2\boldsymbol{d}_h^{n-1} + \boldsymbol{d}_h^{n-2}}{(\Delta t)^2} \cdot \boldsymbol{v}_h \ + a_h(\boldsymbol{d}_h; \boldsymbol{v}_h) + \frac{1}{\varepsilon} \int_{\Gamma_{C_2}} [-g_2(\boldsymbol{d}_h^n, s^n)]_+ \boldsymbol{v}_h \cdot \boldsymbol{n}_{\boldsymbol{\varphi}} \\ \displaystyle + \frac{1}{\varepsilon} \int_{\Gamma_{C_1}} [-g_1(\boldsymbol{d}_h^n)]_+ \boldsymbol{v}_h \cdot \boldsymbol{n}_{\boldsymbol{\varphi}} = 0, \quad \forall \boldsymbol{v}_h \in \mathbf{V}_h^{\text{sh}}, \\ \displaystyle m \frac{s^n - 2s^{n-1} + s^{n-2}}{(\Delta t)^2} = f + \frac{1}{\varepsilon} \int_{\Gamma_{C_2}} [-g_2(\boldsymbol{d}_h^n, s^n)]_+ \ \boldsymbol{e}_y \cdot \boldsymbol{n}_{\boldsymbol{\varphi}}, \end{cases} \tag{3.26}$$

where $\mathbf{V}_h^{\text{sh}}$ is the 3D-shell finite element space (3.17) and, again, $a_h(\boldsymbol{d}_h; \boldsymbol{v}_h)$ represents the discrete stiffness term in the 3D-shell. The implementation details of the Newton iterations on the resolution of (3.26) are presented in Section A.4.3, Appendix A.

3.4 Numerical results

In this section we investigate the performance of the three numerical approaches described in the previous section (augmented Lagrangian, Nitsche and penalty) in three different 3D numerical examples motivated by the simulation of the ROTSAC setup. All the numerical computations have been performed with the FELiScE[1] C++ finite element library.

Since we need to reach extreme force values, it is advantageous not to use a constant time step. Instead, we employ a dynamic time-stepping approach that adjusts based on the convergence behavior of the solution, improving the efficiency of the simulations. The time adaptivity algorithm used in the simulations is presented in Section A.2, Appendix A.

Unlike in Chapter 2, the fiber model described by (2.11) is not used in the numerical results of this chapter, as we are not dealing with vasoactive substances.

Throughout the following sections, all the units are expressed in the centimeter-gram-second (CGS) unit system, unless specified otherwise.

[1] https://gitlab.inria.fr/felisce

3.4.1 Numerical example 1: Contact between a 3D flat elastic body and a rigid cylinder

The first example investigates frictionless contact in a simple geometry. In particular, in this test we study the behavior of a 3D elastic shell falling against a rigid cylinder. This is a preliminary test to validate the different numerical approaches for contact. The mathematical model is the same as the one presented in (3.7), but just considering the contact with the static hook. In other words, all the terms on Γ_{C_2} are omitted, as well as the equation of the moving hook. The considered geometry is shown in Figure 3.4. The elastic solid domain is $\Omega = [0, 0.2] \times [0, 0.2] \times [0, 0.015]$. The rigid cylinder has a radius equal to $r_h = 0.02$.

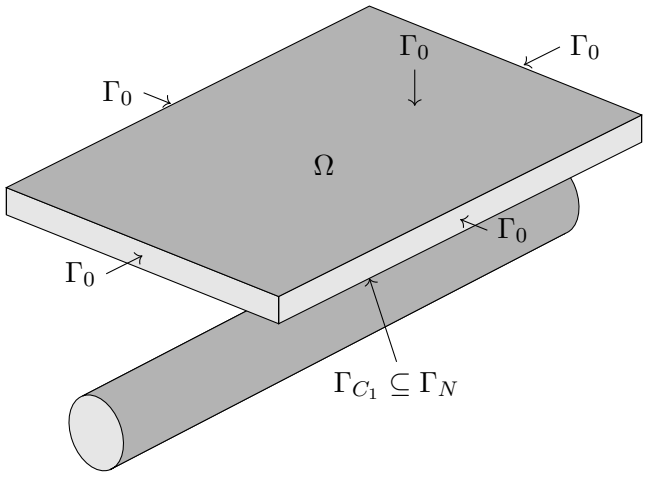

Figure 3.4: Geometric configuration of numerical example 1.

The elastic solid material parameters corresponding to equation (2.6) are[2] $E = 5 \cdot 10^5$, $\nu = 0.47$ and $\rho = 1.2$. The parameter κ of the Ogden's law has been set to $\kappa = 100$. Concerning the boundary conditions, a uniform distributed load is applied on the lower surface of the solid, Γ_N: $f_s(t) = 500 \cdot t$. In the boundary Γ_0, we enforce *do nothing* boundary conditions. The solid is initially at rest and the cylinder cannot move.

The solid mesh is made of $7,200$ prisms (see Figure 3.5). The local size is $h \approx 0.0047$. The considered parameters for the time adaptivity are $I_{coarse} = 5$ and $I_{fix} = 5$. The maximum allowed value for the time step is $\Delta t_{max} = 0.001$ and the final time is set at $T = 0.1$.

We evaluate the time iterations, the sum of the Newton iterations and the penetration for the three methods for different choices of the parameter $\gamma = \gamma_0 \, E/h$, with $\gamma_0 = \{0.1, 1, 10\}$.

With the applied Neumann condition, the elastic solid starts to fall until it reaches the rigid cylinder, where it does a small rebounding before reaching a steady state. For illustration purposes, Figure 3.6 provides snapshots of the solid deformation with penalty method at different time instants. An analogue displacement is observed with augmented

[2]Recall that c_1, c_2 and a can be obtained from the E, ν and κ as illustrated in Section 2.2.2.2, Chapter 2.

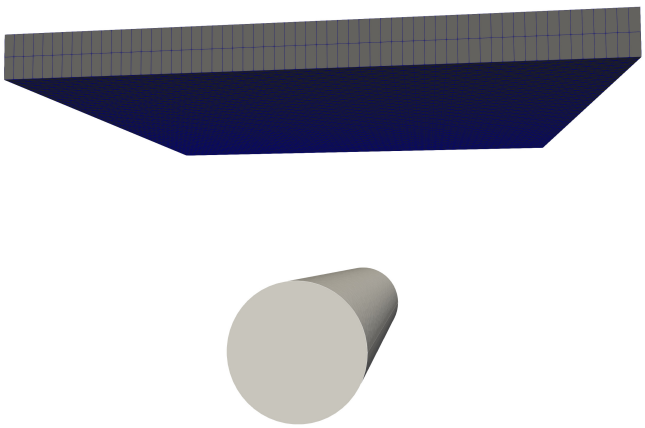

Figure 3.5: Solid mesh for the first numerical example.

Lagrangian or Nitsche.

Tables 3.1-3.3 present the number of time iterations required to reach the final time $T = 0.1$, along with the total sum of Newton iterations. Additionally, the tables show the average gap at the quadrature points in contact, as well as the relative average gap with respect to the mesh thickness.

Key metrics	**Penalty**	**Augmented Lagrangian**	**Nitsche**
# time it	100	100	104
# Newton it	241	250	236
Average gap (cm)	$-1.55 \cdot 10^{-4}$	$1.07 \cdot 10^{-5}$	$4.64 \cdot 10^{-4}$
Average gap / thickness	$-1.0 \cdot 10^{-2}$	$7.1 \cdot 10^{-4}$	$3.1 \cdot 10^{-2}$

Table 3.1: Comparison between penalty, augmented Lagrangian and Nitsche at $T = 0.1$ with $\gamma_0 = 0.1$.

Key metrics	**Penalty**	**Augmented Lagrangian**	**Nitsche**
# time it	100	104	105
# Newton it	236	238	262
Average gap (cm)	$-3.26 \cdot 10^{-5}$	$1.06 \cdot 10^{-5}$	$4.64 \cdot 10^{-4}$
Average gap / thickness	$-2.2 \cdot 10^{-3}$	$7.1 \cdot 10^{-4}$	$3.1 \cdot 10^{-2}$

Table 3.2: Comparison between penalty, augmented Lagrangian and Nitsche at $T = 0.1$ with $\gamma_0 = 1$.

The parameter γ_0 plays a similar role in all three methods: it acts as a penalty parameter in the penalty method, an augmentation parameter in the augmented Lagrangian approach, and the Nitsche's parameter in Nitsche's method. The Nitsche's method requires a minimum value of γ to guarantee stability. In contrast, for the penalty method, a balance must be found between choosing a large γ_0 (see equation (3.24)), which ensures accurate

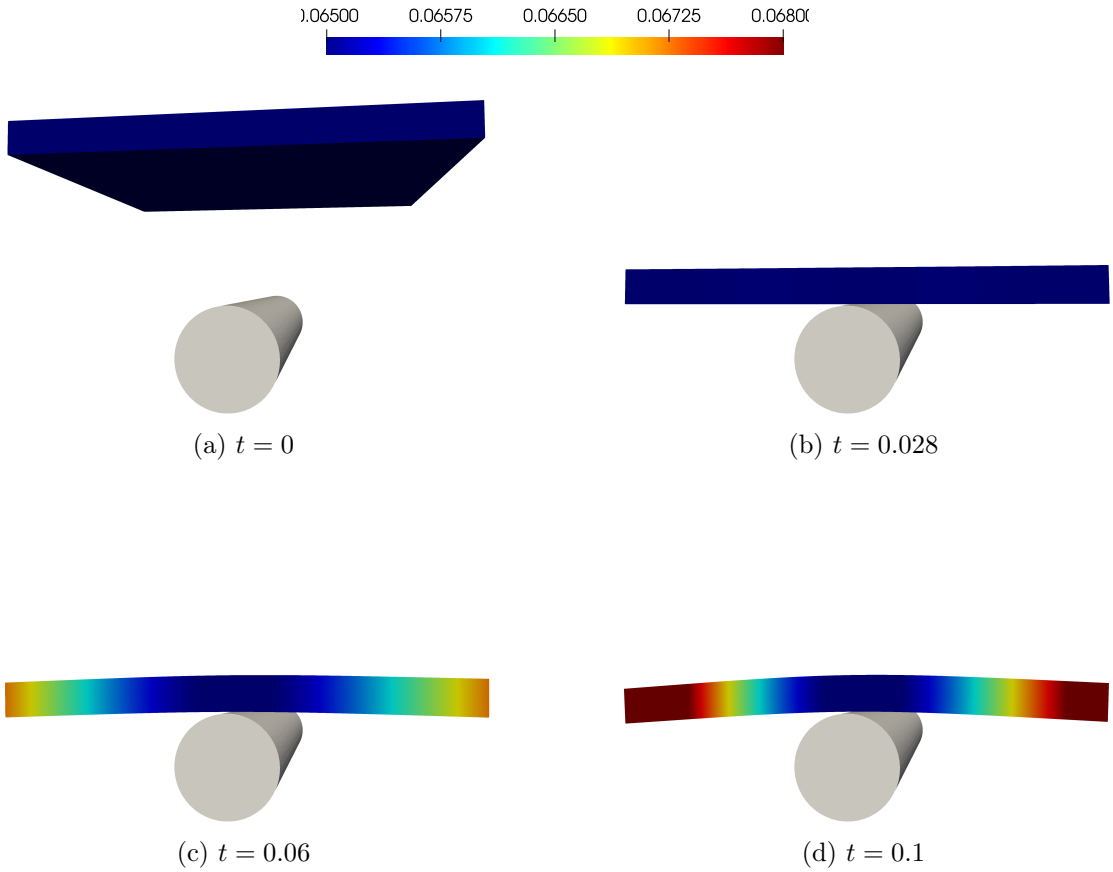

(a) $t = 0$ (b) $t = 0.028$

(c) $t = 0.06$ (d) $t = 0.1$

Figure 3.6: Displacement of the solid obtained with penalty method with $\gamma_0 = 10$.

Key metrics	**Penalty**	**Augmented Lagrangian**	**Nitsche**
# time it	100	109	109
# Newton it	247	280	280
Average gap (cm)	$-5.04 \cdot 10^{-6}$	$1.05 \cdot 10^{-5}$	$4.65 \cdot 10^{-4}$
Average gap / thickness	$-3.4 \cdot 10^{-4}$	$7.1 \cdot 10^{-4}$	$3.1 \cdot 10^{-2}$

Table 3.3: Comparison between penalty, augmented Lagrangian and Nitsche at $T = 0.1$ with $\gamma_0 = 10$.

enforcement of contact conditions, and a moderate value that does not affect Newton's method convergence.

A first observation is that there is not a significant difference in the total number of time iterations. As the parameter γ_0 increases, we observe in general an increase in the number of Newton iterations. Regarding the penetration, we observe that Nitsche and augmented Lagrangian perform better than penalty. It is also worth noting that penetration in penalty is much more sensitive to the γ_0 than for the other two methods. The results presented show similar dynamics with the three methods.

3.4.2 Numerical example 2: Contact between a 3D half hollow elastic cylinder and a rigid cylinder

The second numerical example corresponds to an intermediate step before performing the simulation of the ROTSAC setup. The mathematical model is the same as the one presented in (3.7), but just considering the contact with the static hook, that means omitting all the terms computed in Γ_{C_2} and the equation of the moving hook. In this example, we use the geometry shown in Figure 3.7. Due to the symmetry of the ROTSAC, we can take the half of a hollow 3D cylinder in a longitudinal cut and model the contact with the static hook (rigid cylinder), while a pulling force is applied on the edges. The radius of the half cylinder is $R = 0.05$, the length $L = 0.2$ and the thickness $\varepsilon = 0.0055$. The radius of the hook is $r_h = 0.008009$.

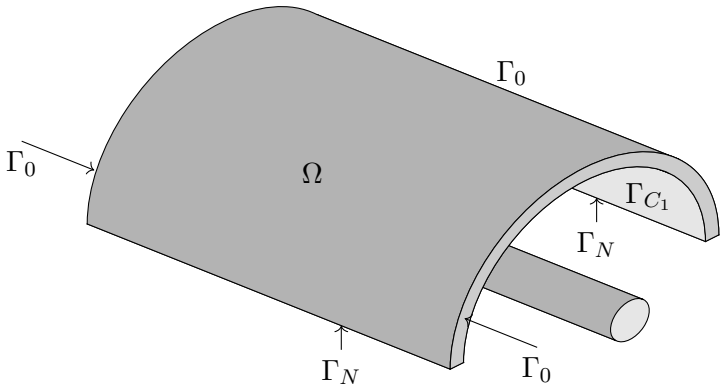

Figure 3.7: Geometric configuration of numerical example 2.

The physical parameters used for the solid in this test are $E = 5 \cdot 10^6$, $\nu = 0.47$ and $\rho = 1.2$. The parameter of the Ogden's law has been set to $\kappa = 100$. Regarding the boundary conditions, a uniform distributed load is applied on the edges of the half cylinder (quadrilateral elements), Γ_N, in terms of the following time-dependent expression: $f_s(t) = 200\,000 \cdot t$. In the boundary Γ_0, we enforce *do nothing* boundary conditions.

The objective is to reach the forces that have been applied during the experimental calibration of the ROTSAC (10, 20, 30, 40 and 50 mN). As in the previous example, we evaluate three different choices of the parameter $\gamma = \gamma_0 \, E/h$, with $\gamma_0 = \{1, 10, 100\}$. Here the parameters have been chosen larger than in the previous numerical example to be able to illustrate the convergence for the three methods. Since the forces are higher, we needed

to increase the values of the parameters because otherwise with penalty the simulations could not be performed.

The solid mesh is composed of $10,780$ prisms. In the area around the cylinder in contact, the considered space discretization parameter is $h \approx 0.0038$ while in the rest $h \approx 0.0044$. The mesh is shown in Figure 3.8.

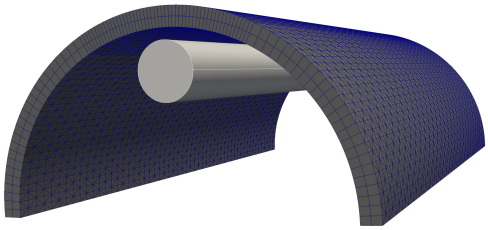

Figure 3.8: Solid mesh and fixed hook.

As in the previous numerical example, we use the time adaptivity Algorithm 1. The maximum allowed value of Δt_{max} is $\Delta t_{max} = 0.001$. The considered parameters for the time adaptivity are $I_{coarse} = 5$ and $I_{fix} = 5$. The final time is set at $T = 5.685$. The body is considered initially at rest.

Figure 3.9 shows snapshots of the solid deformation at different forces obtained with the augmented Lagrangian method. An analogue displacement is observed with Nitsche or penalty. The contact force on the solid for the augmented Lagrangian method is shown in Figure 3.10. Similar results are observed for the other methods.

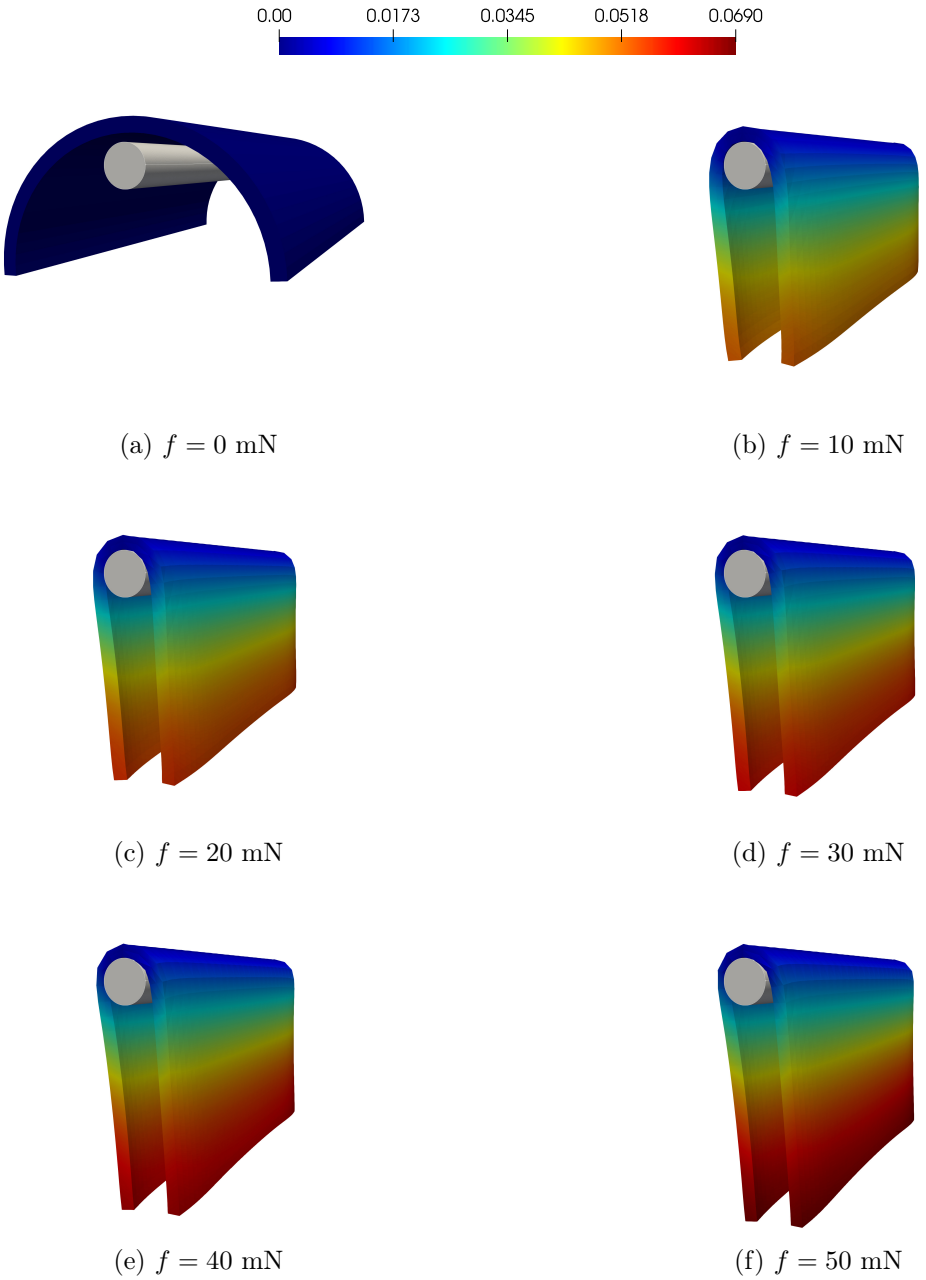

(a) $f = 0$ mN

(b) $f = 10$ mN

(c) $f = 20$ mN

(d) $f = 30$ mN

(e) $f = 40$ mN

(f) $f = 50$ mN

Figure 3.9: Deformed configuration and displacement magnitude obtained with augmented Lagrangian with $\gamma_0 = 1$.

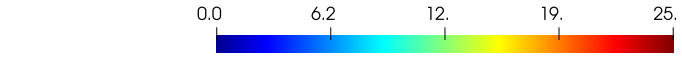

(a) $f = 0$ mN

(b) $f = 10$ mN

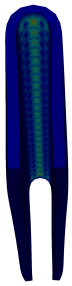

(c) $f = 20$ mN

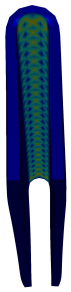

(d) $f = 30$ mN

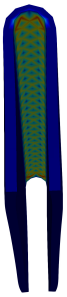

(e) $f = 40$ mN

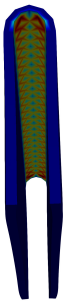

(f) $f = 50$ mN

Figure 3.10: Deformed configuration and contact force obtained with augmented Lagrangian with $\gamma_0 = 1$.

In Tables 3.4-3.6, we provide indicators for each method, including the number of time steps, the sum of Newton iterations, and the penetration for different values of the external force. Additionally, the average gap is computed for all the contact methods, along with the relative gap with respect to the mesh thickness.

Force (mN)	Key metrics	Penal.	Aug. Lag.	Nitsche.
10	# time it	1140	1140	1140
	# Newton it	3543	4552	3711
	Average gap (cm)	$-1.1 \cdot 10^{-4}$	$9.2 \cdot 10^{-7}$	$1.3 \cdot 10^{-6}$
	Average gap / thickness	$-2.00 \cdot 10^{-2}$	$1.67 \cdot 10^{-4}$	$2.36 \cdot 10^{-4}$
20	# time it	2275	2275	2275
	# Newton it	6948	9092	8251
	Average gap (cm)	$-2.1 \cdot 10^{-4}$	$5.2 \cdot 10^{-7}$	$1.1 \cdot 10^{-6}$
	Average gap / thickness	$-3.82 \cdot 10^{-2}$	$9.45 \cdot 10^{-5}$	$2.00 \cdot 10^{-4}$
30	# time it	3420	3420	3420
	# Newton it	10383	13672	15872
	Average gap (cm)	$-3.3 \cdot 10^{-4}$	$3.1 \cdot 10^{-7}$	$1.0 \cdot 10^{-5}$
	Average gap / thickness	$-6.00 \cdot 10^{-2}$	$5.64 \cdot 10^{-5}$	$1.82 \cdot 10^{-3}$
40	# time it	4550	4450	10111
	# Newton it	13773	17888	48463
	Average gap (cm)	$-4.6 \cdot 10^{-4}$	$1.9 \cdot 10^{-8}$	$9.2 \cdot 10^{-5}$
	Average gap / thickness	$-8.36 \cdot 10^{-2}$	$3.45 \cdot 10^{-6}$	$1.67 \cdot 10^{-2}$
50	# time it	5685	5685	21808
	# Newton it	17178	21731	83562
	Average gap (cm)	$-6.1 \cdot 10^{-4}$	$1.2 \cdot 10^{-6}$	$8.9 \cdot 10^{-5}$
	Average gap / thickness	$-1.11 \cdot 10^{-1}$	$2.18 \cdot 10^{-4}$	$1.62 \cdot 10^{-2}$

Table 3.4: Comparison of the three methods for different traction forces and $\gamma_0 = 1$.

From Tables 3.4-3.6, it can be observed that in general the number of Newton iterations in the cases of augmented Lagrangian and Nitsche is bigger with respect to penalty. In general, if the penalty coefficient is well-chosen, the penalty method can be very robust. For Nitsche, we have observed that a smaller time step is needed at higher forces when the deformation is very large, so the total number of iterations is considerably increased. On the other hand, the results show that in the case of penalty there is always penetration, which increases when γ_0 is smaller. However, that is not the case for augmented Lagrangian or Nitsche's method, that generally provide a more accurate physical representation of contact problems.

Force (mN)	Key metrics	Penal.	Aug. Lag.	Nitsche.
10	# time it	1140	1470	1140
	# Newton it	3550	8045	3703
	Average gap (cm)	$-1.2 \cdot 10^{-5}$	$1.5 \cdot 10^{-7}$	$1.1 \cdot 10^{-6}$
	Average gap / thickness	$-2.18 \cdot 10^{-3}$	$2.73 \cdot 10^{-5}$	$2.00 \cdot 10^{-4}$
20	# time it	2275	2605	2275
	# Newton it	6955	13590	8243
	Average gap (cm)	$-2.3 \cdot 10^{-5}$	$1.1 \cdot 10^{-7}$	$8.3 \cdot 10^{-6}$
	Average gap / thickness	$-4.18 \cdot 10^{-3}$	$2.00 \cdot 10^{-5}$	$1.51 \cdot 10^{-3}$
30	# time it	3420	3750	3420
	# Newton it	10390	18178	16166
	Average gap (cm)	$-3.5 \cdot 10^{-5}$	$1.1 \cdot 10^{-7}$	$7.7 \cdot 10^{-5}$
	Average gap / thickness	$-6.36 \cdot 10^{-3}$	$2.00 \cdot 10^{-5}$	$1.40 \cdot 10^{-2}$
40	# time it	4550	4880	10586
	# Newton it	13780	22698	47059
	Average gap (cm)	$-4.9 \cdot 10^{-5}$	$6.4 \cdot 10^{-7}$	$7.8 \cdot 10^{-5}$
	Average gap / thickness	$-8.91 \cdot 10^{-3}$	$1.16 \cdot 10^{-4}$	$1.42 \cdot 10^{-2}$
50	# time it	5685	6015	21426
	# Newton it	17185	27238	79579
	Average gap (cm)	$-6.5 \cdot 10^{-5}$	$7.8 \cdot 10^{-6}$	$7.9 \cdot 10^{-5}$
	Average gap / thickness	$-1.18 \cdot 10^{-2}$	$1.42 \cdot 10^{-3}$	$1.44 \cdot 10^{-2}$

Table 3.5: Comparison of the three methods for different traction forces and $\gamma_0 = 10$.

Force (mN)	Key metrics	Penal.	Aug. Lag.	Nitsche.
10	# time it	1140	2685	1140
	# Newton it	3631	15519	3732
	Average gap (cm)	$-1.9 \cdot 10^{-6}$	$3.2 \cdot 10^{-6}$	$4.5 \cdot 10^{-6}$
	Average gap / thickness	$-3.5 \cdot 10^{-4}$	$5.8 \cdot 10^{-4}$	$8.1 \cdot 10^{-4}$
20	# time it	2275	3820	2275
	# Newton it	7041	21793	8244
	Average gap (cm)	$-2.4 \cdot 10^{-6}$	$3.2 \cdot 10^{-6}$	$9.7 \cdot 10^{-6}$
	Average gap / thickness	$-4.4 \cdot 10^{-4}$	$5.8 \cdot 10^{-4}$	$1.8 \cdot 10^{-3}$
30	# time it	3420	4965	4701
	# Newton it	10476	27227	33083
	Average gap (cm)	$-3.7 \cdot 10^{-6}$	$3.8 \cdot 10^{-6}$	$6.4 \cdot 10^{-5}$
	Average gap / thickness	$-6.3 \cdot 10^{-4}$	$7.0 \cdot 10^{-4}$	$1.2 \cdot 10^{-2}$
40	# time it	4550	6095	13615
	# Newton it	13866	31796	59825
	Average gap (cm)	$-5.1 \cdot 10^{-6}$	$3.8 \cdot 10^{-6}$	$8.8 \cdot 10^{-5}$
	Average gap / thickness	$-9.3 \cdot 10^{-4}$	$6.9 \cdot 10^{-4}$	$1.7 \cdot 10^{-2}$
50	# time it	5685	7230	21726
	# Newton it	16997	36342	84168
	Average gap (cm)	$-6.8 \cdot 10^{-6}$	$4.5 \cdot 10^{-6}$	$9.85 \cdot 10^{-5}$
	Average gap / thickness	$-1.3 \cdot 10^{-3}$	$8.2 \cdot 10^{-4}$	$1.8 \cdot 10^{-2}$

Table 3.6: Comparison of the three methods for different traction forces and $\gamma_0 = 100$.

3.4.3 Numerical example 3: ROTSAC setup

The last example, is the simulation of the experimental ROTSAC setup with a realistic geometry taking into account the contact of the tissue (whose geometry is considered to be a hollow 3D cylinder) between the static and the moving hook (both rigid cylinders). The geometric configuration is shown in Figure 3.11.

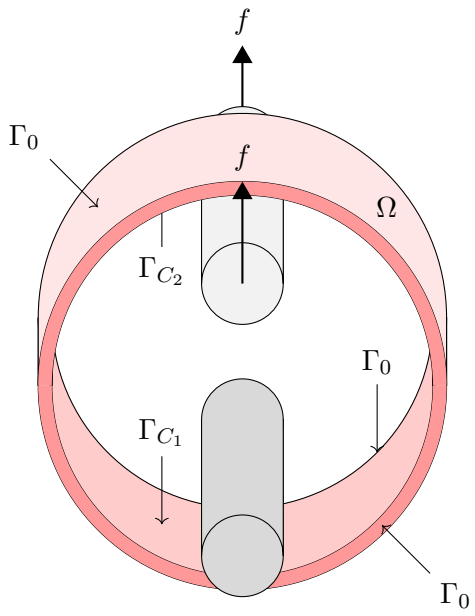

Figure 3.11: Geometric configuration of the ROTSAC setup.

The solid domain is given by the 3D cylinder of radius $R = 0.04$, length $L = 0.2$ and thickness $\varepsilon = 0.0052$. The solid is considered to be initially at rest. The radius of each hook is $r_h = 0.008009$. The physical parameters used for the elastic solid are $E = 5 \cdot 10^6$, $\nu = 0.47$ and $\rho = 1.2$. The parameter of the Ogden's law has been set to $\kappa = 100$. A force is applied on the moving hook (that is the upper one), in terms of the following expression: $f = 10000 \cdot t$.

We compare the time-step, Newton iterations and penetration on the three methods for three different choices of the parameter $\gamma_0 = \{1, 10, 100\}$.

The solid mesh has $19,800$ prisms. In the area around the hooks, the space discretization parameter is $h \approx 0.0037$ while in the rest is $h \approx 0.0043$. Figure 3.12 shows the considered mesh for the solid.

The time adaptivity Algorithm 1 is employed to implement different levels of refinement for the time step, with a maximum allowed value of $\Delta t_{max} = 0.0005$. The final time is set at $T = 0.5$. The considered parameters for the time adaptivity are $I_{coarse} = 5$ and $I_{fix} = 5$. Time adaptivity is necessary in our numerical examples to better align with the requirements of the Newton algorithm for convergence.

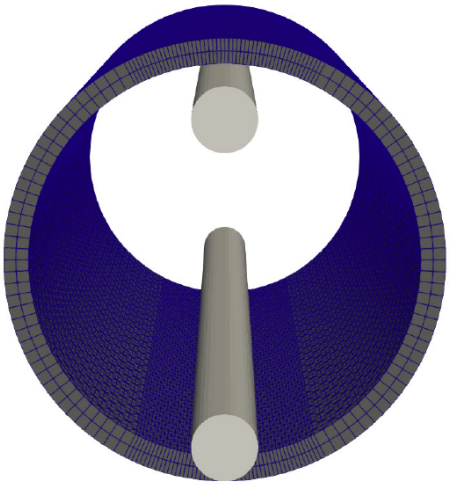

Figure 3.12: Arterial segment mesh for the ROTSAC.

Figure 3.13 presents the simulated solid deformation at the different experimental forces for the Nitsche's method. Similar results are obtained with augmented Lagrangian or penalty, which are omitted here for the sake of conciseness. For comparison purposes, in Figures 3.14 and 3.16 we show some pictures of the deformation of the tissue during the ROTSAC experiment. We can clearly see that the numerical simulation reproduces the experimentally observed length reduction as the force applied in the upper hook increases. We can also note that for the considered physical parameters, the numerical simulations tend in general to overestimate a bit the deformation. This discrepancy could be circumvented by performing parameter estimation, as in Chapter 2. The contact force for Nitsche's method is shown in Figure 3.15.

In Tables 3.7-3.9, we summarize the results from the three methods and different loading steps. To quantify the accuracy properties, we compared the number of time iterations of each method, the sum of Newton iterations and the average gap at the quadrature points in contact with the mesh. In particular, we compare the number of iterations at forces equal to 10, 20, 30, 40 and 50 mN, that are achieved at times $t = (0.1, 0.2, 0.3, 0.4, 0.5)$. In general, the penalty method involves less iterations. However, there is always penetration in the case of penalty but not for augmented Lagrangian or Nitsche.

Tables 3.7-3.9 follow the trend of the results obtained in the previous numerical example in Section 3.4.2. In the simulation with penalty method corresponding to $\gamma_0 = 1$ presented in Table 3.7, we observed that the penetration is too high so that is not possible to apply forces much beyond 40 mN and to reach 50 mN, whereas the other methods allow for higher force levels.

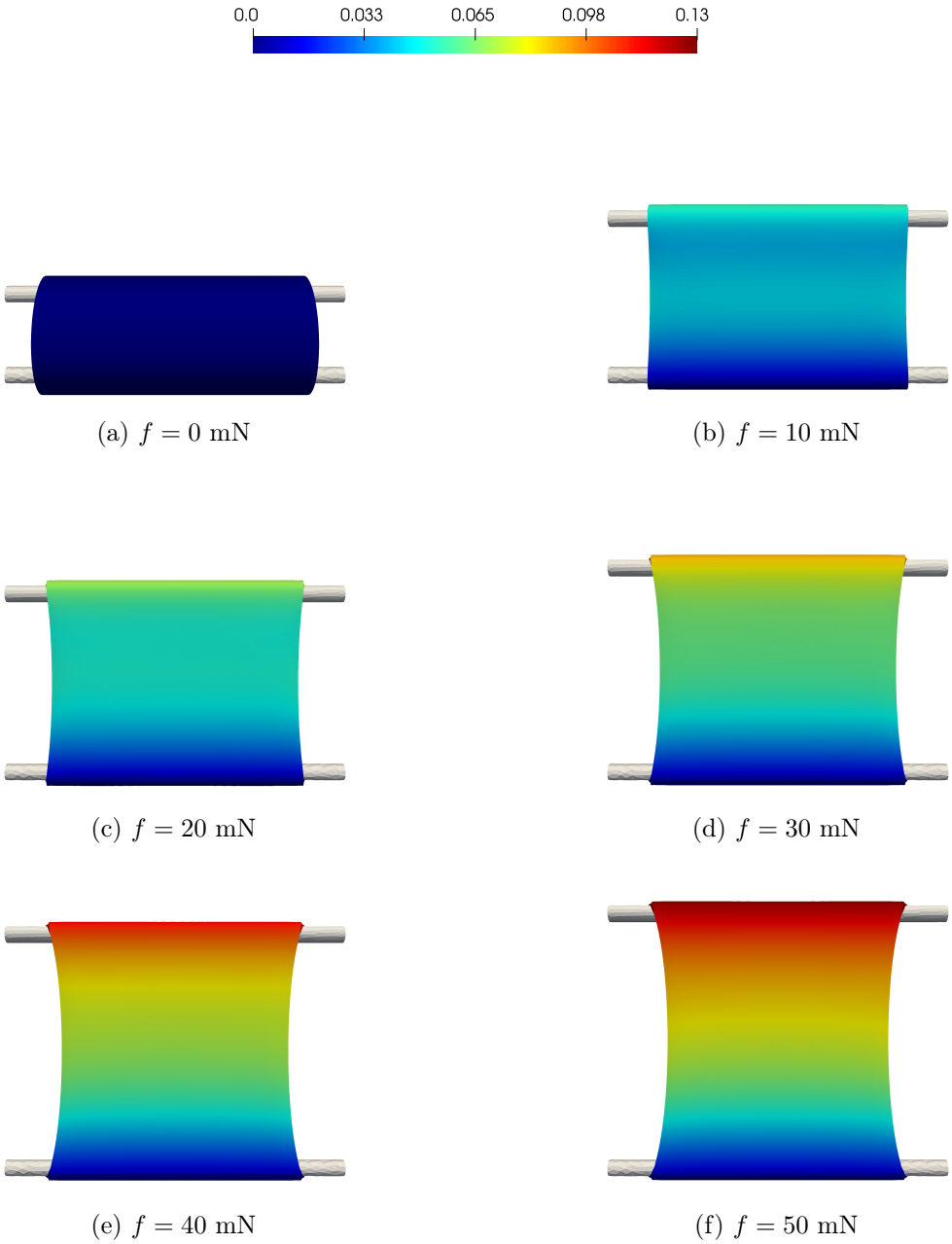

(a) $f = 0$ mN

(b) $f = 10$ mN

(c) $f = 20$ mN

(d) $f = 30$ mN

(e) $f = 40$ mN

(f) $f = 50$ mN

Figure 3.13: Deformed configuration and displacement magnitude with Nitsche's method with $\gamma_0 = 100$.

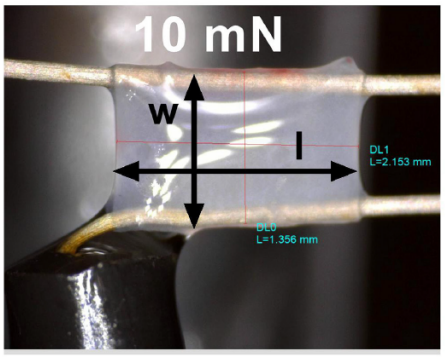

(a) $f = 10$ mN

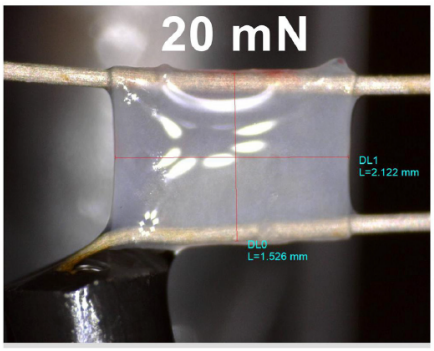

(b) $f = 20$ mN

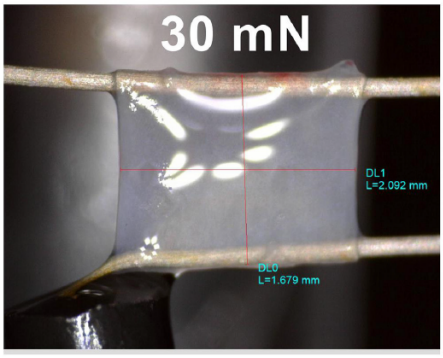

(c) $f = 30$ mN

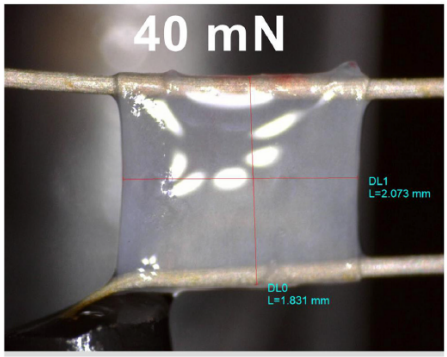

(d) $f = 40$ mN

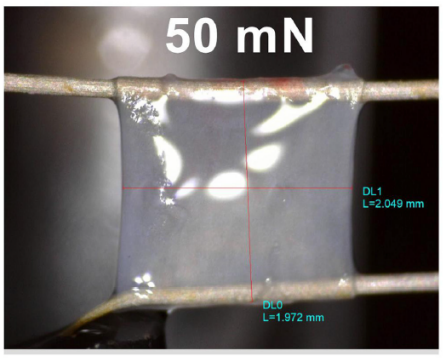

(e) $f = 50$ mN

Figure 3.14: Experimental displacement of the segment (front view). Images from De Moudt et al. (2021).

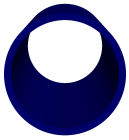

(a) $f = 0$ mN

(b) $f = 10$ mN

(c) $f = 20$ mN

(d) $f = 30$ mN

(e) $f = 40$ mN

(f) $f = 50$ mN

Figure 3.15: Deformed configuration and contact force with Nitsche's method with $\gamma_0 = 100$.

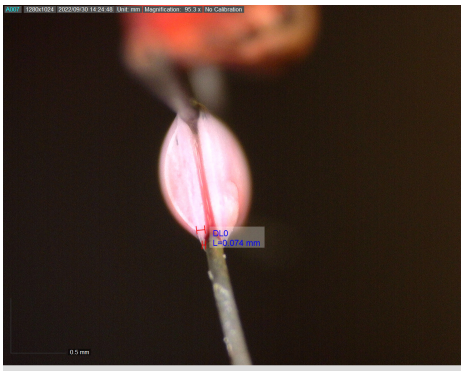

(a) $f = 10$ mN

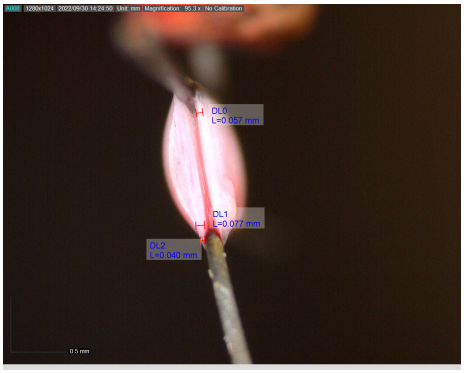

(b) $f = 20$ mN

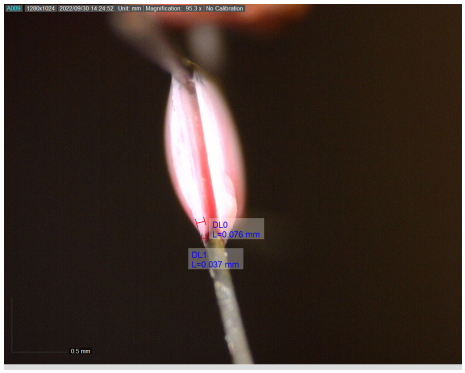

(c) $f = 30$ mN

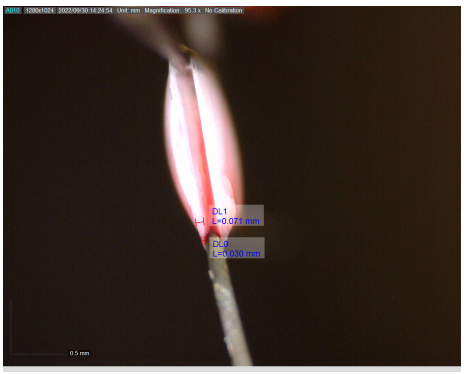

(d) $f = 40$ mN

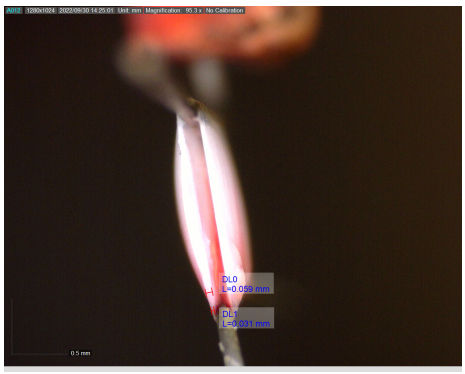

(e) $f = 50$ mN

Figure 3.16: Experimental displacement of the segment (side view).

Force (mN)	Key metrics	Penal.	Aug. Lag.	Nitsche.
10	# time it	200	231	204
	# Newton it	629	891	692
	Average gap (cm)	$-2.67 \cdot 10^{-4}$	$4.76 \cdot 10^{-7}$	$3.40 \cdot 10^{-6}$
	Average gap / thickness	$-5.14 \cdot 10^{-2}$	$9.14 \cdot 10^{-5}$	$6.54 \cdot 10^{-4}$
20	# time it	400	431	736
	# Newton it	1229	1522	2813
	Average gap (cm)	$-5.62 \cdot 10^{-4}$	$5.46 \cdot 10^{-8}$	$8.40 \cdot 10^{-6}$
	Average gap / thickness	$-1.08 \cdot 10^{-1}$	$1.05 \cdot 10^{-5}$	$1.61 \cdot 10^{-3}$
30	# time it	600	631	2674
	# Newton it	1829	2146	8685
	Average gap (cm)	$-9.98 \cdot 10^{-4}$	$5.07 \cdot 10^{-7}$	$7.43 \cdot 10^{-5}$
	Average gap / thickness	$-1.92 \cdot 10^{-1}$	$9.75 \cdot 10^{-5}$	$1.43 \cdot 10^{-2}$
40	# time it	800	831	5814
	# Newton it	2663	2768	19545
	Average gap (cm)	$-1.62 \cdot 10^{-3}$	$2.40 \cdot 10^{-6}$	$9.12 \cdot 10^{-5}$
	Average gap / thickness	$-3.12 \cdot 10^{-1}$	$4.62 \cdot 10^{-4}$	$1.75 \cdot 10^{-2}$
50	# time it	-	1117	11656
	# Newton it	-	4022	37261
	Average gap (cm)	-	$2.83 \cdot 10^{-6}$	$9.84 \cdot 10^{-5}$
	Average gap / thickness	-	$5.45 \cdot 10^{-4}$	$1.89 \cdot 10^{-2}$

Table 3.7: Comparison of the three methods for different traction forces and $\gamma_0 = 1$. Penalty fails to reach 50 mN.

Force (mN)	Key metrics	Penal.	Aug. Lag.	Nitsche.
10	# time it	200	209	200
	# Newton it	665	938	728
	Average gap (cm)	$-2.86 \cdot 10^{-5}$	$4.12 \cdot 10^{-7}$	$2.72 \cdot 10^{-6}$
	Average gap / thickness	$-5.51 \cdot 10^{-3}$	$7.93 \cdot 10^{-5}$	$5.23 \cdot 10^{-4}$
20	# time it	400	409	772
	# Newton it	1265	1747	3051
	Average gap (cm)	$-5.96 \cdot 10^{-5}$	$5.66 \cdot 10^{-8}$	$8.81 \cdot 10^{-6}$
	Average gap / thickness	$-1.15 \cdot 10^{-2}$	$1.09 \cdot 10^{-5}$	$1.69 \cdot 10^{-3}$
30	# time it	600	609	2689
	# Newton it	1865	2552	8766
	Average gap (cm)	$-1.03 \cdot 10^{-4}$	$5.02 \cdot 10^{-7}$	$7.24 \cdot 10^{-5}$
	Average gap / thickness	$-1.98 \cdot 10^{-2}$	$9.65 \cdot 10^{-5}$	$1.39 \cdot 10^{-2}$
40	# time it	800	809	5800
	# Newton it	2465	3362	20147
	Average gap (cm)	$-1.59 \cdot 10^{-4}$	$2.39 \cdot 10^{-6}$	$9.30 \cdot 10^{-5}$
	Average gap / thickness	$-3.06 \cdot 10^{-2}$	$4.60 \cdot 10^{-4}$	$1.79 \cdot 10^{-2}$
50	# time it	1070	1095	11728
	# Newton it	3535	4713	39687
	Average gap (cm)	$-2.30 \cdot 10^{-4}$	$2.83 \cdot 10^{-6}$	$9.87 \cdot 10^{-5}$
	Average gap / thickness	$-4.42 \cdot 10^{-2}$	$5.44 \cdot 10^{-4}$	$1.90 \cdot 10^{-2}$

Table 3.8: Comparison of the three methods for different traction forces and $\gamma_0 = 10$.

Force (mN)	Key metrics	Penal.	Aug. Lag.	Nitsche.
10	# time it	200	200	200
	# Newton it	744	1531	792
	Average gap (cm)	$-3.02 \cdot 10^{-6}$	$3.29 \cdot 10^{-7}$	$1.33 \cdot 10^{-6}$
	Average gap / thickness	$-5.80 \cdot 10^{-4}$	$6.33 \cdot 10^{-5}$	$2.56 \cdot 10^{-4}$
20	# time it	400	400	889
	# Newton it	1344	3154	3331
	Average gap (cm)	$-6.18 \cdot 10^{-6}$	$4.46 \cdot 10^{-8}$	$6.82 \cdot 10^{-6}$
	Average gap / thickness	$-1.19 \cdot 10^{-3}$	$8.58 \cdot 10^{-6}$	$1.31 \cdot 10^{-3}$
30	# time it	600	600	2849
	# Newton it	1946	4701	9376
	Average gap (cm)	$-1.06 \cdot 10^{-5}$	$4.94 \cdot 10^{-7}$	$7.02 \cdot 10^{-5}$
	Average gap / thickness	$-2.04 \cdot 10^{-3}$	$9.50 \cdot 10^{-5}$	$1.35 \cdot 10^{-2}$
40	# time it	804	800	5876
	# Newton it	2598	6101	21897
	Average gap (cm)	$-1.64 \cdot 10^{-5}$	$2.37 \cdot 10^{-6}$	$9.28 \cdot 10^{-5}$
	Average gap / thickness	$-3.16 \cdot 10^{-3}$	$4.57 \cdot 10^{-4}$	$1.79 \cdot 10^{-2}$
50	# time it	1042	1139	11797
	# Newton it	3467	8161	41788
	Average gap (cm)	$-2.36 \cdot 10^{-5}$	$2.88 \cdot 10^{-6}$	$9.91 \cdot 10^{-5}$
	Average gap / thickness	$-4.54 \cdot 10^{-3}$	$5.54 \cdot 10^{-4}$	$1.91 \cdot 10^{-2}$

Table 3.9: Comparison of the three methods for different traction forces and $\gamma_0 = 100$.

3.5 Conclusion and discussion

In this chapter, we introduced a mathematical model for contact mechanics to simulate the ROTSAC experiment using a realistic geometry. In order to treat contact at the discrete level, three numerical methods have been investigated. To the best of our knowledge, this is the first time Nitsche's method has been applied to 3D-shell models.

Comparing CPU time per Newton iteration in the same conditions and using the same machine, we have observed that penalty is the fastest, followed by Nitsche (7% slower) and augmented Lagrangian (10% slower). However, when considering the total CPU time needed to reach the final force of 50 mN (for instance when the parameter is chosen with $\gamma_0 = 10$) in the third numerical example (ROTSAC), we observe the following results: the penalty method is the fastest, Nitsche requires 12 times and augmented Lagrangian 1.5 times the total simulation time of penalty. This indicates that although the per-iteration cost is relatively similar across methods, the total computational cost is significantly higher for augmented Lagrangian and specially for Nitsche.

Nitsche's method is computationally more expensive in terms of the assembly. This increased cost arises from the terms involving the first Piola-Kirchhoff stress tensor and its derivatives in the Jacobian. Additionally, the stress tensor calculations make Nitsche's method more difficult to implement compared to the other approaches and the contact formulation also depends on the chosen hyperelastic law. We also observed that Nitsche necessitates smaller time steps under high forces, significantly increasing computational time. In contrast, penalty and augmented Lagrangian avoid this complexity, leading to simpler and faster assembly of the residual and Jacobian. However, when it comes to solving the linear system within the Newton iterations, penalty and Nitsche may offer advantages over the augmented Lagrangian method, which introduces an additional unknown—the Lagrange multiplier—thereby increasing the system's size and potentially making the resolution of the linear system more computationally expensive.

In terms of accuracy, augmented Lagrangian and Nitsche's methods perform better in preventing penetration. Both methods offer a more physically realistic solution compared to the penalty method, where significant penetration is observed at higher forces. Additionally, the penalty method fails on handling forces beyond 50 mN due to the excessive penetration, whereas augmented Lagrangian and Nitsche's methods allow the simulations beyond 50 mN.

In conclusion, penalty offers the advantage of lower computational cost but shows penetration and limitations at higher forces. Augmented Lagrangian provides more accurate results without penetration and can handle higher forces, although it introduces an additional unknown, increasing the computational cost for solving the Newton's system. Nitsche's method, while accurate and capable of handling high forces, is the most computationally expensive.

Chapter 4

Comparison of Statistical, Machine Learning, and Mathematical modeling Methods to Investigate the Effect of Aging on Dog's Cardiovascular System

The aim of this chapter is to provide a preliminary comparison of different classes of methods to automatically detect the effect of aging from in vivo data. The application which motivated this work is related to safety pharmacology, whose major goal is to determine, in a pre-clinical phase, whether a drug is potentially dangerous for the health (Guns, 2020). In particular, we compare statistical, machine learning and mathematical modeling methods.

This work arose in the context of the CEMRACS 2021 summer school, and it is a collaboration with Elham Ataei Alizadeh (Boehringer Ingelheim Pharma GmbH & Co KG, Biberach an der Riss, Germany), Haibo Liu (Sorbonne Université, COMMEDIA team (Inria) and NOTOCORD, Paris, France), Damiano Lombardi (Sorbonne Université and COMMEDIA team (Inria), Paris, France) Sylvain Bernasconi (NOTOCORD, Paris, France), Pieter-Jan Guns (Laboratory of Physiopharmacology, University of Antwerp, Antwerp, Belgium) and Michael Markert (Boehringer Ingelheim Pharma GmbH & Co KG, Biberach an der Riss, Germany). The results presented in this chapter have been reported in:

- E. Ataei Alizadeh, S. Costa Faya, H. Liu, D. Lombardi, S. Bernasconi, P.-J. Guns, M. Markert. Comparison of statistical, machine learning, and mathematical modelling methods to investigate the effect of ageing on dog's cardiovascular system. *ESAIM: ProcS, 73: 2–27, 2023.* hal-03933957.

Contents

4.1 Introduction

This work has been motivated by some questions arising in safety pharmacology. Safety pharmacology studies are designed to identify and assess the potential clinical risk of undesirable drug properties before they enter clinical trials, as described in Redfern et al. (2002).

Many drug development processes must proceed through several stages to be sure for a product to be safe, efficacious, and has passed all regulatory requirements. The preclinical stage encompasses the use of *in vitro* and *in vivo* studies to develop a drug that can safely and effectively be administered for clinical trials. *In vivo* studies performed in animals are essential to drug development because they have the ability to evaluate the effects a drug has on a living organism. A particular care is taken in assessing adverse effects and drug-drug interactions that cannot be observed *in vitro* (Brake et al., 2017).

When an animal participates in an experiment in safety pharmacology studies, one can anticipate that the compound tested might have an effect on the organism. It is therefore essential to know when the animal can participate again in an experiment after a sufficient wash-out period. This is of particular importance in cross-over design studies (for details, the reader can refer to Chris Delaney and Suissa (2009)). Before an animal will be used in a study, it has to undergo clinical evaluation as well as physiological tests to monitor the condition its cardiovascular system. When these initial tests are successfully performed the particular animal can be labelled as "healthy" and participate in the experiment. Age is one of the factors that has an impact on the function of the cardiovascular system. The effect of age on cardiovascular function in laboratory dogs can be related to decreased blood flow, blood velocity, arterial compliance and distensibility, as well as increased ventricular systolic and diastolic stiffness as a result of prolonged duration of myocardial contraction phase (see Meurs et al. (1996), Paul-Emile Roy and George Rona (1976), and Templeton et al. (1979)). In this study, we test the capabilities of several methods to detect the effect of age using some cardiovascular data collected from laboratory dogs. In addition to detecting aging, we are interested in determining whether we can find unique individual fingerprints in the cardiovascular data of the dogs. Roughly speaking, this could provide some insight on whether aging might impact the interindividual variability.

Among all the questions that pharmacologists and physiologists have, we have tried to answer a pair of questions:

(Q_1) Can we assess if an animal is getting old? This question can be reformulated as follows: given its data at an initial time and assuming that its initial state is conforming to the experimental protocol how far its cardiovascular system is, at subsequent times, from this initial state?

(Q_2) Is it possible to identify an animal by its hemodynamic data by a computer algorithm?

Data about the cardiovascular activity of animals are available over several weeks taken by telemetry. For instance, each hour of recording can be a few gigabytes for each dog. Plus, there are variabilities across several weeks of recording. Therefore, it is necessary to use mathematical methods that can automatically analyze large data sets collected from those initial tests since it is not possible to analyze them manually.

This is a preliminary work to test different methods to answer these questions using a large data set from 4 dogs. Then, the methods can be verified and improved in future work.

4.1.1 Methods

Different viewpoints might be used to address these questions. In this work, we have compared statistical, machine learning, and mathematical modeling methods to analyze some *in vivo* cardiovascular data of 4 dogs. One of the main goals of the project is to assess which methods perform better on these kinds of tasks. In particular, we compare:

1. Statistical methods: Physiologists and pharmacologists typically use statistical methods. This technique involves extracting a set of features from the signals and analyzing them statistically. As a first step, we compute the empirical estimators mean, median, and other statistical criteria to determine if there is any significant difference between the cardiovascular function of young and old animals. Two-tailed Wilcoxon (Mann-Whitney) test is presented to assess the effect of age on the individual features. The final step in the analysis is the K-Means clustering (which could be interpreted as an unsupervised learning approach).

2. Machine learning: Given a database of signals and the outcome of the questions, we can build a map to learn a relationship between the data and the outcome. We use artificial neural networks, which are typical machine learning algorithms. They were used for instance in ECG analysis (Hosseini et al., 2006), cardiac arrhythmia prediction (Adams and Choi, 2012; Silipo and Marchesi, 1998), and drug safety studies (Basile et al., 2019; Shameer et al., 2018).

3. Mathematical modeling: By exploiting a priori information about the system, we build a set of equations to simulate the phenomenon under investigation. These equations provide a way to link observable quantities to the outcome. We use a parametric 0D model to simulate the global circulation (in the spirit of Liang and Liu

(2005); Mirramezani and Shadden (2020); Moulton et al. (2017); Segers et al. (1997); Gul et al. (2016); Gul and Bernhard (2017); Yu et al. (1998)). The parameters of the model, once calibrated, will make it possible to investigate the changes in the animals' cardiovascular system with age.

More precisely, we would like to analyze the advantages and disadvantages of each approach in terms of accuracy and computational cost.

4.1.2 Structure

In section 4.2 we have presented the experimental data set we have used. In section 4.3 we have described methods for analyzing the statistics. In section 4.4 we have explained the Multilayer Perceptron (MLP) method that was implemented to detect the aging of the dogs and distinguish the dogs. In section 4.5 we have presented the model for the left part of the heart coupled with a model of the global circulation and the obtained results after calibration. Finally, some conclusions are given in section 4.6.

4.2 Experimental Data

In this project, we have used cardiovascular data gathered from 4 dogs: two Beagles (Hexe and Happy) and two Labrador-mix mongrel dogs (Simba and Roxy), involved in safety pharmacology studies for several years. During the study, dogs are in pairs in a group housing system. The dogs are calm and in resting mode during the study. A placebo injection was given to the dogs one hour after the study began. In order to avoid the effects of animal excitability during this period, the data during administration time have been excluded. Water is available to them *ad libitum*, and meals are provided after the study period ends. While avoiding all disturbances on the conscious animals is not possible due to the natural environment, the laboratory team managed to minimize cardiovascular disruption during data collection by creating a calm and regular environment and avoiding any intrusion or potential impact.

The data are acquired by telemetry from awake and non-anesthetized animals for many hours (for more details, the reader can refer to Markert et al. (2018)). This data set includes values of the ECG, Arterial Pressure (AP), and Left Ventricular Pressure (LVP) signals, recorded every 2 milliseconds. For each dog, we had data corresponding to two different periods of the dogs' life: the first one when the dog was 6-7 years old (*Historical data*), the second one when it was 8-9 years old (*New data*). We used the cardiovascular data recorded when the animal was in a younger and "healthy" state (referred to as "Historical" data) to compare with the recently recorded data, helping to determine whether this particular animal is "healthy". Each data file includes a seven-hour continuous recording of a placebo cardiovascular safety pharmacology study (pharmacologically inactive substances (Flaten et al., 1999)).

Concerning the measurement of the arterial pressure, according to Fetics et al. (1999), the signal was sampled either by a catheter in the abdominal aorta or in the femoral artery. The LVP is measured by inserting a catheter connected to a fluid-filled transducer into

the left ventricle (Le et al., 2012). From each complete cardiac beat (which in dogs at rest is around 0.8 s), we have extracted 9 quantities (those choices of 9 quantities have been decided by the data provider). All these features have been done by Notocord-Hem™ software. Human supervision and some manual corrections were needed to ensure the features are correctly extracted (especially for ECG). From the ECG we compute (see figure 4.1):

1 QT interval in ms.

2 QRS interval in ms.

3 RR interval in ms.

4 PR interval in ms.

From the LVP signal we extract the following parameters:

5 Left ventricle systolic pressure, LVP systolic, measured in mmHg.

6 Left ventricle diastolic pressure, LVP diastolic, measured in mmHg.

7 Maximum of the left ventricular pressure, LVP dpdt(max), measured in mmHg s^{-1}.

From the AP signal we extract:

8 Systolic AP, measured in mmHg.

9 Diastolic AP, measured in mmHg.

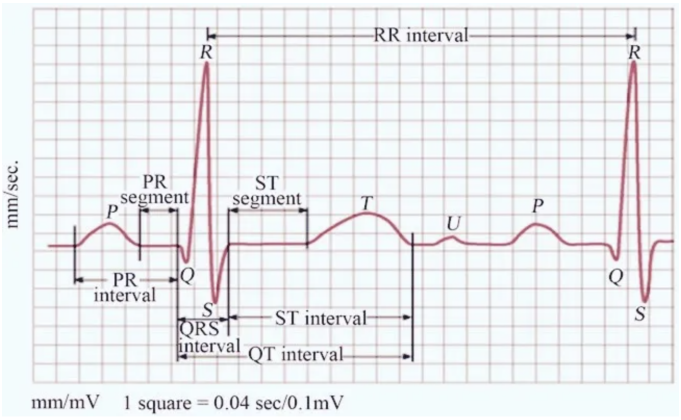

Figure 4.1: Cardiac parameter calculation from the raw ECG signal. See Branch (2014).

4.3 Statistical Analysis

In this section, we present the statistical analysis of the data. This has been performed by using solely the 9 features extracted from the telemetry data. In the next section, we present the methods that have been used and their results.

4.3.1 Methodology

The data set consists of 9 cardiovascular features for every cardiac beat for a total amount of 10887 beats for the young and old animals. We had, henceforth, roughly $N_s = 10^4$ samples. The first analysis consists of computing the mean, first quartile, median, third quartile, and standard deviation for each feature individually by using empirical estimators. Due to the distribution-free nature of the data, a Mann-Whitney U test with a significance level of 0.05 was performed to confirm the results and interpretation provided by the statistical moments estimated (in the spirit of Singh et al. (2015)). The goal was to understand whether age is influencing the features, individually. In Mann-Whitney test, the U_1 and U_2 values were computed as

$$U_1 = n_1 n_2 + n_1(n_1 + 1)/2 - R_1,$$

$$U_2 = n_1 n_2 + n_2(n_2 + 1)/2 - R_2.$$

In these formulas, n_1 and n_2 represent the sample sizes for the "Historical" sample and the "New" sample, and R_1 and R_2 represent the sum of the ranks for the "Historical" and the "New" cardiovascular sample, respectively.

As a second method, K-Means clustering has been used in order to determine whether cardiovascular functionality is unique and how age can affect this function (the reader is referred to Jain et al. (1999); MacKay (2003)). This algorithm was used to identify homogeneous subgroups within the data, such that the data points within each cluster are as similar as possible based on euclidean-based distance. Prior to applying the method, we have normalized the feature values and mapped them into the unit hypercube $[0, 1]^d$. As a similarity metric, we have used the standard $\ell^{2,d}$ norm (the Euclidean distance in renormalized space). The d value for this study is equal to 9 because we have nine cardiovascular features. The way to assign data points to clusters is to compute the squared distance between them and the cluster centroid (arithmetic mean of all the data points in a cluster) at a minimum.

To perform several tests with different purposes using the K-Means algorithm, we specify a different number of clusters that is estimated in all cases using the clustering gap method, based on Tibshirani et al. (2001). Let $k \in \mathbb{N}$ be the number of clusters, we denote the Euclidean distance between two points D_r, the sum of all pairwise distances would be: $W_k = \sum_{r=1}^{k} \frac{1}{2n_r} D_r$. The gap statistic is defined as:

$$\mathrm{Gap}_n(k) = E_n^*\{\log(W_k)\} - \log(W_k),$$

where E_n^* is the expectation under a sample of size n from the reference distribution. Gap statistic is computed to estimate the most optimized K for clustering. The number of K is selected based on the overall behavior of uniformly drawn samples, where the greatest jump in within cluster distance occurred. For each number of clusters k, the algorithm compares $\log(W(k))$ with $E_n^*\{\log(W_k)\}$ where the latter is defined via bootstrapping (Davidson and Satyanarayana, 2003). To eliminate the sampling noise from the data, the optimal K value will only be determined if the change is larger than the others. Figure 4.3 illustrates how K-Means clustering can estimate that we have two different data sets for the first data union of "Historical" and "New" data of one dog as an example.

As a first step, we have considered, as a data set, the union of the "Historical" and "New" data for each dog. As the second data union, we have shuffled all the cardiovascular data of the dogs in both "Historical" and "New" data. W_k has been used to measure the pertinence of the results derived from K-Means on this database.

In order to determine whether age dominates variability within an individual dog to a greater or lesser extent, we divided the first data union into two and the second data union into four groups.

4.3.2 Results from Statistical Analysis

For each cardiovascular feature, we have made box-plot charts to compare the changes over time between "Historical" and "New" data for each dog in order to dynamically analyze the effect of aging on each cardiovascular characteristic. Figure 4.2 shows the box-plot charts[1] of the overall QT interval comparison between dogs as an example of the statistical calculation based on ECG features.

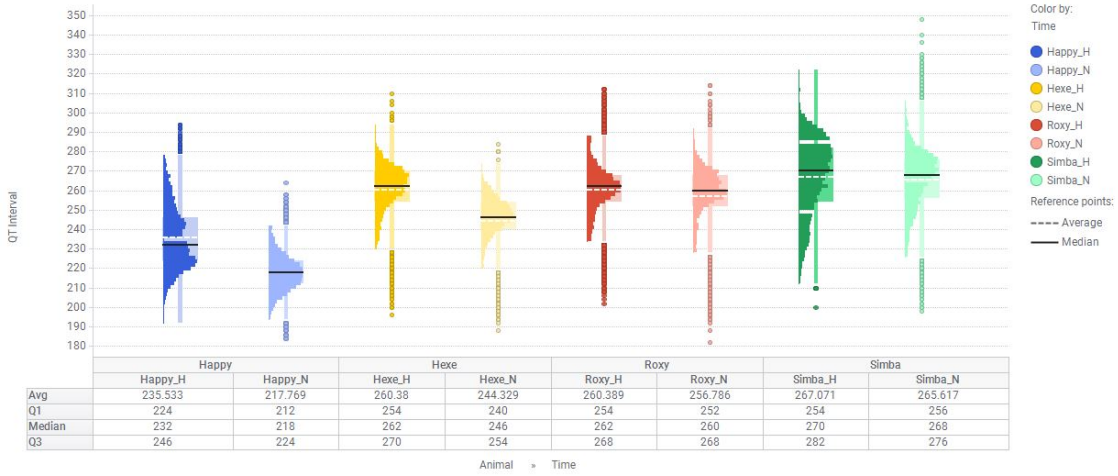

	Happy		Hexe		Roxy		Simba	
	Happy_H	Happy_N	Hexe_H	Hexe_N	Roxy_H	Roxy_N	Simba_H	Simba_N
Avg	235.533	217.769	260.38	244.329	260.389	256.786	267.071	265.617
Q1	224	212	254	240	254	252	254	256
Median	232	218	262	246	262	260	270	268
Q3	246	224	270	254	268	268	282	276

Figure 4.2: QT interval overview of all the dogs at two different ages.

4.3.2.1 Results answering Q_1

It has been found that the Mann-Whitney analysis has confirmed that aging has a significant effect, which has a large and detectable impact on each cardiovascular feature as they relate to aging. These results are presented in Table 4.1.

To answer Q_1, we have provided Table 4.2 that shows the impact of aging on each of our dogs on a case-by-case basis. In order to gain a clearer understanding of the extent to which each dog has been affected by aging over time, it is necessary to average out the changes between "Historical" and "New" data. It has been observed that Simba's cardiovascular data has remained relatively stable over time. The cardiovascular feature

[1] All the charts have been drawn by TIBCO Spotfire® platform.

Cardiovascular Features	Happy		Simba		Roxy		Hexe	
	U value	p-value	U value	p-value	U value	p-value	U value	p-value
LVP Systolic	$6.19 \cdot 10^{7}$	$2.2 \cdot 10^{-16}$	$2.83 \cdot 10^{7}$	$5 \cdot 10^{-3}$	$4.44 \cdot 10^{7}$	$2.2 \cdot 10^{-16}$	$4.64 \cdot 10^{7}$	$2.2 \cdot 10^{-16}$
LVP Diastolic	$1.89 \cdot 10^{7}$	$2.2 \cdot 10^{-16}$	$1.78 \cdot 10^{7}$	$2.2 \cdot 10^{-16}$	$4.82 \cdot 10^{6}$	$2.2 \cdot 10^{-16}$	$1.56 \cdot 10^{7}$	$2.2 \cdot 10^{-16}$
LVP dpdt(max)	$7.47 \cdot 10^{7}$	$2.2 \cdot 10^{-16}$	$2.95 \cdot 10^{7}$	$18 \cdot 10^{-15}$	$3.29 \cdot 10^{7}$	$1.4 \cdot 10^{-4}$	$1.08 \cdot 10^{8}$	$1.4 \cdot 10^{-4}$
QT duration	$7.51 \cdot 10^{7}$	$2.2 \cdot 10^{-16}$	$3.04 \cdot 10^{7}$	$2.2 \cdot 10^{-16}$	$3.27 \cdot 10^{7}$	$1.4 \cdot 10^{-3}$	$9.39 \cdot 10^{7}$	$2.6 \cdot 10^{-2}$
PR duration	$4.42 \cdot 10^{7}$	$1 \cdot 10^{-4}$	$3.17 \cdot 10^{7}$	$2.2 \cdot 10^{-16}$	$2.11 \cdot 10^{7}$	$2.2 \cdot 10^{-16}$	$5.66 \cdot 10^{7}$	$2.2 \cdot 10^{-16}$
RR duration	$5.65 \cdot 10^{7}$	$2.2 \cdot 10^{-16}$	$2.82 \cdot 10^{7}$	$1.1 \cdot 10^{-2}$	$2.39 \cdot 10^{7}$	$2.2 \cdot 10^{-16}$	$6.29 \cdot 10^{7}$	$2.2 \cdot 10^{-16}$
QRS duration	$3.39 \cdot 10^{7}$	$2.2 \cdot 10^{-16}$	$2.53 \cdot 10^{7}$	$2.2 \cdot 10^{-16}$	$4.97 \cdot 10^{6}$	$2.2 \cdot 10^{-16}$	$6.78 \cdot 10^{7}$	$2.2 \cdot 10^{-16}$
AP Systolic	$8.25 \cdot 10^{7}$	$2.2 \cdot 10^{-16}$	$3.96 \cdot 10^{7}$	$2.2 \cdot 10^{-16}$	$5.39 \cdot 10^{6}$	$2.2 \cdot 10^{-16}$	$4.98 \cdot 10^{7}$	$2.2 \cdot 10^{-16}$
AP Diastolic	$1.93 \cdot 10^{7}$	$2.2 \cdot 10^{-16}$	$4.01 \cdot 10^{7}$	$2.2 \cdot 10^{-16}$	$6.02 \cdot 10^{7}$	$2.2 \cdot 10^{-16}$	$4.36 \cdot 10^{7}$	$2.2 \cdot 10^{-16}$

Table 4.1: Two-tailed Mann-Whitney U test to determine the effects of aging on each dog cardiovascular features.

values of Roxy are opposite to the ones of Happy and Hexe (we should also note that Happy and Hexe are Beagles, while Simba and Roxy are Mongrels).

Name	**Data**	**LVP**			**Duration**				**AP**		**Average**
		Systolic	**Diastolic**	**dpdt(max)**	**QT**	**PR**	**RR**	**QRS**	**Systolic**	**Diastolic**	
Happy	Historical	130.73	-4.63	3173.83	232	126	708	40	136.52	90.79	
	New	125.61	-1.83	2746.58	218	126	572	42	123.62	104.47	
	New-Historical	-5.12	2.8	-427.25	-14	0	-136	2	-12.9	13.68	-64.0877
Simba	Historical	114.86	0.48	2075.2	270	114	1256	40	131.99	86.23	
	New	115.72	2.19	2075.2	268	112	1258	40	122.53	76.64	
	New-Historical	0.86	1.71	0	-2	-2	2	0	-9.46	-9.59	-2.0533
Roxy	Historical	98.75	-3.66	1434.33	262	120	1010	46	104.93	81.22	
	New	90.69	1.7	1403.81	260	128	1228	60	92.03	62.83	
	New-Historical	-8.06	5.36	-30.52	-2	8	218	14	-12.9	-18.39	19.2766
Hexe	Historical	117.55	-4.63	3021.24	262	122	978	44	128.62	84.32	
	New	120.48	1.586	2136.23	246	120	832	42	130.21	89.66	
	New-Historical	2.93	6.216	-885.01	-16	-2	-146	-2	1.59	5.34	-114.9926

Table 4.2: Total median of "Historical" and "New" cardiovascular data parameter for per each animal and their comparison.

In the next step, K-Means clustering was performed on the merged "Historical" and "New" data sets for each dog (independently) in order to determine whether aging can comprehensively change the cardiovascular characteristics of individual animals. To avoid over-fitting, data points were grouped into chunks, and for each cardiovascular feature the median of 100 data points was computed.

As a positive outcome of the K-Means clustering test, the data were roughly clustered according to age. The number of samples that fall into the wrong cluster was computed by assuming "Historical" data are labeled cluster 1 and "New" data are labeled cluster 2. The evaluation of the results of this clustering has been shown in Table 4.3. This table shows the rates of wrong labeled K-Means clustering for each animal in each cluster of "Historical" and "New". Regarding this table, the accuracy of K-Means clustering for distinguishing "Historical" and "New" data of Happy, Simba, Roxy, and Hexe are, respectively, 77%, 52%, 87%, and 94%.

	Wrong labeled / Cluster		
	"Historical" data	"New" data	Total data
Happy	45/106 = 0.42	0/86 = 0	45/192 = 0.23
Simba	52/84 = 0.61	20/66 = 0.30	72/150 = 0.48
Roxy	7/78 = 0.09	15/82 = 0.18	22/160 = 0.13
Hexe	0/105 = 0	14/103 = 0.13	14/208 = 0.06

Table 4.3: K-Means cardiovascular clustering of one animal in different ages.

4.3.2.2 Results answering Q_2

To check if it is possible to identify an animal by its hemodynamic data and answering Q_2, we have considered a data set containing data from two dogs. The purpose of this test is to examine inter- and intra-dog variability in order to determine if age is more relevant than individual cardiovascular characteristics. The input data was the union of 4 data sets, two dogs in two different ages. As soon as the data set is divided into two clusters by the K-Means algorithm, it is automatically divided by two individual animals' cardiovascular data. This result illustrates that each individual animal has unique cardiovascular characteristics. As shown in Table 4.4, K-Means clusters the cardiovascular data of each individual dog. The average number of total incorrect classifications was 16 percent, which indicates an 84 percent success rate for distinguishing cardiovascular data between two individual dogs. The K-Means clustering method is thus capable of recognizing differences in age, individual animals, and individual files (each animal in each age group) with acceptable accuracy. Let us point out that if the number of clusters increases, or if the age, gender, and strain of animals are similar, then the accuracy of the K-Means clustering is reduced.

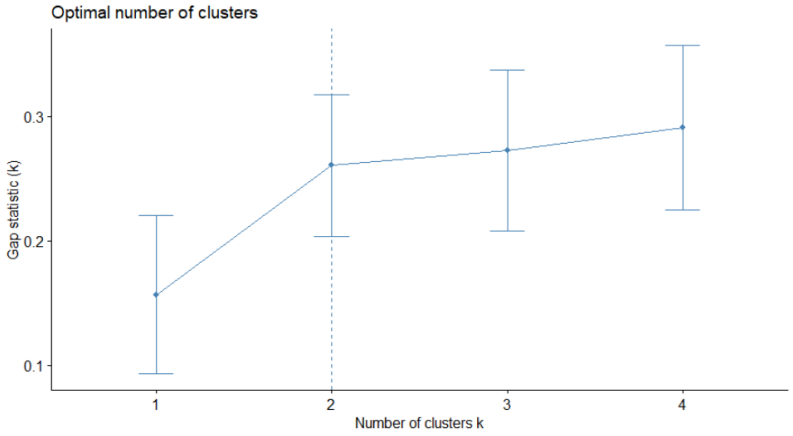

Figure 4.3: K-Means clustering indicates the optimal number of clusters using gap for "Historical" and "New" data combination file for one dog. Gap is within cluster distance, and number of cluster is considering possible cluster number.

	Wrong labeled / Cluster		
Happy-Simba	Happy	Simba	Total
	22/192 = 0.11	20/150 = 0.13	42/342 = 0.12
Happy-Roxy	Happy	Roxy	Total
	0/192 = 0	16/160 = 0.1	16/352 = 0.04
Happy-Hexe	Happy	Hexe	Total
	53/192 = 0.27	38/208 = 0.18	91/400 = 0.22
Simba-Roxy	Simba	Roxy	Total
	0/150 = 0	46/160 = 0.28	46/310 = 0.14
Simba-Hexe	Simba	Hexe	Total
	45/150 = 0.3	75/208 = 0.36	120/358 = 0.33
Roxy-Hexe	Roxy	Hexe	Total
	46/160 = 0.28	0/208 = 0	46/368 = 0.12

Table 4.4: K-Means cardiovascular clustering of two animals in different ages.

4.4 Machine Learning Analysis

Considering the answer to Q_1, we would like to detect if the dogs are still healthy by comparing the "Historical" with the "New" data. We can see this problem either as a binary classification or a semi-supervised learning problem. Firstly, we have considered a binary classification. For each dog, the input consists of the set of cardiovascular features introduced in section 4.2. Given these features, we would like to determine if they were recorded at the younger age (class 0) or at the older age (class 1) for each dog separately. If we get a high classification score, we would conclude that their health conditions have changed. Otherwise, we would consider that they have a similar health condition as when they were young. We have used an MLP to perform this classification.

Secondly, if we consider the aging assessment as a semi-supervised learning problem, we could use a Replicator Neural Networks (RNN) method on the cardiovascular signals. RNN is usually set up to perform anomaly detection in Hawkins et al. (2002): the RNN takes the raw signals as input and tries to reconstruct the input itself, as usually done in autoencoders Karpinski et al. (2018). In the present context, this would translate as follows: we train an RNN model on the "Historical" signals (normal case). Then we can use trained RNN to reconstruct test samples from "Historical" and "New" signals. By comparing the errors in the reconstructions, we would like to be able to classify whether the signal is coming from a young or old animal. Due to the small changes in the signals and the variabilities between signals, the RNN method is not very successful in performing the detection of dogs' age effects and for sake of brevity, we will not discuss any further the results in this chapter.

Moreover, we would also like to see if we can distinguish 4 dogs by using their cardiovascular features (answering Q_2). We can view this question as a multi-class classification problem (see Bisong (2019)). We have tried to classify each dog to see if they are accurately classified in their class[2].

[2]All the Machine Learning models were implemented in Python using *TensorFlow*™.

4.4.1 MLP Method used to Analysis *In vivo* Data

In this section, we tested MLP to answer Q_1 and Q_2. According to Yan et al. (2006), MLP is one of the most commonly used artificial neural networks in medical decision support, aiding in the analysis of cardiovascular data. MLP consists of multiple layers which include the input layer to receive the features, several hidden layers which are the true computational engines of the MLP, and an output layer that produces a decision or prediction results. MLP is often applied to supervised learning problems especially binary classification.

We can train a set of hidden parameters of MLP that are able to learn the relationships between input-output. Then, the trained parameters can be optimized by Back-propagation which computes the gradient of the loss/error with respect to the weights in the network.

We have trained an MLP to discriminate between the "Historical" and "New" state of 4 dogs to answer the first question. "Historical" and "New" data correspond the two classes in the binary classification task. "Historical" and "New" data are mixed in the model training phase. We have used the data set consisting of around 10000 samples of cardiovascular features for each state of each dog to train the MLP model.

Those features are normalized using $MinMaxScaler$, explained in Raju et al. (2020). We have used 80% of the samples to train and validate (with cross validation), and 20% of samples to test the MLP model. Our MLP model consists of 3 fully connected hidden layers, which have 9, 6, and, 3 hidden units. The first hidden layer receives 9 cardiovascular features (LVP Systolic, LVP Diastolic, LVP dpdt(max), RR interval, PR duration, QT interval, QRS duration, AP Systolic, AP Diastolic). The outputs from each hidden layer are transformed by a ReLU function and the results in the output layer will be transformed to a decision boundary by a *sigmoid* function.

4.4.2 Results from MLP Method Answering Q_1

To evaluate the performance of the MLP method, we have computed the success rate which is defined as the number of correctly predicted samples divided by the total number of samples of the dogs as in Table 4.5. We have high success rates, 98.24%, 87.40%, 97.81%, and 98.33% to discriminate between the "Historical" and "New" state of our 4 dogs. As Simba has the lowest success rate than other dogs, maybe Simba has fewer changes in its cardiovascular performance compared to the other 3 dogs.

	Happy	Simba	Roxy	Hexe
Success Rate	98.24%	87.40%	97.81%	98.33%

Table 4.5: Results from MLP model to discriminate "Historical" and "New" state of the dogs.

4.4.3 Results from MLP Method Answering Q_2

We also would like to check if we can identify a dog by using an MLP, to perform a multi-class classification. According to de Carvalho and Freitas (2009), multiclass classification

makes the assumption that each sample is assigned to one and only one label. We have labelled 4 classes Happy, Simba, Roxy, and Hexe. If there are significant differences in their cardiovascular features for each dog, we expect the model will have a high score to label them correctly, which means we can identify a specific dog among the 4. In the multi-class classification, we have used the same cardiovascular features as input. The difference between MLP used for binary classification and multi-class classification is in the output layer, the number of outputs being equal to the number of classes and the results will be transformed by a *softmax* function. In the training and testing phase, only "Historical" data of 4 dogs were used to train and test the multi-class classification model. From the results reported in figure 4.4, we can conclude that over 93% of the time, we can identify one dog among 4 dogs and 7% of the time, we miss identifying the dog.

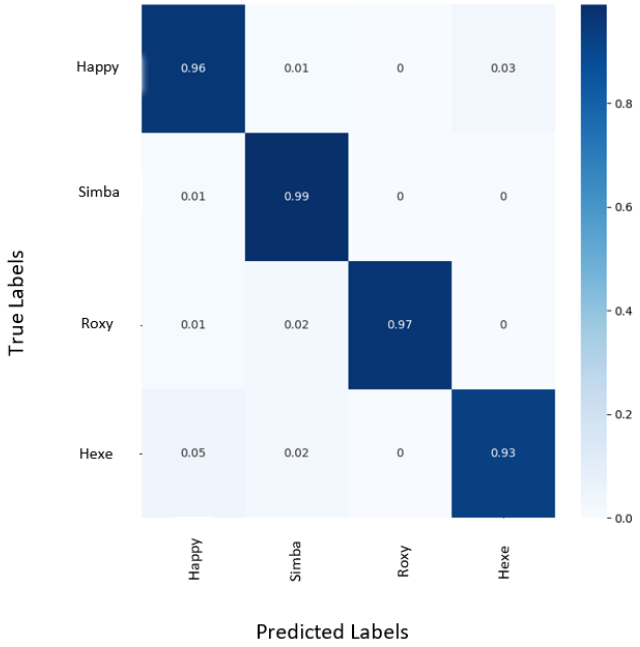

Figure 4.4: Classification results for identifying dogs using MLP method.

4.5 Mathematical Modeling Analysis

In this part of the project, we have considered a 0D model (concerning 0D models the reader is referred to Liang and Liu (2005); Mirramezani and Shadden (2020); Moulton et al. (2017); Segers et al. (1997); Gul et al. (2016); Gul and Bernhard (2017); Yu et al. (1998)) for the left part of the heart coupled to systemic circulation which makes it possible to describe the main observable hemodynamics quantities and their evolution in time. Once the data are reproduced, we can calibrate the model by estimating the values of the parameters. The calibration is performed for the "Historical" state and for the "New" state of the animal and the values for the parameters in each situation will help to assess if the dog has changed significantly with age.

4.5.1 Analog Circuit Model for the Left Ventricle

The heart beat (concerning the physiology the reader is referred to Thiriet and Parker (2009)) is a two stage pumping action over a period of about one second subdivided in 2 stages: systole and diastole. During systole, the pressure in the left ventricle increases, exceeding the left atrium pressure. Then the mitral valve closes, the aortic valve opens, and the blood flows into the aorta and out to the rest of the body. In diastole, the rate of contraction of the myocardium begins to slow and the aortic valve closes. When the ventricle relaxes, the pressure in the left ventricle falls and when it decreases below the pressure in the left atrium, the mitral valve opens and this lets blood flow from the left atrium to the ventricle.

The goal is to build a 0D model of the left part of the heart coupled to system circulation by an electrical analogy (Lafta and Hassanain, 2008). The 0D electric circuit model (see Yu et al. (1998)) for the left ventricle is shown in figure 4.5.

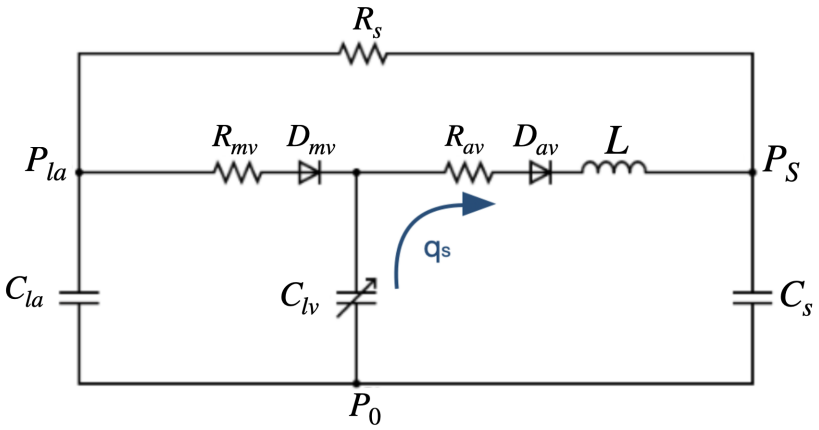

Figure 4.5: Electric circuit model.

The valves are represented by diodes in series with a resistor: R_{mv} and D_{mv} for the mitral valve and R_{av} and D_{av} for the aortic valve and R_s is the resistance of systemic circulation. The coil L represents the inertia of blood in the aorta. The compliance of the left atrium and systemic circulation are represented by C_{la} and C_s, respectively. We have used a time-varying left ventricular compliance $C_{lv}(t)$ to represent the action of the heart muscle. The elastance $E(t)$ is the reciprocal of the compliance ($E(t) = 1/C_{lv}(t)$) and it represents the contractile state of the left ventricle. It relates to the ventricle's pressure and volume (detailed in Suga and Sagawa (1974)) according to the expression:

$$E(t) = \frac{P_{lv}(t)}{V_{lv}(t) - V_0},$$

where $P_{lv}(t)$ is the left ventricular pressure, $V_{lv}(t)$ is the left ventricular volume and V_0 is a reference volume. The time variations in this model are due to the cyclical nature of the ventricle elastance which changes as a function of time within one cardiac cycle. In our

case, we are using the ECG to model the activation of the ventricle and, more precisely, the peaks of the QRS complex. The QRS complex (see figure 4.1) corresponds to the electrical forces generated by ventricular depolarization and represents the pumping action of the ventricles. From the ECG, we save the times at which the R peaks of the QRS complex occur and this is what we call the *activation times* of the ECG.

We approximated $E(t)$ by the following expression:

$$E(t) = \sum_{k=1}^{m} a \cdot [\tanh[b \cdot (t - w_k)] - \tanh[b \cdot (t - w_k - d)]] + h,$$

where $m \in \mathbb{N}^*$, a, b, d and h are constants, $t \in \mathbb{R}$ is the time and $w \in \mathbb{R}^m$ are the activation times of the ECG.

In order to get the equations for the circuit, three different cases have been considered:

- **Case 1: Filling.** The mitral valve is **opened** and the aortic valve is **closed**, so the left ventricle is being filled.
- **Case 2: Ejection.** The mitral valve is **closed** and the aortic valve is **opened**, so blood is being ejected from the left ventricle.
- **Case 3: Isovolumic phase.** Both valves are **closed** and the capacitor has either just being filled (isovolumic contraction) or emptied (isovolumic relaxation).

Each phase of the left ventricle's operation can be modeled by a system of linear ordinary differential equations (ODEs). However, the entire system is nonlinear because each diode has two states, leading to three different cases: the first diode is on and the second is off, the first diode is off and the second is on, or both diodes are off. Each case is modeled by a different equivalent circuit since, when a diode is off, it acts as an open circuit, and when it is on, it behaves as a short circuit.

The system of ODEs has been derived by applying Kirchhoff's Current Law and Ohm's Law (the reader is referred to Dorf and A. Svoboda (2006) for an overview on the topic) to the analog circuit model as follows:

CASE 1: If $P_{la}(t) > P_{lv}(t)$ and $P_{lv}(t) < P_s(t)$

For the first node, with left atrial pressure (LAP) $P_{la}(t)$, we have that

$$C_{la}\frac{dP_{la}}{dt} = \frac{P_{lv} - P_{la}}{R_{mv}} - \frac{P_{la}}{R_s}.$$

For the one in the middle with value $P_{lv}(t)$

$$C_{lv}\frac{dP_{lv}}{dt} + P_{lv}\frac{dC_{lv}}{dt} - P_0\frac{dC_{lv}}{dt} = \frac{P_{la} - P_{lv}}{R_{mv}},$$

and since $E_{lv}(t) = 1/C_{lv}(t)$, we can rewrite the previous expression as

$$\frac{dP_{lv}}{dt} = E\left(\frac{P_{la} - P_{lv}}{R_{mv}}\right) + \frac{P_{lv}}{E}\frac{dE}{dt} - \frac{P_0}{E}\frac{dE}{dt},$$

where $P_0 \in \mathbb{R}$ is just a reference value. Then, for the node on the right, with arterial pressure $P_s(t)$,

$$C_s \frac{dP_s}{dt} = \frac{P_{la} - P_s}{R_s},$$

and, for the aortic flow $q_s(t)$

$$\frac{dq_s}{dt} = 0.$$

The system of equations for the filling phase is then

$$\begin{cases} C_{la}\dfrac{dP_{la}}{dt} &= \dfrac{P_{lv} - P_{la}}{R_{mv}} - \dfrac{P_{la}}{R_s}, \\ \dfrac{dP_{lv}}{dt} &= E\left(\dfrac{P_{la} - P_{lv}}{R_{mv}}\right) + \dfrac{P_{lv}}{E}\dfrac{dE}{dt} - \dfrac{P_0}{E}\dfrac{dE}{dt}, \\ C_s\dfrac{dP_s}{dt} &= \dfrac{P_{la} - P_s}{R_s}, \\ \dfrac{dq_s}{dt} &= 0. \end{cases}$$

CASE 2: If $P_{lv}(t) > P_{la}(t)$ and $P_{lv}(t) > P_s(t)$

Proceeding in an analogue way, we get the following system of ODEs

$$\begin{cases} C_{la}\dfrac{dP_{la}}{dt} &= \dfrac{P_s - P_{la}}{R_s}, \\ \dfrac{dP_{lv}}{dt} &= \dfrac{P_{lv}}{E}\dfrac{dE}{dt} - Eq_s - \dfrac{P_0}{E}\dfrac{dE}{dt}, \\ C_s\dfrac{dP_s}{dt} &= \dfrac{P_{la} - P_s}{R_s} + q_s, \\ \dfrac{dq_s}{dt} &= \dfrac{P_{lv} - P_s}{L} - \dfrac{q_s}{L}R_{av}. \end{cases}$$

CASE 3: If $P_{lv}(t) > P_{la}(t)$ and $P_{lv}(t) < P_s(t)$

In this case, both valves are closed (both diodes are off) and there is no current flow. Then the equations are

$$\begin{cases} C_{la}\dfrac{dP_{la}}{dt} &= \dfrac{P_s - P_{la}}{R_s}, \\ \dfrac{dP_{lv}}{dt} &= \dfrac{P_{lv}}{E}\dfrac{dE}{dt} - \dfrac{P_0}{E}\dfrac{dE}{dt}, \\ C_s\dfrac{dP_s}{dt} &= \dfrac{P_{la} - P_s}{R_s}, \\ \dfrac{dq_s}{dt} &= 0. \end{cases}$$

4.5.2 Results from Mathematical Modeling

To solve the equations in each case according to time we have used a backward differentiation formula (BDF) solver that is implemented in the Python built-in solver *odeint* (see Virtanen et al. (2020) and Hindmarsh and Petzold (2005) for more details). In order to solve the model, we need to give as **input** the parameters $(R_s, R_{mv}, R_{av}, C_a, C_s, L, P_0, a, h)$ and the peaks of the ECG. Then we get as **output** the LVP, the AP, the LAP and the aortic flow.

To obtain the optimized parameters for each dog we have used the Covariance Matrix Adaptation Evolution Strategy (CMA-ES) optimization algorithm that is implemented in Python in the *pycma* module (Hansen, 2016). We need to provide an initial estimation of the parameters and the experimental data for the AP, LVP and ECG as **input**. The initial standard deviation was set to $\sigma_0 = 0.4$, and we have used a population size 1000 times larger than the default value. The objective function needs also to be specified. We have chosen the following function to be minimized

$$J = \sqrt{\sum_{i=1}^{n} \left| P_{lv}^{(i)} - \hat{P_{lv}}^{(i)} \right|^2 + \left| P_s^{(i)} - \hat{P_s}^{(i)} \right|^2},$$

where $P_{lv}^{(i)}$ is the experimental value of the left ventricle pressure at each time, $\hat{P_{lv}}^{(i)}$ is the predicted value of the left ventricle pressure at each time, $P_s^{(i)}$ is the experimental value of the arterial pressure at each time, $\hat{P_s}^{(i)}$ is the predicted value of the arterial pressure at each time and $n \in \mathbb{N}^*$.

The **output** of the CMA-ES algorithm are the optimized parameters of the model.

4.5.2.1 Results answering $\mathbf{Q_1}$

For each dog, we have estimated the parameters for the "Historical" and "New" state. Table 4.6 shows the optimized model parameters for each dog at both times. The solution of the model for its corresponding parameters for each dog is plotted in figures 4.6, 4.7, 4.8 and 4.9. Although the heart pace can look irregular in figures 4.6-4.9, the signal cannot be considered arrhythmia since dogs have a pronounced vagal tone which leads to this "normal" abnormal rhythm and this has no clinical relevance.

We computed the difference between the values predicted by our model and the values observed. For that purpose, we identified the local maxima of the LVP and computed the difference between the real signal and the simulated one at each peak (local maxima) for the LVP. The relative error is

$$\xi(P_{lv}) = \sqrt{\frac{\frac{1}{n}\sum_{i=1}^{n}(y_i - \hat{y}_i)^2}{\frac{1}{n}\sum_{i=1}^{n}(y_i)^2}},$$

where y is the value of the pressure at each peak in the true signal, $\hat{y}$ is the value in the predicted signal and $n \in \mathbb{N}^*$. For the AP we have taken into account not only the difference between maxima, but also the one between minima

$$\xi(P_s) = \sqrt{\frac{\frac{1}{n}\sum_{i=1}^{n}(y_i - \hat{y}_i)^2}{\frac{1}{n}\sum_{i=1}^{n}(y_i)^2}} + \sqrt{\frac{\frac{1}{n}\sum_{i=1}^{n}(w_i - \hat{w}_i)^2}{\frac{1}{n}\sum_{i=1}^{n}(w_i)^2}},$$

where w is the value of the pressure at each minimum peak in the true signal, $\hat{w}$ is the value of the pressure at each minimum peak in the predicted signal and $n \in \mathbb{N}^*$.

Parameters	Happy "H"	Happy "N"	Simba "H"	Simba "N"	Roxy "H"	Roxy "N"	Hexe "H"	Hexe "N"
R_s [mmHg · s/cm^3]	$1.62 \cdot 10^{-3}$	$1.20 \cdot 10^{-1}$	$8.06 \cdot 10^{-2}$	$2.67 \cdot 10^{-1}$	8.78	3.87	$1.45 \cdot 10^{-3}$	$6.26 \cdot 10^{-2}$
R_{mv} [mmHg · s/cm^3]	$2.06 \cdot 10^{-6}$	$1.75 \cdot 10^{-2}$	$5.12 \cdot 10^{-5}$	$1.47 \cdot 10^{-4}$	$1.26 \cdot 10^{-1}$	$1.12 \cdot 10^{-2}$	$7.02 \cdot 10^{-7}$	$7.38 \cdot 10^{-3}$
R_{av} [mmHg · s/cm^3]	$1.85 \cdot 10^{-5}$	$1.18 \cdot 10^{-3}$	$6.33 \cdot 10^{-4}$	$2.45 \cdot 10^{-3}$	$3.57 \cdot 10^{-4}$	$8.18 \cdot 10^{-4}$	$3.55 \cdot 10^{-6}$	$2.95 \cdot 10^{-4}$
C_a [cm^3/mmHg]	$3.65 \cdot 10^{4}$	7.01	$1.36 \cdot 10^{2}$	$5.18 \cdot 10^{1}$	$2.61 \cdot 10^{-1}$	1.72	$4.59 \cdot 10^{4}$	$1.0808 \cdot 10^{1}$
C_s [cm^3/mmHg]	$1.21 \cdot 10^{3}$	9.39	$2.99 \cdot 10^{1}$	9.27	$3.26 \cdot 10^{-1}$	$9.67 \cdot 10^{-1}$	$1.71 \cdot 10^{3}$	$1.63 \cdot 10^{1}$
L [mmHg · s^2/cm^3]	$1.68 \cdot 10^{-7}$	$9.18 \cdot 10^{-6}$	$1.11 \cdot 10^{-5}$	$5.26 \cdot 10^{-5}$	$1.98 \cdot 10^{-4}$	$1.60 \cdot 10^{-4}$	$6.30 \cdot 10^{9}$	$3.41 \cdot 10^{-6}$
P_0 [mmHg]	$1.66 \cdot 10^{4}$	$6.41 \cdot 10^{1}$	$3.05 \cdot 10^{3}$	$7.71 \cdot 10^{2}$	$1.63 \cdot 10^{-1}$	$9.52 \cdot 10^{-1}$	$2.25 \cdot 10^{3}$	$3.16 \cdot 10^{1}$
a [mmHg/cm^3]	$9.08 \cdot 10^{-3}$	$6.90 \cdot 10^{-1}$	$9.27 \cdot 10^{-2}$	$1.95 \cdot 10^{-1}$	$1.07 \cdot 10^{1}$	2.39	$5.36 \cdot 10^{-3}$	$2.87 \cdot 10^{-1}$
h [mmHg/cm^3]	$1.12 \cdot 10^{-2}$	0.00	$6.92 \cdot 10^{-2}$	$6.07 \cdot 10^{-2}$	$3.36 \cdot 10^{-3}$	$3.87 \cdot 10^{-3}$	$1.23 \cdot 10^{-3}$	$1.40 \cdot 10^{-6}$
Relative errors								
$\xi(P_s)$	10.83 %	10.56 %	6.39 %	9.39 %	5.22 %	8.53 %	10.13 %	9.51 %
$\xi(P_{lv})$	8.38 %	4.11 %	8.94 %	3.99 %	3.51 %	7.68 %	6.17 %	4.17 %

Table 4.6: Model parameters (from left to right) for Happy "Historical" (2015), Happy "New" (2018), Simba "Historical" (2018), Simba "New" (2021), Roxy "Historical" (2018), Roxy "New" (2021), Hexe "Historical" (2018) and Hexe "New" (2020). The relative error for the LVP and for the AP is also shown for each dog in both states ("Historical" and "New").

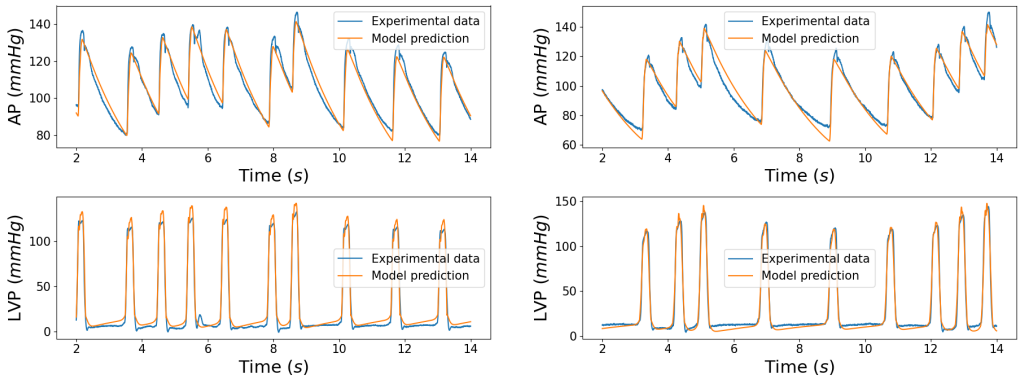

(a) AP and LVP for Simba 2018 ("Historical") (b) AP and LVP for Simba 2021 ("New")

Figure 4.6: Experimental data compared with the model prediction for Simba.

We want to address if the animals are getting old or not by the change in the parameters in the electrical model. To check that, we have made the following steps:

1. We have computed the optimized parameters of the model for each dog in the "Historical" state and also in the "New" state (they are shown in Table 4.6).

2. Afterwards, we have run the parameter optimization in the 0D model for each dog in the "New" state considering as initial guess the optimized parameters for the "Historical" state. The purpose of doing this is to see if having as initial test the parameters of the "Historical" state, the optimizer could find good values for the

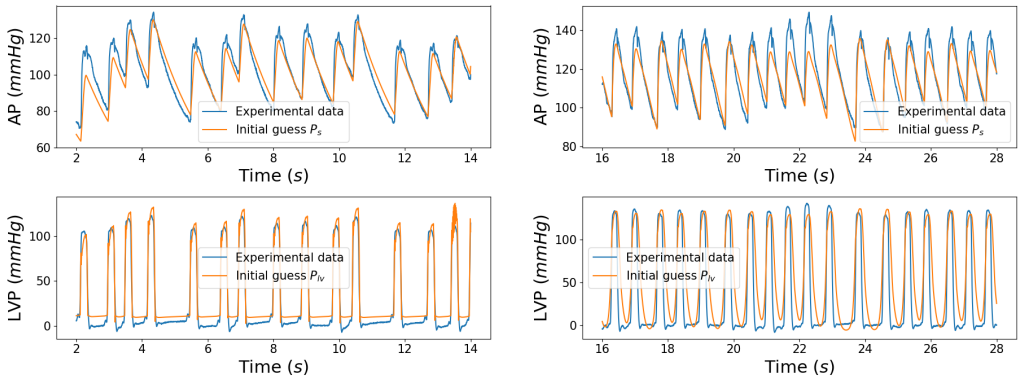

(a) AP and LVP for Happy 2015 ("Historical") (b) AP and LVP for Happy 2018 ("New")

Figure 4.7: Experimental data compared with the model prediction for Happy.

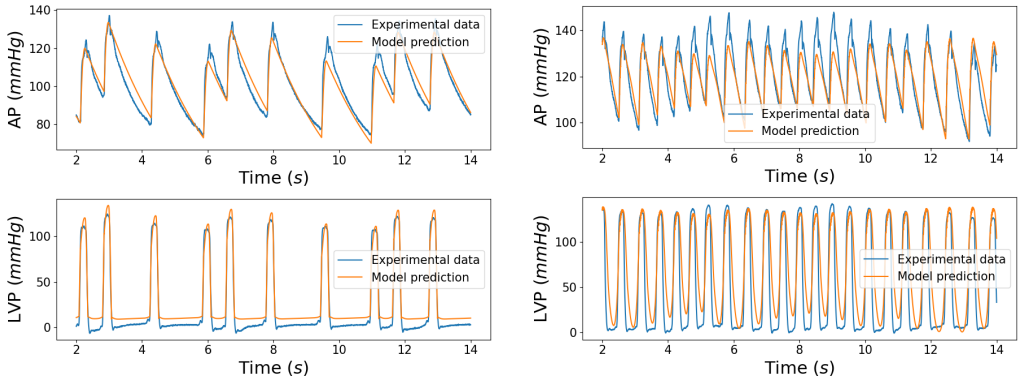

(a) AP and LVP for Hexe 2018 ("Historical") (b) AP and LVP for Hexe 2020 ("New")

Figure 4.8: Experimental data compared with the model prediction for Hexe.

"New" state. The model prediction after the optimization is shown in green in figure 4.10. The initial guess is shown in orange in the same figure.

3. We have also directly solved the model in the "New" state, with the parameters of the "Historical" state. The purpose is to see if we can match the real data in the "New" state with the optimized parameters of the "Historical" state (without running the optimization). This is plotted in figure 4.10 in orange.

After repeating the simulations for several chunks of beats, we have observed that Simba barely changes. With the optimized parameters in the "Historical" state we can reproduce the data in the "New" state. However, we have observed significant changes for Happy, Roxy and Hexe. In Happy and Hexe we have observed that as the dogs are getting older the resistance increase and the capacitance decrease as a general tendency. The capacitance gives us the ability of the vessels to get elastic and since the capacitance decrease, the vessels become less elastic with the years. On the contrary, we have observed in Roxy a different tendency. Roxy has experienced a decrease in the resistance and an

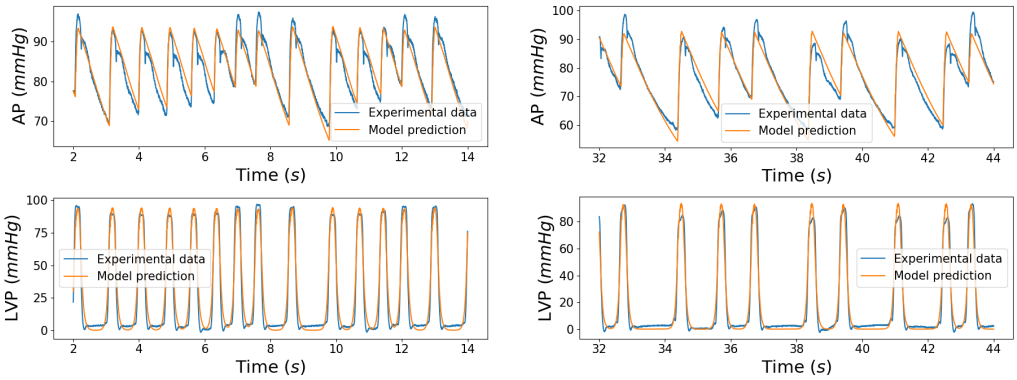

(a) AP and LVP for Roxy 2018 ("Historical") (b) AP and LVP for Roxy 2021 ("New")

Figure 4.9: Experimental data compared with the model prediction for Roxy.

increase in the capacitance which is the opposite behavior to that of in Hexe and Happy and may be interpreted that her condition has improved with age.

To answer properly Q_1, we need to set a threshold of the error that determines that the animal is changing with age. In other words, at which relative error do we claim that the "Historical" parameters do not fit the "New" state because the dog has changed? To establish that threshold, we have solved the model for each dog for several chunks with the parameters of Table 4.6. The maximum of the error that we got for each animal, is going to be our threshold to claim whether the dog experienced changes with age or not. The thresholds to determine if the model is fitting the data are 14% (Happy), 15% (Simba), 16% (Roxy) and 13% (Hexe).

To study the accuracy of the mathematical modeling method answering Q_1, we have solved the model for each dog with our calibrated parameters in other chunks of beats than the ones used for setting the threshold. First, we have considered chunks in the "Historical" state and we have used the "Historical" parameters to solve the model (same applies for the "New" state). If we get a relative error that is less than the threshold, then it means that the model has worked. But if we get a relative error that is bigger than the threshold, it means that the model suggests that the dog changed but it is a mistake since we are just using the calibrated "Historical" parameters but for a different chunk. We have repeated this computation for a certain number of chunks and we have computed the success rate (number of correctly predicted chunks divided by the total number of tested chunks), that was always higher than 95%.

Therefore, we can conclude that we are able to identify from the parameters if a dog is changing with age or not.

4.5.2.2 Results answering Q_2

The second question that we wanted to answer is if we can discriminate between dogs. If we look at the optimized parameters of the model that are shown in Table 4.6, we can see that they substantially change between different dogs. We have solved the model at a

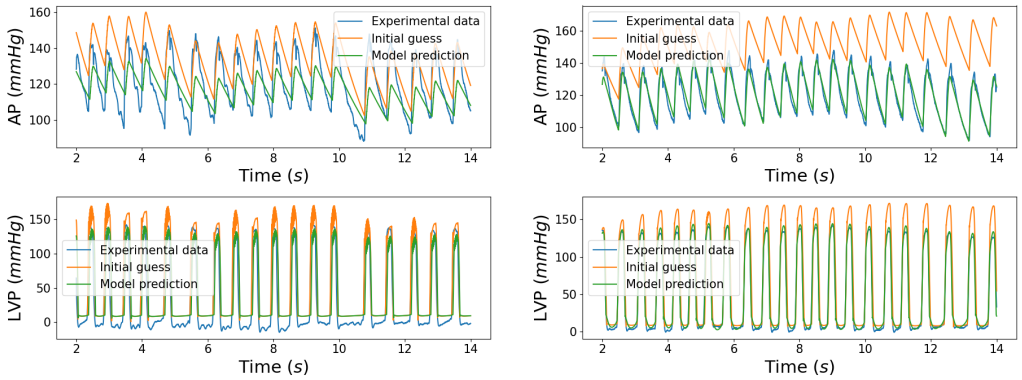

(a) AP and LVP for Happy 2018 starting with parameters of Happy 2015

(b) AP and LVP for Hexe 2020 starting with parameters of Hexe 2018

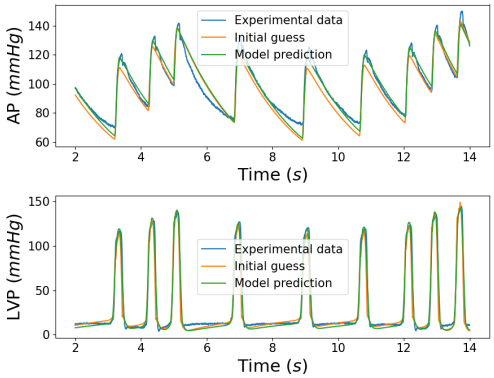

(c) AP and LVP for Simba 2021 starting with parameters of Simba 2018

Figure 4.10: Experimental data compared with the model prediction when we start the optimization from the optimized "Historical" parameters as initial guess.

given state ("New" or "Historical") with the data of a given dog but using the optimized parameters for the same state but for another dog. The result of doing that for every dog, was that the relative error in the left ventricular pressure ($\xi(P_{lv})$) was sometimes below the values of the thresholds but the value for the relative error in the arterial pressure ($\xi(P_s)$) was always above 32 % (higher than the thresholds).

Although it would be necessary to do the study with a larger number of chunks in order to withdraw a strong conclusion, it is already possible to spot some differences between the dogs since the calibrated parameters for one dog can never reproduce the data of a different one. Therefore, we can claim that it is possible to identify an animal by its hemodynamic data after doing the calibration of the model since with the optimized parameters of a dog, it is not possible to reproduce the data of another one.

4.6 Discussion

In this chapter, we have tried to analyze some *in vivo* experiments data for addressing the effect of aging in an animal by using statistical, machine learning and mathematical modeling methods. On the whole, we are able to identify some changes in dogs' cardiovascular data in the "New" state compared to the "Historical" state. Moreover, we can discriminate not only between "New" and "Historical" state of the dog, but also distinguish one dog among the others.

In terms of accuracy, cost, and robustness, we have compared the advantages and disadvantages of each method. Although the way how we answer the questions is very different in mathematical modeling and in statistical and machine learning approaches, we can set a link on how to compare the accuracy of the methods. With respect to the answer to question Q_1 in the statistical method, changes between the "New" and "Historical" state of cardiovascular data for each dog in a positive or negative direction are always measurable, as shown in the statistical results. However, the K-Means clustering method could recognize and cluster these changes for Happy, Simba, Roxy, and Hexe with an accuracy of 77%, 52%, 87%, and 94%, respectively. Machine learning method can correctly (above 97% for Happy, Roxy, and Hexe) distinguish between the "New" and "Historical" state of the dog. When "New" and "Historical" states are more similar for Simba, the error of the machine learning method would be higher (12.60%). Regarding mathematical modeling, we can see that the relative error between the values predicted by our model with the optimized parameters and the values observed, is typically below the thresholds. The accuracy of this approach was above 95%.

According to question Q_2, K-Means clustering accurately identified 84% of dogs among four cardiovascular data of two dogs of different ages. Machine learning method can identify one dog among 4 dogs with more than 93% accuracy. To test the accuracy of the identifiability of the dogs with the mathematical modeling approach, we had the same logic as the one with aging but we have tried the calibrated parameters of one dog on another dog and see if they could fit. It was never the case so the accuracy in this case is around 100%.

Regarding the cost and robustness, K-Means and MLP use the extracted cardiovascular features as input and they would require computational cost in the feature extraction process. Considering that the number of samples and the size of the input is not large, K-Means only takes very small computational cost. We could also train an MLP with high accuracy (above 93%) and very little training cost (less than 20 minutes). In particular, MLP is robust to beat-to-beat variability and provides a promising result for the above biological questions. Regarding the computational cost for mathematical modeling, it requires a light pre-processing of the data. Before running the optimization, the only thing we need to do is to extract the activation times of the ECG and this is almost instantaneous. However, the optimization process to obtain the parameters of the model takes on average 7 hours, although it depends a lot on the initial guess that we consider. Once we have the parameters, model integration in time is cheap from a computational point of view (few seconds). Regarding the robustness of the parameter estimation procedure in mathematical modeling, we have tried so far to run the model with the same parameters for other intervals

to see if we are able to reproduce other windows of time with the parameters fitted from one chunk. Usually, we are able to fit other time intervals if we do not go very far from the original one. It is also important to take into account that if the activity of the dog changes (if it is playing, eating, making digestion...) the parameters could change. In the future, we would like to get the model parameters for a larger number of chunks and analyze their variability of them in the "New" and "Historical" states in order to give a reliable interval for the parameters in each state and to have a better notion of the accuracy of this approach. The same applies for the identifiability of each dog in order to know what is the interval in which the parameters move in each dog. In fact, the parameters may significantly change between different dogs because it is possible that there are several combinations of parameters that fit the data. As stated before, it would be necessary to do a study with a larger set of chunks in order to analyze in detail the variability of the parameters. This will be the object of a further investigation. However, we could already spot differences between the animals based on the parameters (the parameters of a dog do not reproduce the data of another one). Regarding the aging process, it is also possible to assess if the dog is getting old (excluding Simba, we have shown that with the parameters of the "New" state we were not able to fit the data in the "Historical" state).

4.6.1 Limitations and perspectives

The limitation of the statistical algorithms is that when the number of animals is high or strains and genders of dogs are similar, the accuracy may decrease. Statistical methods are modelled using extracted features which require computational resources and the number and choices of features may have an impact on the analysis of the results (missing some information from the raw signals).

Similarly, MLP needs extracted features as input which other types of neural networks like Convolutional Neural Network (CNN) in Jun et al. (2018) do not. CNN can process and learn the important parameters from the signals directly to perform a binary classification. By using CNN, we can avoid the feature extraction process step. However, as the dimension of the signal data is usually high, the CNN method would need more training costs. We can also consider the autoencoder method calibrated by some cardiovascular features to do anomaly detection like in Dau et al. (2014) to perform a semi-supervised learning. In general, the neural network method has a "black box" nature. This method can't help us to understand the mechanism of dogs' cardiovascular system. So we won't be able to use it to answer some questions like how much and which element of cardiovascular function has changed. However, in a mathematical modeling approach, the parameters have a link with age which can give us some information related to how age changes cardiovascular functionality (that is to say if the dog gets older or younger). Moreover, if the number of dogs increases in the future, which means the number of classes also increases, the accuracy of correctly identifying the dogs decreases for machine learning and statistical methods. To test the neural network method and statistical method for a larger number of dogs, we need to find a training strategy that can include enough dogs and acceptable model accuracy. For the mathematical modeling method, it is necessary to do the optimization of the parameters for each dog in each state ("Historical" and "New") and this process takes

a lot of time. Consequently, if the number of dogs is high, it will be computationally very demanding in terms of time to answer the fore-mentioned questions.

From the future perspective, we would like to take into account the data of more dogs to test our methods. It is also very important from the mathematical modeling point of view to do the study with more chunks to be able to perform classification tasks on the parameters. We would also like to work on more experiments with different species and strains to gather more information about the effect of aging on cardiovascular performance. Discovering the impact factors on cardiovascular functionality helps us to understand the reason why some animals have more changes in their cardiovascular data by comparing with others.

Conclusions and perspectives

In this thesis, we have considered the modeling and numerical simulation of the effects of drugs on cardiovascular tissue, integrating experimental data within the context of safety pharmacology.

In Chapter 2, we introduced a mathematical model designed to capture both vasoconstriction and vasodilation, providing insight on the mechanical behavior of arterial segments and the role of smooth muscle cells (SMCs) in arterial stiffness. This model combines passive hyperelasticity with active SMC contributions to simulate vascular dynamics. Initially, we considered a 2D-shell model, but found that it was insufficient to fit the experimental data, as it did not account for variations across tissue thickness and did not allow the use of general hyperelastic laws. To circumvent these shortcomings, a 3D-shell model has been considered, using general 3D hyperelastic laws, particularly the Ogden model, to handle high forces and nonlinear strain-stress relationships. The motivation behind the mathematical model proposed in Chapters 2 and 3, is the simulation of an *ex vivo* setup called ROTSAC (Leloup et al., 2016), designed to study arterial stiffness. The ROTSAC experiment was mainly developed to study elastic behavior of aortic segments while stretched at physiological frequencies and amplitudes. We first considered a simplified geometry of the ROTSAC setup, based on its symmetry, that involved a single lateral side of the tissue mounted on the two parallel hooks, assumed to be flat in the stress-free configuration. We estimated model parameters using an optimization algorithm and explored two distinct scenarios to study the impact of active SMC contributions to arterial stiffness. Our results indicated that alterations in arterial mechanics are primarily driven by SMC activity rather than intrinsic tissue properties. Additionally, the model was validated against experimental data and tested under pressure conditions beyond those used for parameter estimation, which is an indicator of its predictive capabilities.

In Chapter 3, we introduced a comprehensive model of the ROTSAC setup, including a realistic geometry of the experiment and the contact phenomena between the tissue and the supporting rigid hooks. To this purpose, three different numerical methods for contact were explored: augmented Lagrangian, Nitsche and penalty methods. A salient feature of the proposed numerical study is that it includes a combination of Nitsche's method with a 3D-shell model, which is rather unusual in the literature. The penalty method is the easiest to implement among the three, but it suffers from accuracy issues due to the lack of strong consistency. Moreover, it is too sensitive to the choice of the penalty parameter: if it is too small, it causes difficulties with Newton's method convergence; if too high, it results in excessive penetration. The augmented Lagrangian method is strongly consistent but introduces an additional unknown. Nitsche's method is also consistent and avoids additional unknowns, but it is more challenging to implement. Our findings showed that both the augmented Lagrangian and Nitsche's methods exhibited robustness with respect to the magnitude of the applied forces compared to the penalty method. However, the penalty method, despite allowing penetration and facing limitations at higher forces, offered the advantage of lower computational costs.

In Chapter 4, we analyzed real *in vivo* experimental data provided by Boehringer Ingelheim Pharma GmbH & Co. KG to assess the effects of aging on dogs, using statistical methods that are currently employed at the company, along with machine learning and mathematical modeling approaches. In this chapter, we proposed a simple parametric 0D model for the left part of the heart coupled to systemic circulation, effectively linking observable cardiovascular quantities to aging, which is associated with increased arterial stiffness. This model allowed us to estimate parameters for both the *new* and *historical* states of the animals, revealing changes in their cardiovascular systems.

There are several possible directions for extending this work. Among them we can highlight the following:

- The mathematical models introduced in Chapters 2 and 3 could be further refined by incorporating plasticity effects in the case of extreme loads, which may improve the accuracy of parameter estimation, particularly at higher pressure ranges.
- A fundamental limitation of the proposed models is that they assume a monolayer structure in the vessel wall. More realistic multilayer models of the aortic wall could be explored.
- The parameter estimation and validation procedures from Chapter 2 could be performed with the contact mechanics model from Chapter 3 to assess whether this leads to improved experimental data reproduction.
- While we have focused on unilateral contact between a 3D-shell and a rigid solid, it would be worthy to explore bilateral contact scenarios involving two 3D-shells. Comparing in some known benchmarks, augmented Lagrangian, Nitsche and penalty methods would be a valuable numerical study that we plan to carry out shortly.
- The study of aging effects on the cardiovascular system, as presented in Chapter 4, could be expanded by including data from a larger cohort of dogs and exploring different breeds to further validate the methods developed in this work.
- The parameter estimation performed on the 0D model of the left heart in Chapter 4, could be extended by analyzing additional chunks of data, potentially enabling the use of parameter-based classification techniques.

Appendix A

Computer implementation details (Chapter 3)

A.1 Analytical ray-tracing

Since we have a simple parametrization of the master surfaces $\Gamma^R_{C_1,t}$ and $\Gamma^R_{C_2,t}$ of the hooks, which are rigid bodies, the ray-tracing projections $\boldsymbol{\pi}_1$ and $\boldsymbol{\pi}_2$ can be evaluated analytically.

Let us consider $\boldsymbol{y}_t = \boldsymbol{x}_t + a\,\boldsymbol{n}_{\boldsymbol{\varphi}}$, with $a \in \mathbb{R}^+$, as the parametric equation of the half-line with direction $\boldsymbol{n}_{\boldsymbol{\varphi}}$ and origin $\boldsymbol{x}_t = \boldsymbol{\varphi}(\boldsymbol{x})$, where $\boldsymbol{x}_t \in \Gamma_{C_1,t}$ and $\boldsymbol{x} \in \Gamma_{C_1}$. Due to the intrinsic symmetry of the configuration, we consider a section of the rigid body obtained by cutting the lateral surface with a plane parallel to the base of the cylinder, resulting in a circumference. The equation of the circumference with radius r_h and center at $\boldsymbol{r}_c$ can be expressed as $(\boldsymbol{y}_t - \boldsymbol{r}_c) \cdot (\boldsymbol{y}_t - \boldsymbol{r}_c) = r_h^2$. The intersection between the line and the circumference occurs at $(\boldsymbol{\varphi}(\boldsymbol{x}) - \boldsymbol{r}_c + a\boldsymbol{n}_{\boldsymbol{\varphi}}) \cdot (\boldsymbol{\varphi}(\boldsymbol{x}) - \boldsymbol{r}_c + a\boldsymbol{n}_{\boldsymbol{\varphi}}) = r_h^2$, from which we can define

$$\Delta = ((\boldsymbol{\varphi}(\boldsymbol{x}) - \boldsymbol{r}_c) \cdot \boldsymbol{n}_{\boldsymbol{\varphi}})^2 - \|\boldsymbol{n}_{\boldsymbol{\varphi}}\|^2(\|\boldsymbol{\varphi}(\boldsymbol{x}) - \boldsymbol{r}_c\|^2 - r_h^2),$$

and solve for a obtaining:

$$a(\boldsymbol{x}) = -(\boldsymbol{\varphi}(\boldsymbol{x}) - \boldsymbol{r}_c) \cdot \boldsymbol{n}_{\boldsymbol{\varphi}} \pm \sqrt{\Delta}.$$

The possible scenarios are:

- $\Delta > 0$: There are two distinct real solutions, and we consider the smaller one.
- $\Delta = 0$: The quadratic equation has a single solution.
- $\Delta < 0$: There are no real solutions; hence, there is no contact.

For cases where $\Delta \geq 0$, the points of intersection on the hook are given by $\boldsymbol{y}(\boldsymbol{x}) = \boldsymbol{\varphi}(\boldsymbol{x}) + a(\boldsymbol{x})\boldsymbol{n}_{\boldsymbol{\varphi}}$.

Considering $\boldsymbol{y}_t = \boldsymbol{x}_t + a\,\boldsymbol{n}_{\boldsymbol{\varphi}}$, with $\boldsymbol{x}_t = \boldsymbol{\varphi}(\boldsymbol{x})$, where $\boldsymbol{x}_t \in \Gamma_{C_2,t}$ and $\boldsymbol{x} \in \Gamma_{C_2}$, i.e. belonging to the moving hook, the detection follows similarly, with the equation of the circumference given by $(\boldsymbol{y}_t - (\boldsymbol{r}_c + \boldsymbol{s})) \cdot (\boldsymbol{y}_t - (\boldsymbol{r}_c + \boldsymbol{s})) = r_h^2$, with $\boldsymbol{s} = s\boldsymbol{e}_y$ the vertical displacement, so that we have:

$$\Delta = ((\boldsymbol{\varphi}(\boldsymbol{x}) - \boldsymbol{r}_c - \boldsymbol{s}) \cdot \boldsymbol{n}_{\boldsymbol{\varphi}})^2 - \|\boldsymbol{n}_{\boldsymbol{\varphi}}\|^2(\|\boldsymbol{\varphi}(\boldsymbol{x}) - \boldsymbol{r}_c - \boldsymbol{s}\|^2 - r_h^2),$$

and

$$a(\boldsymbol{x}) = -(\boldsymbol{\varphi}(\boldsymbol{x}) - \boldsymbol{r}_c - \boldsymbol{s}) \cdot \boldsymbol{n}_{\boldsymbol{\varphi}} \pm \sqrt{\Delta}.$$

A.2 Time adaptivity

A time adaptivity algorithm, (see, e.g., Kamensky et al. (2018)), dynamically adjusts the time step based on the convergence behavior of the solution. Specifically, it reduces the time step when need to ensure accuracy, and increases it during phases of rapid convergence to expedite computation.

Throughout this discussion, the number of iterations required by Newton's method is denoted by it. We define the following parameters to control the time adaptivity procedure:

- Δt_{max}: the maximum allowable time step;
- I_{coarse}: the threshold number of Newton iterations indicating rapid convergence, suggesting that the time step is unnecessarily small;
- I_{fix}: the number of iterations during which the time step remains fixed after being coarsened;
- it_s: the number of consecutive time steps taken with the same time step size.

The proposed time adaptivity algorithm is outlined in Algorithm 1.

Algorithm 1: Time Adaptivity Algorithm

Parameters : Δt_{max}, I_{coarse}, I_{fix}

```
Initialize Δt ← Δt_max and it_s ← 0;
while t < T do
    Solve the nonlinear system at time t ;
    if Newton converged in it iterations then
        if it < I_coarse and it_s > I_fix then
            Δt ← min(2Δt, Δt_max);
            it_s ← 0;
        end
        else
            it_s ← it_s + 1;
        end
    end
    else
        t ← t − Δt;
        Δt ← Δt/2;
        t ← t + Δt;
        it_s ← 0;
    end
end
```

A.3 Directional derivatives of the gap function

The optimality system (3.13) involves the directional derivatives of the gap functions $g_1(\boldsymbol{d})$ and $g_2(\boldsymbol{d}, s)$ with respect to the displacement $\boldsymbol{d}$ in the virtual direction $\delta\boldsymbol{d}$, and for g_2, with respect to the translation s in the virtual direction δs. Moreover, to compute the contribution of the contact terms to the tangent problem in Newton's method, not only the directional derivative of a gap function is required, but also the directional derivatives of other quantities such as $\boldsymbol{x}_t = \boldsymbol{\varphi}(\boldsymbol{x})$ and $\boldsymbol{n}_{\boldsymbol{\varphi}}$.

In order to obtain an explicit relation for the directional derivative of the gap function, we start by considering the directional derivative of $\boldsymbol{y}_t = \boldsymbol{\pi}(\boldsymbol{x}_t)$, taking into account its dependence on both the deformation $\boldsymbol{\varphi}$ and the coordinate $\boldsymbol{y}$, with $\boldsymbol{y}$ itself being a function of $\boldsymbol{\varphi}$ and possessing its own directional derivatives.

A point $\boldsymbol{y}_t$ in the deformed configuration, corresponding to the point $\boldsymbol{y}$ in the reference configuration, can be expressed via the transformation $\boldsymbol{\varphi}$ as:

$$\boldsymbol{y}_t = \boldsymbol{y}(\boldsymbol{d}) + \boldsymbol{d}\left(\boldsymbol{y}\right), \quad \text{where} \quad \boldsymbol{y} = \boldsymbol{\varphi}^{-1}(\boldsymbol{y}_t). \tag{A.1}$$

The directional derivative of $\boldsymbol{y}_t$ with respect to the displacement $\boldsymbol{d}$ in direction $\delta\boldsymbol{d}$, denoted as $D_{\boldsymbol{d}}\boldsymbol{y}_t(\boldsymbol{d})[\delta\boldsymbol{d}]$, is given by:

$$D_{\boldsymbol{d}}\boldsymbol{y}_t[\delta\boldsymbol{d}] = \lim_{\varepsilon\to 0} \frac{\boldsymbol{y}_t(\boldsymbol{d}+\varepsilon\delta\boldsymbol{d}) - \boldsymbol{y}_t(\boldsymbol{d})}{\varepsilon}, \tag{A.2}$$

when the limit exists. By replacing (A.1) in (A.2), the directional derivative (A.2) can be written as:

$$\begin{aligned} D_{\boldsymbol{d}}\boldsymbol{y}_t[\delta\boldsymbol{d}] &= \lim_{\varepsilon\to 0} \frac{\boldsymbol{y}\left(\boldsymbol{d}+\varepsilon\delta\boldsymbol{d}\right) - \boldsymbol{y}\left(\boldsymbol{d}\right) + \boldsymbol{d}\left(\boldsymbol{y}\left(\boldsymbol{d}+\varepsilon\delta\boldsymbol{d}\right)\right) - \boldsymbol{d}\left(\boldsymbol{y}\left(\boldsymbol{d}\right)\right) + \varepsilon\delta\boldsymbol{d}(\boldsymbol{y})}{\varepsilon} \\ &= D_{\boldsymbol{d}}\boldsymbol{y}[\delta\boldsymbol{d}] + \boldsymbol{\nabla}\boldsymbol{d}\cdot D_{\boldsymbol{d}}\boldsymbol{y}[\delta\boldsymbol{d}] + \delta\boldsymbol{d}\left(\boldsymbol{y}\right) \\ &= \delta\boldsymbol{d}\left(\boldsymbol{y}\right) + (\boldsymbol{\mathcal{I}} + \boldsymbol{\nabla}\boldsymbol{d})\cdot D_{\boldsymbol{d}}\boldsymbol{y}[\delta\boldsymbol{d}], \end{aligned} \tag{A.3}$$

where $\boldsymbol{\mathcal{I}}$ is the identity.

The point $\boldsymbol{y}_t$ can alternatively be expressed, using the projection operator $\boldsymbol{\pi}$, as:

$$\boldsymbol{y}_t = \boldsymbol{\pi}(\boldsymbol{\varphi}(\boldsymbol{x})) = \boldsymbol{x} + \boldsymbol{d}(\boldsymbol{x}) + g(\boldsymbol{d})\boldsymbol{n}_{\boldsymbol{\varphi}},$$

and therefore, its directional derivative with respect to the displacement $\boldsymbol{d}$ in the direction $\delta\boldsymbol{d}$ is given by:

$$D_{\boldsymbol{d}}\boldsymbol{y}_t[\delta\boldsymbol{d}] = \delta\boldsymbol{d}(\boldsymbol{x}) + D_{\boldsymbol{d}}g[\delta\boldsymbol{d}]\boldsymbol{n}_{\boldsymbol{\varphi}} + D_{\boldsymbol{d}}\boldsymbol{n}_{\boldsymbol{\varphi}}[\delta\boldsymbol{d}]g. \tag{A.4}$$

Finally, combining (A.3) and (A.4) we have:

$$\delta\boldsymbol{d}(\boldsymbol{y}) + (\boldsymbol{\mathcal{I}} + \boldsymbol{\nabla}\boldsymbol{d})\cdot D_{\boldsymbol{d}}\boldsymbol{y}[\delta\boldsymbol{d}] = \delta\boldsymbol{d}(\boldsymbol{x}) + D_{\boldsymbol{d}}g[\delta\boldsymbol{d}]\boldsymbol{n}_{\boldsymbol{\varphi}} + D_{\boldsymbol{d}}\boldsymbol{n}_{\boldsymbol{\varphi}}[\delta\boldsymbol{d}]g. \tag{A.5}$$

Since $D_{\boldsymbol{d}}\boldsymbol{y}[\delta\boldsymbol{d}]$ is tangent to Γ_C^R, then $(\boldsymbol{\mathcal{I}} + \boldsymbol{\nabla}\boldsymbol{d})D_{\boldsymbol{d}}\boldsymbol{y}[\delta\boldsymbol{d}]$ is tangent to $\Gamma_{C,t}^R$ and, therefore, orthogonal to $\boldsymbol{n}_{\boldsymbol{\pi}}$. Multiplying (A.5) by $\boldsymbol{n}_{\boldsymbol{\pi}}$, we obtain:

$$\boxed{D_{\boldsymbol{d}}g[\delta\boldsymbol{d}] = \frac{-\boldsymbol{n}_{\boldsymbol{\pi}}}{\boldsymbol{n}_{\boldsymbol{\pi}}\cdot\mathbf{n}_{\varphi}}\left(\delta\boldsymbol{d}(\boldsymbol{x}) + gD_{\boldsymbol{d}}\boldsymbol{n}_{\boldsymbol{\varphi}}[\delta\boldsymbol{d}]\right).} \tag{A.6}$$

It remains to evaluate $D_{\boldsymbol{d}}\boldsymbol{n}_{\boldsymbol{\varphi}}[\delta\boldsymbol{d}]$. Let us define, for $\alpha \in \{1,2\}$, the vectors $\boldsymbol{d}_{*,\alpha} = [\boldsymbol{d}_{1,\alpha}, \boldsymbol{d}_{2,\alpha}, \boldsymbol{d}_{3,\alpha}] \in \mathbb{R}^3$, where $\boldsymbol{d}_{i,\alpha} = \frac{\partial \boldsymbol{d}_i}{\partial \boldsymbol{a}_\alpha}$. The normal $\boldsymbol{n}_{\boldsymbol{\varphi}}$ can be written as:

$$\boldsymbol{n}_{\boldsymbol{\varphi}} = \frac{\boldsymbol{a}_{3,t}}{\|\boldsymbol{a}_{3,t}\|} = \frac{\boldsymbol{a}_{1,t} \times \boldsymbol{a}_{2,t}}{\|\boldsymbol{a}_{1,t} \times \boldsymbol{a}_{2,t}\|} = \frac{(\boldsymbol{a}_1 + \boldsymbol{d}_{*,1}) \times (\boldsymbol{a}_2 + \boldsymbol{d}_{*,2})}{\|(\boldsymbol{a}_1 + \boldsymbol{d}_{*,1}) \times (\boldsymbol{a}_2 + \boldsymbol{d}_{*,2})\|}.$$

Consequently, the directional derivative of $\boldsymbol{n}_{\boldsymbol{\varphi}}$ in direction $\delta\boldsymbol{d}$ is given by:

$$D_{\boldsymbol{d}}\boldsymbol{n}_{\boldsymbol{\varphi}}[\delta\boldsymbol{d}] = \frac{1}{\|\boldsymbol{a}_{3,t}\|} D_{\boldsymbol{d}}\boldsymbol{a}_{3,t}[\delta\boldsymbol{d}] + \boldsymbol{a}_{3,t} D_{\boldsymbol{d}} \frac{1}{\|\boldsymbol{a}_{3,t}\|}[\delta\boldsymbol{d}]. \tag{A.7}$$

Moreover, treating the two terms in (A.7) separately, we have:

$$D_{\boldsymbol{d}}\boldsymbol{a}_{3,t}[\delta\boldsymbol{d}] = \delta\boldsymbol{d}_{*,1} \times \boldsymbol{a}_{2,t} + \boldsymbol{a}_{1,t} \times \delta\boldsymbol{d}_{*,2}, \tag{A.8}$$

and

$$D_{\boldsymbol{d}} \frac{1}{\|\boldsymbol{a}_{3,t}\|}[\delta\boldsymbol{d}] = D_{\boldsymbol{d}} \frac{1}{\sqrt{\boldsymbol{a}_{3,t} \cdot \boldsymbol{a}_{3,t}}}[\delta\boldsymbol{d}] = -\frac{1}{\|\boldsymbol{a}_{3,t}\|^3} \boldsymbol{a}_{3,t} \cdot D_{\boldsymbol{d}}(\boldsymbol{a}_{3,t})[\delta\boldsymbol{d}]. \tag{A.9}$$

Hence, using (A.7)-(A.9) and the relations $\boldsymbol{a}_{3,t} \cdot \boldsymbol{b} = \|a_{3,t}\|\,(\boldsymbol{n}_{\boldsymbol{\varphi}} \cdot \boldsymbol{b})$ and $\boldsymbol{n}_{\boldsymbol{\varphi}} \cdot \boldsymbol{b} = (\boldsymbol{n}_{\boldsymbol{\varphi}} \otimes \boldsymbol{n}_{\boldsymbol{\varphi}})\boldsymbol{b}$, for every $\boldsymbol{b} \in \mathbb{R}^3$, we get:

$$\boxed{D_{\boldsymbol{d}}\boldsymbol{n}_{\boldsymbol{\varphi}}[\delta\boldsymbol{d}] = \frac{1}{\|\boldsymbol{a}_{3,t}\|}(\boldsymbol{\mathcal{I}} - \boldsymbol{n}_{\boldsymbol{\varphi}} \otimes \boldsymbol{n}_{\boldsymbol{\varphi}})(\delta\boldsymbol{d}_{*,1} \times \boldsymbol{a}_{2,t} + \boldsymbol{a}_{1,t} \times \delta\boldsymbol{d}_{*,2}).} \tag{A.10}$$

In order to obtain the expression for the directional derivatives of the gap function with respect to the translation $\boldsymbol{s} := s\boldsymbol{e}_y$, where $\boldsymbol{e}_y$ is the unit vector in the vertical direction and $s(t) \in \mathbb{R}$. We consider a generic point $\boldsymbol{y}_t$ in the deformed configuration that lies on the potential contact boundary. Similarly to the previous case, the point $\boldsymbol{y}_t$ can be obtained from a point in the reference configuration $\boldsymbol{y}$ through the transformation $\boldsymbol{\varphi}$ and the translation $\boldsymbol{s}$ as follows:

$$\boldsymbol{y}_t(\boldsymbol{d}, \boldsymbol{s}) = \boldsymbol{y}(\boldsymbol{d}, \boldsymbol{s}) + \boldsymbol{s}.$$

The directional derivative of $\boldsymbol{y}_t$ with respect to $\boldsymbol{s}$ reads as:

$$\begin{aligned} D_{\boldsymbol{s}}\boldsymbol{y}_t(\boldsymbol{d}, \boldsymbol{s})[\delta\boldsymbol{s}] &= \lim_{\varepsilon \to 0} \frac{\boldsymbol{y}(\boldsymbol{d}, \boldsymbol{s} + \varepsilon\delta\boldsymbol{s}) - \boldsymbol{y}(\boldsymbol{d}, \boldsymbol{s}) + (\boldsymbol{s} + \varepsilon\delta\boldsymbol{s}) - \boldsymbol{s}}{\varepsilon} \\ &= D_{\boldsymbol{s}}\boldsymbol{y}(\boldsymbol{d}, \boldsymbol{s})[\delta\boldsymbol{s}] + \delta\boldsymbol{s}. \end{aligned} \tag{A.11}$$

On the other hand, $\boldsymbol{y}_t$ can be expressed, using the projection operator $\boldsymbol{\pi}$, as:

$$\boldsymbol{y}_t(\boldsymbol{d}, \boldsymbol{s}) = \boldsymbol{x} + \boldsymbol{d}(\boldsymbol{x}) + g(\boldsymbol{d}, \boldsymbol{s})\boldsymbol{n}_{\boldsymbol{\varphi}},$$

and therefore, its directional derivative with respect to the translation $\boldsymbol{s}$ in the direction $\delta\boldsymbol{s}$ is given by:

$$D_{\boldsymbol{s}}\boldsymbol{y}_t(\boldsymbol{d}, \boldsymbol{s})[\delta\boldsymbol{s}] = D_{\boldsymbol{s}}g(\boldsymbol{d}, \boldsymbol{s})[\delta\boldsymbol{s}]\boldsymbol{n}_{\boldsymbol{\varphi}}. \tag{A.12}$$

Combining and (A.11) and (A.12), we obtain:

$$D_{\boldsymbol{s}}g(\boldsymbol{d}, \boldsymbol{s})[\delta\boldsymbol{s}]\boldsymbol{n}_{\boldsymbol{\varphi}} = D_{\boldsymbol{s}}\boldsymbol{y}(\boldsymbol{d}, \boldsymbol{s})[\delta\boldsymbol{s}] + \delta\boldsymbol{s}.$$

Multiplying the previous expression by $\boldsymbol{n}_{\boldsymbol{\pi}}$, taking into account that since $D_{\boldsymbol{s}}\boldsymbol{y}[\delta\boldsymbol{s}]$ is tangent to Γ_C^R, we have $\boldsymbol{n}_{\boldsymbol{\pi}} \cdot D_{\boldsymbol{s}}\boldsymbol{y}[\delta\boldsymbol{s}] = 0$, we get:

$$\boxed{D_{\boldsymbol{s}}g(\boldsymbol{d}, \boldsymbol{s})[\delta\boldsymbol{s}] = \frac{\boldsymbol{n}_{\boldsymbol{\pi}}}{\boldsymbol{n}_{\boldsymbol{\pi}} \cdot \boldsymbol{n}_{\boldsymbol{\varphi}}}\delta\boldsymbol{s}.} \tag{A.13}$$

A.4 Tangent problem derivation

In order to address the numerical resolution of the highly nonlinear contact problems (3.20), (3.22), and (3.26), Newton's method is employed. At each time step t (omitted to simplify the notation), this method requires the iterative solution of a tangent problem, which is formulated as:

$$\left\langle D_{\boldsymbol{d},\lambda_2,\lambda_1,s} R(\boldsymbol{d}_h^n, \lambda_{2,h}^n, \lambda_{1,h}^n, s^n)[\delta\boldsymbol{d}, \delta\lambda_2, \delta\lambda_1, \delta s], \boldsymbol{v}_h, \mu_{2,h}, \mu_{1,h} \right\rangle = \\ - \left\langle R(\boldsymbol{d}_h^n, \lambda_{2,h}^n, \lambda_{1,h}^n, s^n), \boldsymbol{v}_h, \mu_{2,h}, \mu_{1,h} \right\rangle,$$

where $R(\boldsymbol{d}_h^n, \lambda_{2,h}^n, \lambda_{1,h}^n, s^n)$ denotes the residual of the system and $D_{\boldsymbol{d},\lambda_2,\lambda_1,s} R(\boldsymbol{d}_h^n, \lambda_{2,h}^n, \lambda_{1,h}^n, s^n)$ represents the Jacobian matrix. In this context, n refers to the current iteration of the Newton method. The solution to this equation provides the necessary update for the unknowns $(\boldsymbol{d}_h^n, \lambda_{2,h}^n, \lambda_{1,h}^n, s^n)$, ensuring convergence toward an equilibrium state at each time step. The complete Newton method is presented in Algorithm 2.

In the following sections, we will focus on deriving the expressions for the Jacobian and residual contributions specifically related to the contact terms for each method. This involves computing the derivatives of quantities that include the positive and negative part operators.

To begin, recall the definition of the negative part operator:

$$[x]_- := \max\{-x, 0\},$$

which can alternatively be written as:

$$[x]_- = -x \cdot (1 - \mathcal{H}(x)),$$

where $\mathcal{H}(x)$ denotes the Heaviside step function. For any $x \in \mathbb{R}$, the Heaviside function is defined as:

$$\mathcal{H}(x) := \begin{cases} 1 & \text{if } x > 0, \\ 0 & \text{if } x \leq 0. \end{cases}$$

To compute the derivative of the negative part operator $[x]_-$, we apply the chain rule to the expression above. The derivative is given by:

$$D[x]_-[\delta x] = (-1 + \mathcal{H}(x))\delta x.$$

This indicates that for $x > 0$, the derivative vanishes ($D[x]_-[\delta x] = 0$), while for $x \leq 0$, the derivative is $-\delta x$.

Algorithm 2: Newton's method for nonlinear equations

Initialization: Choose an initial guess $\boldsymbol{d}_h^n = \boldsymbol{d}_h^{n-1}$;
while *convergence not achieved* **do**
  Evaluate the nonlinear residual: Compute $R(\boldsymbol{d}_h^n)$;
  Solve the tangent problem: Solve $\langle D_{\boldsymbol{d}} R(\boldsymbol{d}_h^n)[\delta \boldsymbol{d}], \boldsymbol{v}\rangle = -\langle R(\boldsymbol{d}_h^n), \boldsymbol{v}\rangle$;
  Update solution: $\boldsymbol{d}_h^{n+1} = \boldsymbol{d}_h^n + \delta \boldsymbol{d}$;
end

A.4.1 Augmented Lagrangian method

The algebraic form of the tangent problem (3.20) can be written as follows:

$$\left[J^n(\boldsymbol{d}_h^n, \lambda_{2,h}^n, \lambda_{1,h}^n, s^n)\right] \begin{bmatrix} \delta \boldsymbol{d} \\ \delta \lambda_2 \\ \delta \lambda_1 \\ \delta s \end{bmatrix} = \left[-R^n(\boldsymbol{d}_h^n, \lambda_{2,h}^n, \lambda_{1,h}^n, s^n)\right],$$

with

$$\left[J^n(\boldsymbol{d}_h^n, \lambda_{2,h}^n, \lambda_{1,h}^n, s^n)\right] = \begin{bmatrix} D_{\boldsymbol{d}} R_1(\boldsymbol{d}_h^n, \lambda_{2,h}^n, \lambda_{1,h}^n, s^n) & D_{\lambda_2} R_1(\boldsymbol{d}_h^n, \lambda_{2,h}^n, \lambda_{1,h}^n, s^n) & D_{\lambda_1} R_1(\boldsymbol{d}_h^n, \lambda_{2,h}^n, \lambda_{1,h}^n, s^n) & D_s R_1(\boldsymbol{d}_h^n, \lambda_{2,h}^n, \lambda_{1,h}^n, s^n) \\ D_{\boldsymbol{d}} R_2(\boldsymbol{d}_h^n, \lambda_{2,h}^n, s^n) & D_{\lambda_2} R_2(\boldsymbol{d}_h^n, \lambda_{2,h}^n, s^n) & 0 & D_s R_2(\boldsymbol{d}_h^n, \lambda_{2,h}^n, s^n) \\ D_{\boldsymbol{d}} R_3(\boldsymbol{d}_h^n, \lambda_{1,h}^n) & 0 & D_{\lambda_1} R_3(\boldsymbol{d}_h^n, \lambda_{1,h}^n) & 0 \\ D_{\boldsymbol{d}} R_4(\boldsymbol{d}_h^n, \lambda_{2,h}^n, s^n) & D_{\lambda_2} R_4(\boldsymbol{d}_h^n, \lambda_{2,h}^n, s^n) & 0 & D_s R_4(\boldsymbol{d}_h^n, \lambda_{2,h}^n, s^n) \end{bmatrix}, \tag{A.14}$$

and

$$\left[R^n(\boldsymbol{d}_h^n, \lambda_{2,h}^n, \lambda_{1,h}^n, s^n)\right] = \begin{bmatrix} R_1(\boldsymbol{d}_h^n, \lambda_{2,h}^n, \lambda_{1,h}^n, s^n) \\ R_2(\boldsymbol{d}_h^n, \lambda_{2,h}^n, s^n) \\ R_3(\boldsymbol{d}_h^n, \lambda_{1,h}^n) \\ R_4(\boldsymbol{d}_h^n, \lambda_{2,h}^n, s^n) \end{bmatrix}. \tag{A.15}$$

The terms of the residuals in (A.15) read:

$$\begin{aligned}
\langle R_1(\boldsymbol{d}_h^n, \lambda_{2,h}^n, \lambda_{1,h}^n, s^n), \boldsymbol{v}_h\rangle = &\underbrace{\int_\Omega \rho \frac{\boldsymbol{d}_h^n - 2\boldsymbol{d}^{n-1} + \boldsymbol{d}^{n-2}}{(\Delta t)^2} \cdot \boldsymbol{v}_h \; + a_h(\boldsymbol{d}_h^n; \boldsymbol{v}_h)}_{\langle R_{1,\text{Shell}}(\boldsymbol{d}_h^n), \boldsymbol{v}_h\rangle} \\
&+ \underbrace{\int_{\Gamma_{C_2}} \left[\lambda_{2,h}^n + \gamma g_2(\boldsymbol{d}_h^n, s^n)\right]_- \boldsymbol{v}_h \cdot \boldsymbol{n}_{\boldsymbol{\varphi}}}_{\langle R_{1,\text{Moving}}(\boldsymbol{d}_h^n, \lambda_{2,h}^n, s^n), \boldsymbol{v}_h\rangle} \\
&+ \underbrace{\int_{\Gamma_{C_1}} \left[\lambda_{1,h}^n + \gamma g_1(\boldsymbol{d}_h^n)\right]_- \boldsymbol{v}_h \cdot \boldsymbol{n}_{\boldsymbol{\varphi}}}_{\langle R_{1,\text{Static}}(\boldsymbol{d}_h^n, \lambda_{1,h}^n), \boldsymbol{v}_h\rangle}, \quad \forall \boldsymbol{v}_h \in \mathbf{V}_h^{\text{sh}}, \\
\langle R_2(\boldsymbol{d}_h^n, \lambda_{2,h}^n, s^n), \mu_h\rangle = &-\frac{1}{\gamma} \int_{\Gamma_{C_2}} \left(\lambda_{2,h}^n + \left[\lambda_{2,h}^n + \gamma g_2(\boldsymbol{d}_h^n, s^n)\right]_-\right) \mu_h, \quad \forall \mu_h \in \Lambda_{2,h}, \\
\langle R_3(\boldsymbol{d}_h^n, \lambda_{1,h}^n), \mu_h\rangle = &-\frac{1}{\gamma} \int_{\Gamma_{C_1}} \left(\lambda_{1,h}^n + \left[\lambda_{1,h}^n + \gamma g_1(\boldsymbol{d}_h^n)\right]_-\right) \mu_h, \quad \forall \mu_h \in \Lambda_{1,h}, \\
R_4(\boldsymbol{d}_h^n, \lambda_{2,h}^n, s^n) = &\, m \frac{s^n - 2s^{n-1} + s^{n-2}}{(\Delta t)^2} - f \\
&- \int_{\Gamma_{C_2}} \left[\lambda_{2,h}^n + \gamma g_2(\boldsymbol{d}_h^n, s^n)\right]_- \boldsymbol{e}_y \cdot \boldsymbol{n}_{\boldsymbol{\varphi}}.
\end{aligned}$$

In the following, we obtain the expressions for each term of the Jacobian matrix (A.14), computing the derivatives of the different residuals with respect to the variables $(\boldsymbol{d}, \lambda_2, \lambda_1, s)$ in the directions $(\delta\boldsymbol{d}, \delta\lambda_2, \delta\lambda_1, \delta s)$.

We start by computing the directional derivatives of the residual coming from the momentum conservation. The derivative can be split into three terms: shell, moving hook, and static hook contributions.

$$\begin{aligned}
\langle D_{\boldsymbol{d}} R_1(\boldsymbol{d}_h^n, \lambda_{2,h}^n, \lambda_{1,h}^n, s^n)[\delta\boldsymbol{d}], \boldsymbol{v}_h\rangle = &\langle D_{\boldsymbol{d}} R_{1,\text{Shell}}(\boldsymbol{d}_h^n)[\delta\boldsymbol{d}], \boldsymbol{v}_h\rangle \\
&+ \langle D_{\boldsymbol{d}} R_{1,\text{Moving}}(\boldsymbol{d}_h^n, \lambda_{2,h}^n, s^n)[\delta\boldsymbol{d}], \boldsymbol{v}_h\rangle \\
&+ \langle D_{\boldsymbol{d}} R_{1,\text{Static}}(\boldsymbol{d}_h^n, \lambda_{1,h}^n)[\delta\boldsymbol{d}], \boldsymbol{v}_h\rangle.
\end{aligned}$$

We do not present the derivation corresponding to the term $\langle D_{\boldsymbol{d}} R_{1,\text{Shell}}(\boldsymbol{d}_h^n)[\delta\boldsymbol{d}], \boldsymbol{v}_h\rangle$ as it has been analyzed in Chapter 2 (see Section 2.2.2.2).

Now we derive the directional derivative of the residual term coming from the momentum conservation associated with the moving and static hooks. The derivative of

$\langle R_{1,\text{Moving}}(\boldsymbol{d}_h^n, \lambda_{2,h}^n, s^n), \boldsymbol{v}_h\rangle$ in the direction $\delta\boldsymbol{d}$ reads:

$$\begin{aligned}
&\langle D_{\boldsymbol{d}} R_{1,\text{Moving}}\ (\boldsymbol{d}_h^n, \lambda_{2,h}^n, s^n)[\delta\boldsymbol{d}], \boldsymbol{v}_h\rangle \\
&\qquad = \int_{\Gamma_{C_2}} D_{\boldsymbol{d}} \left[\lambda_{2,h}^n + \gamma g_2(\boldsymbol{d}_h^n, s^n)\right]_- [\delta\boldsymbol{d}]\boldsymbol{v}_h \cdot \boldsymbol{n}_{\boldsymbol{\varphi}} \\
&\qquad = \int_{\Gamma_{C_2}} \gamma \left[-1 + \mathcal{H}\left(\lambda_{2,h}^n + \gamma g_2(\boldsymbol{d}_h^n, s^n)\right)\right] D_{\boldsymbol{d}} g_2(\boldsymbol{d}_h^n, s^n)[\delta\boldsymbol{d}]\ \boldsymbol{v}_h \cdot \boldsymbol{n}_{\boldsymbol{\varphi}} \\
&\qquad\quad + \int_{\Gamma_{C_2}} \left[\lambda_{2,h}^n + \gamma g_2(\boldsymbol{d}_h^n, s^n)\right]_- \boldsymbol{v}_h \cdot D_{\boldsymbol{d}} \boldsymbol{n}_{\boldsymbol{\varphi}}[\delta\boldsymbol{d}], \quad \forall \boldsymbol{v}_h \in \mathbf{V}_h^{\text{sh}},
\end{aligned} \tag{A.16}$$

where $D_{\boldsymbol{d}} g_2(\boldsymbol{d}_h^n, s^n)[\delta\boldsymbol{d}]$ and $D_{\boldsymbol{d}}\boldsymbol{n}_{\boldsymbol{\varphi}}[\delta\boldsymbol{d}]$ can be found in equations (A.6) and (A.10), respectively. An analogue expression applies for $\langle D_{\boldsymbol{d}} R_{1,\text{Static}}(\boldsymbol{d}_h^n, \lambda_1^n)[\delta\boldsymbol{d}], \boldsymbol{v}_h\rangle$.

The directional derivative of $\langle R_1(\boldsymbol{d}_h^n, \lambda_{2,h}^n, \lambda_{1,h}^n, s^n), \boldsymbol{v}_h\rangle$ in direction $\delta\lambda_2$, reads:

$$\begin{aligned}
&\langle D_{\lambda_2} R_1\ (\boldsymbol{d}_h^n, \lambda_{2,h}^n, \lambda_{1,h}^n, s^n)[\delta\lambda_2], \boldsymbol{v}_h\rangle \\
&\qquad = \langle D_{\lambda_2} R_{1,\text{Moving}}(\boldsymbol{d}_h^n, \lambda_{2,h}^n, s^n)[\delta\lambda_2], \boldsymbol{v}_h\rangle \\
&\qquad = \int_{\Gamma_{C_2}} D_{\lambda_2} \left[\lambda_{2,h}^n + \gamma g_2(\boldsymbol{d}_h^n, s^n)\right]_- [\delta\lambda_2]\boldsymbol{v}_h \cdot \boldsymbol{n}_{\boldsymbol{\varphi}} \\
&\qquad = \int_{\Gamma_{C_2}} \left[-1 + \mathcal{H}\left(\lambda_{2,h}^n + \gamma g_2(\boldsymbol{d}_h^n, s^n)\right)\right] \delta\lambda_2 \boldsymbol{v}_h \cdot \boldsymbol{n}_{\boldsymbol{\varphi}}, \quad \forall \boldsymbol{v}_h \in \mathbf{V}_h^{\text{sh}}.
\end{aligned} \tag{A.17}$$

The term $\langle D_{\lambda_1} R_{1,\text{Static}}(\boldsymbol{d}_h^n, \lambda_{1,h}^n)[\delta\lambda_1], \boldsymbol{v}_h\rangle$ can be obtained similarly. Finally, for the term corresponding to the directional derivative of $\langle R_1(\boldsymbol{d}_h^n, \lambda_{2,h}^n, \lambda_{1,h}^n, s^n), \boldsymbol{v}_h\rangle$ in direction δs, we get:

$$\begin{aligned}
&\langle D_s R_1\ (\boldsymbol{d}_h^n, \lambda_{2,h}^n, \lambda_{1,h}^n, s^n)[\delta s], \boldsymbol{v}_h\rangle \\
&\qquad = \int_{\Gamma_{C_2}} D_s \left[\lambda_{2,h}^n + \gamma g_2(\boldsymbol{d}_h^n, s^n)\right]_- [\delta s]\boldsymbol{v}_h \cdot \boldsymbol{n}_{\boldsymbol{\varphi}} \\
&\qquad = \int_{\Gamma_{C_2}} \gamma \left[-1 + \mathcal{H}\left(\lambda_{2,h}^n + \gamma g_2(\boldsymbol{d}_h^n, s^n)\right)\right] D_s g_2(\boldsymbol{d}_h^n, s^n)[\delta s]\boldsymbol{v}_h \cdot \boldsymbol{n}_{\boldsymbol{\varphi}}, \quad \forall \boldsymbol{v}_h \in \mathbf{V}_h^{\text{sh}},
\end{aligned}$$

where $D_s g_2(\boldsymbol{d}_h^n, s^n)[\delta s]$ is given by (A.6).

Now we compute the directional derivative of the residual term related to the equation of the Lagrange multiplier associated with the moving hook. The derivative of $\langle R_2(\boldsymbol{d}_h^n, \lambda_{2,h}^n, s^n), \mu_h\rangle$ in the direction $\delta\boldsymbol{d}$ reads:

$$\begin{aligned}
&\langle D_{\boldsymbol{d}} R_2\ (\boldsymbol{d}_h^n, \lambda_{2,h}^n, s^n)[\delta\boldsymbol{d}], \mu_h\rangle \\
&\qquad = -\frac{1}{\gamma} \int_{\Gamma_{C_2}} D_{\boldsymbol{d}} \left(\lambda_{2,h}^n + \left[\lambda_{2,h}^n + \gamma g_2(\boldsymbol{d}_h^n, s^n)\right]_-\right) [\delta\boldsymbol{d}]\mu_h \\
&\qquad = -\int_{\Gamma_{C_2}} \left[-1 + \mathcal{H}\left(\lambda_{2,h}^n + \gamma g_2(\boldsymbol{d}_h^n, s^n)\right)\right] D_{\boldsymbol{d}} g_2[\delta\boldsymbol{d}]\mu_h, \quad \forall \mu_h \in \Lambda_{2,h},
\end{aligned} \tag{A.18}$$

where $D_{\boldsymbol{d}} g_2(\boldsymbol{d}_h^n, s^n)[\delta \boldsymbol{d}]$ is given by (A.6). The derivative of $\langle R_2(\boldsymbol{d}_h^n, \lambda_{2,h}^n, s^n), \mu_h \rangle$ in the direction of $\delta\lambda_2$ reads:

$$\begin{aligned}\left\langle D_{\lambda_2} R_2(\boldsymbol{d}_h^n, \lambda_{2,h}^n, s^n)\ [\delta\lambda_2], \mu_h \right\rangle & \\ = -\frac{1}{\gamma} \int_{\Gamma_{C_2}} D_{\lambda_2} \left(\lambda_{2,h}^n + \left[\lambda_{2,h}^n + \gamma g_2(\boldsymbol{d}_h^n, s^n) \right]_- \right) [\delta\lambda_2] \mu_h & \\ = -\frac{1}{\gamma} \int_{\Gamma_{C_2}} \mathcal{H}\left(\lambda_{2,h}^n + \gamma g_2(\boldsymbol{d}_h^n, s^n) \right) \delta\lambda_2\ \mu_h, \quad \forall \mu_h \in \Lambda_{2,h}. &\end{aligned} \tag{A.19}$$

The derivative of $\langle R_2(\boldsymbol{d}_h^n, \lambda_{2,h}^n, s^n), \mu_h \rangle$ in the direction of δs reads:

$$\begin{aligned}\langle D_s R_2(\boldsymbol{d}_h^n, \lambda_{2,h}^n, s^n)[\delta s], \mu_h \rangle &= -\frac{1}{\gamma} \int_{\Gamma_{C_2}} D_s \left(\lambda_{2,h}^n + \left[\lambda_{2,h}^n + \gamma g_2(\boldsymbol{d}_h^n, s^n) \right]_- \right) [\delta s] \mu_h \\ &= -\int_{\Gamma_{C_2}} \left[-1 + \mathcal{H}\left(\lambda_{2,h}^n + \gamma g_2(\boldsymbol{d}_h^n, s^n) \right) \right] D_s g_2[\delta s] \mu_h, \quad \forall \mu_h \in \Lambda_{2,h},\end{aligned}$$

where $D_s g_2(\boldsymbol{d}_h^n, s^n)[\delta s]$ is given by (A.6).

The terms $\langle D_{\boldsymbol{d}} R_3(\boldsymbol{d}_h^n, \lambda_{1,h}^n)[\delta \boldsymbol{d}], \mu_h \rangle$ and $\langle D_{\lambda_1} R_3(\boldsymbol{d}_h^n, \lambda_{1,h}^n)[\delta\lambda_1], \mu_h \rangle$ can be obtained in an analogous way as (A.18) and (A.19), respectively.

Finally, it remains to derive the terms corresponding to the residual associated with the hook motion. The derivative of $R_4(\boldsymbol{d}_h^n, \lambda_{2,h}^n, s^n)$ in direction $\delta \boldsymbol{d}$ reads:

$$\begin{aligned}D_{\boldsymbol{d}} R_4(\boldsymbol{d}_h^n, \lambda_{2,h}^n, s^n)[\delta \boldsymbol{d}] &= -\int_{\Gamma_{C_2}} D_{\boldsymbol{d}} \left[\lambda_{2,h}^n + \gamma g_2(\boldsymbol{d}_h^n, s^n) \right]_- [\delta \boldsymbol{d}] \boldsymbol{n}_{\boldsymbol{\varphi}} \cdot \boldsymbol{e}_y \\ &\quad - \int_{\Gamma_{C_2}} \left[\lambda_{2,h}^n + \gamma g_2(\boldsymbol{d}_h^n, s^n) \right]_- D_{\boldsymbol{d}} \boldsymbol{n}_{\boldsymbol{\varphi}}[\delta \boldsymbol{d}] \cdot \boldsymbol{e}_y \\ &= -\int_{\Gamma_{C_2}} \gamma \left[-1 + \mathcal{H}\left(\lambda_{2,h}^n + \gamma g_2(\boldsymbol{d}^n, s^n) \right) \right] D_{\boldsymbol{d}} g_2[\delta \boldsymbol{d}] \boldsymbol{n}_{\boldsymbol{\varphi}} \cdot \boldsymbol{e}_y \\ &\quad - \int_{\Gamma_{C_2}} \left[\lambda_{2,h}^n + \gamma g_2(\boldsymbol{d}_h^n, s^n) \right]_- D_{\boldsymbol{d}} \boldsymbol{n}_{\boldsymbol{\varphi}}[\delta \boldsymbol{d}] \boldsymbol{e}_y,\end{aligned}$$

where $D_{\boldsymbol{d}} g_2(\boldsymbol{d}_h^n, s^n)[\delta \boldsymbol{d}]$ and $D_{\boldsymbol{d}} \boldsymbol{n}_{\boldsymbol{\varphi}}[\delta \boldsymbol{d}]$ can be found in equations (A.6) and (A.10), respectively. The derivative of $R_4(\boldsymbol{d}_h^n, \lambda_{2,h}^n, s^n)$ in direction $\delta\lambda_2$ reads:

$$\begin{aligned}D_{\lambda_2} R_4(\boldsymbol{d}_h^n, \lambda_{2,h}^n, s^n)[\delta\lambda_2] &= -\int_{\Gamma_{C_2}} D_{\lambda_2} \left[\lambda_{2,h}^n + \gamma g_2(\boldsymbol{d}_h^n, s^n) \right]_- [\delta\lambda_2] \boldsymbol{n}_{\boldsymbol{\varphi}} \cdot \boldsymbol{e}_y \\ &= -\int_{\Gamma_{C_2}} \gamma \left[-1 + \mathcal{H}\left(\lambda_{2,h}^n + \gamma g_2(\boldsymbol{d}_h^n, s^n) \right) \right] \delta\lambda_2\ \boldsymbol{n}_{\boldsymbol{\varphi}} \cdot \boldsymbol{e}_y.\end{aligned}$$

The derivative of $R_4(\boldsymbol{d}_h^n, \lambda_{2,h}^n, s^n)$ in direction δs reads:

$$
\begin{aligned}
&D_s R_4(\boldsymbol{d}_h^n, \lambda_{2,h}^n, s^n)[\delta s] \\
&\quad = m\, D_s \left(\frac{s^n - 2s^{n-1} + s^{n-2}}{(\Delta t)^2} \right) [\delta s] - \int_{\Gamma_{C_2}} D_s \left[\lambda_{2,h}^n + \gamma g_2(\boldsymbol{d}_h^n, s^n) \right]_- [\delta s] \boldsymbol{e}_y \cdot \boldsymbol{n}_{\boldsymbol{\varphi}} \\
&\quad = m \frac{\delta s}{(\Delta t)^2} - \int_{\Gamma_{C_2}} \left[-1 + \mathcal{H} \left(\lambda_{2,h}^n + \gamma g_2(\boldsymbol{d}_h^n, s^n) \right) \right] \frac{\boldsymbol{n}_{\boldsymbol{\pi}}}{\boldsymbol{n}_{\boldsymbol{\pi}} \cdot \boldsymbol{n}_{\boldsymbol{\varphi}}} \delta s\, \boldsymbol{e}_y \cdot \boldsymbol{n}_{\boldsymbol{\varphi}}.
\end{aligned}
$$

A.4.2 Nitsche's method

The residuals of (3.22) are:

$$
\begin{aligned}
\langle R_1(\boldsymbol{d}_h^n, s^n), \boldsymbol{v}_h \rangle &= \langle R_{1,\text{Shell}}(\boldsymbol{d}_h^n), \boldsymbol{v}_h \rangle + \langle R_{1,Moving}(\boldsymbol{d}_h^n, s^n), \boldsymbol{v}_h \rangle + \langle R_{1,Static}(\boldsymbol{d}_h^n), \boldsymbol{v}_h \rangle \\
&= \underbrace{\int_\Omega \rho \frac{\boldsymbol{d}_h^n - 2\boldsymbol{d}^{n-1} + \boldsymbol{d}^{n-2}}{(\Delta t)^2} \cdot \boldsymbol{v}_h \; + a_h(\boldsymbol{d}_h^n; \boldsymbol{v}_h)}_{\langle R_{1,\text{Shell}}(\boldsymbol{d}_h^n), \boldsymbol{v}_h \rangle} \\
&\quad + \underbrace{\int_{\Gamma_{C_2}} [-\gamma g_2(\boldsymbol{d}_h^n, s^n) - \boldsymbol{\Pi}(\boldsymbol{d}_h^n) \boldsymbol{n}_x \cdot \boldsymbol{n}_{\boldsymbol{\varphi}})]_+ \boldsymbol{v}_h \cdot \boldsymbol{n}_{\boldsymbol{\varphi}}}_{\langle R_{1,Moving}(\boldsymbol{d}_h^n, s^n), \boldsymbol{v}_h \rangle} \\
&\quad + \underbrace{\int_{\Gamma_{C_1}} [-\gamma g_1(\boldsymbol{d}_h^n) - \boldsymbol{\Pi}(\boldsymbol{d}_h^n) \boldsymbol{n}_x \cdot \boldsymbol{n}_{\boldsymbol{\varphi}}]_+ \boldsymbol{v}_h \cdot \boldsymbol{n}_{\boldsymbol{\varphi}}}_{\langle R_{1,Static}(\boldsymbol{d}_h^n), \boldsymbol{v}_h \rangle},
\end{aligned}
$$

where the first contribution is the residual of the 3D-shell and the last two are the contact contributions of the moving hook and of the static one, respectively, and

$$
R_2(\boldsymbol{d}_h^n, s^n) = m \frac{s^n - 2s^{n-1} + s^{n-2}}{(\Delta t)^2} - f - \int_{\Gamma_{C_2}} [-g_2(\boldsymbol{d}_h^n, s^n)]_+ \boldsymbol{e}_y \cdot \boldsymbol{n}_{\boldsymbol{\varphi}}.
$$

To solve numerically the previous nonlinear system, we apply a Newton based algorithm approach (see Algorithm 2) that requires the solution of a tangent problem with the following block structure:

$$
\underbrace{\begin{bmatrix} D_{\boldsymbol{d}} R_1(\boldsymbol{d}_h^n, s^n) & D_{\boldsymbol{s}} R_1(\boldsymbol{d}_h^n, s^n) \\ D_{\boldsymbol{d}} R_2(\boldsymbol{d}_h^n, s^n) & D_{\boldsymbol{s}} R_2(\boldsymbol{d}_h^n, s^n) \end{bmatrix}}_{J^n(\boldsymbol{d}_h^n, s^n)} \begin{bmatrix} \delta \boldsymbol{d} \\ \delta s \end{bmatrix} = \begin{bmatrix} -R_1(\boldsymbol{d}_h^n, s^n) \\ -R_2(\boldsymbol{d}_h^n, s^n) \end{bmatrix}.
$$

To compute the Jacobian, we need the directional derivative of the first Piola-Kirchhoff stress tensor in direction $\delta \boldsymbol{d}$, that involves obtaining the directional derivatives of the deformation gradient tensor and of the second Piola-Kirchhoff stress tensor. The directional derivatives of $\boldsymbol{F}(\boldsymbol{d})$ and $\boldsymbol{\Sigma}(\boldsymbol{d})$ in direction $\delta \boldsymbol{d}$ are:

$$
D_{\boldsymbol{d}} \boldsymbol{F}(\boldsymbol{d})[\delta \boldsymbol{d}] = \nabla_x (\delta \boldsymbol{d}), \tag{A.20}
$$

$$
D_{\boldsymbol{d}} \boldsymbol{\Sigma}(\boldsymbol{d})[\delta \boldsymbol{d}] = D_{\boldsymbol{d}} \left(\frac{\partial W}{\partial \boldsymbol{E}} \right) [\delta \boldsymbol{d}] = \frac{\partial^2 W}{\partial \boldsymbol{E}^2}(\boldsymbol{d}) : D_{\boldsymbol{d}} \boldsymbol{E}(\boldsymbol{d})[\delta \boldsymbol{d}],
$$

where we have considered that for an hyperelastic law it holds that $\boldsymbol{\Sigma} = \frac{\partial W}{\partial \boldsymbol{E}}$. Applying the chain rule, and recalling that $\boldsymbol{\Pi}(\boldsymbol{d}) = \boldsymbol{F}(\boldsymbol{d})\boldsymbol{\Sigma}(\boldsymbol{d})$, it follows that:

$$D_{\boldsymbol{d}}\boldsymbol{\Pi}(\boldsymbol{d})[\delta\boldsymbol{d}] = D_{\boldsymbol{d}}\boldsymbol{F}(\boldsymbol{d})[\delta\boldsymbol{d}]\boldsymbol{\Sigma}(\boldsymbol{d}) + \boldsymbol{F}(\boldsymbol{d})D_{\boldsymbol{d}}\boldsymbol{\Sigma}(\boldsymbol{d})[\delta\boldsymbol{d}].$$

As before, we can split the directional derivative of $R_1(\boldsymbol{d}_h^n, s^n)$ in three terms:

$$\begin{aligned}\langle D_{\boldsymbol{d}}R_1(\boldsymbol{d}_h^n, s^n)[\delta\boldsymbol{d}], \boldsymbol{v}_h\rangle = &\langle D_{\boldsymbol{d}}R_{1,\text{Shell}}(\boldsymbol{d}_h^n)[\delta\boldsymbol{d}], \boldsymbol{v}_h\rangle \\ &+ \langle D_{\boldsymbol{d}}R_{1,Moving}(\boldsymbol{d}_h^n, s^n)[\delta\boldsymbol{d}], \boldsymbol{v}_h\rangle \\ &+ \langle D_{\boldsymbol{d}}R_{1,Static}(\boldsymbol{d}_h^n)[\delta\boldsymbol{d}], \boldsymbol{v}_h\rangle,\end{aligned}$$

and

$$\langle D_s R_1(\boldsymbol{d}_h^n, s^n)[\delta s], \boldsymbol{v}_h\rangle = \langle D_s R_{1,Moving}(\boldsymbol{d}_h^n, s^n)[\delta s], \boldsymbol{v}_h\rangle.$$

The part that corresponds to the shell, is explained in Section 2.2.2.2, Chapter 2. Then, the Jacobian for the contact part for the moving hook is:

$$\begin{aligned}&\langle D_{\boldsymbol{d}}R_{1,Moving}\ (\boldsymbol{d}_h^n, s^n)[\delta\boldsymbol{d}], \boldsymbol{v}_h\rangle \\ &\quad= \int_{\Gamma_{C_2}} D_{\boldsymbol{d}}[-\gamma g_2(\boldsymbol{d}_h^n, s^n) - \boldsymbol{\Pi}(\boldsymbol{d}_h^n)\boldsymbol{n}_x\cdot\boldsymbol{n}_{\boldsymbol{\varphi}}]_+[\delta\boldsymbol{d}]\boldsymbol{v}_h\cdot\boldsymbol{n}_{\boldsymbol{\varphi}} \\ &\quad+ \int_{\Gamma_{C_2}} [-\gamma g_2(\boldsymbol{d}_h^n, s^n) - \boldsymbol{\Pi}(\boldsymbol{d}_h^n)\boldsymbol{n}_x\cdot\boldsymbol{n}_{\boldsymbol{\varphi}}]_+\boldsymbol{v}_h\cdot D_{\boldsymbol{d}}\boldsymbol{n}_{\boldsymbol{\varphi}}[\delta\boldsymbol{d}] \\ &\quad= -\int_{\Gamma_{C_2}} \mathcal{H}\left(-\gamma g_2(\boldsymbol{d}_h^n, s^n) - \boldsymbol{\Pi}(\boldsymbol{d}_h^n)\boldsymbol{n}_x\cdot\boldsymbol{n}_{\boldsymbol{\varphi}}\right)\gamma D_{\boldsymbol{d}}g_2(\boldsymbol{d}_h^n, s^n)[\delta\boldsymbol{d}]\boldsymbol{v}_h\cdot\boldsymbol{n}_{\boldsymbol{\varphi}} \\ &\quad- \int_{\Gamma_{C_2}} \mathcal{H}\left(-\gamma g_2(\boldsymbol{d}_h^n, s^n) - \boldsymbol{\Pi}(\boldsymbol{d}_h^n)\boldsymbol{n}_x\cdot\boldsymbol{n}_{\boldsymbol{\varphi}}\right) D_{\boldsymbol{d}}\boldsymbol{F}[\delta\boldsymbol{d}]\frac{\partial W}{\partial \boldsymbol{E}}\boldsymbol{n}_x\cdot\boldsymbol{n}_{\boldsymbol{\varphi}}\boldsymbol{v}_h\cdot\boldsymbol{n}_{\boldsymbol{\varphi}} \\ &\quad- \int_{\Gamma_{C_2}} \mathcal{H}\left(-\gamma g_2(\boldsymbol{d}_h^n, s^n) - \boldsymbol{\Pi}(\boldsymbol{d}_h^n)\boldsymbol{n}_x\cdot\boldsymbol{n}_{\boldsymbol{\varphi}}\right)\boldsymbol{F}\frac{\partial^2 W}{\partial \boldsymbol{E}^2} : D_{\boldsymbol{d}}\boldsymbol{E}[\delta\boldsymbol{d}]\boldsymbol{n}_x\cdot\boldsymbol{n}_{\boldsymbol{\varphi}}\boldsymbol{v}_h\cdot\boldsymbol{n}_{\boldsymbol{\varphi}} \\ &\quad- \int_{\Gamma_{C_2}} \mathcal{H}\left(-\gamma g_2(\boldsymbol{d}_h^n, s^n) - \boldsymbol{\Pi}(\boldsymbol{d}_h^n)\boldsymbol{n}_x\cdot\boldsymbol{n}_{\boldsymbol{\varphi}}\right)\boldsymbol{\Pi}(\boldsymbol{d}_h^n)\boldsymbol{n}_x\cdot D_{\boldsymbol{d}}\boldsymbol{n}_{\boldsymbol{\varphi}}[\delta\boldsymbol{d}]\boldsymbol{v}_h\cdot\boldsymbol{n}_{\boldsymbol{\varphi}} \\ &\quad+ \int_{\Gamma_{C_2}} [-\gamma g_2(\boldsymbol{d}_h^n, s^n) - \boldsymbol{\Pi}(\boldsymbol{d}_h^n)\boldsymbol{n}_x\cdot\boldsymbol{n}_{\boldsymbol{\varphi}}]_+\boldsymbol{v}_h\cdot D_{\boldsymbol{d}}\boldsymbol{n}_{\boldsymbol{\varphi}}[\delta\boldsymbol{d}], \quad \forall\boldsymbol{v}_h\in\mathbf{V}_h^{\text{sh}},\end{aligned}$$

with $D_{\boldsymbol{d}}g_2(\boldsymbol{d}_h^n, s^n)[\delta\boldsymbol{d}]$ and $D_{\boldsymbol{d}}\boldsymbol{n}_{\boldsymbol{\varphi}}[\delta\boldsymbol{d}]$ given by equations (A.6) and (A.10), respectively. The directional derivative of $\boldsymbol{F}(\boldsymbol{d})$ is given by equation (A.20). Similar applies for the term of the static hook.

The derivative of the residual on momentum conservation in direction δs can be obtained similarly as in penalty with the term given by equation (A.22).

The derivative of the hook motion residual, $R_2(\boldsymbol{d}_h^n, s^n)$, in direction $\delta\boldsymbol{d}$, is given by:

$$
\begin{aligned}
&D_{\boldsymbol{d}} R_2(\boldsymbol{d}_h^n, s^n)[\delta\boldsymbol{d}] \\
&\quad = -\int_{\Gamma_{C_2}} D_{\boldsymbol{d}}[-\gamma g_2(\boldsymbol{d}_h^n, s^n) - \boldsymbol{\Pi}(\boldsymbol{d}_h^n)\boldsymbol{n}_x \cdot \boldsymbol{n}_{\boldsymbol{\varphi}}]_+[\delta\boldsymbol{d}]\boldsymbol{e}_y \cdot \boldsymbol{n}_{\boldsymbol{\varphi}} \\
&\quad - \int_{\Gamma_{C_2}} [-\gamma g_2(\boldsymbol{d}_h^n, s^n) - \boldsymbol{\Pi}(\boldsymbol{d}_h^n)\boldsymbol{n}_x \cdot \boldsymbol{n}_{\boldsymbol{\varphi}}]_+ \boldsymbol{e}_y \cdot D_{\boldsymbol{d}}\boldsymbol{n}_{\boldsymbol{\varphi}}[\delta\boldsymbol{d}] \\
&\quad = \int_{\Gamma_{C_2}} \mathcal{H}\left(-\gamma g_2(\boldsymbol{d}_h^n, s^n) - \boldsymbol{\Pi}(\boldsymbol{d}_h^n)\boldsymbol{n}_x \cdot \boldsymbol{n}_{\boldsymbol{\varphi}}\right) \gamma D_{\boldsymbol{d}} g_2(\boldsymbol{d}_h^n, s^n)[\delta\boldsymbol{d}]\boldsymbol{e}_y \cdot \boldsymbol{n}_{\boldsymbol{\varphi}} \\
&\quad + \int_{\Gamma_{C_2}} \mathcal{H}\left(-\gamma g_2(\boldsymbol{d}_h^n, s^n) - \boldsymbol{\Pi}(\boldsymbol{d}_h^n)\boldsymbol{n}_x \cdot \boldsymbol{n}_{\boldsymbol{\varphi}}\right) D_{\boldsymbol{d}}\boldsymbol{F}[\delta\boldsymbol{d}] \frac{\partial W}{\partial \boldsymbol{E}} \boldsymbol{n}_x \cdot \boldsymbol{n}_{\boldsymbol{\varphi}} \boldsymbol{e}_y \cdot \boldsymbol{n}_{\boldsymbol{\varphi}} \\
&\quad + \int_{\Gamma_{C_2}} \mathcal{H}\left(-\gamma g_2(\boldsymbol{d}_h^n, s^n) - \boldsymbol{\Pi}(\boldsymbol{d}_h^n)\boldsymbol{n}_x \cdot \boldsymbol{n}_{\boldsymbol{\varphi}}\right) \boldsymbol{F} \frac{\partial^2 W}{\partial \boldsymbol{E}^2} : D_{\boldsymbol{d}}\boldsymbol{E}[\delta\boldsymbol{d}]\boldsymbol{n}_x \cdot \boldsymbol{n}_{\boldsymbol{\varphi}} \boldsymbol{e}_y \cdot \boldsymbol{n}_{\boldsymbol{\varphi}} \\
&\quad + \int_{\Gamma_{C_2}} \mathcal{H}\left(-\gamma g_2(\boldsymbol{d}_h^n, s^n) - \boldsymbol{\Pi}(\boldsymbol{d}_h^n)\boldsymbol{n}_x \cdot \boldsymbol{n}_{\boldsymbol{\varphi}}\right) \boldsymbol{\Pi}(\boldsymbol{d}_h^n)\boldsymbol{n}_x \cdot D_{\boldsymbol{d}}\boldsymbol{n}_{\boldsymbol{\varphi}}[\delta\boldsymbol{d}]\boldsymbol{e}_y \cdot \boldsymbol{n}_{\boldsymbol{\varphi}} \\
&\quad - \int_{\Gamma_{C_2}} [-\gamma g_2(\boldsymbol{d}_h^n, s^n) - \boldsymbol{\Pi}(\boldsymbol{d}_h^n)\boldsymbol{n}_x \cdot \boldsymbol{n}_{\boldsymbol{\varphi}}]_+ \boldsymbol{e}_y \cdot D_{\boldsymbol{d}}\boldsymbol{n}_{\boldsymbol{\varphi}}[\delta\boldsymbol{d}],
\end{aligned}
$$

with $D_{\boldsymbol{d}} g_2(\boldsymbol{d}_h^n, s^n)[\delta\boldsymbol{d}]$ and $D_{\boldsymbol{d}}\boldsymbol{n}_{\boldsymbol{\varphi}}[\delta\boldsymbol{d}]$ given by equations (A.6) and (A.10), respectively. The directional derivative of $\boldsymbol{F}(\boldsymbol{d})$ is given by equation (A.20). Finally, $D_s R_2(\boldsymbol{d}_h^n, s^n)[\delta s]$ is given by:

$$
\begin{aligned}
D_s R_2(\boldsymbol{d}_h^n, s^n)[\delta s] &= m\, D_s \left(\frac{s^n - 2s^{n-1} + s^{n-2}}{(\Delta t)^2} \right)[\delta s] \\
&\quad - \int_{\Gamma_{C_2}} D_{\boldsymbol{s}} \left[-\gamma g_2(\boldsymbol{d}_h^n, s^n) - \boldsymbol{\Pi}(\boldsymbol{d}_h^n)\boldsymbol{n}_x \cdot \boldsymbol{n}_{\boldsymbol{\varphi}}\right]_+ [\delta\boldsymbol{s}]\boldsymbol{e}_y \cdot \boldsymbol{n}_{\boldsymbol{\varphi}} \\
&= m\frac{\delta s}{(\Delta t)^2} + \int_{\Gamma_{C_2}} \mathcal{H}\left(-\gamma g_2(\boldsymbol{d}_h^n, s^n) - \boldsymbol{\Pi}(\boldsymbol{d}_h^n)\boldsymbol{n}_x \cdot \boldsymbol{n}_{\boldsymbol{\varphi}}\right)) \gamma \frac{\boldsymbol{n}_{\boldsymbol{\pi}}}{\boldsymbol{n}_{\boldsymbol{\pi}} \cdot \boldsymbol{n}_{\boldsymbol{\varphi}}} \delta s\, \boldsymbol{e}_y \cdot \boldsymbol{n}_{\boldsymbol{\varphi}}.
\end{aligned}
$$

A.4.3 Penalty method

The residuals of (3.26) are:

$$
\begin{aligned}
\langle R_1(\boldsymbol{d}_h^n, s^n), \boldsymbol{v}_h\rangle &= \langle R_{1,\text{Shell}}(\boldsymbol{d}_h^n), \boldsymbol{v}_h\rangle + \langle R_{1,Moving}(\boldsymbol{d}_h^n, s^n), \boldsymbol{v}_h\rangle + \langle R_{1,Static}(\boldsymbol{d}_h^n), \boldsymbol{v}_h\rangle \\
&= \underbrace{\int_\Omega \rho \frac{\boldsymbol{d}_h^n - 2\boldsymbol{d}_h^{n-1} + \boldsymbol{d}_h^{n-2}}{(\Delta t)^2} \cdot \boldsymbol{v}_h \; + a_h(\boldsymbol{d}_h^n; \boldsymbol{v}_h)}_{\langle R_{1,\text{Shell}}(\boldsymbol{d}_h^n), \boldsymbol{v}_h\rangle} \\
&\quad + \underbrace{\frac{1}{\varepsilon}\int_{\Gamma_{C_2}} [-g_2(\boldsymbol{d}_h^n, s^n)]_+ \boldsymbol{v}_h \cdot \boldsymbol{n}_{\boldsymbol{\varphi}}}_{\langle R_{1,Moving}(\boldsymbol{d}_h^n, s^n), \boldsymbol{v}_h\rangle} + \underbrace{\frac{1}{\varepsilon}\int_{\Gamma_{C_1}} [-g_1(\boldsymbol{d}_h^n)]_+ \boldsymbol{v}_h \cdot \boldsymbol{n}_{\boldsymbol{\varphi}}}_{\langle R_{1,Static}(\boldsymbol{d}_h^n), \boldsymbol{v}_h\rangle},
\end{aligned}
$$

where the first contribution is the residual of the 3D-shell and last two are the contact contributions of the moving hook and of the static one, respectively, and

$$R_2(\boldsymbol{d}_h^n, s^n) = m\frac{s^n - 2s^{n-1} + s^{n-2}}{(\Delta t)^2} - f - \frac{1}{\varepsilon}\int_{\Gamma_{C_2}} [-g_2(\boldsymbol{d}_h^n, s^n)]_+ \, \boldsymbol{e}_y \cdot \boldsymbol{n}_{\boldsymbol{\varphi}}.$$

To solve numerically the previous nonlinear system, we apply a Newton based algorithm approach (see Algorithm 2) that requires the solution of a tangent problem with the following block structure:

$$\underbrace{\begin{bmatrix} D_{\boldsymbol{d}}R_1(\boldsymbol{d}_h^n, s^n) & D_{\boldsymbol{s}}R_1(\boldsymbol{d}_h^n, s^n) \\ D_{\boldsymbol{d}}R_2(\boldsymbol{d}_h^n, s^n) & D_{\boldsymbol{s}}R_2(\boldsymbol{d}_h^n, s^n) \end{bmatrix}}_{J^n(\boldsymbol{d}_h^n, s^n)} \begin{bmatrix} \delta\boldsymbol{d} \\ \delta s \end{bmatrix} = \begin{bmatrix} -R_1(\boldsymbol{d}_h^n, s^n) \\ -R_2(\boldsymbol{d}_h^n, s^n) \end{bmatrix}.$$

We can split the directional derivative of the residual on momentum conservation, $\langle R_1(\boldsymbol{d}_h^n, s^n), \boldsymbol{v}_h\rangle$, in direction $\delta\boldsymbol{d}$ in three terms:

$$\begin{aligned}\langle D_{\boldsymbol{d}}R_1(\boldsymbol{d}_h^n, s^n)[\delta\boldsymbol{d}], \boldsymbol{v}_h\rangle = {} & \langle D_{\boldsymbol{d}}R_{1,\text{Shell}}(\boldsymbol{d}_h^n)[\delta\boldsymbol{d}], \boldsymbol{v}_h\rangle + \langle D_{\boldsymbol{d}}R_{1,Moving}(\boldsymbol{d}_h^n, s^n)[\delta\boldsymbol{d}], \boldsymbol{v}_h\rangle \\ & + \langle D_{\boldsymbol{d}}R_{1,Static}(\boldsymbol{d}_h^n)[\delta\boldsymbol{d}], \boldsymbol{v}_h\rangle.\end{aligned}$$

The derivation of the term related with the derivative of the shell will be omitted since it has already been explained in Section 2.2.2.2, Chapter 2. The term $\langle D_{\boldsymbol{d}}R_{1,Moving}(\boldsymbol{d}_h^n, s^n)[\delta\boldsymbol{d}], \boldsymbol{v}_h\rangle$ is obtained as follows:

$$\begin{aligned}\langle D_{\boldsymbol{d}}R_{1,Moving}(\boldsymbol{d}_h^n, s^n)[\delta\boldsymbol{d}], \boldsymbol{v}_h\rangle = {} & -\frac{1}{\varepsilon}\int_{\Gamma_{C_2}} \mathcal{H}\left(-g_2(\boldsymbol{d}_h^n, s^n)\right) D_{\boldsymbol{d}}g_2(\boldsymbol{d}_h^n, s^n)[\delta\boldsymbol{d}]\boldsymbol{v}_h \cdot \boldsymbol{n}_{\boldsymbol{\varphi}} \\ & + \frac{1}{\varepsilon}\int_{\Gamma_{C_2}} [-g_2(\boldsymbol{d}_h^n, s^n)]_+ \, \boldsymbol{v}_h \cdot D_{\boldsymbol{d}}\boldsymbol{n}_{\boldsymbol{\varphi}}[\delta\boldsymbol{d}], \quad \forall \boldsymbol{v}_h \in \mathbf{V}_h^{\text{sh}},\end{aligned} \tag{A.21}$$

where $D_{\boldsymbol{d}}g_2(\boldsymbol{d}_h^n, s^n)[\delta\boldsymbol{d}]$ is given by (A.6) and $D_{\boldsymbol{d}}\boldsymbol{n}_{\boldsymbol{\varphi}}[\delta\boldsymbol{d}]$ by (A.10). The derivation of $\langle D_{\boldsymbol{d}}R_{1,Static}(\boldsymbol{d}_h^n)[\delta\boldsymbol{d}], \boldsymbol{v}_h\rangle$ is analogue to the one of equation (A.21). Finally, for the term whose derivative is in direction δs:

$$\langle D_sR_1(\boldsymbol{d}_h^n, s^n)[\delta s], \boldsymbol{v}_h\rangle = \langle D_sR_{1,Moving}(\boldsymbol{d}_h^n, s^n)[\delta s], \boldsymbol{v}_h\rangle,$$

$$\begin{aligned}\langle D_sR_1(\boldsymbol{d}^n, s^n)[\delta s], \boldsymbol{v}\rangle = {} & \frac{1}{\varepsilon}\int_{\Gamma_{C_2}} D_{\boldsymbol{s}}\left[-g_2(\boldsymbol{d}^n, s^n)\right]_+ [\delta s] \, \boldsymbol{v} \cdot \boldsymbol{n}_{\boldsymbol{\varphi}} \\ = {} & -\frac{1}{\varepsilon}\int_{\Gamma_{C_2}} \mathcal{H}\left(-g_2(\boldsymbol{d}^n, s^n)\right) D_sg_2(\boldsymbol{d}^n, s^n)[\delta s] \, \boldsymbol{v} \cdot \boldsymbol{n}_{\boldsymbol{\varphi}}, \quad \forall \boldsymbol{v}_h \in \mathbf{V}_h^{\text{sh}},\end{aligned} \tag{A.22}$$

where $D_sg_2(\boldsymbol{d}^n, s^n)[\delta s]$ is given by (A.6).

For the directional derivative of the residual on the hook motion, $R_2(\boldsymbol{d}_h^n, s^n)$, in direction $\delta\boldsymbol{d}$, it follows that:

$$\begin{aligned} D_{\boldsymbol{d}} R_2(\boldsymbol{d}_h^n, s^n)[\delta\boldsymbol{d}] &= -\frac{1}{\varepsilon}\int_{\Gamma_{C_2}} D_{\boldsymbol{d}}\left[-g_2(\boldsymbol{d}_h^n, s^n)\right]_+ [\delta\boldsymbol{d}]\boldsymbol{e}_y \cdot \boldsymbol{n}_{\boldsymbol{\varphi}} \\ &\quad - \frac{1}{\varepsilon}\int_{\Gamma_{C_2}} \left[-g_2(\boldsymbol{d}_h^n, s^n)\right]_+ \boldsymbol{e}_y \cdot D_{\boldsymbol{d}}\boldsymbol{n}_{\boldsymbol{\varphi}}[\delta\boldsymbol{d}] \\ &= \frac{1}{\varepsilon}\int_{\Gamma_{C_2}} \mathcal{H}\left(-g_2(\boldsymbol{d}_h^n, s^n)\right) D_{\boldsymbol{d}} g_2(\boldsymbol{d}_h^n, s^n)[\delta\boldsymbol{d}]\boldsymbol{e}_y \cdot \boldsymbol{n}_{\boldsymbol{\varphi}} \\ &\quad - \frac{1}{\varepsilon}\int_{\Gamma_{C_2}} \left[-g_2(\boldsymbol{d}_h^n, s^n)\right]_+ \boldsymbol{e}_y \cdot D_{\boldsymbol{d}}\boldsymbol{n}_{\boldsymbol{\varphi}}[\delta\boldsymbol{d}], \end{aligned}$$

with $D_{\boldsymbol{d}} g_2(\boldsymbol{d}_h^n, s^n)[\delta\boldsymbol{d}]$ and $D_{\boldsymbol{d}}\boldsymbol{n}_{\boldsymbol{\varphi}}[\delta\boldsymbol{d}]$ given by equations (A.6) and (A.10), respectively. Finally, $D_{\boldsymbol{s}} R_2(\boldsymbol{d}_h^n, s^n)[\delta s]$ can be obtained as:

$$\begin{aligned} &D_s R_2(\boldsymbol{d}_h^n, s^n)[\delta s] \\ &\qquad = m\, D_s\left(\frac{s^n - 2s^{n-1} + s^{n-2}}{(\Delta t)^2}\right)[\delta s] - \frac{1}{\varepsilon}\int_{\Gamma_{C_2}} D_s\left[-g_2(\boldsymbol{d}_h^n, s^n)\right]_+ [\delta\boldsymbol{s}]\boldsymbol{e}_y \cdot \boldsymbol{n}_{\boldsymbol{\varphi}} \\ &\qquad = m\frac{\delta s}{(\Delta t)^2} + \frac{1}{\varepsilon}\int_{\Gamma_{C_2}} \mathcal{H}\left(-g_2(\boldsymbol{d}_h^n, s^n)\right)\frac{\boldsymbol{n}_{\boldsymbol{\pi}}}{\boldsymbol{n}_{\boldsymbol{\pi}} \cdot \boldsymbol{n}_{\boldsymbol{\varphi}}}\delta s\, \boldsymbol{e}_y \cdot \boldsymbol{n}_{\boldsymbol{\varphi}}. \end{aligned}$$

References

Adams, E. R. and Choi, A. (2012). Using neural networks to predict cardiac arrhythmias. In *2012 IEEE international conference on systems, man, and cybernetics (smc)*, pages 402–407. IEEE.

Akhtar, R., Cruickshank, J. K., Zhao, X., Derby, B., and Weber, T. (2016). A pilot study of scanning acoustic microscopy as a tool for measuring arterial stiffness in aortic biopsies. *Artery Research*, 13:1–5.

Akhtar, R., Sherratt, M. J., Cruickshank, J. K., and Derby, B. (2011). Characterizing the elastic properties of tissues. *Materials Today*, 14(3):96–105.

Alart, P. and Curnier, A. (1988). A generalized newton method for contact problems with friction. *Journal of Theoretical and Applied Mechanics*, 7(1):67–82.

Aletti, M., Gerbeau, J.-F., and Lombardi, D. (2015). Modeling autoregulation in three-dimensional simulations of retinal hemodynamics. *Modeling and Artificial Intelligence in Ophthalmology*, 1:12.

Ambrosi, D. and Pezzuto, S. (2012). Active stress vs. active strain in mechanobiology: Constitutive issues. *Journal of Elasticity*, 107:199–212.

Angus, J. A., Wright, C. E., Jennings, G. L., and Korner, P. I. (2000). Techniques to study the pharmacodynamics of isolated large and small blood vessels. *Journal of Pharmacological and Toxicological Methods*, 44(2):395–407.

Anon (2001). International conference on harmonisation; guidance on s7a safety pharmacology studies for human pharmaceuticals; availability. notice. *Federal Register*, 66(135):36791–36792.

Aston, P. J. e. a. (2018). Title. *Physiological Measurement*, 39:024001.

Atienzar, F. A., Blomme, E. A., Chen, M., Hewitt, P., Kenna, J. G., Labbe, G., Moulin, F., Pognan, F., Roth, A. B., Suter-Dick, L., et al. (2016). Key challenges and opportunities associated with the use of in vitro models to detect human dili: Integrated risk assessment and mitigation plans. *BioMed Research International*, 1.

Bae, Y. H., Liu, S., Byfield, F. J., Janmey, P. A., and Assoian, R. K. (2016). Measuring the stiffness of ex vivo mouse aortas using atomic force microscopy. *Journal of Visualized Experiments*, 116:e54630.

Bardin, M. (2022). *Lipid Mediators of the Resolution of Inflammation in Vascular Ageing*. Doctoral dissertation, Université de Lorraine. English.

Barone, A. C., Salerno, M., Patra, N., Gastaldi, D., Bertarelli, E., Carnelli, D., and Vena, P. (2010). Calibration issues for nanoindentation experiments: direct atomic force microscopy measurements and indirect methods. *Microscopy Research and Technique*, 73(11):996–1004.

Basile, A. O., Yahi, A., and Tatonetti, N. P. (2019). Artificial intelligence for drug toxicity and safety. *Trends in pharmacological sciences*, 40(9):624–635.

Bass, A., Kinter, L., and Williams, P. (2004). Origins, practices and future of safety pharmacology. *Journal of Pharmacological and Toxicological Methods*, 49(3):145–151.

Bass, A. S., Hombo, T., Kasai, C., Kinter, L. B., and Valentin, J. P. (2015). A historical view and vision into the future of the field of safety pharmacology. In Pugsley, M. and Curtis, M., editors, *Principles of Safety Pharmacology*, volume 229 of *Handbook of Experimental Pharmacology*, pages 1–23. Springer, Berlin, Heidelberg.

Belcik, J. T., Qi, Y., Kaufmann, B. A., Xie, A., Bullens, S., Morgan, T. K., Bagby, S. P., Kolumam, G., Kowalski, J., Oyer, J. A., Bunting, S., and Lindner, J. R. (2012). Cardiovascular and systemic microvascular effects of anti-vascular endothelial growth factor therapy for cancer. *Journal of the American College of Cardiology*, 60(7):618–625.

Bellien, J., Iacob, M., and Thuillez, C. (2010). New insights into endothelial dysfunction and arterial stiffness: role of endothelial nitric oxide synthase. *Circulation*, 121(12):1437–1443.

Bellini, C., Ferruzzi, J., Roccabianca, S., Di Martino, E. S., and Humphrey, J. D. (2014). A microstructurally motivated model of arterial wall mechanics with mechanobiological implications. *Annals of Biomedical Engineering*, 42(3):488–502.

Belytschko, T., Liu, W. K., and Moran, B. (2000). *Nonlinear Finite Elements for Continua and Structures*. Wiley.

Benson, D. J. and Hallquist, J. O. (1990). A single surface contact algorithm for the post-buckling analysis of shell structures. *Computer Methods in Applied Mechanics and Engineering*, 78(2):141–163.

Bhatt, S., Northcott, C., Wisialowski, T., Li, D., and Steidl-Nichols, J. (2019). Preclinical to clinical translation of hemodynamic effects in cardiovascular safety pharmacology studies. *Toxicological Sciences*, 169(1):272–279.

Bischoff, M. and Ramm, E. (1997). Shear deformable shell elements for large strains and rotations. *International Journal for Numerical Methods in Engineering*, 40(23):4427–4449.

Bisong, E. (2019). *Building machine learning and deep learning models on Google cloud platform*. Apress, Berkeley, CA, USA.

Bit, A., Suri, J. S., and Ranjani, A. (2020). *Anatomy and physiology of blood vessels*. IOP Publishing.

Boese, J., Bock, M., Schoenberg, S., et al. (2000). Estimation of aortic compliance using magnetic resonance pulse wave velocity measurement. *Physics in Medicine & Biology*, 45:1703–1713.

Bonet, J. and Wood, R. D. (2008). *Nonlinear Continuum Mechanics for Finite Element Analysis*. Cambridge University Press, Cambridge, New York.

Bowes, J., Brown, A. J., Hamon, J., Jarolimek, W., Sridhar, A., Waldron, G., and Whitebread, S. (2012). Reducing safety-related drug attrition: The use of *In Vitro* pharmacological profiling. *Nature Reviews Drug Discovery*, 11(12):909–922.

Brake, K., Gumireddy, A., Tiwari, A., Chauhan, H., and Kumari, D. (2017). In vivo studies for drug development via oral delivery: Challenges, animal models and techniques. *Pharmaceutica Analytica Acta*, 8.

Branch, D. (2014). Ekg interpretation. SlideServe, 16.

Bursztyn, L., Eytan, O., Jaffa, A., and Elad, D. (2007). Mathematical model of excitation–contraction in a uterine smooth muscle cell. *American Journal of Physiology: Cell Physiology*, 292(5):C1816–C1829.

Butlin, M., Tan, I., Spronck, B., and Avolio, A. P. (2020). Measuring arterial stiffness in animal experimental studies. *Arteriosclerosis, Thrombosis, and Vascular Biology*, 40(5):1068–1077.

Cain, J. W. (2011). Mathematics, cardiac phenomena and the diagnosis of pathology. *Future Cardiology*, 7(5):587–590.

Chalapathy, R. and Chawla, S. (2019). Deep learning for anomaly detection: A survey. *arXiv preprint arXiv:1901.03407*.

Chang, Y., Hawkins, B., Du, J., Groundwater, P., Hibbs, D., and Lai, F. (2022). A guide to in silico drug design. *Pharmaceutics*, 15(1):49.

Chapelle, D. and Bathe, K.-J. (2010). *The Finite Element Analysis of Shells - Fundamentals*. Springer-Verlag.

Chapelle, D., Ferent, A., and Bathe, K. J. (2004a). *3d-shell elements and their underlying mathematical model*, volume 14. World Scientific Publishing.

Chapelle, D., Ferent, A., and Bathe, K. J. (2004b). 3D-shell elements and their underlying mathematical model. *Math. Models Methods Appl. Sci.*, 14(1):105–142.

Chen, H., Luo, T., Zhao, X., Lu, X., Huo, Y., and Kassab, G. S. (2013). Microstructural constitutive model of active coronary media. *Biomaterials*, 34(31):7575–7583.

Chen, R. and Snyder, M. (2013). Promise of personalized omics to precision medicine. *Wiley Interdisciplinary Reviews: Systems Biology and Medicine*, 5(1):73–82.

Chouly, F., Fabre, M., Hild, P., Mlika, R., Pousin, J., and Renard, Y. (2017). An overview of recent results on nitsche's method for contact problems. In *Geometrically Unfitted Finite Element Methods and Applications*, pages 93–141. Springer.

Chouly, F. and Hild, P. (2012). On convergence of the penalty method for unilateral contact problems. *Applied Numerical Mathematics*, 65.

Chouly, F. and Hild, P. (2013). Nitsche-based method for unilateral contact problems: Numerical analysis. *SIAM Journal on Numerical Analysis*, 51:1295–1307.

Chouly, F., Hild, P., and Renard, Y. (2015). Symmetric and non-symmetric variants of nitsche's method for contact problems in elasticity: Theory and numerical experiments. *Mathematics of Computation*, 84:1089–1112.

Chouly, F., Hild, P., and Renard, Y. (2023). *Finite Element Approximation of Contact and Friction in Elasticity*. Advances in Mechanics and Mathematics. Birkhäuser Cham, 1 edition.

Chris Delaney, J. A. and Suissa, S. (2009). The case-crossover study design in pharmacoepidemiology. *Statistical Methods in Medical Research*, 18(1):53–65.

Ciarlet, P. G. (1988). *Mathematical Elasticity. Vol. I. Three-dimensional Elasticity*, volume 20 of *Studies in Mathematics and Its Applications*. North-Holland Publishing, Amsterdam.

Clark, J. M. and Glagov, S. (1985). Transmural organization of the arterial media. the lamellar unit revisited. *Arteriosclerosis*, 5:19–34.

Coccarelli, A., Carson, J. M., Aggarwal, A., and Pant, S. (2021). A framework for incorporating 3d hyperelastic vascular wall models in 1d blood flow simulations. *Biomech Model Mechanobiol*, 20(4):1231–1249.

Coccarelli, A., Edwards, D. H., Aggarwal, A., Nithiarasu, P., and Parthimos, D. (2018). A multiscale active structural model of the arterial wall accounting for smooth muscle dynamics. *J R Soc Interface*, 15(139):20170732.

Committee, I. R. A. (1985). *Principles for the Utilization and Care of Vertebrate Animals Used in Testing, Research, and Training*. Office of Science and Technology Policy, Washington, DC.

Cook, D., Brown, D., Alexander, R., March, R., Morgan, P., Satterthwaite, G., and Pangalos, M. N. (2014). Lessons learned from the fate of astrazeneca's drug pipeline: A five-dimensional framework. *Nature Reviews Drug Discovery*, 13:419.

Dahl, S. L. M., Vaughn, M. E., Hu, J. J., Driessen, N. J. B., Baaijens, F. P. T., and Humphrey, J. D. (2008). A microstructurally motivated model of the mechanical behavior of tissue engineered blood vessels. *Ann Biomed Eng*, 36:1782–1792.

Dau, H. A., Ciesielski, V., and Song, A. (2014). Anomaly detection using replicator neural networks trained on examples of one class. In *Asia-Pacific Conference on Simulated Evolution and Learning*, pages 311–322.

Davidson, I. and Satyanarayana, A. (2003). Speeding up k-means clustering by bootstrap averaging. In *IEEE data mining workshop on clustering large data sets*.

de Carvalho, A. and Freitas, A. (2009). A tutorial on multi-label classification techniques. In *Foundations of Computational Intelligence*, volume 5 of *Studies in Computational Intelligence*. Springer, Berlin, Heidelberg.

De Moudt, S., Hendrickx, J., Neutel, C., De Munck, D., Leloup, A., De Meyer, G., Martinet, W., and Fransen, P. (2022a). Aortic stiffness in l-name treated c57bl/6 mice displays a shift from early endothelial dysfunction to late-term vascular smooth muscle cell dysfunction. *Frontiers in Physiology*, 13:874015.

De Moudt, S., Hendrickx, J. O., Neutel, C., De Munck, D., Leloup, A., De Meyer, G. R. Y., and et al. (2022b). Progressive aortic stiffness in aging c57bl/6 mice displays altered contractile behaviour and extracellular matrix changes. *Communications Biology*, 5(1):605.

De Moudt, S., Leloup, A., and Fransen, P. (2021). Aortic stiffness hysteresis in isolated mouse aortic segments is intensified by contractile stimuli, attenuated by age, and reversed by elastin degradation. *Frontiers in Physiology*, 12:723972.

Decoene, A., Martin, S., and Vergnet, F. (2023). A continuum active structure model for the interaction of cilia with a viscous fluid. *Journal of Applied Mathematics and Mechanics / Zeitschrift für Angewandte Mathematik und Mechanik*.

Deore, A. B., Dhumane, J. R., Wagh, H. V., and Sonawane, R. B. (2019). The stages of drug discovery and development process. *Asian Journal of Pharmaceutical Research and Development*, 7(6):62–67.

Dorf, R. and A. Svoboda, J. (2006). *Introduction to Electric Circuits*. John Wiley, 7th edition.

Doupis, J., Papanas, N., Cohen, A., McFarlan, L., and Horton, E. (2016). Pulse wave analysis by applanation tonometry for the measurement of arterial stiffness. *The Open Cardiovascular Medicine Journal*, 10:188–195.

Easter, A., Bell, M. E., Damewood, J. R., J., Redfern, W. S., Valentin, J. P., Winter, M. J., Fonck, C., and Bialecki, R. A. (2009). Approaches to seizure risk assessment in preclinical drug discovery. *Drug Discovery Today*, 14(17):876–884.

Ebenstein, D. M. and Pruitt, L. A. (2006). Nanoindentation of biological materials. *Nano Today*, 1(3):26–33.

Fabre, M., Pozzolini, C., , and Renard, Y. (2021). Nitsche-based models for the unilateral contact of plates. *ESAIM: M2AN*, 55:S941–S967.

Fay, F. and Delise, C. (1973). Contraction of isolated smooth-muscle cells—structural changes. *Proceedings of the National Academy of Sciences of the United States of America*, 70(3):641–645.

Ferri, N., Siegl, P., Corsini, A., Herrmann, J., Lerman, A., and Benghozi, R. (2013). Drug attrition during pre-clinical and clinical development: understanding and managing drug-induced cardiotoxicity. *Pharmacology & Therapeutics*.

Fetics, B., Nevo, E., Chen, C.-H., and Kass, D. (1999). Parametric model derivation of transfer function for noninvasive estimation of aortic pressure by radial tonometry. *IEEE Transactions on Biomedical Engineering*, 46(6):698–706.

Flaten, M. A., Simonsen, T., and Olsen, H. (1999). Drug-related information generates placebo and nocebo responses that modify the drug response. *Psychosomatic Medicine*, 61(2):250–255.

Francavilla, A. and Zienkiewicz, O. C. (1975). A note on numerical computation of elastic contact problems. *International Journal for Numerical Methods in Engineering*, 9(4):913–924.

Gasser, T. C., Ogden, R. W., and Holzapfel, G. A. (2006). Hyperelastic modelling of arterial layers with distributed collagen fibre orientations. *J. R. Soc. Interface*, 3:15–35.

Gestrelius, S. and Borgström, P. (1986). A dynamic model of smooth muscle contraction. *Biophys J*, 50:157–169.

Geymonat, G. and Ciarlet, P. G. (1982). Sur les lois de comportement en élasticité non linéaire compressible. *CR Acad. Sci. Paris Sér. II*, 295:423–426.

Ghosh, A., Dharmarajan, A., Swain, P. K., Das, D., Verma, P., and Tripathy, P. R. (2019). Impact of cardiovascular factors on pulse wave velocity and total vascular resistance in different age group patients with cardiovascular disorders. *Curr Aging Sci*, 11(4):261–268.

Gimbrone, M. A. and García-Cardeña, G. (2016). Endothelial cell dysfunction and the pathobiology of atherosclerosis. *Circulation Research*, 118(4):620–636.

Gintant, G., Sager, P. T., and Stockbridge, N. (2016). Evolution of strategies to improve preclinical cardiac safety testing. *Nature Reviews Drug Discovery*, 15(7):457–471.

Goh, J.-Y., Weaver, R. J., Dixon, L., Platt, N. J., and Roberts, R. A. (2015). Development and use of in vitro alternatives to animal testing by the pharmaceutical industry 1980-2013. *Toxicology Research*, 4(6):1297–1307.

Gonzalez-Clemente, J.-M., Albert, A., Albert, L., Giménez-Palop, O., Romero, A., Eugenio, B., Vendrell, J., and Llauradó, G. (2021). Arterial stiffness in type 1 diabetes: The case for the arterial wall itself as a target organ. *Journal of Clinical Medicine*, 10(16).

Graham, H. K., Akhtar, R., Kridiotis, C., Derby, B., Kundu, T., Trafford, A. W., et al. (2011). Localised micro-mechanical stiffening in the ageing aorta. *Mechanisms of Ageing and Development*, 132:459–467.

Greene, N. and Naven, R. (2009). Early toxicity screening strategies. *Current opinion in drug discovery and development*, 12:90–7.

Grotenhuis, H. B., Westenberg, J. J. M., Steendijk, P., van der Geest, R. J., Ottenkamp, J., Bax, J. J., Jukema, J. W., and de Roos, A. (2009). Validation and reproducibility of aortic pulse wave velocity as assessed with velocity-encoded mri. *Journal of Magnetic Resonance Imaging*, 30(3):521–526.

Gu, T., Korosec, F., Block, W., et al. (2005). Pc vipr: a high-speed 3d phase-contrast method for flow quantification and high-resolution angiography. *AJNR American Journal of Neuroradiology*, 26:743–749.

Gul, R. and Bernhard, S. (2017). Optimal measurement locations for diagnosis of aortic stenosis and aneurysms in a lumped parameter model of systemic circulation using sensitivity analysis. *International Journal of Biomath*, 10:175116.

Gul, R., Schuette, C., and Bernhard, S. (2016). Mathematical modeling and sensitivity analysis of arterial anastomosis in arm arteries. *Applied Mathematics and Computation*, 40:7724–7738.

Guns, P. D., Guth, B. D., Braam, S., Kosmidis, G., Matsa, E., Delaunois, A., Gryshkova, V., Bernasconi, S., Knot, H. J., Shemesh, Y., Chen, A., Markert, M., Fernández, M. A., Lombardi, D., Grandmont, C., Cillero-Pastor, B., Heeren, R. M. A., Martinet, W., Woolard, J., Skinner, M., Segers, V. F. M., Franssen, C., Van Craenenbroeck, E. M., Volders, P. G. A., Pauwelyn, T., Braeken, D., Yanez, P., Correll, K., Yang, X., Prior, H., Kismihók, G., De Meyer, G. R. Y., and Valentin, J.-P. (2020). Inspire: A european training network to foster research and training in cardiovascular safety pharmacology. *Journal of Pharmacological and Toxicological Methods*, 105:106889.

Guns, P. J. (2020). "inspire": A european training network in safety pharmacology creating opportunities for 15 phd students. *Journal of Pharmacological and Toxicological Methods*, 105:106838.

Gustafsson, T., Stenberg, R., and Videman, J. (2019). A stabilised finite element method for the plate obstacle problem. *BIT*, 59(1):97–124.

Hallquist, J., Goudreau, G., and Benson, D. (1985). Sliding interfaces with contact-impact in large-scale lagrangian computations. *Computer Methods in Applied Mechanics and Engineering*, 51(1):107–137.

Hansen, N. (2016). The cma evolution strategy: A tutorial. *arXiv*. https://arxiv.org/abs/1604.00772.

Hansen, T. R., Dineen, D. X., and Pullen, G. L. (1980). Orientation of arterial smooth muscle and strength of contraction of aortic strips from doca-hypertensive rats. *Blood Vessels*, 17:302–311.

Harrison, R. K. (2016). Phase ii and phase iii failures: 2013–2015. *Nature Reviews Drug Discovery*, 15:817.

Hasselgren, C., Muthas, D., Ahlberg, E., Andersson, S., Carlsson, L., Noeske, T., Stå lring, J., and Boyer, S. (2013). Chemoinformatics and beyond. In Bajorath, J., editor, *Chemoinformatics for Drug Discovery*. Wiley Online Library, Hoboken, NJ.

Hawkins, S., He, H., Williams, G., and Baxter, R. (2002). Outlier detection using replicator neural networks. In *DaWaK 2002*, volume 2454 of *Lecture Notes in Computer Science*, page 170–180. Springer, Heidelberg.

Hindmarsh, A. C. and Petzold, L. R. (2005). Lsoda, ordinary differential equation solver for stiff or non-stiff system. NEA. http://www.nea.fr/abs/html/uscd1227.html.

Hodge, V. and Austin, J. (2004). A survey of outlier detection methodologies. *Artificial Intelligence Review*, 22(2):85–126.

Hollander, Y., Durban, D., Lu, X., Kassab, G. S., and Lanir, Y. (2011). Experimentally validated microstructural 3d constitutive model of coronary arterial media. *J Biomech Eng*, 133:031007.

Holzapfel, G. A., Gasser, T. C., and Ogden, R. W. (2000). A new constitutive framework for arterial wall mechanics and a comparative study of material models. *J. Elast.*, 61:1–48.

Holzapfel, G. A., Sommer, G., Gasser, C. T., and Regitnig, P. (2005). Determination of layer-specific mechanical properties of human coronary arteries with nonatherosclerotic intimal thickening and related constitutive modeling. *American Journal of Physiology-Heart and Circulatory Physiology*, 289(5):H2048–H2058.

Hope, M., Sedlic, T., and Dyverfeldt, P. (2013). Cardiothoracic magnetic resonance flow imaging. *Journal of Thoracic Imaging*, 28:217–230.

Hornberg, J. J., Laursen, M., Brenden, N., Persson, M., Thougaard, A. V., Toft, D. B., and Mow, T. (2014). Exploratory toxicology as an integrated part of drug discovery. part i: Why and how. *Drug Discovery Today*, 19(8):1131–1136.

Hosseini, H. G., Luo, D., and Reynolds, K. J. (2006). The comparison of different feed forward neural network architectures for ecg signal diagnosis. *Medical engineering & physics*, 28(4):372–378.

Hughes, T. J., Taylor, R. L., Sackman, J. L., Curnier, A., and Kanoknukulchai, W. (1976). A finite element method for a class of contact-impact problems. *Computer Methods in Applied Mechanics and Engineering*, 8(3):249–276.

Ingber, D. (2022). Human organs-on-chips for disease modelling, drug development and personalized medicine. *Nature Reviews Genetics*, 23:467–491.

International Council for Harmonisation of Technical Requirements for Pharmaceuticals for Human Use (2015). Ich guidelines for good clinical practice. ICH. Available at: https://www.ich.org/page/ich-guidelines.

Jackson, S. J., Andrews, N., Ball, D., Bellantuono, I., Gray, J., Hachoumi, L., Holmes, A., Latcham, J., Petrie, A., Potter, P., Rice, A., Ritchie, A., Stewart, M., Strepka, C., Yeoman, M., and Chapman, K. (2017). Does age matter? the impact of rodent age on study outcomes. *Lab Animal*, 51(2):160–169.

Jain, A. K., Murty, M. N., and Flynn, P. J. (1999). Data clustering. *ACM Computing Surveys*, 31(3):264–323.

Jin, W., Chowienczyk, P., and Alastruey, J. (2020). An in silico simulation of flow-mediated dilation reveals that blood pressure and other factors may influence the response independent of endothelial function. *Am J Physiol Heart Circ Physiol*, 318(5):H1337–H1345.

Johnson, S. G. (2014). The nlopt nonlinear-optimization package. http://github.com/stevengj/nlopt.

Jun, T. J., Nguyen, H. M., Kang, D., Kim, D., Kim, D., and Kim, Y. H. (2018). Ecg arrhythmia classification using a 2-d convolutional neural network. arXiv preprint arXiv:1804.06812.

Kabil, J., Belguerras, L., Trattnig, S., Pasquier, C., Felblinger, J., and Missoffe, A. (2016). A review of numerical simulation and analytical modeling for medical devices safety in mri. *Yearbook of Medical Informatics*, pages 152–158.

Kaelo, P. and Ali, M. M. (2006). Some variants of the controlled random search algorithm for global optimization. *Journal of Optimization Theory and Applications*, 130(2):253–264.

Kamensky, D., Xu, F., Lee, C.-H., Yan, J., Bazilevs, Y., and Hsu, M.-C. (2018). A contact formulation based on a volumetric potential: Application to isogeometric simulations of atrioventricular valves. *Computer Methods in Applied Mechanics and Engineering*, 330:522–546.

Karpinski, M., Khoma, V., Dudvkevych, V., Khoma, Y., and Sabodashko, D. (2018). Autoencoder neural networks for outlier correction in ecg-based biometric identification. In *2018 IEEE 4th international symposium on wireless systems within the international conferences on intelligent data acquisition and advanced computing systems (IDAACS-SWS)*, pages 210–215.

Kerage, D., Brindley, D. N., and Hemmings, D. G. (2014). Review: novel insights into the regulation of vascular tone by sphingosine 1-phosphate. *Placenta*, 35:S86–S92.

Kikuchi, N. and Oden, J. T. (1988). *Contact Problems in Elasticity: A Study of Variational Inequalities and Finite Element Methods*. Society for Industrial and Applied Mathematics (SIAM).

Kikuchi, N. and Song, Y. (1981). Penalty/finite-element approximation of a class of unilateral problems in linear elasticity. *Quarterly of Applied Mathematics*, 39.

Kovalcsik, R., Devlin, T., Loux, S., Martinek, M., May, J., Pickering, T., Tapp, R., Wilson, S., and Serota, D. (2006). Animal reuse: Balancing scientific integrity and animal welfare. *Lab Animal (NY)*, 35(9):49–53.

Laborde, P. and Renard, Y. (2008). Fixed point strategies for elastostatic factional contact problems. *Mathematical Methods in the Applied Sciences*, 31:415 – 441.

Lacolley, P., Regnault, V., Segers, P., and Laurent, S. (2017). Vascular smooth muscle cells and arterial stiffening: Relevance in development, aging, and disease. *Physiol Rev*, 97(4):1555–1617.

LaDisa, J. F., Guler, I., Olson, L. E., Hettrick, D. A., Kersten, J. R., Warltier, D. C., and Pagel, P. S. (2003). Three-dimensional computational fluid dynamics modeling of alterations in coronary wall shear stress produced by stent implantation. *Annals of Biomedical Engineering*, 31(8):972–980.

Laffon, E., Marthan, R., Montaudon, M., et al. (2005). Feasibility of aortic pulse pressure and pressure wave velocity mri measurement in young adults. *Journal of Magnetic Resonance Imaging*, 21:53–58.

Lafta, M. and Hassanain, A. (2008). Engineering modeling of human cardiovascular system. *AlNahrain University, College of Engineering Journal - NUCEJ*, 11:307–314.

Langewouters, G., Goedhard, W., and Wesseling, K. (1985a). The effect of aging and sclerosis on the viscoelastic properties of the human thoracic aorta. *Tijdschrift voor Gerontologie en Geriatrie*, 16:61–70.

Langewouters, G., Wesseling, K., and Goedhard, W. (1985b). The pressure dependent dynamic elasticity of 35 thoracic and 16 abdominal human aortas in vitro described by a five component model. *Journal of Biomechanics*, 18:613–620.

Lanir, Y. (1983). Constitutive equations for fibrous connective tissues. *J Biomech*, 16:1–12.

Laurent, S., Boutouyrie, P., Asmar, R., Gautier, I., Laloux, B., Guize, L., Ducimetiere, P., and Benetos, A. (2001). Aortic stiffness is an independent predictor of all-cause and cardiovascular mortality in hypertensive patients. *Hypertension*, 37:1236–1241.

Laursen, T. A. (2002). *Computational Contact and Impact Mechanics*. Springer, Berlin.

Laverty, H., Benson, C., Cartwright, E., Cross, M., Garland, C., Hammond, T., Holloway, C., McMahon, N., Milligan, J., Park, B., et al. (2011). How can we improve our understanding of cardiovascular safety liabilities to develop safer medicines? *British Journal of Pharmacology*, 163:675–693.

Lawton, P. F., Lee, M. D., Saunter, C. D., Girkin, J. M., McCarron, J. G., and Wilson, C. (2019). Vasotracker, a low-cost and open source pressure myograph system for vascular physiology. *Frontiers in Physiology*, 10(FEB):1–17.

Le, V. P., Kovacs, A., and Wagenseil, J. E. (2012). Measuring left ventricular pressure in late embryonic and neonatal mice. *Journal of Visualized Experiments*, 60.

Lee, S. and Schmid-Schönbein, G. (1996). Biomechanical model for the myogenic response in the microcirculation. Part 1 - - formulation and initial testing. *Journal of Biomechanical Engineering*, 118(2):145–151.

Leeson, C., Robinson, M., Francis, J., et al. (2006). Cardiovascular magnetic resonance imaging for non-invasive assessment of vascular function: validation against ultrasound. *Journal of Cardiovascular Magnetic Resonance*, 8:381–387.

Leloup, A. J. A., Van Hove, C. E., De Moudt, S., De Meyer, G. R. Y., De Keulenaer, G. W., and Fransen, P. (2019). Vascular smooth muscle cell contraction and relaxation in the isolated aorta: a critical regulator of large artery compliance. *Physiol Rep*, 7(4):e13934.

Leloup, A. J. A., Van Hove, C. E., Kurdi, A., De Moudt, S., Martinet, W., De Meyer, G. R. Y., and et al. (2016). A novel set-up for the ex vivo analysis of mechanical properties of mouse aortic segments stretched at physiological pressure and frequency. *J Physiol*, 594(21):6105–6115.

Li, X., Lyu, P., Ren, Y., An, J., and Dong, Y. (2017). Arterial stiffness and cognitive impairment. *Journal of the Neurological Sciences*, 380:1–10.

Liang, F. and Liu, H. (2005). A closed-loop lumped parameter computational model for human cardiovascular system. *JSME International Journal Series C Mechanical Systems, Machine Elements and Manufacturing*, 48(4):484–493.

Liang, H.-D. and Blomley, M. J. (2003). The role of ultrasound in molecular imaging. *The British Journal of Radiology*, 76(Spec No 2):S140–S150.

Libai, A. and Simmonds, J. (2005). *The nonlinear theory of elastic shells*. Cambridge University Press.

Liu, S. (1998). Influence of tensile strain on smooth muscle cell orientation in rat blood vessels. *Journal of Biomechanical Engineering*, 120(3):313–320.

Liu, T. (2014). A constitutive model for cytoskeletal contractility of smooth muscle cells. *Proc. R. Soc. A.*, 470(20130771).

Lohr, M. J., Sugerman, G. P., Kakaletsis, S., Lejeune, E., and Rausch, M. K. (2022). An introduction to the ogden model in biomechanics: benefits, implementation tools and limitations. *Philos Trans A Math Phys Eng Sci*, 380:20210365.

Lokshin, O. and Lanir, Y. (2009). Micro and macro rheology of planar tissues. *Biomaterials*, 30:3118–3127.

Lopez-Andres, N., Rousseau, A., Akhtar, R., Calvier, L., Inigo, C., Labat, C., et al. (2012). Cardiotrophin 1 is involved in cardiac, vascular, and renal fibrosis and dysfunction. *Hypertension*, 60(3):563–573.

Luo, J., Li, R., and Konofagou, E. (2012). Pulse wave imaging of the human carotid artery: an in vivo feasibility study. *IEEE Transactions on Ultrasonics, Ferroelectrics, and Frequency Control*, 59:174–181.

MacKay, D. (2003). *Information Theory, Inference and Learning Algorithms*. Cambridge University Press.

Markert, M., Trautmann, T., Krause, F., Cioaga, M., Mouriot, S., Wetzel, M., and Guth, B. D. (2018). A new telemetry-based system for assessing cardiovascular function in group-housed large animals. taking the 3rs to a new level with the evaluation of remote measurement via cloud data transmission. *Journal of Pharmacological and Toxicological Methods*, 93:90–97.

Markl, M., Chan, F., Alley, M., et al. (2003). Time-resolved three-dimensional phase-contrast mri. *Journal of Magnetic Resonance Imaging*, 17:499–506.

McEniery, C. M., Yasmin, Hall, I. R., Qasem, A., Wilkinson, I. B., Cockcroft, J. R., and Investigators, A. (2005). Normal vascular aging: differential effects on wave reflection and aortic pulse wave velocity: the anglo-cardiff collaborative trial (acct). *Journal of the American College of Cardiology*, 46:1753–1760.

Meurs, K., Miller, M., and Slater, M. (1996). Comparison of the indirect oscillometric and direct arterial methods for blood pressure measurements in anesthetized dogs. *Journal of the American Animal Hospital Association*, 32(6):471–475.

Mirramezani, M. and Shadden, S. C. (2020). A distributed lumped parameter model of blood flow. *Annals of Biomedical Engineering*, 48(12):2870–2886.

Mlika, R., Renard, Y., and Chouly, F. (2017). An unbiased nitsche's formulation of large deformation frictional contact and self-contact. *Computer Methods in Applied Mechanics and Engineering*, 325:265–288.

Mohiaddin, R. (1992). Magnetic resonance imaging of peripheral vascular disease. the state of the artery. *Echocardiography*, 9:553–577.

Mohiaddin, R. and Longmore, D. (1989). Mri studies of atherosclerotic vascular disease: structural evaluation and physiological measurements. *British Medical Bulletin*, 45(4):968–990.

Morgan, P., Brown, D. G., Lennard, S., Anderton, M. J., Barrett, J. C., Eriksson, U., Fidock, M., Hamrén, B., Johnson, A., March, R. E., et al. (2018). Impact of a five-dimensional framework on r&d productivity at astrazeneca. *Nature Reviews Drug Discovery*, 17:167.

Morimoto, B. H., Castelloe, E., and Fox, A. W. (2015). Safety pharmacology in drug discovery and development. In *Handbook of Experimental Pharmacology*, volume 229, pages 65–80. Springer.

Moulton, M. J., Hong, B. D., and Secomb, T. W. (2017). Simulation of left ventricular dynamics using a low-order mathematical model. *Cardiovascular engineering and technology*, 8(4):480–494.

Mulvany, M. J. and Halpern, W. (1977). Contractile properties of small arterial resistance vessels in spontaneously hypertensive and normotensive rats. *Circulation Research*, 41(1):19–26.

Murtada, S., Kroon, M., and Holzapfel, G. (2010). A calcium-driven mechanochemical model for prediction of force generation in smooth muscle. *Biomechanics and Modelling in Mechanobiology*, 9(6):749–762.

Murtada, S. C., Arner, A., and Holzapfel, G. A. (2012). Experiments and mechanochemical modeling of smooth muscle contraction: significance of filament overlap. *J Theor Biol*, 297:176–186.

Murtada, S.-I. and Holzapfel, G. A. (2014). Investigating the role of smooth muscle cells in large elastic arteries: a finite element analysis. *J. Theor. Biol.*, 358:1–10.

Musuamba, F. T., Skottheim Rusten, I., Lesage, R., Russo, G., Bursi, R., Emili, L., Wangorsch, G., Manolis, E., Karlsson, K. E., Kulesza, A., Courcelles, E., Boissel, J.-P., Rousseau, C. F., Voisin, E. M., Alessandrello, R., Curado, J. N., Dall'ara, M. E., Rodriguez, B., Pappalardo, F., and Geris, L. (2021). Scientific and regulatory evaluation of mechanistic in silico drug and disease models in drug development: Building model credibility. *CPT: Pharmacometrics & Systems Pharmacology*, 10(8):804–825.

Myatt, G. J., Ahlberg, E., Akahori, Y., Allen, D., Amberg, A., Anger, L. T., Aptula, A., Auerbach, S., Beilke, L., Bellion, P., et al. (2018). In silico toxicology protocols. *Regulatory Toxicology and Pharmacology*, 96:1–17.

Navindaran, K., Kang, J. S., and Moon, K. (2023). Techniques for characterizing mechanical properties of soft tissues. *Journal of the Mechanical Behavior of Biomedical Materials*, 138:105575.

Nedrelow, D. S., Townsend, J. M., and Detamore, M. S. (2023). The ogden model for hydrogels in tissue engineering: Modulus determination with compression to failure. *Journal of Biomechanics*, 152:111592.

Organisation for Economic Co-operation and Development (2020). Oecd guidelines for the testing of chemicals. OECD Publishing, Paris. Available at: https://www.oecd.org/chemicalsafety/testing/.

O'Rourke, M. F. and Hashimoto, J. (2007). Mechanical factors in arterial aging: a clinical perspective. *Journal of the American College of Cardiology*, 50:1–13.

Owens, R. (2023). Advanced tissue engineering for in vitro drug safety testing. *MRS Communications*, 13:685–694.

O'Connell, M. K., Murthy, S., Phan, S., Xu, C., Buchanan, J., Spilker, R., et al. (2008). The three-dimensional micro- and nanostructure of the aortic medial lamellar unit measured using 3d confocal and electron microscopy imaging. *Matrix Biol*, 27:171–181.

Passini, E., Britton, O. J., Lu, H., Rohrbacher, J., Hermans, A. N., Gallacher, D. J., Greig, R. J. H., Bueno-Orovio, A., and Rodriguez, B. (2017). Human in silico drug trials demonstrate higher accuracy than animal models in predicting clinical pro-arrhythmic cardiotoxicity. *Frontiers in Physiology*, 8:668.

Paul-Emile Roy, M. and George Rona, M. (1976). Recent advances in studies of cardiac structure and metabolism: Vol. 10, the metabolism of contraction. *American Heart Journal*, 92(3):411.

Polaka, S., Tella, J. D., Tekade, M., Sharma, M. C., and Tekade, R. K. (2022). Impact of ageing on the pharmacokinetics and pharmacodynamics of the drugs. In Tekade, R. K., editor, *Advances in Pharmaceutical Product Development and Research: Pharmacokinetics and Toxicokinetic Considerations*, volume 2, pages 241–261. Academic Press.

Poulios, K. and Renard, Y. (2015). An unconstrained integral approximation of large sliding frictional contact between deformable solids. *Computers and Structures*, 153:75–90.

Price, W. L. (1978). A controlled random search procedure for global optimization. *Toward Global Optimization 2*, pages 71–84.

Price, W. L. (1983). Global optimization by controlled random search. *Journal of Optimization Theory and Applications*, 40:333–348.

Qian, L. and Zhao, H. (2018). Nanoindentation of soft biological materials. *Micromachines*, 9(12):654.

Rachev, A. and Hayashi, K. (1999). Theoretical study of the effects of vascular smooth muscle contraction on strain and stress distributions in arteries. *Annals of Biomedical Engineering*, 27(4):459–468.

Rachev, A. and Shazly, T. (2019). A structure-based constitutive model of arterial tissue considering individual natural configurations of elastin and collagen. *J Mech Behav Biomed Mater*, 90:61–72.

Radmacher, M. (1997). Measuring the elastic properties of biological samples with the afm. *IEEE Engineering in Medicine and Biology Magazine*, 16(2):47–57.

Raju, V. G., Lakshmi, K. P., Jain, V. M., Kalidindi, A., and Padma, V. (2020). Study the influence of normalization/transformation process on the accuracy of supervised classification. In *2020 Third International Conference on Smart Systems and Inventive Technology (ICSSIT)*, pages 729–735.

Redfern, W. S., Ewart, L., Hammond, T. G., Bialecki, R., Kinter, L., and Lindgren, S. (2010). Impact and frequency of different toxicities throughout the pharmaceutical life cycle. *The Toxicologist*, 114:1081.

Redfern, W. S., Wakefield, I. D., Prior, H., Pollard, C. E., Hammond, T. G., and Valentin, J. P. (2002). Safety pharmacology - a progressive approach. *Fundamental and Clinical Pharmacology*, 16(3):161–173.

Rousseeuw, P. J. and Hubert, M. (2018). Anomaly detection by robust statistics. *Wiley Interdisciplinary Reviews: Data Mining and Knowledge Discovery*, 8(2):e1236.

Russell, W. M. S. and Burch, R. L. (1959). *The Principles of Humane Experimental Technique*. Methuen, London.

Sahani, A. K., Shah, M. I., Radhakrishnan, R., Joseph, J., and Sivaprakasam, M. (2016). An imageless ultrasound device to measure local and regional arterial stiffness. *IEEE Trans Biomed Circuits Syst*, 10(1):200–208.

Schmitz, A. and Böl, M. (2011). On a phenomenological model for active smooth muscle contraction. *Journal of Biomechanics*, 44(11):2090–2095.

Segers, P., Rietzschel, E. R., and Chirinos, J. A. (2020a). How to measure arterial stiffness in humans. *Arteriosclerosis, Thrombosis, and Vascular Biology*, 40(5).

Segers, P., Rietzschel, E, R., and Chirinos, J. A. (2020b). How to measure arterial stiffness in humans. *Arteriosclerosis, Thrombosis, and Vascular Biology*, 40(5).

Segers, P., Stergiopulos, N., Verdonck, P., and Verhoeven, R. (1997). Assessment of distributed arterial network models. *Medical and Biological Engineering and Computing*, 35(6):729–736.

Sehgel, N. L., Zhu, Y., Sun, Z., Trzeciakowski, J. P., Hong, Z., Hunter, W. C., and et al. (2013). Increased vascular smooth muscle cell stiffness: a novel mechanism for aortic stiffness in hypertension. *Am J Physiol Heart Circ Physiol*, 305(9):H1281–H1287.

Service, P. H. (1993). Position statement on the use of animals in research. NIH Guide. 26 February 1993.

Shameer, K., Johnson, K. W., Glicksberg, B. S., Dudley, J. T., and Sengupta, P. P. (2018). Machine learning in cardiovascular medicine: are we there yet? *Heart*, 104(14):1156–1164.

Shan, Y., Lin, J., Xu, P., et al. (2012). Comprehensive assessment of aortic compliance and brachial endothelial function using 3.0-t high-resolution mri: a feasibility study. *Journal of Computer Assisted Tomography*, 36:437–442.

Sharif, S., Visseren, F. L. J., Spiering, W., de Jong, P. A., Bots, M. L., and Westerink, J. (2019). Arterial stiffness as a risk factor for cardiovascular events and all-cause mortality in people with type 2 diabetes. *Diabet Med*, 36(9):1125–1132.

Shirwany, N. A. and Zou, M. H. (2010). Arterial stiffness: a brief review. *Acta Pharmacol Sin*, 31(10):1267–1276.

Silipo, R. and Marchesi, C. (1998). Artificial neural networks for automatic ecg analysis. *IEEE transactions on signal processing*, 46(5):1417–1425.

Simo, J. and Laursen, T. (1992). An augmented lagrangian treatment of contact problems involving friction. *Computers & Structures*, 42(1):97–116.

Singh, K. P., Bartolucci, A., and Bae, S. (2015). *Introduction to Statistical Analysis of Laboratory Data*. Wiley, 1st edition.

Sommer, G. and Holzapfel, G. A. (2012). 3d constitutive modeling of the biaxial mechanical response of intact and layer-dissected human carotid arteries. *Journal of the Mechanical Behavior of Biomedical Materials*, 5:116–128.

Stergiopulos, N., Porret, C. A., de Brouwer, S., and Meister, J. J. (1998). Arterial vasomotion: Effect of flow and evidence of nonlinear dynamics. *American Journal of Physiology-Heart and Circulatory Physiology*, 274(6):H1858–H1864.

Strasser, A., Niedermüller, H., Hofecker, G., and Laber, G. (1993). The effect of aging on laboratory values in dogs. *Journal of Veterinary Medicine Series A*, 40(10):720–730.

Stylianou, A., Kontomaris, S.-V., Grant, C., and Alexandratou, E. (2019). Atomic force microscopy on biological materials related to pathological conditions. *Scanning*, 2019:8452851.

Stålhand, J., Klarbring, A., and Holzapfel, G. (2008). Smooth muscle contraction: mechanochemical formulation for homogeneous finite strains. *Progress in Biophysics and Molecular Biology*, 96(1-3):465–481.

Stålhand, J., Klarbring, A., and Holzapfel, G. A. (2011). A mechanochemical 3d continuum model for smooth muscle contraction under finite strains. *J Theor Biol*, 268:120–130.

Stålhand, J., McMeeking, R. M., and Holzapfel, G. A. (2016). A microstructurally motivated model of arterial wall mechanics with mechanobiological implications. *Journal of the Mechanics and Physics of Solids*, 94:490–503.

Suga, H. and Sagawa, K. (1974). Instantaneous pressure-volume relationships and their ratio in the excised, supported canine left ventricle. *Circ Res*, 35(1):117–126.

Templeton, G. H., Platt, M. R., Willerson, J. T., and Weisfeldt, M. L. (1979). Influence of aging on left ventricular hemodynamics and stiffness in beagles. *Circulation Research*, 44(2):189–194.

Thiriet, M. and Parker, K. H. (2009). Physiology and pathology of the cardiovascular system: a physical perspective. In Formaggia, L., Quarteroni, A., and Veneziani, A., editors, *Cardiovascular Mathematics: Modeling and simulation of the circulatory system*, pages 1–45. Springer, Milano. InTech.

Thomas, B. and Sumam, K. S. (2016). Blood flow in human arterial system-a review. *Procedia Technology*, 24:339–346.

Tibshirani, R., Walther, G., and Hastie, T. (2001). Estimating the number of clusters in a data set via the gap statistic. *Journal of the Royal Statistical Society: Series B (Statistical Methodology)*, 63(2):411–423.

Timoshenko, S. P. and Goodier, J. N. (1970). *Theory of Elasticity*. McGraw-Hill.

Trabelsi, K. (2004). *On the modeling of thin plates in nonlinear elasticity*. PhD thesis, Université Pierre et Marie Curie-Paris VI.

Trame, M. N., Biliouris, K., Lesko, L. J., and Mettetal, J. T. (2016). Systems pharmacology to predict drug safety in drug development. *European Journal of Pharmaceutical Sciences*, 94:93–95.

Valentin, A., Cardamone, L., Baek, S., and Humphrey, J. D. (2009). Complementary vasoactivity and matrix remodelling in arterial adaptations to altered flow and pressure. *Journal of the Royal Society Interface*, 6(33):293–306.

Valentin, J.-P., Keisu, M., and Hammond, T. G. (2010). *Predicting Human Adverse Drug Reactions from Nonclinical Safety Studies*, chapter 4, pages 1–27. John Wiley & Sons, Ltd.

Valentin, J. P. and Redfern, W. S. (2017). Prevalence, frequency and impact of safety related issues throughout the pharmaceutical life cycle. *Toxicologist*, 150:170.

van de Waterbeemd, H. (2009). Improving compound quality through in vitro and in silico physicochemical profiling. *Chemistry & Biodiversity*, 6(10):1760–1766.

van der Bruggen, M. M., Reesink, K. D., Spronck, P. J. M., Bosboom, E. M. H., Heusinkveld, M. H. G., and Op't Roodt, J. (2021). An integrated set-up for ex vivo characterisation of biaxial murine artery biomechanics under pulsatile conditions. *Scientific Reports*, 11(1):2671.

van der Meer, R., Diamant, M., Westenberg, J., et al. (2007). Magnetic resonance assessment of aortic pulse wave velocity, aortic distensibility, and cardiac function in uncomplicated type 2 diabetes mellitus. *Journal of Cardiovascular Magnetic Resonance*, 9:645–651.

Versmissen, J., Mirabito Colafella, K. M., Koolen, S. L. W., and Danser, A. H. J. (2019). Vascular cardio-oncology: Vascular endothelial growth factor inhibitors and hypertension. *Cardiovascular Research*, 115(5):904–914.

Virtanen, P., Gommers, R., Oliphant, T. E., Haberland, M., Reddy, T., Cournapeau, D., Burovski, E., Peterson, P., Weckesser, W., Bright, J., van der Walt, S. J., Brett, M., Wilson, J., Millman, K. J., Mayorov, N., Nelson, A. R. J., Jones, E., Kern, R., Larson, E., Carey, C. J., Polat, İ., Feng, Y., Moore, E. W., VanderPlas, J., Laxalde,

D., Perktold, J., Cimrman, R., Henriksen, I., Quintero, E. A., Harris, C. R., Archibald, A. M., Ribeiro, A. H., Pedregosa, F., van Mulbregt, P., and SciPy 1.0 Contributors (2020). SciPy 1.0: Fundamental Algorithms for Scientific Computing in Python. *Nature Methods*, 17:261–272.

Vlachopoulos, C. (2010). Prediction of cardiovascular events and all-cause mortality with arterial stiffness: a systematic review and meta-analysis. *J Am Coll Cardiol*, 55(12):1318–1327.

Wang, M., Monticone, R. E., and Lakatta, E. G. (2016). Chapter 13 - the aging arterial wall. In Kaeberlein, M. R. and Martin, G. M., editors, *Handbook of the Biology of Aging (Eighth Edition)*, pages 359–389. Academic Press.

Weaver, R. J. and Valentin, J. P. (2019). Today's challenges to de-risk and predict drug safety in human "mind-the-gap". *Toxicological Sciences*, 167(2):307–321.

Weisbecker, H., Unterberger, M. J., and Holzapfel, G. A. (2015). Constitutive modelling of arteries considering fibre recruitment and three-dimensional fibre distribution. *Journal of the Royal Society Interface*, 12(106):20150111.

Wentland, A. L., Grist, T. M., and Wieben, O. (2014). Review of mri-based measurements of pulse wave velocity: a biomarker of arterial stiffness. *Cardiovascular Diagnosis and Therapy*, 4(2):193–206.

Westerhof, N., Elzinga, G., and Sipkema, P. (1971). An artificial arterial system for pumping hearts. *J Appl Physiol*, 31(5):776–81.

Williams, P. D. (1990). The role of pharmacological profiling in safety assessment. *Regulatory Toxicology and Pharmacology*, 12(3, Part 2):204–211.

Wolinsky, H. and Glagov, S. (1967). A lamellar unit of aortic medial structure and function in mammals. *Circ Res*, 20:99–111.

Wriggers, P. (2006). *Computational Contact Mechanics (2nd edn)*. Springer, Berlin.

Wu, G., Gotthardt, M., and Gollasch, M. (2020). Assessment of nanoindentation in stiffness measurement of soft biomaterials: kidney, liver, spleen and uterus. *Scientific Reports*, 10(1):18784.

Wuyts, F. L., Vanhuyse, V. J., Langewouters, G. J., Decraemer, W. F., Raman, E. R., and Buyle, S. (1995). Elastic properties of human aortas in relation to age and atherosclerosis: a structural model. *Phys Med Biol*, 40:1577–1597.

Yan, H., Jiang, Y., Zheng, J., Peng, C., and Li, Q. (2006). A multilayer perceptron-based medical decision support system for heart disease diagnosis. *Expert Systems with Applications*, 30(2):272–281.

Yang, J., Clark, J., Bryan, R., and Robertson, C. (2003a). The myogenic response in isolated rat cerebrovascular arteries: smooth muscle cell model. *Medical Engineering & Physics*, 25(8):691–709.

Yang, J., Clark, J., Bryan, R., and Robertson, C. (2003b). The myogenic response in isolated rat cerebrovascular arteries: vessel model. *Medical Engineering & Physics*, 25(8):711–717.

Yazdan Mehr, M., Bahrami, A., Fischer, H., Gielen, S., Corbeij, R., Driel, W., and Zhang, G. (2015). An overview of scanning acoustic microscope a reliable method for non-destructive failure analysis of microelectronic components. *2015 16th International Conference on Thermal, Mechanical and Multi-Physics Simulation and Experiments in Microelectronics and Microsystems*, pages 1–4.

Yosibash, Z. and Priel, E. (2012). Artery active mechanical response: High order finite element implementation and investigation. *Computer Methods in Applied Mechanics and Engineering*, 237-240:51–66.

Yu, H. (2020). Scanning acoustic microscopy for material evaluation. *Applied Microscopy*, 50.

Yu, Y. C., Boston, J., Simaan, M., and Antaki, J. (1998). Estimation of systemic vascular bed features for artificial heart control. *IEEE Transactions on Automatic Control*, 43:765–777.

Zhang, Y., Agnoletti, D., Xu, Y., Wang, J. G., Blacher, J., and Safar, M. E. (2014). Carotid-femoral pulse wave velocity in the elderly. *J Hypertens*, 32(8):1572–1576.

Zulliger, M. A., Rachev, A., and Stergiopulos, N. (2004). A constitutive formulation of arterial mechanics including vascular smooth muscle tone. *American Journal of Physiology-Heart and Circulatory Physiology*, 287(3):H1335–H1344.